Application of Methods to Characterize V_{S30} in Alabama

by

Patricia S. Carcamo

A dissertation submitted to the Graduate Faculty of
Auburn University
in partial fulfillment of the
requirements for the Degree of
Doctor of Philosophy

Auburn, Alabama
August 6, 2022

Keywords: Shear wave velocity, MASW, Seismic Refraction, P-wave Method, Proxy

Approved by

Jack Montgomery, Ph. D., P.E., Chair, Assistant Professor, Department of Civil Engineering
J. Brian Anderson, Ph. D., P.E., Associate Professor, Department of Civil Engineering
Kadir Sener, Ph. D., P.E., Assistant Professor, Department of Civil Engineering
Lorraine Wolf, Ph. D., Emeritus Professor, Department of Geosciences

ABSTRACT

One of the most important characteristics of a soil that is a basis for seismic analysis, is shear wave velocity (V_S). V_S has proved to be a valuable tool for site response analysis for seismic design since it has the potential to significantly affect the amplitude and frequency content of expected ground motion. Understanding how the site characteristics will affect the seismic response is necessary for designing robust structures for seismic hazards. Several codes and standards have considered the impacts of site characteristics on anticipated ground vibrations through the site classification. Current design codes have incorporated the V_S profile of the soil in the upper 30 m, known as V_{S30}, as a proxy for the stiffness of the soil and its response under dynamic loading, taking into account the potential amplification and changes in the frequency content of the ground motion.

Direct methods to measure V_{S30} have been developed worldwide through invasive and non-invasive testing. Invasive methods require excavations, in most cases, to be conducted and specific equipment to develop V_{S30} measurements. Non-invasive testing has become increasingly popular due to its quick implementation and relatively low cost compared to invasive testing methods. Researchers have developed different methods to estimate V_S in cases where direct methods are not available or cannot be applied. The indirect methods rely on a property or characteristic of the soil, such as fundamental frequency, geology, and topographic slope, which is correlated with V_{S30} measurements available in the area of study. However, V_S testing is less common in regions with relatively low seismicity, like Alabama, which challenges validating any indirect approaches developed for these areas. The absence of measurements also prevents the generation of local correlations and the evaluation of the validity of alternative methodologies.

Direct and indirect methods were applied to several locations in Alabama to compute and estimate V_{S30}. The direct methods applied in this study include multichannel analysis of surface waves (MASW) and seismic refraction, while the indirect methods used are the P-wave seismogram method, HVSR correlations, joint inversion with R-wave ellipticity, and proxy methods that were applied to sites and seismic stations. The different approaches were applied to different sites and seismic stations located in Alabama and surrounding states and compared to provide recommendations. Direct methods were applied to a total of 11 sites in this study, and another four V_{S30} values were collected from the publicly available profiles. Indirect methods were applied to the seismic stations available in the state.

The measurements and estimates presented in this work are preliminary approaches to providing V_{S30} values for Alabama. From the results generated by this study, the use of direct methods such as MASW is recommended because they are more reliable. MASW combined with R-wave ellipticity can provide additional constraints on the inversion. The P-wave seismogram method is very useful in sites where permanent or longer-term seismometer installations are available. When using the P-wave seismogram method in Alabama, it should be considered using the original amplitude ratio correlation and the proposed lower boundary of the 95% confidence interval. However, several recorded earthquakes are required, which limits the application of the method. Proxy methods can be employed at sites without any measurements but tend to underestimate V_{S30} at stiffer sites. All three proxy methods should be considered in the Gulf Coast region, while the hybrid geology-slope and topographic methods should be considered in Southern Appalachian and Central Tennessee regions. Furthermore, incorporating new measurements of V_{S30}, especially in the north part of the state where the seismic hazard is higher, would allow an

accurate assessment of the reliability of the proxy methods and potential modifications to the amplitude ratio correlation for the P-wave method for use in Alabama.

ACKNOWLEDGEMENTS

This journey would not be possible without the help and support of many people that joined me during this process. I would like to start by thanking Dr. Montgomery for giving me this opportunity to work with him, for his incredible patience, and for his amazing guidance thought the research. I believe that Dr. Montgomery's enthusiasm in all his classes and care for all his students inspire the geotechnical group daily to work as a team.

I would like to thank my committee members and the University reader: Dr. Wolf, Dr. Anderson, Dr. Sener, and Dr. Beidaghi, for accepting being part of my committee, for the time taken to review this work, and for the insightful comments provided to improve this research. To Dr. Wolf for the insightful perspective provided for this research and the help to make me think outside of the box to find new ways to approach the problem. To Dr. Anderson for his mentorship and much-appreciated advice for my student and professional life.

This research would have been impossible without the funding provided by the Alabama Department of Transportation and the AU Highway Research Center. I would like to thank some collaborators for their hard work: Dan Jackson, Michael Kiernan, Ashton Babb, Tyler Belk, Chukwuma Charles Okafor, Mengwei Xuan, and Olaniyi Afolayan. Without them, the measurement taken for this study would not have been possible. I will always be grateful for their help, and all the fun moments we shared during the field work.

The decision to start this Ph.D. leaving my country was not easy. My dearest friends: Pipe & Pazi, Riffo & Mon, Oscar & Bea, Pauli & Mauro, Lore &Victor, Anita & Jorge, and Anto, your friendship and encouragement through the distance smooth this transition and helped me find resilience during all this process.

The beginning of this journey not have been possible without Victor. So, thank you, my friend, for convincing me to take this path and for your advice. Arriving at Auburn would not have been easy without Anjan, who helped us settle in and offered his friendship. During my years at Auburn, I met some great people. I want to give a special thanks to my girls: Sylwia, Jaime, Billur, Faustina, Veronica, and Olga. The friendship and example of these fantastic women inspired me every day and will continue to do so in the future. To my friends: Carlos, Devdeep, Wu, Alfredo & Maria, Evelyn, Gabriel, and Ale.

To my fiancé Pablo for his incredible patience during all this process and for always encouraging me. I know it was not easy sometimes, but your love got me through all the difficult moments, and I could not have made it without you. I would like to thank your family for always being there. To Nala for her company during all those late nights processing data and writing. To my father, Hector, and my brothers, Roberto and Miguel, for always believing in me and providing their support.

TABLE OF CONTENTS

LIST OF FIGURES

LIST OF TABLES

CHAPTER 1 INTRODUCTION

1.1 BACKGROUND OF SHEAR WAVE VELOCITY

Shear wave velocity (V_S) profiles are critical inputs for site response analyses because they considerably influence the amplitude and frequency content of predicted ground motion (e.g., Abrahamson et al., 2008; Garofalo et al., 2016; Teague & Cox, 2016). Common input parameters for seismic site response analyses include the shear stiffness and thickness of the soil layers, the impedance ratio between bedrock and the soil, and estimates of damping (Hunter & Crow, 2012). The shear stiffness relates directly to the V_S and soil density. V_S is commonly used to perform site amplification studies, semi-empirical ground motion modeling, and assessment of soil aging. In addition V_S is employed as input for semi-empirical liquefaction triggering and soil-structure interaction models (Wang et al., 2019).

This influence of the V_S profile at a site has been incorporated into seismic design codes through site class estimates meant to help account for possible amplification and changes in the frequency content of the ground motion (e.g., Borcherdt, 2012; Dobry et al., 2000; Holzer et al., 2005). Building codes and standards often rely on the V_S profile of the upper 30 m (100 ft), V_{S30}, as a proxy for these local site effects through site classifications based on this parameter.

V_{S30} values can be obtained from V_S measurements performed at the site (direct method) or correlated with other *in situ* measurements (indirect method). Direct measurements of V_{S30} values are more reliable (e.g., Comina et al., 2011; Garofalo et al., 2016), but in regions with relatively low seismic activity, such as Alabama, V_S testing is less common. In fact, there are very few publicly available V_S profiles for sites in Alabama. McPhillips et al. (2020) compiled V_S data from government sponsored reports from the U.S. Geological Survey (USGS), online databases, and

scientific and engineering journals. This work compiled 4,369 values of V_{S30} in the United States and found only one profile in Alabama with two near the border in Tennessee, as shown in Figure 1-1.

Figure 1-1: V_S profiles in Alabama and surrounding states (McPhillips et al., 2020)

The direct methods to measure V_{S30} can be classified into invasive and non-invasive tests. Non-invasive tests for V_S profiles (e.g., surface-based seismic surveys or microtremor recordings) can often be performed more quickly and at a lower cost than invasive tests (e.g., borehole-based methods or *in situ* tests). However, the non-invasive tests can have more uncertainty than invasive tests and may need to be validated with invasive tests or other data sources.

In cases where direct methods are not available, researchers have developed different approaches to estimate V_{S30} through indirect methods. Indirect methods are based on correlations between a property of the soil (e.g., amplification, fundamental frequency, geology, topographic slope) and V_{S30} measurements available in the study area. Most of these methods were developed in active seismic regions where more V_{S30} measurements are accessible, then expanded to other regions and calibrated with the existing data. Among the indirect methods available are the P-wave seismogram method, Horizontal to Vertical Spectral Ratio (HVSR) correlations, and proxy methods (e.g., correlations with topography and/or geology). Indirect methods can be a valuable way to obtain preliminary V_{S30} estimates, but they need to be validated for the regions where they will be applied through comparison with direct measurements. However, V_S testing is less common in areas with relatively low seismicity, such as Alabama, and validating these indirect methods for these regions is challenging. The lack of measurements also means that local correlations cannot be generated, and the reliability of other different approaches cannot be addressed.

1.2 SEISMIC WAVE PROPAGATION

There are two types of seismic waves: body waves and surface waves. The body waves are named this way because they travel through the body of the Earth, while the surface waves, as their name says, can only travel along the Earth's surface. Body waves are divided into compressional waves and shear waves (Hunter & Crow, 2012) based on the direction of particle movement relative to wave propagation. Surface waves can be classified as Rayleigh waves (R-waves) and Love waves (L-waves).

Compressional or primary waves (P-wave) travel through longitudinal waves. The particle motion of the P-wave is in the same direction as the travel direction of the wave (Hobiger et al.,

2012), as shown in Figure 1-2. The shear waves or secondary waves (S-waves) have particle motion transverse to travel direction and can have vertical and horizontal components (Figure 1-2). The P-wave travels faster than the S-wave in soil and rock. Besides the particle motion direction and speed, the main difference between the body waves and shear waves is the medium in which the wave can propagate. The S-wave cannot transmit in a fluid medium, while P-waves can.

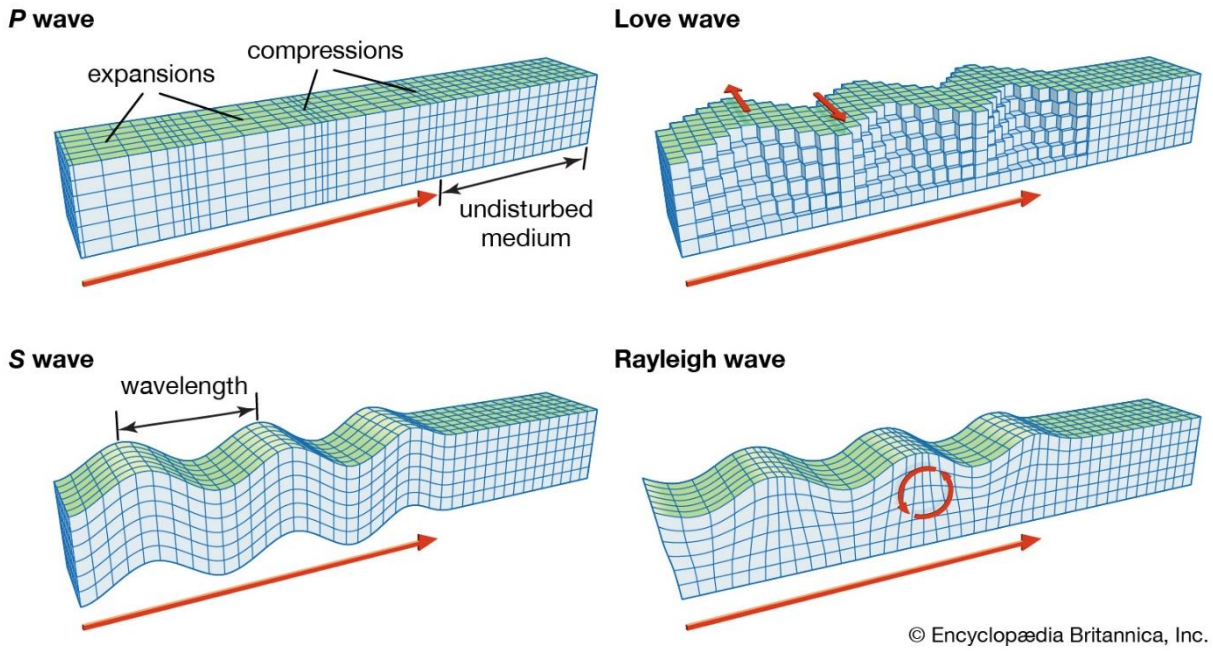

Figure 1-2: Types of seismic waves (Science Learning Hub – Pokapū Akoranga Pūtaiao, 2014)

Surface waves are also divided into several types of waves. The most common are R-waves and L-waves. Surface waves have amplitudes that decrease with depth and are dispersive in layered soils, meaning their velocity will vary with frequency. R-waves are characterized by an elliptical prograde or retrograde motion of the particle. L-waves have a particle motion horizontal with a movement perpendicular to the direction of propagation. Due to their elliptical movement, R-waves have horizontal and vertical components, while L-waves have only horizontal components (Figure 1-2).

1.3 SEISMICITY OF ALABAMA

The seismicity of Alabama is closely affected by two of the most active zones in the eastern United States, the New Madrid and the Eastern Tennessee seismic zone, as shown in the hazard map (Figure 1-3). These zones influence the seismic hazard in the state, and the effects of this influence decrease towards the south of the state. The seismic hazard has been incorporated into several design codes and standards through the ground motion maps. The hazard map, shown in Figure 1-3, was constructed based on the most recent USGS models, considering the seismicity and the fault-slip rates (USGS, 2018).

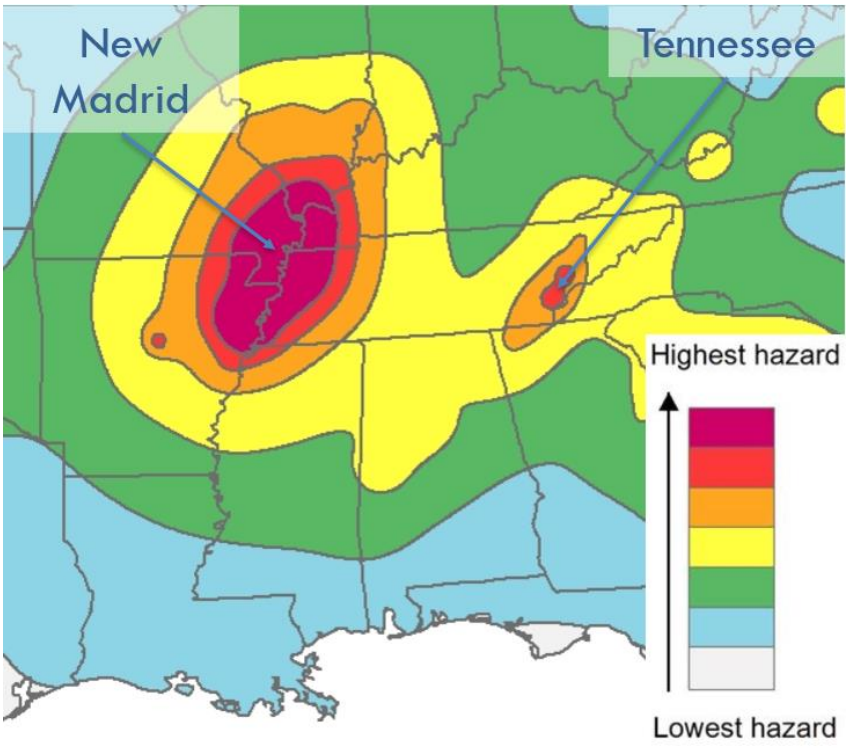

Figure 1-3: Hazard map and identification of faults located near Alabama (USGS, 2018)

The New Madrid seismic zone (NMSZ) is the most active seismic area in the eastern United States (Liu & Zoback, 1997). The zone is characterized by two parallel strike slip faults that border the Reelfoot rift, along with a cross-over reverse fault (Sexton & B, 1986; Tuttle, 2002). The

NMSZ has intraplate activity with earthquakes of small to moderate intensity. The largest earthquakes experienced in this region occurred in the winter of 1811 and 1812, with magnitudes greater than 7 (Liu & Zoback, 1997). The damage caused by the earthquakes included settlements, landslides, liquefaction, structural damage, bank failures in the Mississippi River, uplift, and subsidence of large tracts of the Mississippi River. It has been estimated that the probability of occurrence of an earthquake of magnitude six or greater is between 25-40% in the next 50 years (USGS, 2022).

The Eastern Tennessee seismic zone (ETSZ) is the second most active zone in the eastern United States based on the seismic strain energy released (Powell et al., 1994). This seismic zone is in a mountainous region in Georgia, Tennessee, and Alabama. The seismic zone area is approximately 50 km wide and 300 km long (Dunn & Chapman, 2006). The ETSZ has a complex geology with focal mechanism controlled by strike-slip displacements and a deep crustal break. (King & Zietz, 1978; Powell & Thomas, 2016). The earthquakes in this zone have not exceeded a magnitude of 4.6, with depths ranging between 5 to 26 km (Chapman et al., 1997).

1.4 SITE CLASSIFICATION AND V_{S30}

Designing resilient structures for seismic hazards requires understanding how the site conditions will influence the seismic response. Many codes and standards have accounted for the effects of site conditions on the expected ground motions through the site class, which serves as a proxy for the stiffness of the soil. Typical site classification ranges from hard rock (Type A) to very soft soil (type F) on most of the codes and standards (AASHTO, 2020; ASCE/SEI, 2022; ICC, 2015).

The National Earthquake Hazards Reduction Program (NEHRP) *Provisions* have provided technical resources to translate research results into design standards for improving seismic design and construction practices since its first edition in 2009. The latest version of the NEHRP *Recommended Seismic Provisions for New Buildings and Other Structures* (NEHRP, 2020) provides the specifications for seismic design criteria and requirements adopted by the Minimum Design Loads and Associated Criteria for Buildings and Other Structures (ASCE/SEI, 2022).

NEHRP *Provisions* (NEHRP, 2020) provided one of the most significant changes to site class definitions of Chapter 20 of ASCE 7-22 (2022) by performing the site classification only using $V_{S30,}$ as shown in Table 1-1. Another change in the standard is the addition of 3 new sites classes (BC, CD, and DE). The new sites classes allow a better resolution of the site class and site amplification for similar site characteristics.

Table 1-1: Site class definitions (NEHRP, 2020)

Site Class	**V_{S30} Calculated Using Measured or Estimated V_S Profile**
A. Hard Rock	> 1,524 m/s (5,000 ft/s)
B. Medium hard	> 914.4 m/s (3,000ft/s) to 1,524 m/s (5,000 ft/)
BC. Soft rock	> 640.1 m/s (2,100 ft/s) to 914.4 m/s (3,000 ft/s)
C. Very dense sand or hard clay	> 442 m/s (1,450 ft/s) to 640.1 m/s (2,100 ft/s)
CD. Dense sand or very stiff clay	> 304.8 m/s (1,000 ft/s) to 442 m/s (1,450 ft/s)
D. Medium dense sand or stiff clay	> 213.4 m/s (700 ft/s) to 304.8 m/s (1,000 ft/s)
DE. Loose sand or medium stiff clay	> 152.4 m/s (500 ft/s) to 213.4 m/s (700 ft/s)
E. Very loose sand or soft clay	< 152.4 m/s (500 ft/s)
F. Soils requiring site response analysis	

The NEHRP *Provisions* (NEHRP, 2020) do not provide specific details on the method used to measure shear wave velocity. However, if the V_S profile is not measured, it can be estimated using correlations with other tests, such as the Standard Penetration Test (SPT), Cone Penetration Test (CPT), shear strength, or other geotechnical parameters. If correlations are used the estimated

V_{S30} shall be estimated using ±30% range $(V_{S30}/1.3 - 1.3V_{S30})$ due to the uncertainty inherent to the correlations. A factor less than 1.3 may be applied if approved by local building officials using specific local correlations than have been shown to have a higher accuracy (NEHRP, 2020).

The computation of V_{S30} is shown in the equation 1.1.

$$V_{S30} = \frac{\sum_{i=1}^{n} d_i}{\sum_{i=1}^{n} \frac{d_i}{V_{Si}}} \quad 1.1$$

Where:

$\sum_{i=1}^{n} d_i = 30m$

V_{Si} = shear wave velocity in m/s of a layer

d_i = thickness of each individual layer between 0 and 30m

1.5 SEISMIC HAZARD ASSESSMENT

The seismic hazard is commonly assessed for a given site using design response spectrums, which depend on the site class. The new provisions from NEHRP provide a Multi-Period Design Response Spectrum (MPDR) and a Two-Period Design Response Spectrum (TPDR) for site classes from A to E. When the site is classified as site class F, a site-specific ground motion procedure is required for seismic design. This procedure requires a ground motion hazard analysis, including regional tectonic setting, geology, seismic motion recurrence rates, and maximum magnitudes of earthquakes on known faults, among other requirements (NEHRP, 2020).

The MPDR spectrum is the general method and uses the 5%-damped design spectral response acceleration, S_a, taken as two-thirds of the multi-period 5%-damped risk-targeted maximum considered earthquake (MCE_R) response spectrum of the USGS Seismic Design

Geodatabase (Luco et al., 2021). The spectral acceleration response obtained from the geodatabase is dependent on the site classification, as shown in Figure 1-4. When values of the multi-period 5%-damped MCE_R response spectrum are not available, the provisions permit the use of the TPDR spectrum (Figure 1-5), which can be developed based on the site classification and spectral response acceleration parameters SM_S and SM_1 from the USGS Seismic Design Geodatabase (Luco et al., 2021) or the maps included in the provisions. The site-specific MCE_R response spectrum is determined from probabilistic or deterministic ground motions analysis for each period. The design response spectrum for the site-specific analysis is taken as two-thirds of the MCE_R response spectrum.

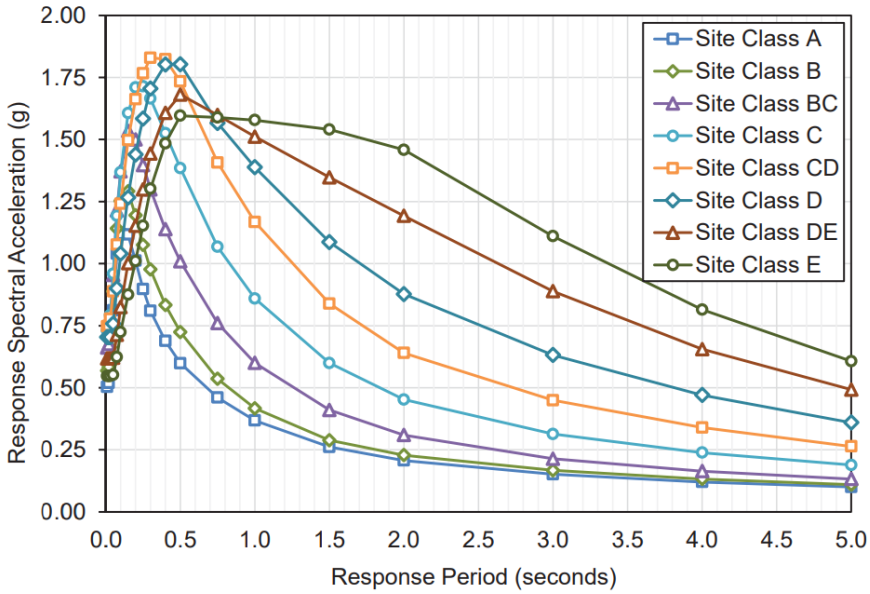

Figure 1-4: Plots of the MPRS (up to 5 seconds) proposed for the lower limit deterministic MCER response spectra of Table 21.2-1 (up to 5.0 seconds) of the *2020 NEHRP Provisions* and *ASCE 7-22* (Kircher et al., 2019)

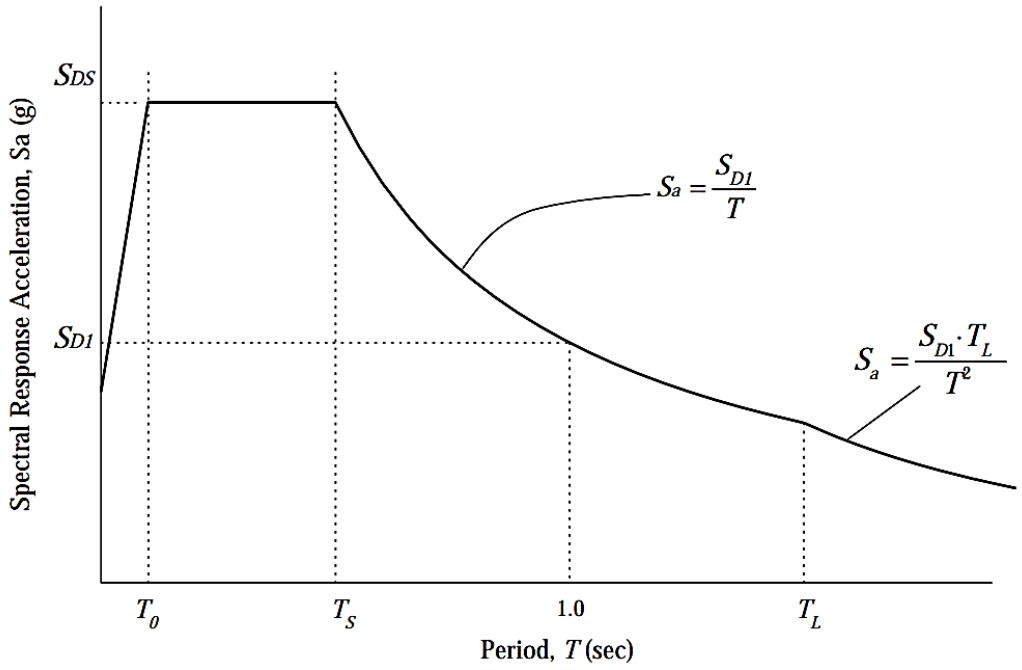

Figure 1-5: Two-period design response spectrum (NEHRP, 2020)

Seismic Design Category (SDC) is a classification assigned to a structure based on its Risk Category and the severity of the design earthquake ground motion at a specific site (ASCE/SEI, 2022). Risk Categories are assigned to buildings and other structures based on the risk for human life, health, and welfare associated with the damage or failure of the structures (ASCE/SEI, 2022). This risk is from I to IV, I being the lower risk and IV for essential facilities, as shown in Table 1-2.

SDC can be assigned to any structure based on the mapped spectral acceleration design parameters SD_S (short period) and SD_1(1-s period). SDCs can be based on either of the design response acceleration parameters (SD_S or SD_1), following the limitations of

Table 1-3Table 1-4. Using these tables, the design categories are dependent on the risk category and vary from A to D. For structures with Risk Category I, II, or III and spectral acceleration parameter S_1 greater or equal to 0.75, SDC E shall be assigned, while for Risk

Category IV and spectral acceleration parameter S_1 greater or equal to 0.75, SDC F is assigned. With these requirements, SDCs vary from A to E.

Table 1-2: Risk Category of Buildings and Other Structures for Flood, Wind, Snow, Earthquake, and Ice Loads (Table 1.5-1, ASCE/SEI, 2022)

Use or Occupancy of Buildings and Structures	**Risk Category**
Buildings and other structures that represent low risk to human life in the event of failure	I
All buildings and other structures except those listed in Risk Categories I, III, and IV	II
Buildings and other structures, the failure of which could pose a substantial risk to human life	III
Buildings and other structures, not included in Risk Category IV, with potential to cause a substantial economic impact and/or mass disruption of day-to-day civilian life in the event of failure	
Buildings and other structures not included in Risk Category V (including, but not limited to, facilities that manufacture, process, handle, store, use, or dispose of such substances as hazardous fuels, hazardous chemicals, hazardous waste, or explosives) containing toxic or explosive substances where the quantity of the material exceeds a threshold quantity established by the Authority Having Jurisdiction and is sufficient to pose a threat to the public if released	
Buildings and other structures, the failure of which could pose a substantial hazard to the community	IV
Buildings and other structures (including, but not limited to, facilities that manufacture, process, handle, store, use, or dispose of such substances as hazardous fuels, hazardous chemicals, or hazardous waste) containing sufficient quantities of highly toxic substances where the quantity of the material exceeds a threshold quantity established by the Authority Having Jurisdiction and is sufficient to pose a threat to the public if released	
Buildings and other structures required to maintain the functionality of other Risk Category IV structures	

Table 1-3: Seismic Design Category Based on Short-Period Response Acceleration Parameter (Table 11.6-1, ASCE/SEI, 2022)

Value of S_{DS}	Risk Category	
	I or II or III	IV
$S_{DS} < 0.167$	A	A
$0.167 \leq S_{DS} < 0.330$	B	C
$0.330 \leq S_{DS} < 0.500$	C	D
$0.500 \leq S_{DS}$	D	D

Table 1-4: Seismic Design Category Based on 1-s-Period Response Acceleration Parameter (Table 11.6-2, ASCE/SEI, 2022)

Value of S_{D1}	Risk Category	
	I or II or III	IV
$S_{D1} < 0.067$	A	A
$0.067 \leq S_{D1} < 0.133$	B	C
$0.133 \leq S_{D1} < 0.200$	C	D
$0.200 \leq S_{D1}$	D	D

The SDCs establish the design requirements and structural system limitations for structural buildings and nonstructural elements. Structures assigned with SDC A need only to comply with structural integrity. Seismic Force-Resisting Systems (Section 12.2.1 ASCE/SEI, 2022) include bearing walls, special building frames, and moment-resisting frames. Specific limitations regarding the application of these systems for different structural heights apply to SDC from B to F. These design requirements include the application of seismic loads in the orthogonal directions and the combination of horizontal and vertical components for the design. Additional requirements for geotechnical investigations apply to SDCs from C through F, that include evaluation of slope stability, liquefaction, settlements, and surface displacement and recommendations for foundation designs.

These examples show the structural design requirements for acceptable seismic performance depending on the Seismic Design Categories, which is a function of both the Risk Category and the site classification, including the response acceleration parameters. The design requirements are more restrictive for SDC C through F, being E and F the most restrictive cases. Determining the site class from shear wave velocity profiles either from direct measurements or validated correlations is a critical step in defining the Seismic Design Category and is an essential parameter for the adequate seismic design of structures.

1.6 MOTIVATIONS AND GOALS

Earthquake damage to essential infrastructure facilities can have a high impact on communities and the national transportation network. Bridges are essential transportation infrastructure, and adequate seismic design of all its components is to be achieved using the current and most updated provisions that account for seismic hazards and the expected ground motions during the event of an earthquake. Seismic demand on bridges differs from building structures, and the stiffness or ductility of the structural systems plays a fundamental role in their structural behavior when subjected to earthquake loads. Shear wave velocity measurements in the upper 30 m are used for site classification and are an essential soil parameter for assessing the seismic hazard. National seismic design maps in conjunction with the site classification are the first input when determining design response spectrums for a specific site. Therefore, adequate site classification is a critical parameter in predicting site response and performing acceptable structural seismic design.

V_S profiles, especially in the upper 30 m, have a fundamental role in site response analysis and site characterization. As discussed before, different direct and indirect methods have been

created to measure and estimate V_{S30}. However, V_S testing is less common in areas with relatively low seismicity, such as Alabama. The lack of data in Alabama means that indirect methods are not calibrated for use in this region. There is a need to collect V_{S30} measurements across the state to evaluate the applicability of the indirect methods and assess which direct methods can be effectively applied in different areas. Evaluating and comparing the different approaches will allow recommendations on suitable approaches for different regions of the state to be developed.

This work aims to evaluate different non-invasive techniques to measure and estimate V_{S30} in Alabama, compare the results, highlight the benefits and drawbacks of each method, and provide recommendations and data for future studies seeking to estimate V_{S30} in Alabama. While the study is focused on data collected in Alabama and surrounding states, the findings of this study will also be useful for other regions with similar geologic conditions and low seismicity. The first goal of this study is to apply the P-wave seismogram method to recordings from seismic stations in Alabama and surrounding states. This method has not previously been applied in low seismicity regions where fewer recordings are available. An implementation approach to applying this method in Alabama is developed and described in this study. The second goal of this study is to compare the values acquired using the P-wave seismogram method with geotechnical data and geophysical measurements at these sites. Comparing the different approaches will allow assessing the accuracy and uncertainty of the P-wave seismogram method. The third goal is to assess the applicability of previously developed proxy methods to sites in Alabama. The results will then be combined to provide information on the benefits and drawbacks of each of the approaches to estimate V_{S30} and offer recommendations on which method to apply in different regions in Alabama. This study will also provide a suite of V_{S30} measurements at different sites in the state.

Future researchers can use these measurements to validate new approaches or to develop new proxy methods.

1.7 RESEARCH OBJECTIVES

Primary research objectives for this dissertation are outlined below:

- Develop a P-wave seismogram approach that can be applied to areas with relatively low seismic activity
- Assess the accuracy and uncertainty in V_{S30} estimates from the proposed P-wave seismogram method using geotechnical and geophysical measurements at selected locations
- Evaluate the applicability of various proxy methods for estimating V_{S30} to Alabama
- Compare the different methods and provide recommendations
- Provide a suite of V_{S30} measurements at sites across Alabama.

1.8 DISSERTATION ORGANIZATION

This dissertation is divided into seven chapters as follows:

- Chapter 1 – Introduction: This chapter provides general background on the importance of V_S for engineering practices and different methods to compute it. Motivation for this research and objectives are delivered. The organization of content within this dissertation is also outlined.
- Chapter 2 – Literature Review: This chapter describes the methods available to compute and estimate V_S for a site. The chapter focuses on non-invasive methods using direct and indirect methods to measure and estimate V_{S30}, respectively. The direct

methods include surface wave methods and seismic refraction. The indirect methods include the P-wave seismogram method, HVSR, R-wave ellipticity, and proxy methods.

- Chapter 3 – Methodology: This chapter provides the methodology used to compute and estimate the V_{S30} profiles using direct and indirect methods. The area of study and the data collection and processing used for each of the methods applied are outlined.
- Chapter 4 – Results of Direct Methods: This chapter shows the results of V_{S30} from Surface waves and seismic refraction analysis. Each site describes the location, geology, and specific data collection parameters.
- Chapter 5 – Results of Indirect Methods: This chapter shows the results of V_{S30} using indirect methods such as P-wave seismogram, HVSR, R-wave ellipticity, and proxy methods.
- Chapter 6 – Comparison of Different Methods: This chapter compares the results using the direct and indirect methods for the sites selected for the study.
- Chapter 7 –Conclusions and Future Research: This chapter summarizes the research conclusions covered in this dissertation. In addition, the relevance of research findings to practicing engineers and potential options for future research are discussed.

CHAPTER 2 LITERATURE REVIEW

2.1 INTRODUCTION

Due to the importance of V_{S30} as input for seismic hazard analyses and site amplification, researchers worldwide have developed different techniques to estimate and measure this parameter. The studies have been performed at specific locations for site characterization and across large areas to develop V_{S30} maps for specific regions or even countries. Several methods can be used to compute V_S profiles and, therefore, to calculate V_{S30}. This chapter describes how different methods are used worldwide to calculate and estimate V_{S30}. A few examples are provided in the next section.

The direct methods used to compute V_{S30} can be classified as invasive and non-invasive. Invasive tests (e.g., downhole, cross-hole, suspension logging) require the insertion of the equipment used to measure the V_S profile into the soil. A boring (drill hole) is usually required depending on the test to be implemented. Non-invasive tests (e.g., refraction, surface wave analysis) involve placing an array of sensors along the ground surface and recording seismic waves from active and/or passive sources. Non-invasive tests do not require drilling and can be completed with minimal disturbance to the site. The data obtained from non-invasive testing contribute essential information about wave propagation across a site (Griffiths et al., 2016). The logistics behind the transportation of equipment to the site and the need for drilling lead to higher costs and longer working hours when compared with non-invasive tests (Hollender et al., 2018). Invasive testing directly measures V_S over a relatively small volume of soil or rock. At the same time, non-invasive tests often average over a wider area based on the setup of the testing devices. Non-invasive testing often requires inversion to obtain V_S profiles, which can introduce uncertainty due

to the non-uniqueness of the solution. This study is focused on non-invasive methods because they have proved to be economical and time effective while providing reliable estimations as invasive approaches (Garofalo et al., 2016a; Foti et al., 2016).

The methods reviewed in detail in this research will be classified as direct and indirect. The direct methods can measure V_{S30} through direct measurement of the V_S profile. The indirect methods estimate V_{S30} using correlations between a property or characteristic of the site and V_{S30}. The direct methods considered in this study include Multichannel Analysis of Seismic Waves (MASW) and seismic refraction. The indirect methods include the P-wave seismogram, HVSR, R-wave ellipticity, and proxy methods. For all the methods, details about the data collection, signal processing, inversion, and examples of the results obtained by applying these methods are presented in the following sections.

2.2 PREVIOUS STUDIES

Many previous studies have examined and compared different approaches to measure and estimate V_S at both the local and regional scales. Some of the regions where these studies have been completed include India (Anbazhagan & Sitharam, 2008; Mhaske & Choudhury, 2011; Singh et al., 2021), Bangladesh (Haque & Kamal, 2013; Rahman et al., 2016, 2018), Turkey (Kanlı et al., 2006; Pamuk et al., 2017, Pamuk et al., 2019), Korea (Jung & Kim, 2014; Kang et al., 2021; Lee et al., 2022), Spain (Martínez-Pagán et al., 2014; Rosa-Cintas et al., 2017; Martínez-Pagán et al., 2018), Italy (Forte et al., 2019) and Japan (Matsuoka et al. 2006). There have also been multiple studies in different regions of the US (e.g., Ahdi et al., 2018; McPhillips et al., 2020; Park & Elrick, 1998; Yong et al., 2012). This section highlights findings from some of these studies most closely related to the current work.

In Spain, Martínez-Pagán et al. (2018) investigated the seismic response in the town of Adra. This study used the methods of Spatial Autocorrelation (SPAC), MASW, and HVSR. The methods generated discrete one-dimensional (1D) and continuous two-dimensional (2D) V_S subsurface models. Then, the area was classified in terms of V_{S30} to acquire a detailed soil microzonation of Adra. The detailed map generated for Adra provides predictive insight into the possible distribution of building damage and contributes to appropriate urban planning for future projects.

In France, Hollender et al. (2018) characterized 33 seismic stations from the French permanent Accelerometric Network (RAP) by using active and passive surface waves. Hollender et al. (2018) applied active MASW of R- and L-waves and passive ambient vibration measurements. The processing of ambient vibrations used frequency-wavenumber (FK), high-resolution frequency-wavenumber (HRFK), and modified spatial autocorrelation (MSPAC) methods. The dispersion curves from the active and passive methods were combined for the inversion process. This study compared the measurements of V_{S30} with indirect estimations of V_{S30} performed in the past, concluding that the measurements of V_{S30} were in general lower than the V_{S30} estimates. Additionally, the authors stated that surface-based methods were appropriate to characterize the site of seismic stations, even on rock sites.

Michel et al. (2014) proposed a procedure to characterize 30 new stations from the Strong Motion Network (SSM Net) in Switzerland. The site characterization was developed with geophysical investigations using surface waves. Active and passive measurements were taken at the stations. Three processing steps were applied to the data collected at the sites. First, HVSR and polarization analysis were used to retrieve the fundamental mode of R-waves and identify 2D resonance or unstable rock slopes. Second, an analysis of the array was performed to retrieve the

dispersion curves of R- and L-waves. Third, a combined inversion of the dispersion, resonance, and ellipticity curves was performed. After comparing the different processing steps applied to the sites, the authors obtained a 1D profile for each station and analyzed the 2D and 3D site amplifications. The authors concluded that 1D profiles are representative of the seismic response for the sites analyzed.

Forte et al. (2019) performed a soil classification based on surface geology and V_S measurements in Italy. The method proposed by Forte et al. (2019) correlated surface geology maps with site-specific investigations. As a result of this investigation, a simple stand-alone software (SSC-Italy) was developed for public access with the soil classification for all of Italy. The map of V_{S30} generated for Italy is shown in Figure 2-1. This map cannot be used in place of site-specific studies, but it can be suitable for large-scale seismic risk studies. Other regional studies have been developed by Boaga et al. (2010) and Di Fiore et al. (2016).

Due to the high seismic activity in Japan, several studies have been conducted to measure and estimate V_S. Among the studies, a map of V_S was developed using the Japan Engineering Geomorphologic Classification MAP (JEGM) by Matsuoka et al. (2006). This study collected 2,000 sites with V_S profiles measured all over Japan and estimated V_{S30} values. The V_{S30} values were then correlated with the JEGM geomorphological units. The map generated using this method is shown in Figure 2-2. In this figure, average V_S values are shown for Japan. Another study performed by Kwak et al. (2015) created prediction equations through empirical models for the Japanese seismic network (K-NET) based on standard penetration resistance (N-value). This study used 16,845 collected measurements of V_S and N-values at 1,102 sites to generate the prediction equations. The results were compared with geomorphology-based proxy methods concluding that N-values can improve the prediction of V_{S30} when direct measurements are not available. Other

regional studies have used seismic tomography and microseismic data to investigate V_S in the crustal structure of Japan (Zhao et al., 1992; Nishida et al., 2008; Suemoto et al., 2020).

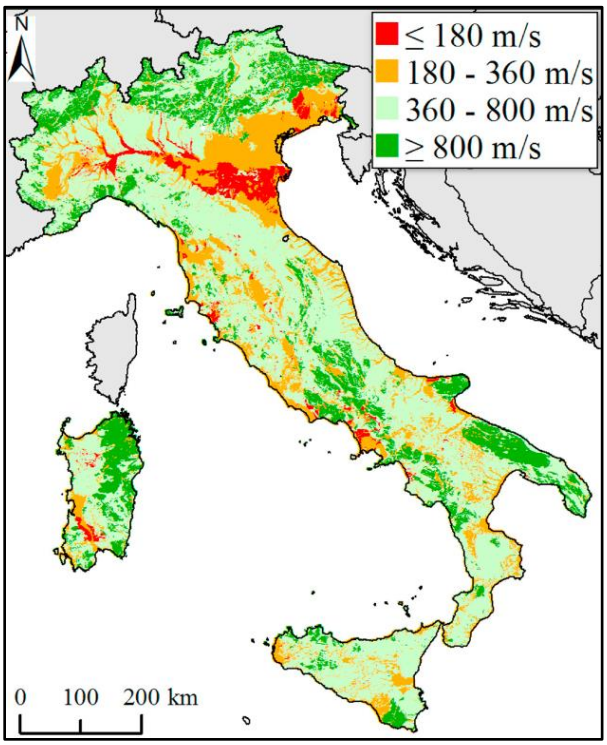

Figure 2-1: Map of V_{S30} for Italy (Forte et al., 2019)

Most of the studies on V_S in the U.S. are performed in zones with higher seismic risk, such as the western U.S. and Charleston regions. Ahdi et al. (2018) compiled more than 1,739 V_S profiles in California, with 1,232 of them in digital format, as shown in Figure 2-3. These data collected by Ahdi et al. (2018) represents the first open-access database of V_S profiles in the U.S. Wang et al. (2019) also included 834 V_S profiles from Central and Eastern North America (CENA), 90 V_S profiles in Alaska, 608 V_S profiles in the northwest region (Oregon, Washington), and 814 V_S profiles from the intermountain west region (Idaho, Nevada, Utah, and Wyoming). The database from CENA included only one profile in Alabama located at the seismic station LRAL. The information was collected from different data sources and included boreholes and other

geotechnical data to augment the geophysical test results. The geophysical testing included invasive tests (i.e., downhole and cross-hole testing, P-S suspension logging, and seismic CPT) and non-invasive tests (i.e., active and passive surface waves methods and refraction). The active surface wave methods involved SASW and MASW of R- and L-waves. The passive surface waves were analyzed using SPAC and extended spatial autocorrelation (ESAC).

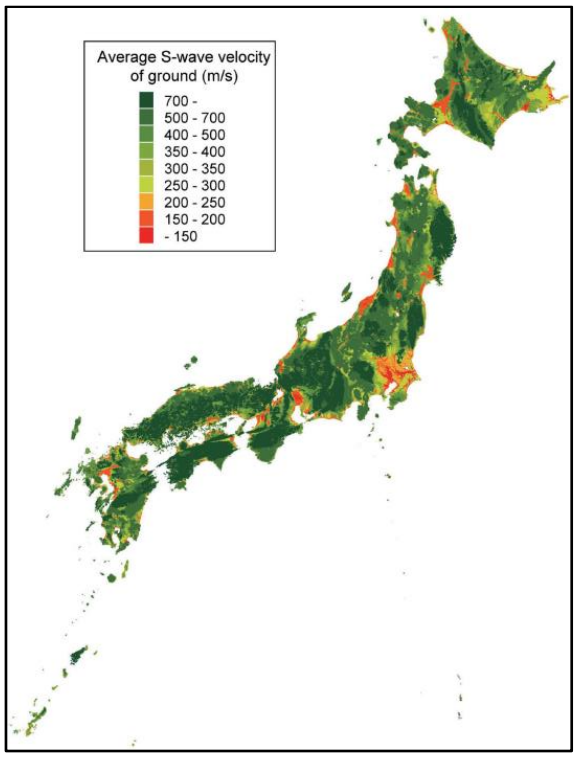

Figure 2-2: Average V_S distribution estimated using JEGM (Matsuoka et al. 2006)

Proxy methods rely on developing correlations between site parameters and V_S or V_{S30}. Examples of previously developed proxy methods include methods based on terrain (Yong et al., 2012), surface geology (Park & Elrick, 1998), combinations of geology and topography (Wills et al., 2000; Wills et al., 2015), and *in situ* measurements such as CPT (e.g., Andrus et al., 2007). These methods rely on large databases of V_S profiles and so are often biased towards active seismic

regions like the western U.S. Validating these methods for use in low seismicity regions can be difficult due to the lack of available profiles.

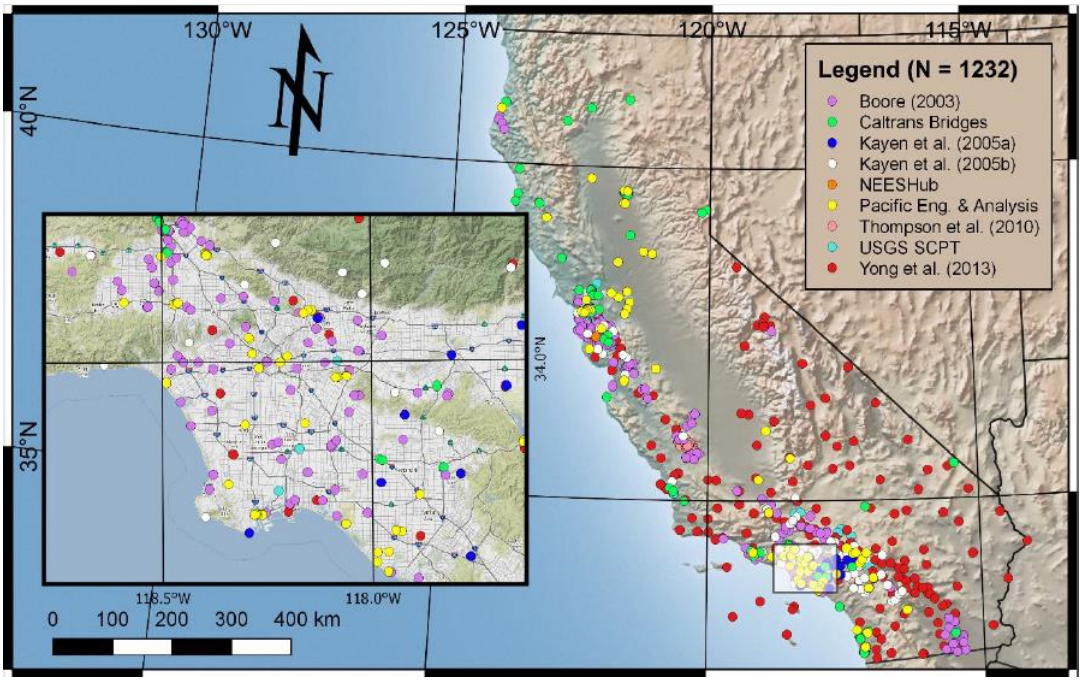

Figure 2-3: Digitized V_S profiles in California with an inset map of Los Angeles (Ahdi et al., 2018).

Alabama is one of the regions with few publicly available V_S profiles and even fewer to sufficient depths to estimate V_{S30}. Chen & Liu (2018) applied geophysical testing at the Citronelle oil field in Alabama to monitor CO_2 injections. The geophysical testing used non-invasive passive seismic methods to detect geohazard risk and monitor the injection. The V_S profiles computed by Chen & Liu (2018) are very deep, reaching 3,180 m, therefore, it is not possible to retrieve from the profile a V_{S30} measurement. Xia (2022) used MASW to identify the shallow geological features at Maxwell AFB in Montgomery. Site characterization performed for the Bellefonte Nuclear Plant project (TVA, 2007) included five geophysical surveys: seismic refraction survey, Seismic Cone Penetrometer Testing (SCPT), suspension and downhole logging test, microgravity surveys, and natural gamma borehole surveys. Figure 2-4 shows the results of the seismic refraction, a 2D

profile of V_P conducted through unit 4. This lack of data highlights the need for additional work to collect and interpret V_{S30} results in Alabama.

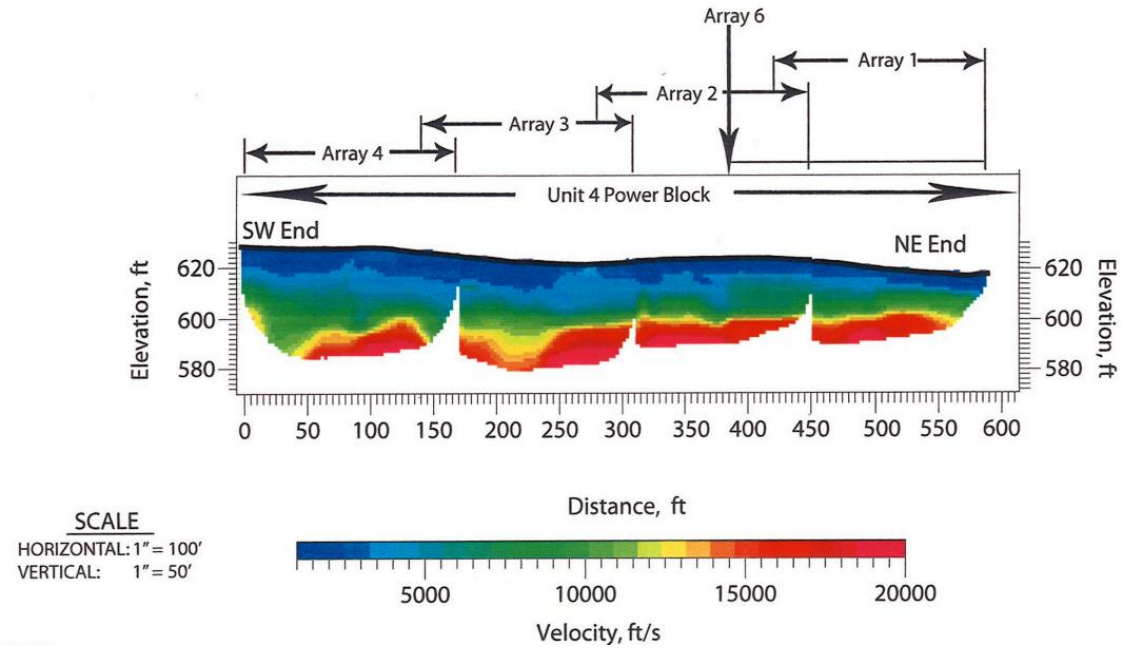

Figure 2-4: 2D V_P profiles at the Bellefonte Nuclear Plant for unit 4 (TVA, 2007).

2.3 DIRECT METHODS TO MEASURE SHEAR WAVE VELOCITY

The measurement of V_S profiles can be performed using both invasive and non-invasive methods. Invasive methods involve placing either the source and/or the receiver of the wave at several different depths below the ground surface. These methods require drilling a hole or using a penetrometer to reach the desired depth. Some examples of invasive methods include seismic cone penetrometer (Campanella et al., 1986; Robertson et al., 1986), seismic flat dilatometer (Hepton, 1988), and borehole-based methods such as downhole (McDonald et al., 1958; Raikes & White, 1984), crosshole (Ballard, 1976; Butler & Curro, 1981), and P-S suspension logging (Kaneko et al., 1990; Ohya et al., 1984).

The non-invasive methods are performed on the surface of the site and do not require drilling a hole or using a penetration device. Examples of non-invasive methods include seismic refraction (Hagedoorn, 1959; M. W. Palmer, 1990; Cardarelli & De Nardis, 2001), seismic reflection (Tarantola, 1984; Clark et al., 1994; Symes, 2009), and surface wave methods (Miller et al., 1999; Park et al., 2000; Foti, 2000; Stokoe & Santamarina, 2000). Depending on how the data are acquired and how they are processed, there are several different methods for surface wave analysis, such as spectral analysis of seismic waves (SASW), MASW, microtremor array measurements (MAM), ambient vibration array (AVA), refraction microtremors (ReMi), and SPAC (Garofalo et al., 2016). Non-invasive techniques are widely applied because the procedures used are time- and cost-effective (Foti et al., 2011).

2.3.1 Multichannel Analysis of Surface Waves (MASW)

The MASW method uses the surface wave information of the recorded seismic waves to estimate the subsurface properties. This is commonly done using the dispersive behavior of R-waves. For MASW, the recorded signal is transformed from the time-space domain to the frequency-wavenumber domain to observe the dispersion curve of the R-waves. After this, the V_S profile of the soil is computed by the inversion of the dispersion curve (Miller et al., 1999). MASW methods can be performed with active and/or passive sources. Active sources (e.g., sledgehammers, controlled frequency vibrators) usually provide better information at the higher frequencies, which is associated with the shallower structure of the soil. In contrast, passive sources (e.g., ambient vibrations) are better at retrieving lower frequency ranges and providing information about deeper soil layers (Foti et al., 2009; Gouveia et al., 2018). The combination of passive and active sources provides the ability to include both the high-frequency content of the

active source and low-frequency content from ambient vibrations, improving the resolution and depth of investigation of the survey (Rix et al., 2002; Foti et al., 2009).

Among the disadvantages of surface wave methods are the inaccuracy in locating low-velocity layers or bedrock depth at a given lithological interface (Garofalo et al., 2016b). However, using other dispersion characteristics such as polarization, ellipticity, L-wave dispersion curves, or a large set of ground model parametrization can help constrain the V_S profiles and the uncertainties in the process (Michel et al., 2014). Passive MASW is controlled by the energy provided by passive sources. A strong ambient energy will provide a strong passive source to be measured in the field. However, for isolated sites without a strong passive source, passive MASW will not be useful (Baglari et al., 2018).

Data Collection

The data for MASW are collected by positioning equidistant receivers, usually geophones, on the surface of the ground. The receivers are connected to an acquisition system that converts the signal from analog to digital data and stores the signal for further processing. The signal recorded by the receiver originated from a source that will excite seismic wave motions over a range of frequencies. This source could be active and/or passive, as mentioned before. A diagram of how data are collected is shown in Figure 2-5.

The field parameters used to collect the data, such as the total length of the survey line and the distance between the geophones, are very important for the processing and inversion of the data. The arrangement of the geophones used for the survey will restrict the part of the dispersion curve that can be extracted. The distance between the receivers and the array length of the survey is associated with the maximum and minimum wavelength (λ) that can be collected from the

survey. The minimum wavelength is approximately two times the spacing of the receivers, and the maximum wavelength is estimated as the total array length of the survey. The minimum depth of the profile is approximately half the minimum wavelength, and the maximum depth is approximately half the maximum wavelength (Foti et al., 2018).

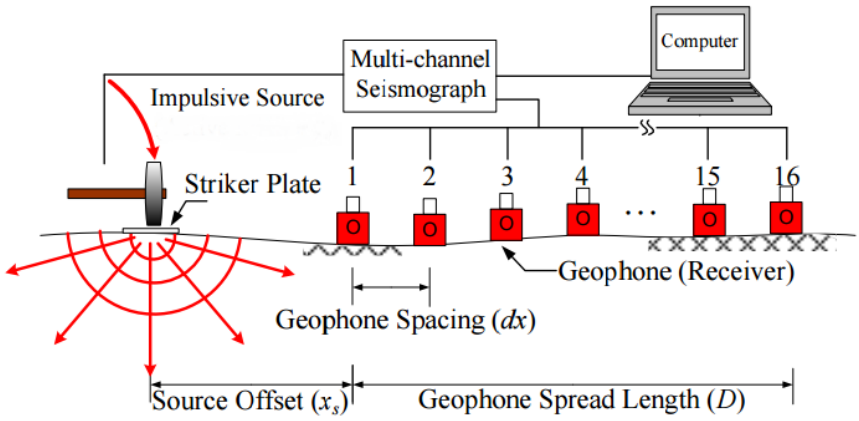

Figure 2-5: Diagram of active MASW setup (Sahadewa et al., 2012)

Processing

For MASW analysis, the data collected in the field is processed to extract the experimental dispersion curve. For this purpose, the signal is transformed from the time-space domain to another domain (i.e., frequency-wavenumber or frequency-slowness) to obtain the phase velocity in terms of the frequency (Socco et al., 2010). The transformation into frequency-wavenumber involves the application of a 2D Fourier transformation to obtain a 2D amplitude spectrum of the data (Gabriels et al., 1987; Lin et al., 2004). The transformation into frequency-slowness involves two linear transformations of the data. The first transformation is a slant stack which results in a wave field of the ray parameter-time intercept plane. Then, a 1D Fourier transformation over the time intercept is applied (Mcmechan, 1981). After the transformation, the dispersion curve of the fundamental mode is selected for the inversion. The overtone image and the chosen dispersion

curve for the fundamental mode are shown in Figure 2-6. Also, an example of the constraints given by the field parameters is shown in the image.

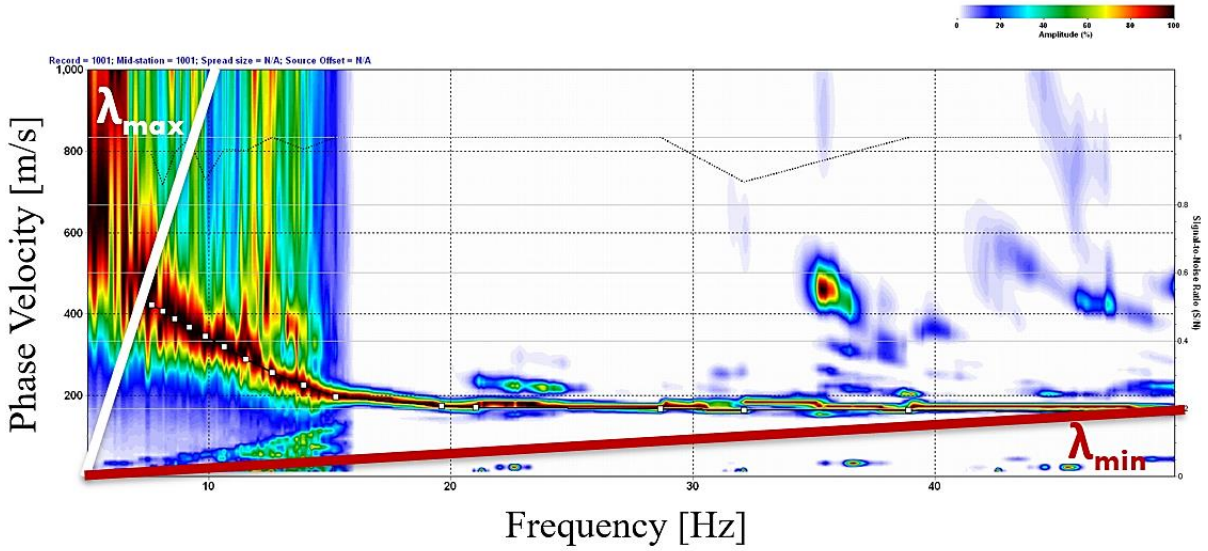

Figure 2-6: Dispersion Curve for site TU01 using SurfSeis Software (SurfSeis, 2010) example with minimal and maximum wavelength constraints

Inversion

The inversion methods generate a large number of different parameters that are ensembled to create trial soil profiles. Then, the dispersion curve is computed for each one of the soil profiles generated. This theoretical dispersion curve is compared with the dispersion curve acquired from the field to evaluate how well the model fits. Therefore, several soil profiles can have a match with the field data. Suitable data are measured through a misfit function, among other approaches to consider the uncertainties of the model.

The inversion stage attempts to find a V_S profile that matches the measured dispersion curve. Multiple approaches are available to solve this inverse problem. The early methods used for inversion were based on linearized methods (Nolet, 1981; Tarantola, 1984) and the damped least-

squares method (Herrmann, 1987). These first approaches could not provide any information on the objective function, and the solutions generated were often related to its local minima (Cauchie & Saccorotti, 2013). Among the most recent approaches, the direct search methods have become widely used in geophysics in the past three decades. Examples of direct search methods include simulated annealing (Kirkpatrick et al., 1983; Sen et al., 1995), genetic algorithms (Stoffa & Sen, 1991; Sambridge & Drijkoningen, 1992; Lomax & Snieder, 1994), and the Neighbourhood algorithm (Sambridge, 1999a). These methods are based on the uniform pseudo-random sampling of the parameter space (Sambridge, 1999; Wathelet et al., 2004).

Results after Inversion

The results obtained from the inversion process for MASW are several 1D V_S profiles. Each V_S profile is associated with a numerical dispersion curve and a misfit, which describes the difference between the measured curve and the numerical one. Figure 2-7 shows the results of an inversion performed on the dispersion curve shown in Figure 2-6. The inversion was performed using the open-source software package Geopsy (Geopsy.org). The blue lines in the figure show all of the inverted profiles (over 100,000 profiles), while the profiles highlighted in orange represent the 25% of profiles with the lowest misfit. The 25% of the V_S profiles with the lowest misfit are in good agreement until a depth of approximately 16 meters, below which there is more spread between the V_S profiles. The 25% of profiles highlighted in orange have similar misfit values, demonstrating the non-uniqueness of the inversion.

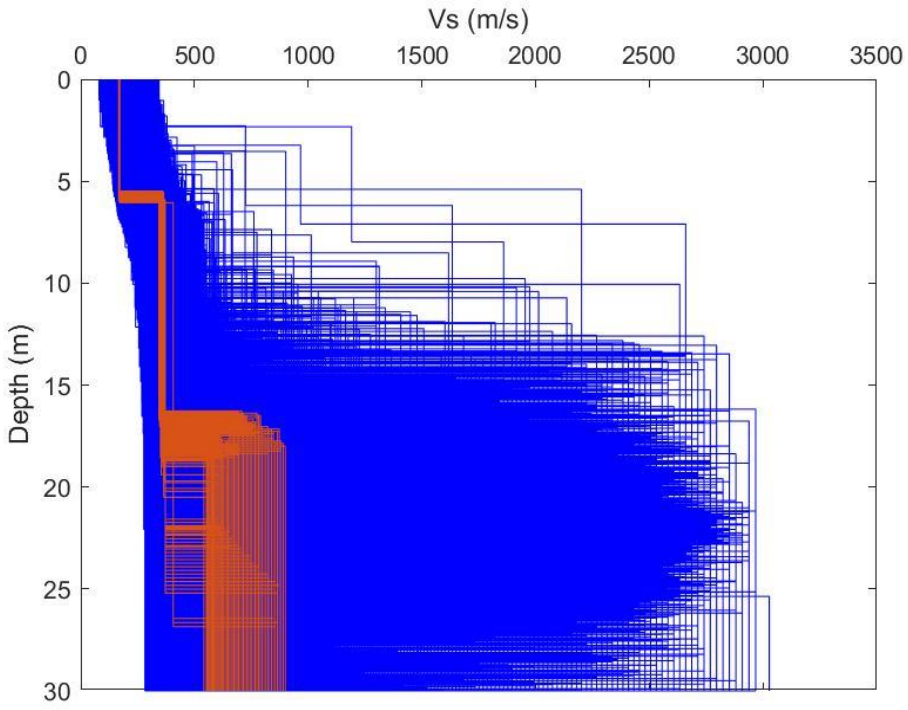

Figure 2-7: V_S profiles of TU01 site. The V_S profiles were generated using Geopsy and are shown in blue color. The best 25% V_S profiles with the lower misfit are shown in orange color.

Non-Inversion

Other approaches have been developed to avoid the demanding computational effort to acquire V_S profiles. A non-inversion approach proposed by Lin et al. (2021) is based on the concept that the phase velocity of surface waves at a specific frequency is proportional to the average V_S within one-half of a wavelength (Vidale, 1964). The method allows determining V_{S30} from the dispersion curve of the fundamental mode without the need for inversion.

The procedure to estimate V_{S30} is performed through a sequence-deduction method. It begins with the division of the upper 30 m into thin layers of even thickness. Then the estimation of V_S would be computed for the first layer from the phase velocity of the surface waves at the highest frequency (f) from the dispersion curve. The next layer is calculated using the V_S computed

from the previous layer, and the phase velocity (V_R) of the surface waves within half-wavelengths of the layer is calculated (Lin et al., 2021).

The method is based on the relationship shown in the equation 2.1, which associates the wavelength and the frequency at a point of the dispersion curve. After the upper 30 m are divided into even layers, the V_S of these layers can be computed using the equation 2.2.

$$\lambda = \frac{V_R}{f} \tag{2.1}$$

$$V_{Si} = \frac{\overline{\left(V_{R,i}\left(\lambda_i\right)/\beta\right)\lambda_i/2 - \sum_{j=1}^{i-1} V_{Sj} h_j}}{\lambda_i/2}, \quad \sum_{j=1}^{i-1} h_j < \lambda_i/2 < \sum_{j=1}^{i} h_j \tag{2.2}$$

V_{Sj} and V_{Si} as the shear wave velocities of the *j*th and *i*th layers ($i=j+1$), h_j is the thickness of the jth layer, and λ_i is the wavelength of the R-wave reaching within the *i*th layer, $V_{R,i}$ is the average V_S in a depth of one-half of Rayleigh wavelength, β is a correction factor expressed as a function of the Poisson's ratio (based on the work of Richart et al., 1970)

For the case where the half-wavelength is less than the thickness of the first layer, the V_S can be estimated using an equation 2.3. When the minimal half- wavelength is greater than the depth of the upper layers, V_S can be approximated with the equation 2.4.

$$V_{S1} = \overline{V_R(\lambda)}/\beta, \qquad \lambda/2 \le h_1 \tag{2.3}$$

$$V_{Si} = V_R\left(\lambda_{\min}\right)/\beta, \qquad \lambda_{\min}/2 > \sum_{j=1}^{i} h_j \tag{2.4}$$

After the V_S of each layer is computed, V_{S30} can be calculated with the equation 1.1. The dispersion curves selected from the MASW are the input for the non-inversion method.

Lin et al. (2021) applied their proposed approach to five case studies covering typical geotechnical structures. The first analysis was developed using two real sites in which V_S increases

progressively with depth. The second analysis was performed at two real locations with mixed high and low-velocity layers. The third analysis was done on 25 artificial sites characterized by increments in velocity by depth. The estimates of V_{S30} computed using the non-inversion method were compared to V_{S30} results from invasive tests and inversion techniques, showing close agreement.

The non-inversion approach generates V_S profiles, as shown in Figure 2-8, for a real site near the Kansas Geological Survey in Lawrence, Kansas (Lin et al., 2021). The site showed a gradual increase in V_S, as shown in Figure 2-8 (left). After the velocity profile is computed, the values of V_{S30} can be acquired. The results of V_{S30} applying the non-inversion method were compared with the results using the downhole test and inversion techniques, as shown in Figure 2-8 (right). The V_{S30} computation using the non-inversion method falls between the results acquired using downhole testing and MASW inversion.

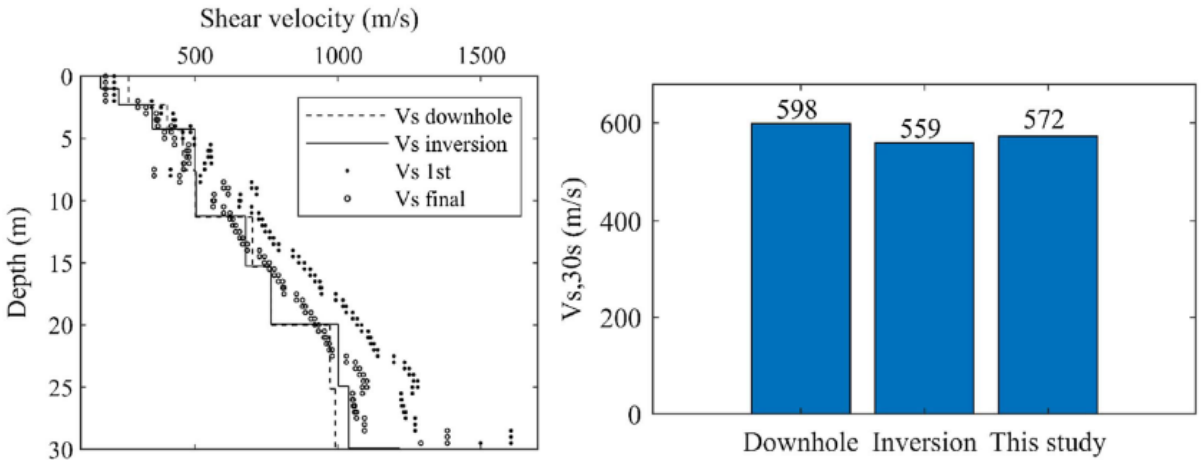

Figure 2-8: Example of V_S estimation at a real site: V_S profiles (left), comparison of V_{S30} results (right) (Lin et al., 2021)

2.3.2 Seismic Refraction

The seismic refraction method is derived from the principle that the direction of the primary waves (longitudinal or compressional waves) as they pass through the soil structure is influenced by the velocity difference between the layers. As the waves travel in the soil, the contrast in velocity between the layers causes a portion of the wave to be reflected and a portion of the wave to be refracted (i.e., change direction). The change in the direction of the wave is controlled by the difference in velocities between the soil boundaries and follows Snell's Law (Reynolds, 2011), as shown in Figure 2-9. When a source generates seismic energy, some of the waves traveling from A to B are reflected and some refracted. If the velocity of the second layer (V_2) is larger than the velocity of the first layer (V_1), the refracted waves travel faster than the other waves; these waves are called head waves and are refracted at the critical angle (i_c) following Snell's law, as shown by the ray path from C to D in Figure 2-9.

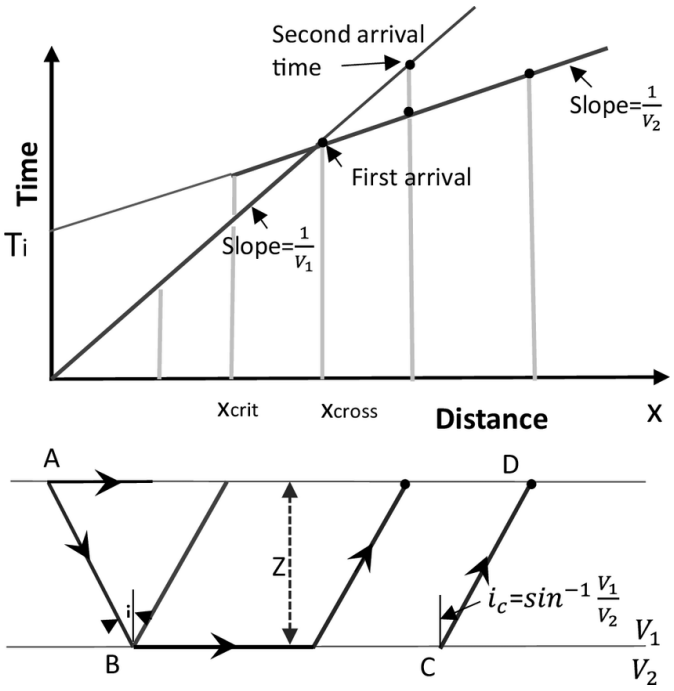

Figure 2-9: Ray paths and time distance curve for two layers separated by a horizontal interface; x_{crit} is the critical distance, and x_{cross} is the crossover distance (Azhar et al., 2019)

The P-wave arrivals are picked from the time-space domain to generate a time-distance plot to identify the velocity and the thickness of the layers. The slopes of the time-distance curve are based on the speed of the arrivals of the P-wave. The velocity of the layers is computed using the inverse of the slope. The number of slope breaks observed in the time-distance plot provides the number of layers in the substructure. The crossover distance (x_{cross}) is the distance in which the slopes intersect. The thickness of the layer (Z) is computed using the crossover distance.

The seismic refraction method usually focuses on the first arrival of the waves and therefore provides a velocity profile for the primary wave. S-wave can also be collected using seismic refraction with the appropriate equipment that involves horizontally polarized geophones (Aziman et al., 2016). In the case when only a p-wave velocity profile is acquired, this must be converted to an S-wave through knowledge or assumptions about Poisson's ratio or the ratio between the p- and s- wave. Next, the data collection, processing, and inversion steps for obtaining V_S profiles from seismic refraction data are described.

Data Collection

The data collection for the seismic refraction method is similar to active MASW in layout geometry, so the same array can be used to collect data for both tests (Foti et al., 2003). The technique requires the active source to be triggered at least at the beginning and at the end of the survey line to observe a dipping layer under the soil structure. However, it is recommended that some shots be performed along the survey line to capture irregular interfaces.

Processing

The signal is processed by picking the first arrivals of the seismic wave in the time-space domain for the inversion (Redpath, 1973). An example of the P-wave arrivals selection using SeisImager software from Geometrics (2009) is shown in Figure 2-10. The P-wave has a small

amplitude compared with the S-wave and surface waves. Then, the signal needs to be amplified to observe and pick the arrivals. Also, the signal is clipped, so the waves with a larger amplitude do not overlap.

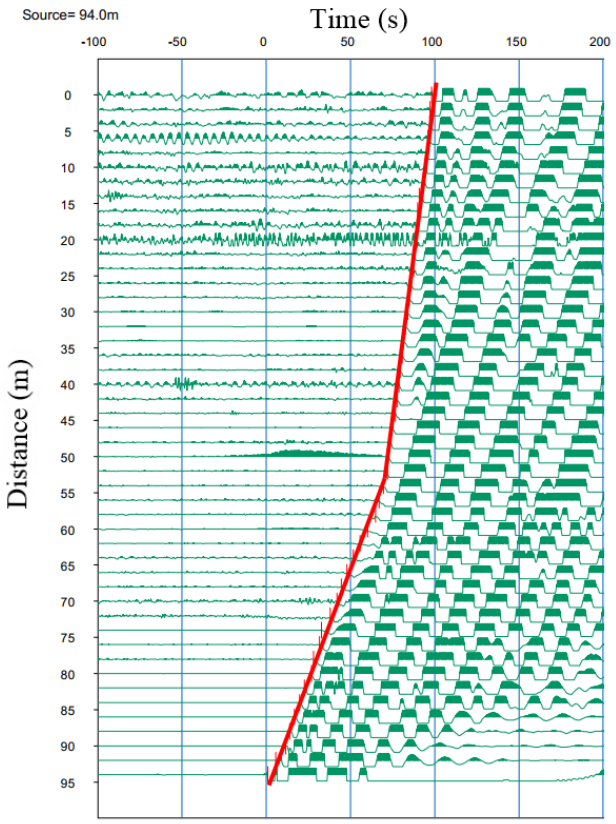

Figure 2-10: Primary wave arrival selection for seismic station Y47A using SeisImager (Geometrics, 2009)

Inversion

Several interpretation procedures for the seismic refraction data are referred to in the literature. These methods follow two approaches: delay-time and wave front construction. It is essential to check the travel time-distance graph and the quality of the data before choosing an interpretation method. Some of the anomalies required to be checked are misplots of travel-time

values, velocity/thickness changes in the near-surface, topography changes, and planar or irregular refractors (Reynolds, 2011).

The first methods used to compute seismic refraction inversion were Hagedoorn's plus-minus method (Hagedoorn, 1959) and the generalized reciprocal method (Palmer, 1980). Both methods were developed to analyze irregular interfaces and are based on the concept of the delay time or time term (Kearey et al., 2002). The delay time is the difference between a refracting wave reaching a planar interface and the same wave reaching a sloped interface, as shown in Figure 2-11. Hagedoorn (1959) proposed the plus-minus method, which solves the delay times to compute the local depths of an irregular refractor, assuming a planar interface between the individual detectors. The generalized method proposed by Palmer (1980) solves the same problem by providing a smother solution for the irregular interface with more detail in the solution. These procedures had potential advantages over other proposed methods, such as computational stability and speed, because of the linear equations developed in the computations.

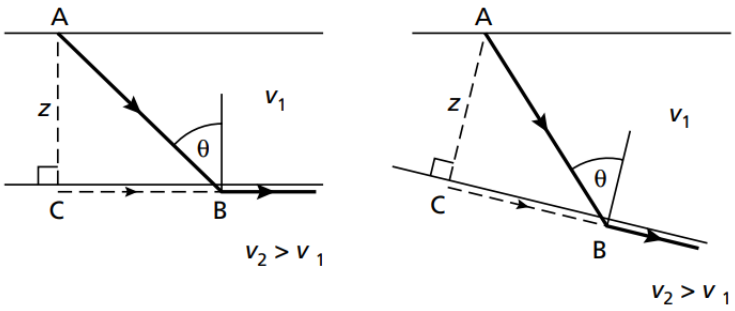

Figure 2-11: Delay time concept (Kearey et al., 2002)

New techniques have been developed with the seismic refraction software, including seismic refraction tomography or modifications/improvements to the past methods. The tomographic method starts with an initial model of the subsoil. Once the initial model is set, the travel times from the model are computed. Then, the travel times of the models are compared with the measured

travel times from the field. This follows an iterative process, modifying the model until the difference between the travel times is minimized. The complexity of the math in this process requires more extensive computational time.

Results After Inversion

The results for the seismic refraction method are presented in a 2D velocity model of the subsurface, as shown in Figure 2-12. The values of the P-wave are computed for each layer of the soil. These values are converted into V_S using common ratios found in the literature. Estimated V_P/V_S ratios for sandstone, limestone, and dolomite are in the range of 1.6 to 1.9 (Pickett, 1963). The V_P/V_S ratios for unconsolidated sediments ranged from 2.0 to 4.0 (Herath et al., 2020).

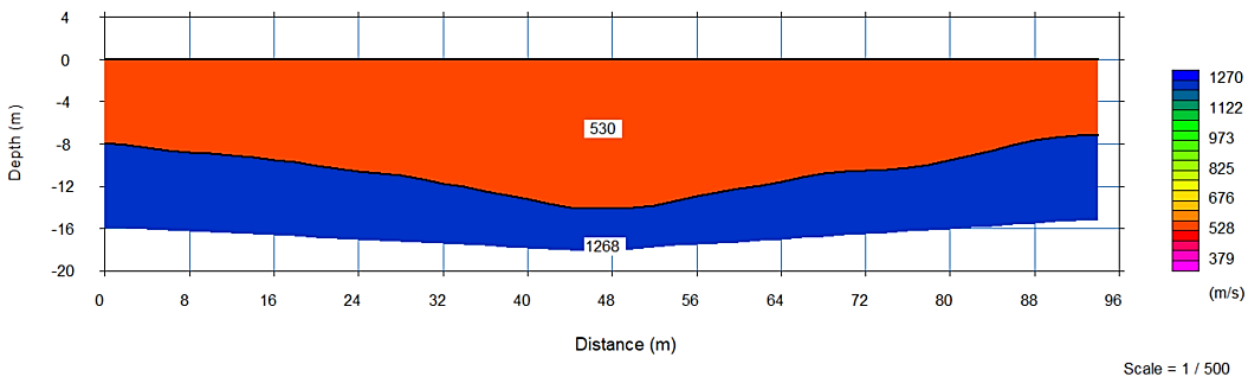

Figure 2-12: Primary wave velocity results for seismic station Y47A using the software SeisImager (Geometrics, 2009)

Careful interpretation needs to be taken when analyzing V_P profiles due to saturated layers that might affect V_P values, while V_S values are less affected by changes in saturation (Stümpel et al., 1984). It has been investigated that soil under completely saturated conditions, as below the water table, has values of V_P that are very close to those of water when sediments are present. Additionally, the identification of groundwater in sediments is characterized by a sharp increment in velocity reaching to values between 1,300 to 2,000 m/s. Therefore, for these sites V_P/V_S ratios

need to be increment to 5-7 to account for the water effect in the sediments (Stümpel et al., 1984; Grelle & Guadagno, 2009).

2.4 INDIRECT METHODS TO ESTIMATE SHEAR WAVE VELOCITY

Indirect methods can provide reasonable estimates of V_{S30} when measurements are not available or cannot be performed. Indirect methods rely on correlations between a property or characteristic of the soil with a measure of V_{S30}. These methods are usually generated in areas where several V_S profiles are available to generate the correlations. After the correlations are made, the method is expanded to other regions and validated with available V_S profiles. The indirect methods presented in this study are the P-wave seismogram method, HVSR, R-wave ellipticity, and proxy methods.

2.4.1 P-wave Seismogram Method

The P-wave seismogram method proposed by Ni et al. (2014) is used to estimate the time-average V_S from the surface to a depth z (V_{SZ}) with the initial part of the seismic records. The method uses the analytical solutions of the P-wave displacement at the free surface proposed by Aki & Richards (2002). The expressions correlate the V_S to the ratio between the initial amplitude of the vertical and radial components of a seismic record signal, as shown in the equation 2.5 (Kim et al., 2016).

$$\frac{\dot{U}_R}{\dot{U}_Z} = \frac{2V_S\, p \cos j}{1 - 2p^2 {V_S}^2} \qquad 2.5$$

$\dot{U}_R$ and $\dot{U}_Z$ are the particle velocity at the first peak of the initial P-wave for the radial and vertical components, respectively, at the same time. V_S is the shear wave velocity, p is the ray parameter, and j is the reflected SV-wave angle, as shown in Figure 2-13. The vertical and radial amplitudes

are obtained from the P-wave arrival in the velocity time series. The velocity-time series are obtained by integration of the acceleration time series.

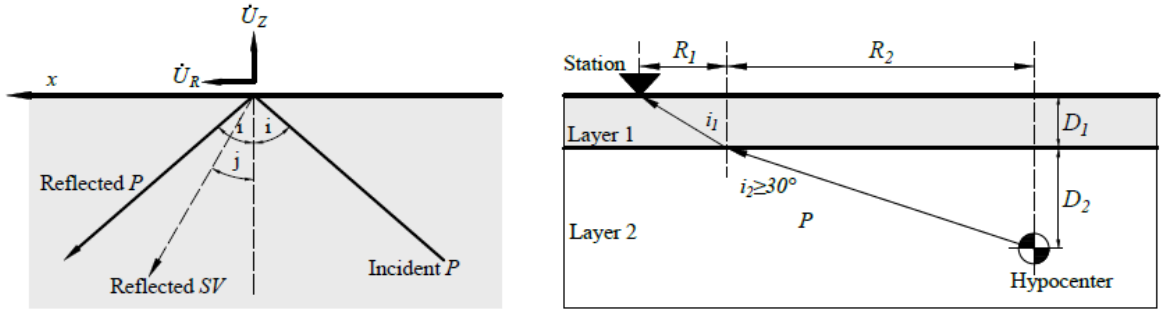

Figure 2-13: Schematic of the incident P-wave and reflected P-and SV- waves (left) and the ray path for the simplified crustal structure (right) (after Kim et al., 2016).

The ray parameter (p) and the angle j can be expressed as (Kim et al., 2016):

$$p = \frac{\sin i}{V_P} = \frac{\sin j}{V_S} \quad 2.6$$

$$j = \sin^{-1}(pV_S) \quad 2.7$$

Data Collection

The data collection of the P-wave seismogram starts with the selection of seismic stations with recorded earthquake activity. The records shall be from 3-components of seismic sensors: North-South, East-West, and Vertical. The recorded signal by the stations can be acceleration times series or velocity time series. The earthquakes selected for this method are recommended to be in a range of magnitudes between 2 and 5. These magnitudes of earthquakes are better for estimating V_S at relatively shallow depths because of the short source duration (Kim et al., 2020).

Processing

The data processing involves, as a first step, the correction of the earthquake recording. The corrections involve instrumental correction, filtering of the time series to remove background

noise of the raw signal, and a baseline correction. The filtering of the signal is usually performed with a bandpass filter such as a Butterworth filter with polynomial coefficients and corner frequencies. The baseline correction is performed to find the zero-base line of the accelerogram and remove the baseline shift when the accelerogram is integrated to compute velocities and displacements (R. Wang et al., 2011). If the earthquake recording is an acceleration time series, the signal needs to be integrated to obtain velocity time series. Before further processing, the signal-to-noise ratio (SNR) needs to be checked for each individual component. All signals with an SNR lower than 2 need to be discarded, as suggested by Kim et al. (2020), to provide reliable estimates.

Afterward, the horizontal components of the velocities are rotated, so one of them is aligned with the azimuth between the epicenter of the earthquake and the seismic station. The rotation of the signal generates radial and tangential components. The next step of the P-wave seismogram method is to identify the P-wave arrival in the radial and vertical components of the signal. The selection of the amplitude is performed first in the vertical component. Then, the corresponding amplitude of the radial component is selected for the same time as the amplitude of the vertical component, as shown in Figure 2-14.

Subsequently, the ray parameter and the angle *j* need to be calculated. The ray parameter is estimated from a simplified crustal model, as shown in Figure 2-13 (right). A crustal velocity model is acquired for the region in which the station is located, and the ray parameter is calculated with the relationship shown in the equation 2.8. Crustal models usually have more than two layers. Therefore, they need to be simplified to a two-layer model. The first layer of the crustal model is assumed as the first layer of the simplified crustal model, providing V_{P1}. Then, the velocity of the

second layer (V_{P2}) is computed as the depth-weighted average P-wave velocity between the bottom of the first layer and the hypocentral depth of the earthquake.

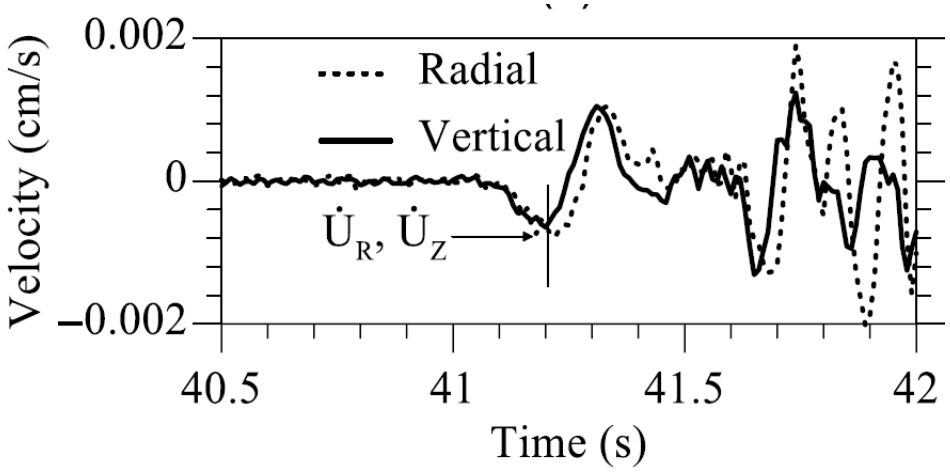

Figure 2-14: Time series for the vertical and radial components zoomed in for the P-wave arrival. Hawkesbury earthquake of the 16 March 2011 M 4.3 recorded at station CN.OTT (Kim et al., 2020)

$$p=\frac{\sin\left(\tan^{-1}\left(\frac{R_1}{D_1}\right)\right)}{V_{P_1}}=\frac{\sin\left(\tan^{-1}\left(\frac{R_2}{D_2}\right)\right)}{V_{P_2}} \qquad 2.8$$

R_1 and R_2 are the horizontal distances between the epicenter and the station in the upper and lower layer of the simplified model (Figure 2-13). D_1 and D_2 are the upper- and lower-layer thicknesses between the epicenter and the station in the simplified model. V_{P1} and V_{P2} are the P-wave velocities of the upper and lower layers, respectively. V_{P1} and D_1 are the velocity and thickness of the first layer of the crustal model. V_{P2} is the depth-weighted average P-wave velocity between the bottom of the first layer and the hypocentral depth. D_2 is the difference between the hypocentral depth and D_1. The horizontal distances, R_1 and R_2, are iterated with the limitation that their sum must be the epicentral distance. Subsequently, a value for the *j* angle is assumed, and the V_S is computed using the equation 2.5. Afterward, the *j* angle is calculated again using the values

of V_S with the equation 2.7. This process is repeated until the difference between the values of the *j* angle reaches a certain level of tolerance.

Results

Kim et al. (2016) studied the applicability of this method to 31 stations in the CENA region. The results applying the P-wave seismogram method are in terms of V_{SZ}, as shown in Figure 2-15. The plot represents the measured values for the multiple recordings for each station. The caps at the ends of the boxplot are the minimum and maximum V_{SZ} values computed. The box is the first and third quartiles, and the circle and the bar inside the box are the median and mean values, respectively. The diamond point shows the measured value for each station.

V_{SZ} estimates range from 109 and 3,877 m/s for NM.MCAR and CN.OTT stations, respectively. The results were compared with other proxy methods and showed less dispersion in the data using the P-wave seismogram method. Kim et al. (2016) also proposed 2 correlations to compute V_{S30}, presented in the next section.

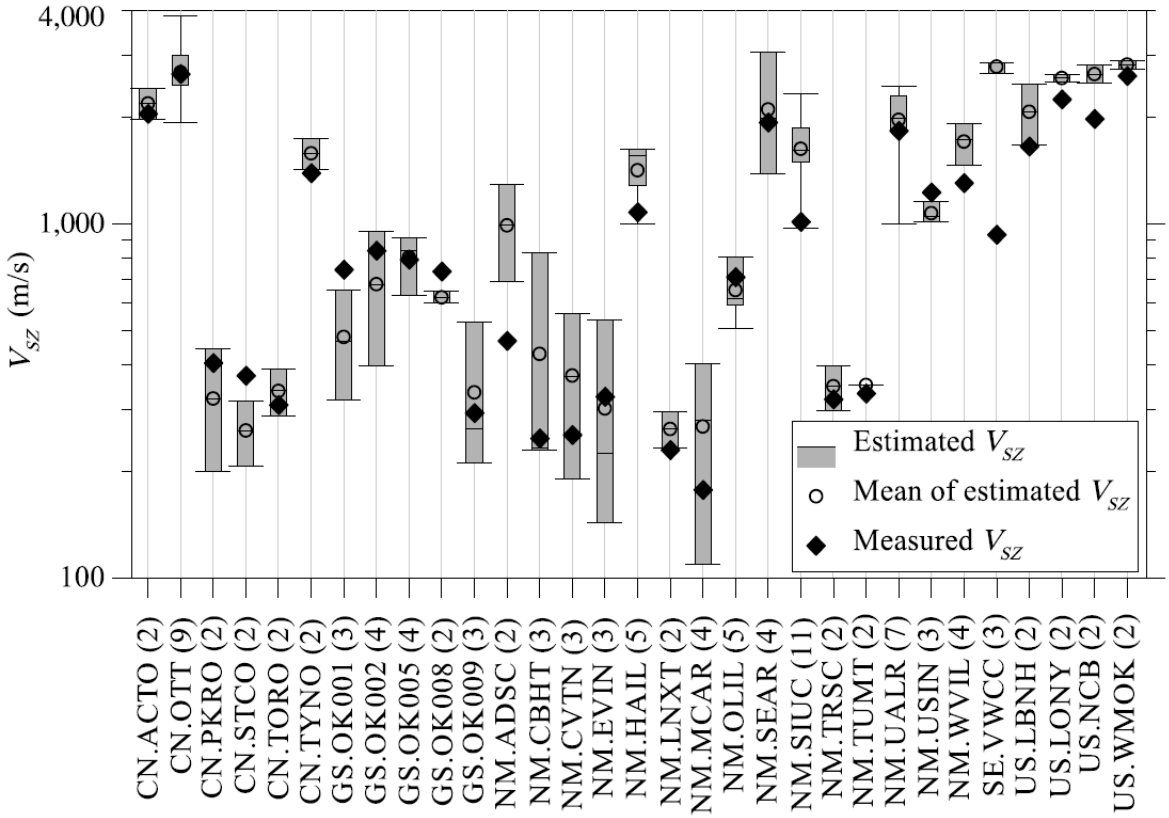

Figure 2-15: V_S to a depth z (V_{SZ}) estimated and measured for 31 selected stations. The orizontal axis shows the stations, and the number next to it corresponds to the number of earthquake events used to estimate V_{SZ}. Minimum and maximum values for the stations are shown as the extremes of dashed lines, and the 25th and 75th percentiles are the lower and upper values within the box plot. Mean values are shown as a bar in the boxplot (Kim et al., 2016)

Correlations between V_{SZ} and V_{S30}

As mentioned before, the V_S computed with the P-wave seismogram method characterizes the time-average velocity from the surface to a particular depth z (V_{SZ}). Then V_{SZ} estimates need to be correlated to V_{S30}. Two correlations were proposed by Kim et al. (2016). The first correlation, called V_{SZ} correlation, is between V_{SZ} and V_{S30} for glaciated and non-glaciated regions, as shown in the equation 2.9. The second correlation, the amplitude ratio correlation, is an empirical relation between the ratio and V_{S30}, as shown in the equation 2.10.

$$\log V_{S30} = c_0 + c_1 \log V_{SZ} + \varepsilon \qquad 2.9$$

$$\log V_{S30} = 0.4837 \ln\left(\dot{U}_R / \dot{U}_Z\right) + 6.9750 \quad (2.10)$$

The coefficients c_0, c_1, and ε can be obtained from Kim et al. (2016) and depend on the classification of the region (glaciated, non-glaciated) and the depth of V_{SZ}. The depth z can be estimated as the product of the V_{SZ} multiplied by the pulse duration (τ_p), $z=\tau_p V_{SZ}$. This duration was recommended as 0.1 s by (Kim et al., 2016).

Several authors (Kim et al., 2016; Zalachoris et al., 2017; Miao et al., 2018; Kim et al., 2020; Kang et al., 2020) have applied the method with good agreement between the estimations and the *in situ* measurements. Some of them even proposed local correlations for the study region. Zalachoris et al. (2017) applied the P-wave seismogram method with data from 251 seismic stations in Texas, Oklahoma, and Kansas. In this study, they classified the stations according to the geologic age of the site using the Parker et al. (2017) classification to compare the estimations acquired from the P-wave seismogram method. They found that the V_{S30} estimates by the P-wave seismogram method, in general, were larger than the proxy method, except for the stations located in Mesozoic age.

Miao et al. (2018) estimated V_S using the P-wave seismogram method for the Kiban-Kyoshin network (KiK-Net) in Japan. They analyzed 298 seismic stations and generated correlations between V_{S30} and V_{SZ} for Japan, as shown in the equation 2.11. Kang et al. (2020) developed an automated procedure based on the P-wave seismogram method to estimate V_S in 630 seismic stations of the KiK-Net in Japan. This study accomplished an automatization of all the steps required to compute V_S, including detecting P-wave arrival.

$$\log V_{S30} = 0.3896 \ln\left(\dot{U}_R / \dot{U}_Z\right) + 6.8590 \quad (2.11)$$

Kim et al. (2020) applied the P-wave seismogram method to 50 stations in Korea and validated the results with measurements. The validated method was then used in 118 stations where V_S measurements were unavailable. The P-wave seismogram method has not yet been applied to less seismically active regions like Alabama, where fewer seismic records are available.

2.4.2 Horizontal To Vertical Spectral Ratio (HVSR)

The HVSR (or H/V) method is a fast and popular technique for site characterization. The HVSR method, also known as the "Nakamura method," estimates the amplification and resonant frequency of the ground motions affected by a surface layer (Nakamura, 2019). The theory behind the technique proposes that the ground motion amplifies the horizontal components near the fundamental frequency while the vertical component does not experience significant amplification (Hassani & Atkinson, 2016). HVSR is a practical method because it can be computed with only ambient noise recordings at a single station, which is especially useful for locations without seismograph equipment already installed on the site as relatively short recordings (~30 min) can be used to get HVSR results. In cases where it is difficult to perform another type of testing due to difficult access, dense vegetation, or dense urban environments, HVSR can provide a reasonable estimate for site characterization (Stanko & Markušić, 2020).

The HVSR method is usually applied in microzonation studies and local response investigations. However, the method has demonstrated limitations in cases where there are very low resonant frequencies (lower than 5Hz) in thick sedimentary structures (Lachetl & Bard, 1994). In the presence of complex basin structures, it is challenging to relate the amplification of HVSR to the subsoil structure, as in the case of the Nari basin in Korea (Chávez-García & Kang, 2014). Near-surface explorations found similar results in the Baoding area of Hebei Province, China

(Wei-Jun et al., 2011). This study concluded that HVSR curves could be affected by environmental conditions such as wind, topography, and near-station transient sources.

The peak of the HVSR curve is associated with the resonant site frequency (f_{peak}) and the amplification (A_{peak}) of that frequency (Yilar et al., 2017; Nakamura, 2019; Yaghmaei-Sabegh & Rupakhety, 2020). HVSR provides the fundamental mode of the site; however, this parameter can also be correlated with V_{S30} values through empirical correlations generated from the V_{S30} database. For a single-layered system, the fundamental frequency (f_{peak}) can be associated with the thickness (H) of the surface layer and the velocity of the S-wave (V_{S1}) with the equation 2.12 (Kramer, 1996).

$$f_{peak} = \frac{V_{S1}}{4H} \tag{2.12}$$

The Site EffectS assessment using AMbient Excitations (SESAME) European research project developed some guidelines for the implementation of the HVSR technique on ambient vibrations. The guidelines covered how the measurements need to be taken, the processing of the signal, and the interpretation of the HVSR curves. Recommendations from the guidelines were extracted and summarized from the document and included in the following sections.

Data collection

The HVSR requires a three-component (North-South, East-West, and Vertical) seismic sensor. The signal can be acquired from earthquake ground motions or ambient noise. The duration of the record needs to be considered according to the minimum expected frequency peak of the HVSR curve, which is shown in Table 2-1. Also, it is recommended not to use a single measurement point to record at least 3 points.

Table 2-1: Recommended recording duration according to expected frequency peak (SESAME, 2004)

Minimum Expected f_0 (Hz)	**Recommended minimum recording duration [min]**
0.2	30
0.5	20
1	10
2	5
5	3
10	2

Some guidelines provided by SESAME (2004) that should be considered when acquiring the data are summarized in this paragraph. The sensor is required to be installed directly to the ground for *in situ* soil-sensor couplings, avoiding, if possible soft ground, such as mud or tall grass. Avoid soft materials such as rubber or cardboard if an artificial soil-sensor coupling is required. Nearby structures can influence the HVSR curves, so the measurement should be avoided near buildings, trees, or underground structures. Additionally, weather conditions should be indicated when taking the measurements, avoiding measurements under heavy rain, and protecting the equipment under fast winds.

Processing

Once the signal is acquired, the typical process includes dividing the signal into shorter time windows. An anti-trigger algorithm can be applied to the data to avoid transient noise (Bard, 1999). The anti-triggers select only the windows where a ratio between short-term average (STA) and long-term average (LTA) is under a given value. Additionally, a threshold can be used to avoid drastic variations in amplitude. The threshold defines the amplitude level tolerated for each window, discarding the data that did not fulfill this requirement.

The horizontal components of the signal North-South and East-West need to be combined to obtain the horizontal spectrum. The combinations available are square-averaged, total horizontal energy, and directional energy. Once the horizontal components are combined, the amplitude spectrum is calculated for each window, and the horizontal and vertical components are divided. Smoothing the spectrum is recommended to avoid false peaks generally associated with sharp troughs of the vertical component spectrum (Bard, 1999). Several smoothing types are available, such as Konno and Ohmachi smoothing (Konno & Ohmachi, 1998), Constant Smoothing, and proportional smoothing.

Results

The results acquired after processing the HVSR curves are shown in Figure 2-16. From the image, 13 windows were selected from the data, shown in different colors, and each one of those windows was used to compute an HVSR curve. As observed in Figure 2-16, each curve has a peak of around 2 Hz with different amplification. An average curve is computed from all the HVSR curves, and the standard deviation is provided for the peak and amplification values to be used in further analysis.

The results from the HVSR curves need to be checked to fulfill the requirements provided by SESAME guidelines (SESAME 2004). The criteria for a reliable H/V curve and a clear H/V peak are summarized in Figure 2-17. The guidelines ensure the reliability of the HVSR curve by constraining the minimum number of time windows used to compute HVSR curves, limiting the minimum number of significant cycles for each time window, and maintaining the standard deviation values around the fundamental frequency under specified boundaries. The criteria for a clear HVSR peak are achieved if at least five of the six criteria are fulfilled. The clear peak criteria limit the amplification of the peak at the fundamental frequency and surround this value and the

amplification with respect to other curve peaks. Also, the standard deviation of the amplification and highest frequencies need to be held to a certain threshold, as specified in Figure 2-17.

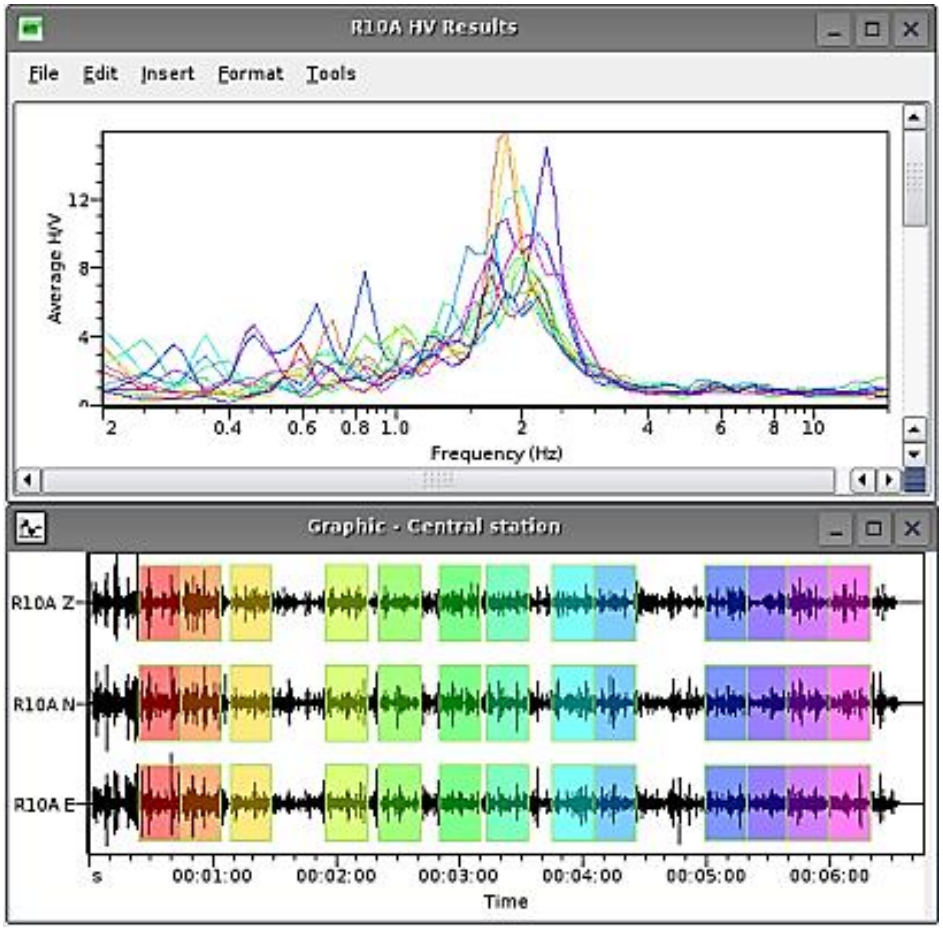

Figure 2-16: Windows selected in the signal and the HVSR curve from Geopsy software (Wathelet et al., 2020)

Criteria for a reliable H/V curve

i) $f_0 > 10 / l_w$

and

ii) $n_c(f_0) > 200$

and

iii) $\sigma_A(f) < 2$ for $0.5f_0 < f < 2f_0$ if $f0 > 0.5Hz$

or $\sigma_A(f) < 3$ for $0.5f_0 < f < 2f_0$ if $f0 < 0.5Hz$

Criteria for a clear H/V peak

(at least 5 out of 6 criteria fulfilled)

i) $\exists\, f^- \in [f_0/4, f_0] \mid A_{H/V}(f^-) < A_0/2$

ii) $\exists\, f^+ \in [f_0, 4f_0] \mid A_{H/V}(f^+) < A_0/2$

iii) $A_0 > 2$

iv) $f_{peak}[A_{H/V}(f) \pm \sigma_A(f)] = f_0 \pm 5\%$

v) $\sigma_f < \varepsilon(f_0)$

vi) $\sigma_A(f_0) < \theta(f_0)$

- l_w = window length
- n_w = number of windows selected for the average H/V curve
- $n_c = l_w \cdot n_w$. f_0 = number of significant cycles
- f = current frequency
- f_{sensor} = sensor cut-off frequency
- f_0 = H/V peak frequency
- σ_f = standard deviation of H/V peak frequency ($f_0 \pm \sigma_f$)
- $\varepsilon(f_0)$ = threshold value for the stability condition $\sigma_f < \varepsilon(f_0)$
- A_0 = H/V peak amplitude at frequency f_0
- $A_{H/V}(f)$ = H/V curve amplitude at frequency f
- f^- = frequency between $f_0/4$ and f_0 for which $A_{H/V}(f^-) < A_0/2$
- f^+ = frequency between f_0 and $4f_0$ for which $A_{H/V}(f^+) < A_0/2$
- $\sigma_A(f)$ = "standard deviation" of $A_{H/V}(f)$, $\sigma_A(f)$ is the factor by which the mean $A_{H/V}(f)$ curve should be multiplied or divided
- $\sigma_{logH/V}(f)$ = standard deviation of the $logA_{H/V}(f)$ curve, $\sigma_{logH/V}(f)$ is an absolute value which should be added to or subtracted from the mean $logA_{H/V}(f)$ curve
- $\theta(f_0)$ = threshold value for the stability condition $\sigma_A(f) < \theta(f_0)$
- $V_{s,av}$ = average S-wave velocity of the total deposits
- $V_{s,surf}$ = S-wave velocity of the surface layer
- h = depth to bedrock
- h_{min} = lower-bound estimate of h

Threshold Values for σ_f and $\sigma_A(f_0)$

Frequency range [Hz]	< 0.2	0.2 – 0.5	0.5 – 1.0	1.0 – 2.0	> 2.0
$\varepsilon(f_0)$ [Hz]	0.25 f_0	0.20 f_0	0.15 f_0	0.10 f_0	0.05 f_0
$\theta(f_0)$ for $\sigma_A(f_0)$	3.0	2.5	2.0	1.78	1.58
log $\theta(f_0)$ for $\sigma_{logH/V}(f_0)$	0.48	0.40	0.30	0.25	0.20

Figure 2-17: Criteria for a Reliable H/V curve (left), criteria for a clear H/V peak (right) (SESAME, 2004)

Correlations of F_0 with V_{S30} measurements

Several authors have sought relationships to correlate HVSR parameters (A_{peak} and f_{peak}) to V_{S30}. Ghofrani & Atkinson (2014) used the international Next Generation Attenuation-West2 (NGA-West2) database along with the Japanese databases (K-NET and KiK-NET) to generate a correlation between f_{peak} and V_{S30}. The correlation used all the events recorded between the years 1996 and 2009. Ghofrani & Atkinson (2014) proposed correlations using the HVSR parameters (A_{peak} and f_{peak}) separated and with a global model incorporating both parameters, as shown in the equation 2.13. The standard variation of this method for the correlation using f_{peak} was computed as 1.45. For the relationship using A_{peak}, the standard deviation was calculated as 1.14, and for the

global model was 1.41. The correlations examined the regional variability between HVSR parameters and V_{S30}.

$$\begin{aligned}
&\log_{10}(V_{S30}) = 2.56(\pm 0.01) + 0.20(\pm 0.02)\log_{10}(f_{peak}) && f_{peak} > 1Hz \\
&\log_{10}(V_{S30}) = 2.86(\pm 0.01) - 0.46(\pm 0.02)\log_{10}(A_{peak}) && \\
&\log_{10}(V_{S30}) = 2.80(\pm 0.02) + 0.16(\pm 0.02)\log_{10}(f_{peak}) - 0.50(\pm 0.03)\log_{10}(A_{peak}) &&
\end{aligned} \quad 2.13$$

A new proxy method to measure V_{S30} for CENA was developed by Hassani & Atkinson (2016). The proxy method was created using 5,783 three-component ground motions of the NGA-East database. As shown in the equation 2.14, a bilinear equation was used to estimate V_{S30}. The standard deviation of the method is 1.38. The results showed that f_{peak} could be used as a proxy to estimate values of V_{S30} in CENA with lower uncertainty values than other proxy methods, such as topographic slope and surface geology proxy.

$$\log_{10}(V_{S30}) = \begin{cases} 2.2(\pm 0.04) + 0.63(\pm 0.06)\log_{10}(f_{peak}) & f > 2Hz \\ \log_{10}(250) & f \leq 2Hz \end{cases} \quad 2.14$$

Another correlation was proposed by Stanko & Markušić (2020). The relationship was developed by collecting microtremor data with a three-component tomograph in Croatia. A total of 244 HVSR curves were used over the study area. The HVSR measurements were correlated with geophysical measurements (MASW and seismic refraction) taken near or at the exact location as the microtremor data were collected. The study proposed empirical correlations of V_{S30} for different frequency ranges, as shown in the equation 2.15. The authors of the study emphasized that the results of this study can be applied to regions with the same characteristics and cannot be generalized to other areas.

$$\begin{aligned} \ln(V_{S30}) &= \ln(208 \pm 20) && f_0 < 1Hz \\ \ln(V_{S30}) &= 5.34(\pm 0.9) + 0.46(\pm 0.15)\ln(f_0) && 1Hz \leq f_0 \leq 1Hz \\ \ln(V_{S30}) &= \ln(600 \pm 80) && 10Hz < f_0 < 30Hz \end{aligned} \quad 2.15$$

2.4.3 Rayleigh Wave Ellipticity

The elliptical movement of R-waves can be characterized as the ratio between the horizontal and vertical axis of the elliptical wave motion. This parameter is called ellipticity, and it is a function of the site frequency (Hobiger et al., 2012). A common way to compute the ellipticity is the HVSR technique. However, a signal usually contains other surface waves, such as L-waves. L-waves particle movement is performed only in the horizontal plane. Therefore, if this wave has a significant presence in the signal, the ellipticity is overestimated (Hobiger et al., 2009). The R-wave ellipticity can be computed after separating the R-wave from the rest of the signal. Several methods are available for performing this separation, as discussed in the signal processing section.

The R-wave ellipticity shows singularities when a strong impedance contrast (2.5-3.0) in the subsoil is presented, and the energy of the vertical component dissipates (Wathelet, 2005; van Ginkel et al., 2020). In a signal that only contains R-waves, the theoretical curve should have a peak at the fundamental frequency of the site and a trough at higher frequencies, as shown in Figure 2-18 (Malischewsky & Scherbaum, 2004; SESAME, 2004; van Ginkel et al., 2020).

The ellipticity curve with multiple peaks can be interpreted as higher modes at some frequency ranges indicating the presence of layers with low velocity, but also can be understood as several strong impedance contrasts in the substructure of the soil (Hobiger et al., 2013). The R-wave ellipticity provides information for the relative shape of the velocity profile. However, for a given soil-structure model, if the same factor is used to scale the wave velocity and the depth, the

ellipticity remains the same (Hobiger et al., 2013). Therefore, numerous authors have concluded that the ellipticity curve by itself cannot provide a V_S profile. Instead, it has to be combined with other methods, such as surface waves (Love's or Rayleigh's dispersion curves), or the inversion of the ellipticity curve needs to be constrained by limiting the thickness of the layers or the velocity of particular layers (Bonnefoy-Claudet et al., 2008; Hobiger, 2011; Hobiger et al., 2013).

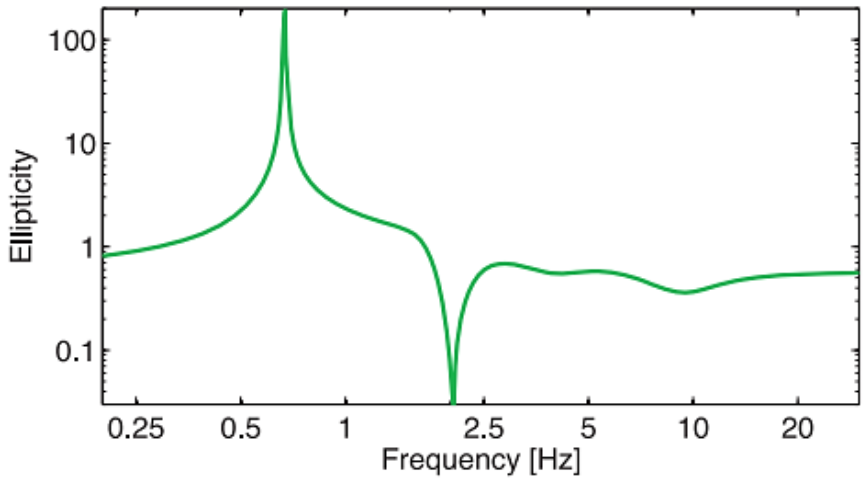

Figure 2-18: R-wave ellipticity curve with singularities (Hobiger et al., 2013)

Data collection

The data collection process is very similar to the HVSR method. R-wave ellipticity requires a three-component (North-South, East-West, and Vertical) seismic sensor. Usually, ambient vibration recordings are used for processing. The data collection can be performed using a single-station measurement or array measurements. Depending on the number of sensors employed in the field, the methods for processing differ. The recommendations provided by SESAME (2004) can be applied to the data collection.

Processing

Different methods can be used to compute the R-wave ellipticity. The technique used will depend on the number of sensors available for measurements. These methods can be separated into single-station and array measurement techniques. Single-station methods aim to identify the R-wave in the signal or suppress the other waves (excepting HVSR), while multiple sensor techniques intend to extract the wave polarization. Standard single-station techniques are HVSR, Horizontal to vertical Time-Frequency Analysis (HVTA), the Degree of Polarization (DOP), the Direct ELlipse FItting (DELFI), and the random decrement technique (RayDec). Among the array measurement techniques are the Poggi and Fäh method (2010) and the MUSIQUE algorithm. Several other methods are available in the literature (i.e., Maranò et al., 2012; Poggi et al., 2012; Tanimoto et al., 2013; Workman et al., 2017).

The HVSR method was reviewed in the previous section. The HVTFA method reduces the influence of the horizontal S-waves by identifying compressional and vertical shear wavelengths in the signal. Afterward, the HVTFA computes the spectral ratio only for those identified waves (Fäh et al., 2009). The DOP method calculates the ellipticity by measuring the stability of a signal with an arbitrary degree of polarization (Fotouhimehr et al., 2021). DELFI method estimates the ellipticity of the R-wave by fitting an ellipse to the filtered data (Hobiger, 2011). This method is performed in 2 steps. The first step is identifying the vertical plane in which the signal is confined, and then the signal is projected in a 2D plane. The second step is fitting an ellipse to the signal projected in the 2D plane. The RayDec method measures the ellipticity of the R-waves using a single seismic sensor based on the random decrement technique (Cole, 1971; Asmussen, 1997). RayDec applies statistical means to highlight the R-waves and suppress L-waves and body waves from the signal (Hobiger, 2011). The ellipticity computation using the RayDec technique showed

better agreement with the theoretical R-wave ellipticity curve than the ones provided by HVSR and DELFI curves (Hobiger et al., 2009).

For array measurements, the Poggi and Fäh method is an advanced version of the high-resolution frequency-wavenumber (HRFK). This method is based on the assumption that the true power amplitude of the signal is represented in the f-k cross-spectrum maxima (Poggi & Fäh, 2010). The MUSIQUE method was generated from a combination between the "classical" MUltiple SIgnal Classification (MUSIC) and the quaternion-MUSIC. This method used a two-step process to compute the R-wave ellipticity. The first step uses the classical MUSIC method to identify the azimuth and the velocity of the incoming wave. The second step uses the quaternion-MUSIC to estimate the polarization parameters of the wave, separating the noise from the signal to estimate the signal parameters (Hobiger et al., 2009).

Results

A comparison of the R-wave ellipticity computation is shown in Figure 2-19 from the study performed by Hobiger et al. (2009). A synthetic seismic ambient vibration signal of 620 seconds duration with random orientation was used. The R-wave ellipticity was computed using the HVSR (labeled as H/V in Figure 2-19) and the RayDec method. The results using each method were computed for 60 seismic sensors. Then the average curve and the error range were compared with the theoretical ellipticity curve. The results of the H/V technique showed an overestimation of the ellipticity compared to the RayDec method.

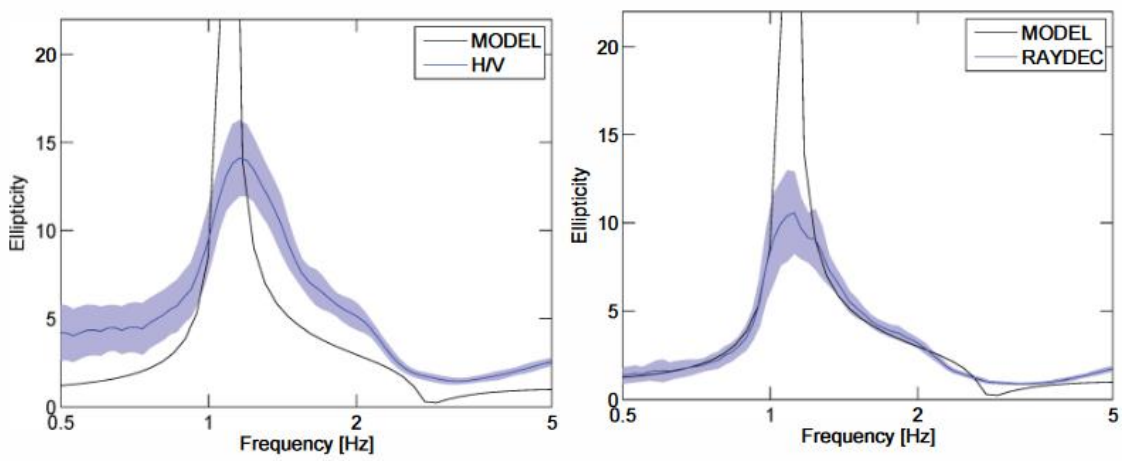

Figure 2-19: R-wave ellipticity curves using HVSR (left) and RayDec (right) methods. The theoretical ellipticity curve is plotted in black, the ellipticity curve computed using the methods is in blue, and the error range is shown in blue color (Hobiger et al., 2009).

Joint Inversion of Surface waves and Ellipticity

As mentioned before, the R-wave ellipticity curve can be combined with other techniques to constrain the bedrock depth (Gouveia et al., 2018). Hobiger et al. (2013) investigated V_S profiles using a joint inversion of the R-wave ellipticity curve and the dispersion curve from surface wave analysis (MASW and SPAC). An example of this implementation is shown in Figure 2-20. This study analyzed the influence of R-wave ellipticity that was used to perform the inversion and acquire the V_S profiles for theoretical data. The ellipticity curves analyzed in this study were significant and without singularities in the curve. In general, the results showed the best fit when the right flank of the ellipticity curve was used. In the case where the curve exhibited significant singularities, the best model was acquired when the trough, the lowest point of the curve, was not considered for analysis. If no singularities were detected in the curve, the best model was computed by selecting from the peak to the trough for joint inversion.

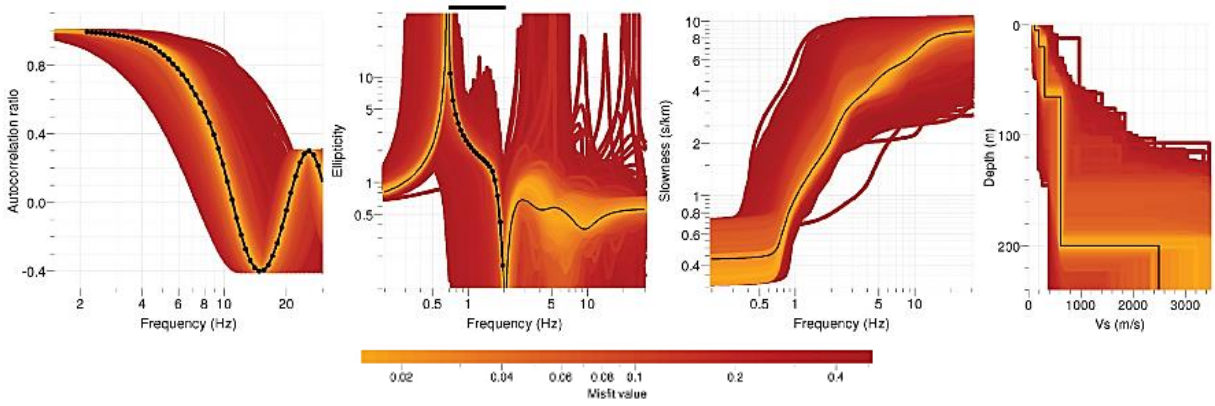

Figure 2-20: Joint inversion using R-wave ellipticity with SPAC method. SPAC curve (left), ellipticity curve (center left), dispersion curves (center right), and V_S profiles (right). The data points used for the inversion are shown as black dots, the curves corresponding to the true model as solid lines (Hobiger et al., 2013)

2.4.4 Proxy Methods

Proxy methods are another approach to obtain estimates of V_{S30} where *in situ* measurements are unavailable. The proxy methods are based on correlations between measured V_{S30} with a physical characteristic of the site, such as the geology, the topographic slope, and the terrain classification, among others (e.g., surface geology, fundamental site frequency, geotechnical categories). Most of these methods are generated in active seismic regions where sufficient measurements of V_{S30} are available to generate the correlations required. Then, the methods are expanded to other regions to generate estimates of V_{S30}. Many proxy methods are available, but this study will focus on the most commonly available proxy methods. These methods were reviewed and evaluated for the PEER NGA-East Database (Goulet et al., 2021) to evaluate the relative efficacy of the different proxy-based estimations of V_{S30}.

The terrain-based proxy method proposed by Yong et al. (2012) used the terrain classification performed by Iwahashi & Pike (2007). The terrain classification is based on the taxonomic criteria of the site, such as slope gradient, local convexity, and surface texture. These

taxonomic characteristics are the manifestation of near surface geology and allow to predict the material properties that have a large influence in site conditions and amplification. Slope gradient is the most important parameter in terrain classification due to its significant role controlling the geomorphologic process. Local convexity helps to differentiate in different low-relief features, as alluvial fans, flood plains, among others. Surface texture is related to the ridges and valleys which can be associated with the relative ages of the sedimentary deposits.

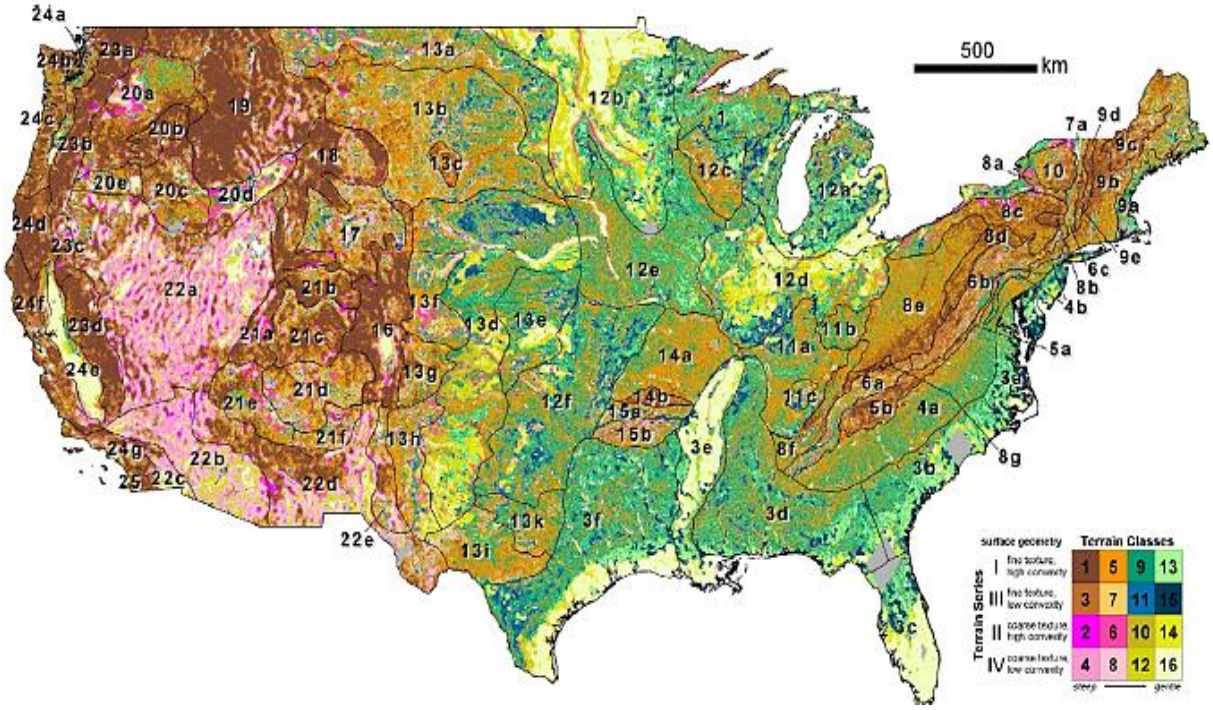

Figure 2-21:Terrain map for the United States (Iwahashi & Pike, 2007)

The terrain classification performed by Iwahashi & Pike (2007) involves 16 different terrain types. The terrain types were identified using digital elevation models with 1 km spatial resolution (30 arcsec) Shuttle Radar Topography Mission (SRTM30). The authors used the Next Generation Attenuation (NGA) strong motion database to acquire V_{S30} values from measured and inferred values. The terrain classification was applied to California and then correlated with V_{S30} values. The study was then extended to the contiguous United States. A map with the terrain

classification for the United States is shown in Figure 2-21.The only terrain group without any values associated was number 13, as shown in Figure 2-22.

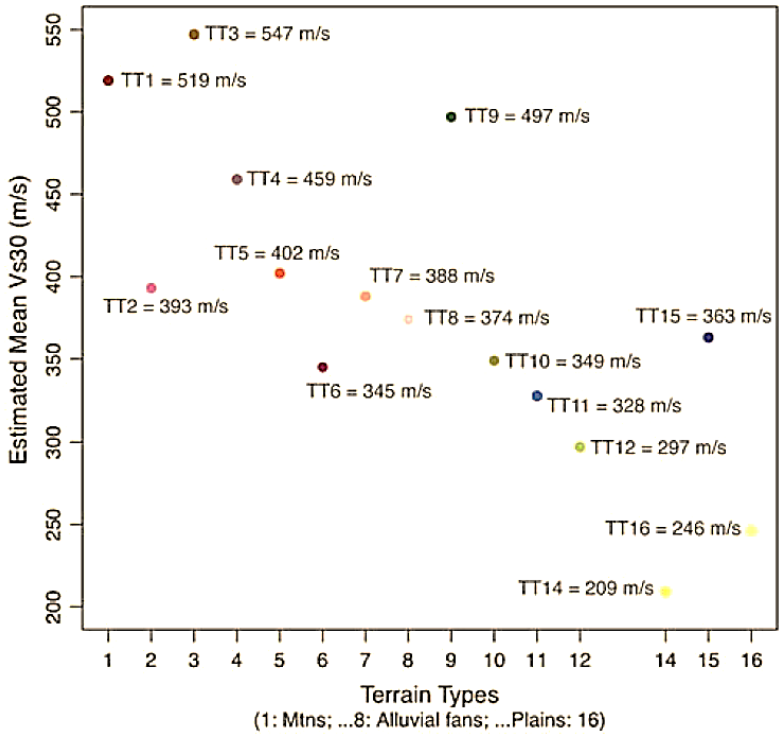

Figure 2-22: Plot of mean V_{S30} values for the terrain types, no estimate is provided for terrain type 13 (Yong et al., 2012)

Parker et al. (2017) developed the hybrid slope-geology proxy method using CENA data. The method categorized different sites into 18 groups based on the geologic era of formation. The classification designed by Parker et al. (2017) separates the geologic eras into different groups, and then the groups are broken down into subdivisions by geologic period and epoch when possible, as shown in Table 2-2. The groups were then correlated with seismic velocities acquired from measurements performed in CENA. A database of 2,755 V_{S30} values was compiled for this study. After the classification was performed, the authors analyzed the trends using semilog and log-log regressions with the topographic gradient method. Relationships were developed for some

of the groups, as shown in Table 2-2. An example of the trends developed for one of the groups is shown in Figure 2-23. Note the significant scatter in this data for a given slope.

Table 2-2: Summary of Proposed V_{S30} Estimation Procedures Based on Large-Scale Geologic Maps, Wisconsin Glaciation, Location of Site in a Basin, and Topographic Gradient (Parker et al., 2017)

Category*							Group Moments		Gradient Relationship				
									Semilog		Log–Log		
Group	Era	Period	Epoch	Wisconsin Glaciation?	Other Criteria	N	$\mu_{\ln V}$ (m/s)	$\sigma_{\ln V}$	c_0	c_1	c_2	c_3	$\sigma_{\ln V}$
1	C	Q	H	No	Alluvium, fluvial, and deltaic	308	210	0.23					
2	C	Q	H	No	All other lithology	183	221	0.29					
3	C	Q	H	Yes	In Ottawa, Canada	981	232	0.67	5.38	9.30			0.67
4	C	Q	H	Yes	Not in Ottawa, Canada	51	308	0.72			7.47	0.295	0.67
5	C	Q	Pli	No		284	271	0.36	5.47	31.4			0.31
6	C	Q	Pli	Yes	Till in Ottawa, Canada	104	777	0.57	6.51	22.4			056
7	C	Q	Pli	Yes	Other in Ottawa, Canada	60	377	0.65			7.20	0.22	0.63
8	C	Q	Pli	Yes	Not in Ottawa, Canada	63	448	0.65					
9	C	Q	U	No	Not in sedimentary basin	154	296	0.43			6.21	0.096	0.41
10	C	Q	U	No	In sedimentary basin	151	280	0.29					
11	C	Q	U	Yes	Not in sedimentary basin†	66	209	0.31	5.28	24.7			0.29
12	C	T				111	315	0.31			6.07	0.059	0.30
13	M					20	822	0.68					
14	P				In the Illinois basin‡	5	513	0.23					
15	P			No	Not in the Illinois basin	96	684	0.61					
16	P			Yes	Not in the Illinois basin	76	972	0.77					
17	pЄ					37	699	0.85					
18	pЄ				Site visit; hard-rock confirmation		2000						

*C, Cenozoic; Q, Quaternary; H, Holocene; Pli, Pleistocene; U, undivided; T, Tertiary; M, Mesozoic; P, Paleozoic, pЄ, Precambrian.
†Can be applied for within-basin sites with increased epistemic uncertainty (category unpopulated).
‡Because of the small population size, the mean and standard deviation carry a larger degree of epistemic uncertainty than for other groups.

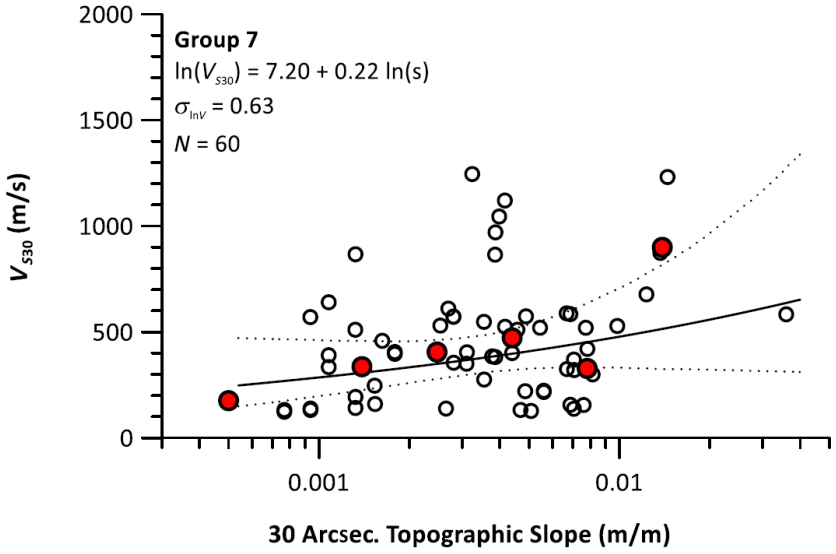

Figure 2-23: V_{S30} as a function of 30 arcsec topographic gradient for group 7 (Parker et al., 2017)

The topographic slope method, proposed by Wald & Allen (2007), is based on the hypothesis that the topography of a site shares similarities with the geology, specifically the slope of the topography. Then, this relationship can be used to provide an estimate of the seismic hazard of the site. The first step of this analysis was to develop correlations between the 30 arc-second topographic data with the V_{S30} measurements in seismically active areas. The analysis was then repeated for stable continental regions, and then it was assumed that the correlations could be applied to areas with limited V_{S30} measurements.

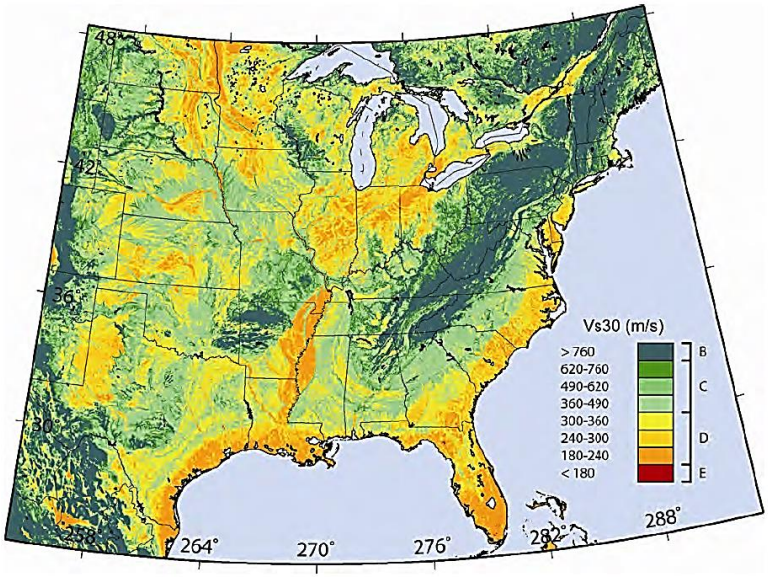

Figure 2-24: Estimated site-condition map for the continental United States east of the Rocky Mountains, derived from topographic slope and slope- V_{S30} correlations for stable continental regions (Wald & Allen, 2007).

The topographic slope was acquired using the Shuttle Radar Topography Mission 30-sec (SRTM30) global topographic data set (Farr & Kobrick, 2000). A map of the estimated V_{S30} values for the eastern United States proposed by Wald & Allen (2007) is shown in Figure 2-24. Among the limitations of the method is the deficient prediction of geological conditions in which the topographic slope cannot predict the composition of the geologic materials, such as unweathered volcanic plateaus or flat-lying carbonates.

The surface geology proxy method proposed by Kottke et al. (2012) compiled a database of 1930 measured and inferred V_{S30} values in CENA to develop the surface geology method. The method divided CENA into geologic classes are based on setting (i.e., glaciated or non-glaciated), age, and depositional environment (Kottke, 2012). Three major geologic classes are identified in CENA glaciated, non-glaciated, and residual soils. Then, the major units were subdivided, generating 19 different geologic classes as shown in the map, Figure 2-25. Each geologic class was correlated with V_{S30} values, as shown in Table 2-3. However, some of the geologic classes had few V_{S30} measurements available to generate reliable correlations, and only nine of them could be correlated to a V_{S30} value.

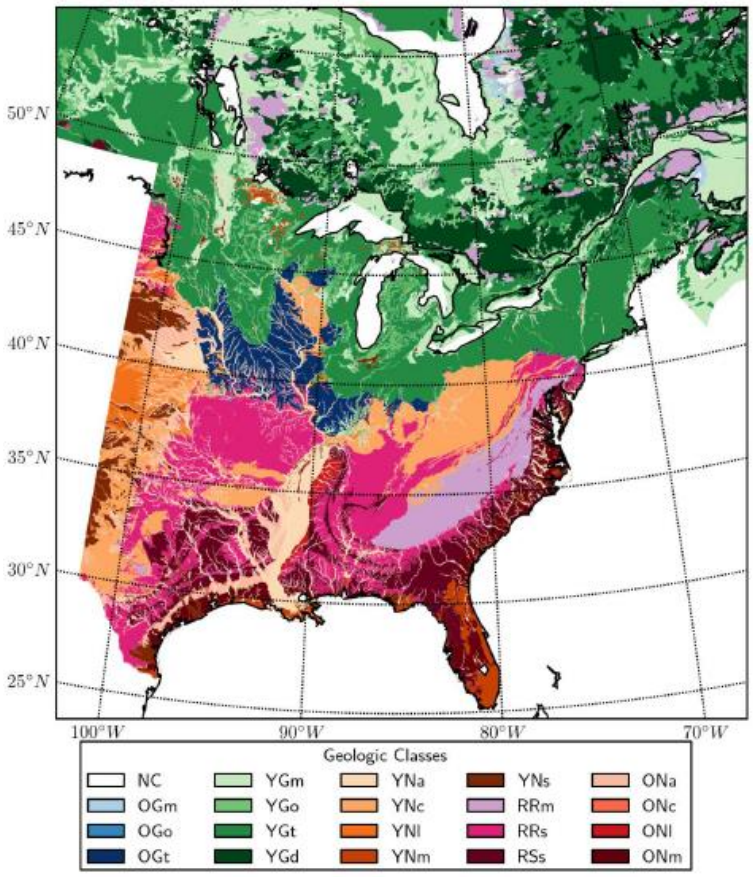

Figure 2-25: Map of the geologic classes for CENA (Kottke, 2012)

Table 2-3: Geologic classes for CENA (Kottke, 2012)

Major Unit (Age)	**Sub-unit**	**Abbrev.**	**Thick. (m)**	**Soil Class**	**Mean V_{s30} (m/s)**	**σ_{lnV} (m/s)**
Old Glacial Sediments (Older than Wisconsin)	Glaciomarine and Lacustrine	OGm	9	ONm	--	--
	Outwash and alluvium	OGo	7	ONa	--	--
	Tills	OGt	16	ONa	--	--
Young Glacial Sediments (Wisconsin and younger)	Glaciomarine and Lacustrine	YGm	8	YNm	520	0.53
	Outwash and alluvium	YGo	11	YNa	470	0.67
	Tills	YGt	16	YNa	300	0.45
	Discontinuous Till	YGd	5	YNa	1050	0.39
Old Non-Glacial Sediments (Mid-Pleistocene and older)	Alluvium	ONa			--	--
	Colluvium	ONc			--	--
	Loess	ONl			250	0.11
	Lacustrine, Marine and Marsh	ONm			290	0.22
Young Non-Glacial Sediments (Holocene and late Pleistocene)	Alluvium	YNa			220	0.14
	Colluvium	YNc			--	--
	Loess	YNl			--	--
	Lacustrine, Marine and Marsh	YNm			230	0.12
	Beach, dune, and sheet sands	YNs			210	0.18
Residual Sediments	Residual from metamorphic and igneous rock	RRm			--	--
	Residual from sedimentary rock	RRs			--	--
	Residual from soils	RSs			--	--

CHAPTER 3 METHODOLOGY

3.1 INTRODUCTION

This chapter describes the methodology used to compute and estimate V_{S30} for the current study. The methods described in this chapter are non-invasive methods classified as direct and indirect methods. The location of the seismic stations and sites analyzed in this study are shown in Figure 3-1. From the figure, the locations are separated into the sites and seismic stations in which direct methods were applied and the seismic stations where only indirect methods were applied. The V_{S30} measurements from direct methods of the sites and seismic stations were performed for this study and collected from publicly available reports. An emphasis was placed on sites where seismic stations were currently located or previously located to allow for comparisons between the seismogram-based approaches and the other methods.

Direct methods were applied to 15 locations, 11 of them were measured by this study, and four of them were collected from publicly available reports. Of the 11 sites measured by this study, five are located on the same site as former seismic stations or very close to them. The four sites and seismic stations collected from publicly available reports are BLF1, AFBM, SWET, and LRAL. The direct methods applied to each site and seismic station are summarized in Table 3-1. The results computed using the direct methods are shown in Chapter 4.

The indirect methods were applied to all the sites and seismic stations located in Alabama and close to the border in neighboring states (Tennessee, Georgia, and Florida), as shown in Figure 3-1. A total of 56 seismic stations and seven sites were selected for this study to apply the indirect methods. Of the 56 stations, 14 are operative to this date, four have been active for more than ten years, and the rest were recorded for shorter periods, varying from 1 month to several years.

Several of the stations found in the state were part of the USARRAY/Earthscope project. Details about the stations used in this study can be found in Chapter 5, including a summary in Table 5-2. As mentioned before, many of the indirect methods required a 3-component seismic sensor. Therefore, the data required to estimate V_{S30} was retrieved from seismic station recordings. The data were obtained directly from the IRIS Database web services using the Timeseries v.1® (IRIS, 2021)

Table 3-1: Geophysical methods applied to the seismic stations and sites

Site/ Station	MASW Active	MASW Passive	Seismic Refraction	Other
ASEL	X	X	X	
TU01	X	X	X	
SR-21	X		X	
SR-219	X		X	
AN01	X	X	X	
BLF1*	X			
AFBM*				P-S Suspension Logging
X50B	X	X	X	
S1AL	X	X	X	
S2AL	X	X	X	
Y47A	X	X	X	
X48A	X	X	X	
B01X	X	X	X	
SWET*				MALW-SASW
LRAL*				SASW

* Sites and seismic stations collected from publicly available reports

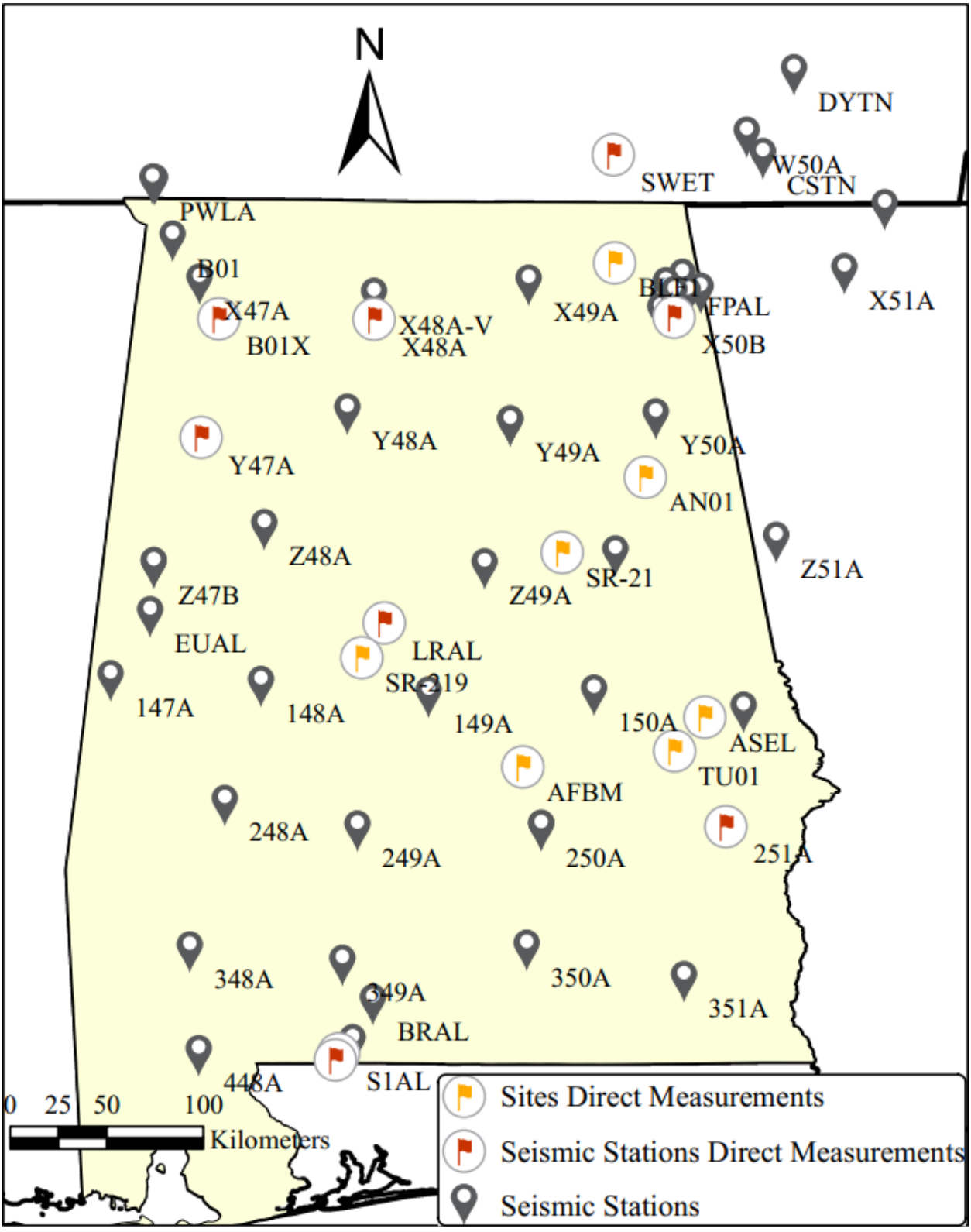

Figure 3-1: General location of seismic stations and sites analyzed in this study.

3.2 DIRECT METHODS

The direct methods used in this study were MASW and seismic refraction. The MASW method included both active and passive measurements where possible. Also, in this section, a non-inversion approach is described to compute V_{S30}. For these methods, a detailed description of the equipment used is presented. Descriptions of the data collection, the processing parameters, and the software used to compute the results are also provided. As each site has its own characteristics, some data acquisition and processing parameters were adapted to retrieve reliable results. These specific parameters are described in the next chapter (Chapter 4).

3.2.1 Multichannel Analysis of Seismic Waves (MASW)

Data Collection

The data collection for MASW surveys was performed using vertical geophones, brand R.T. Clark and Geostuff, with a natural frequency of 4.5 Hz. The geophones were connected to a Geode seismic recorder manufactured by the Geometrics company. The equipment is shown in Figure 3-2.

Figure 3-2: Vertical geophone (left) and Geode seismic recorder (right)

The active seismic survey used 24 or 48 geophones arranged in a linear array with a spacing of 1 or 2 m, obtaining a survey line from 23 m to 94 m depending on the site characteristics. The data were recorded with a sampling frequency of 2,000 Hz for 1.5 seconds for the active survey. The active source was a sledgehammer (45 and 90 Newtons) located at the beginning and the end of the survey line, and three to five shots were recorded at each position.

The passive seismic survey used 24 geophones positioned in an L shape array with an angle of 90 degrees or a linear array using a similar location as the active survey. The geophones were spaced 5 m apart for a total array length of 115 m. The data were recorded with a sampling frequency of 250 Hz for 240-260 seconds. Several measurements were performed to achieve a total recording time of approximately 30 min. A summary of the parameters used to collect the data for the passive and active seismic survey can be found in Table 3-2.

Table 3-2: Parameters used for geophysical seismic surveys

	Active	**Passive**
Number of Geophones	24-48	24
Spacing	1-2 m	5 m
Array	Linear	L-shape / Linear
Survey Line Length	23-94 m	90m
Sampling Frequency	2,000 Hz	250 Hz
Record Length	1.5 s	240-260 s
Source	Sledgehammer	Ambient Noise
Number of records	3-5	7-8

Processing

The data collected for the active survey was processed using the software Geopsy (Wathelet et al., 2020), open-source software for geophysical research and applications. The data were processed using the tool "linear FK for active experiments." It used a 2D transform to convert the data to the frequency domain and obtained the phase velocity dispersion curve for each recorded shot (Wathelet, 2008). One dispersion curve was handpicked for each shot performed at the site to proceed with the inversion.

The data collected for the passive survey was processed using the SurfSeis software developed by Kansas Geological survey (SurfSeis, 2010). The software gathers the information from all the recorded files and combines them to calculate the fundamental mode from the dispersion curve of the phase velocity. For some of the sites, no dispersion curve could be observed from the passive data. As mentioned before, the use of passive MASW depends on the energy of the passive source; when the site is isolated, there is not enough energy to capture by the equipment. Therefore, for these sites, only active data were used. For the sites in which a dispersion curve could be observed from the passive recordings, the overtone images (phase velocity versus frequency) were combined in SurfSeis software. From the combined file, the dispersion curve of the fundamental mode was retrieved and used for inversion.

The phase velocity dispersion was computed using a minimal distance of the source of 20 m to avoid near-field effects, which cause distortions in the phase velocity estimation (Foti et al., 2018).

Inversion

The inversion generates a 1D V_S profile that will be positioned in the middle of the array. Afterward, the selected dispersion curves were imported on Dinver software. This software solves

the inversion problem through a random process that generates V_S profiles based on parameters provided by the user. Then, the software computes the dispersion curves for these profiles and compares them with those measured on the survey to compute a mismatch. Commonly, many profiles will have a similar level of mismatch to the provided curve. Since the solution is not unique, the software outputs different profiles with their corresponding mismatch (Wathelet et al., 2020).

Each site had multiple dispersion curves from the different shots. The dispersion curves from the survey were first resampled with Dinver software from Geopsy package to improve the smoothness of the curve. Afterward, an average dispersion curve was computed to perform the inversion. The main goal of the inversion is to provide a good model that fits the data. For this purpose, over 100,000 models were simulated for each site. This number provides good convergence for data inversions (Hobiger et al., 2013).

Non-Inversion

The non-inversion approach used the same dispersion curve that was used for inversion, the average dispersion curve from the shots acquired from active measurements. This dispersion curve was the input to compute V_{S30}. The code to calculate the V_{S30} profiles is a MATLAB function, and it was provided by S. Lin (personal communication, June 8, 2021).

3.2.2 Seismic Refraction

Data Collection

The data collection for seismic refraction surveys was performed using the same equipment and array as the active MASW. The data included several shots along with the array at a distance of 3 to 10 m from the end of the survey line.

Processing

For the seismic refraction method, the data were processed in the SeisImager package, (Geometrics, 2009). In the software, the file is read and displayed on the screen. The screen can be adjusted to observe the first arrivals of the P-wave. The traces were normalized to the maximum amplitude of each trace and clipped to prevent them from visually interfering with one another. Filters were not used for processing in this study. The traces with higher noise content that did not allow the first arrival detection were removed or not considered for the inversion. The first arrivals were handpicked, and the software saved the selected points for each one of the shots performed.

Inversion

The seismic refraction inversion was performed in Plotrefra Software from the SeisImager package (Geometrics, 2009). The first arrivals picked in the previous stage were opened in the software, as shown in Figure 3-3. The time-term method was used for the inversion of the data.

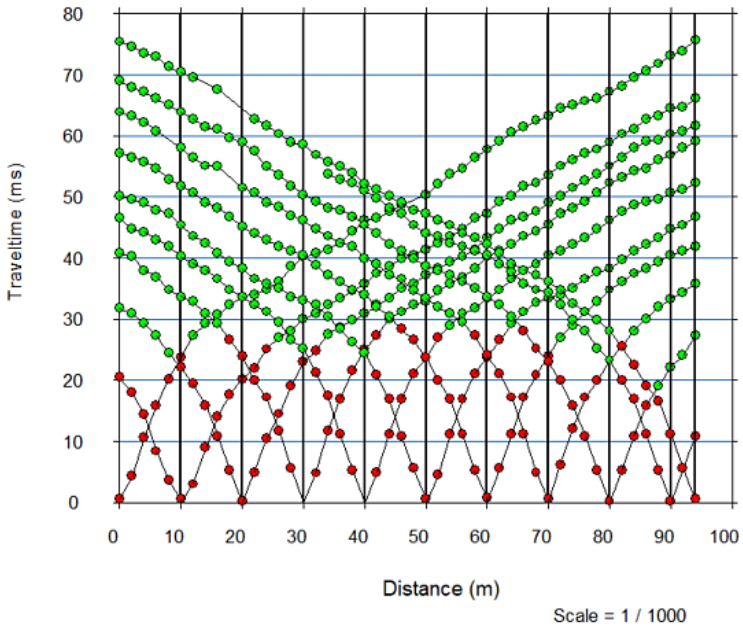

Figure 3-3: Time travel selection for several shots at station S1AL using Plotrefra Software (Geometrics, 2009)

For the inversion, the number of layers is assigned to each curve by picking the point where the curve changes its direction. For station S1AL, shown in the image, a two-layer model was selected for this site. The first layer is shown in red and the second layer in green. For the estimation of $V_{S,}$ a range of $0.4V_P$ to $0.6V_P$ will be used. Lower values, 0.14 V_P to 0.2 V_P, were used when the presence of water was identified in the sites to correct for the effect of water in $V_{P.}$

3.3 INDIRECT METHODS TO ESTIMATE SHEAR WAVE VELOCITY

The indirect methods include the P-wave seismogram, the HVSR method, the R-wave ellipticity method, and the proxy methods. The P-wave seismogram method section incorporates a complete description of the application of the approach, the selection of the stations and seismic records, and the correlations used to estimate V_{S30}. The HVSR section describes the data collection and processing used to compute the HVSR curves and the correlations available to estimate V_{S30}. The R-wave ellipticity method describes the data collection and processing used to compute the ellipticity curves and a joined inversion with the MASW method to acquire V_{S30}. Finally, the proxy method section describes the implementation of selected methods for this study.

3.3.1 P-wave Seismogram Method

Data Collection

The P-wave seismogram method was applied to seismic stations located in Alabama and close to the border in neighboring states (Tennessee, Georgia, and Florida). The earthquakes selected for this method are shown in Figure 3-4. The earthquake waveforms were acquired from the IRIS database, with the correction for the instrument response already performed in the record. The selected seismic records for each station considered in this study were constrained by two factors, the distance between the station and the epicenter of the earthquake and the magnitude of

the event. The events selected were located within a radius of 300 km from each station with magnitudes between 2 and 4.4, based on the recommendations from Kim et al. (2016). A total of 56 stations were selected to apply the P-wave seismogram method. Details about the stations used in this study and the number of records can be found in Table 5-2, located in section 5.2.

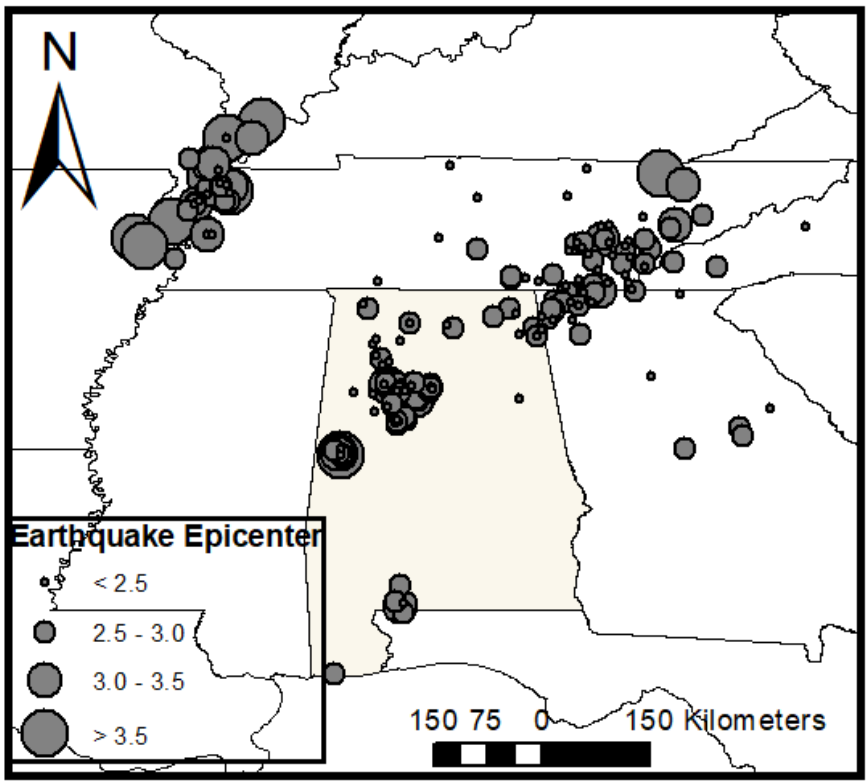

Figure 3-4: Earthquake epicenter location of selected records in the study area. The location of the earthquakes is represented by circle scales by the earthquake magnitude.

Processing

A MATLAB code was implemented to request and process the signals following the methodology proposed by Kang et al. (2020). Acceleration time series were used if available, but only velocity times series were available for some of the stations. The recorded acceleration and velocity time series with the instrument correction applied were further corrected (detrend and demean), filtered, and baseline corrected. A band-pass Butterworth filter with corner frequencies

of 0.5 and 30 Hz was applied to the accelerograms as Kang et al. (2020) recommended. For the velocity time series, the lower filter was increased to 2 Hz, and the upper filter was decreased to 15 Hz. The lower filter was increased to remove the longer period of noise in the signal (Hosseini et al., 2016), while the upper filter was decreased to remove the high-frequency noise in the data. The accelerograms were integrated to compute the velocity time series, and the horizontal components were rotated to obtain radial and tangential components using the azimuth of the epicenter.

The P-wave arrival detection was performed using the software PPHASE PICKER (Kalkan, 2016). The algorithm detects the time before the arrival of the P-wave in a broadband velocity time series. A manual check was performed on each record to observe if the time selected by the software was prior to the P-wave arrival, and manual corrections were performed if needed. An example of the selection of the picks is shown in Figure 3-5.

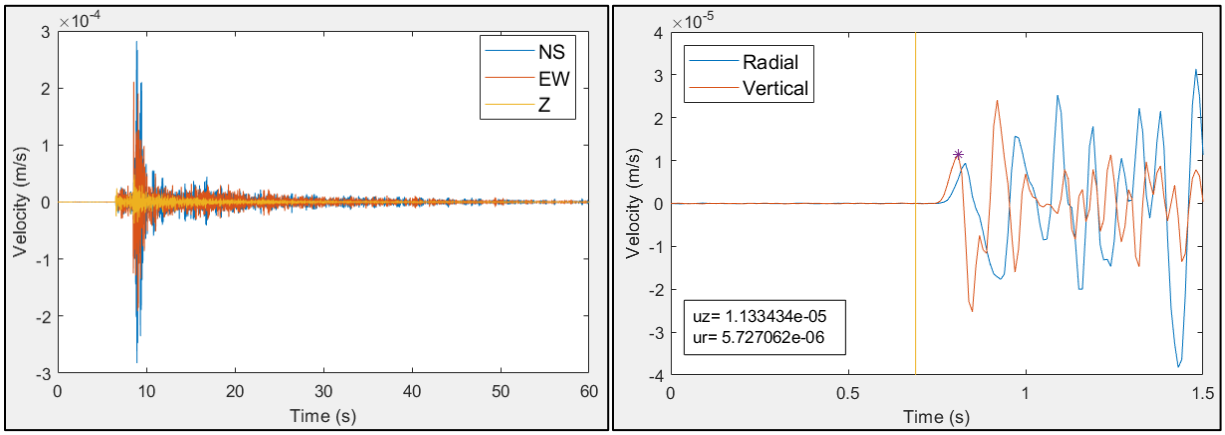

Figure 3-5: Velocity time series for EW, NS, and vertical components (left), zoomed-in time series of radial and vertical components (right) for the 11 March 2017 earthquake M2.7 recorded at station X48A.

Another baseline correction was performed to the data based on the 0.5 seconds before the P-wave arrival to improve the estimation of V_{S30} as suggested by Kang et al. (2020). The baseline

correction is computed for each one of the ground motions and applied to a smaller data window around the P-wave arrival (window of 1.7 sec). The signal-to-noise ratio (SNR) was computed using 0.5 seconds of the recording before the P-wave arrival as the noise, and the records with an SNR less than 1.5 were discarded.

The ray parameter was computed using the equation 2.6 and simplified crustal velocity structure of two layers following the procedure described by Kim et al. (2016). For this purpose, the study area was divided into three regions: Southern Appalachian, Central Tennessee, and Gulf Coast, as shown in Figure 3-6.

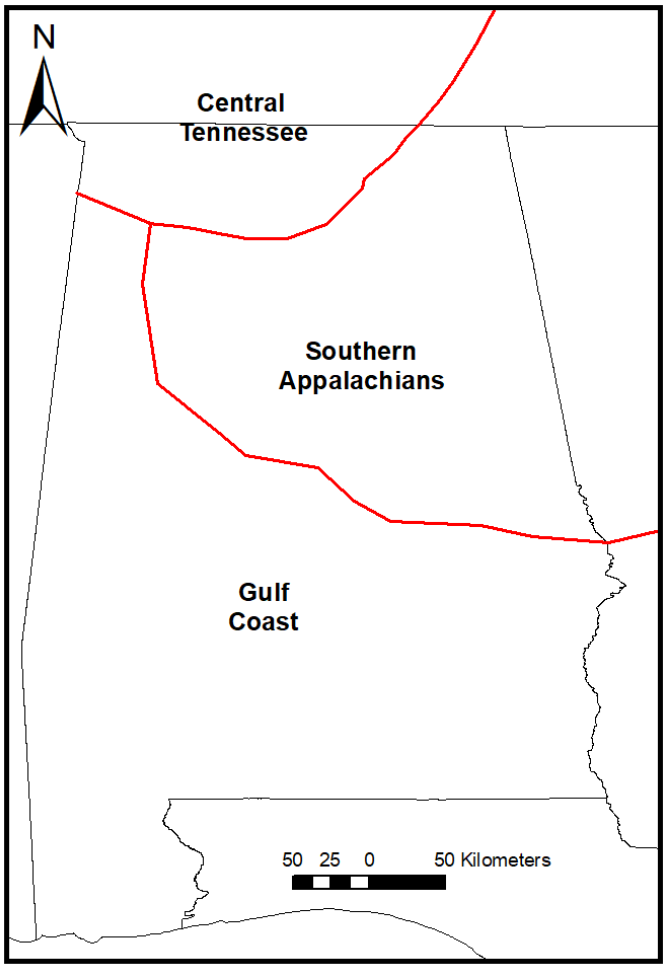

Figure 3-6: Study area with the delimitations of the regions of the crustal models.

The crustal velocity models were acquired from EPRI (1993) for the Southern Appalachian and Central Tennessee regions. The crustal model for the Gulf Coast region was obtained from Dreiling et al. (2014). The values of P-wave velocity and depths for each layer for the models are shown in Table 3-3. The process for developing a simplified two-layer model from these crustal models is described in the next paragraph.

Table 3-3: Crustal velocity models (EPRI, 1993; Dreiling et al., 2014)

Layer	Southern Appalachian (SA)		Central Tennessee (CT)		Gulf Coast (GC)	
	P-wave Velocity (km/s)	Depth (km)	P-wave Velocity (km/s)	Depth (km)	P-wave Velocity (km/s)	Depth (km)
1	4.9	1	4.9	1	5.9	4
2	5.63	6	6.4	20	6.2	16.5
3	6.05	15	6.8	35	6.6	30
4	6.53	50	7.3	50	7.3	41
5	8.18		7.9		8	

The seismic station location determined the crustal model used for the computation of V_{SZ}. The crustal models shown in Table 3-3 have five layers extending until 41 to 50 km depth. A simplified two-layer model must be developed to apply the P-wave seismogram method. For this study, the first layer of the applicable crustal model for the region (Table 3-3) was used as the first layer in the two-layer model. The velocity of the second layer was computed as the depth-weighted average P-wave velocity between the bottom of the first layer and the hypocentral depth of the earthquake, as recommended by Kim et al. (2016). An iteration process is then performed to compute V_{SZ}, as described in Section 2.4.1. This process was repeated until the difference between the values of the j angle reached a level of tolerance of 0.5 degrees.

3.3.2 Horizontal to Vertical Spectral Ratio (HVSR)

Data Collection

The data for the HVRS were acquired from the IRIS website for three-component seismic sensors. The duration of the signal retrieved from the website was 12 hours of duration. Several days were examined from the available recordings on each station. The time frame was constrained by the dates that the equipment was operatively functioning and the available recordings of each station. Some of these stations did not have continuous recordings; as mentioned before, some were only recording for a limited time frame. The trial day and time frame were selected to ensure that the recording had the least transient noise possible in the acquired signal. For this study, the signals were obtained from ambient noise. The duration of the signal selected for further processing was over 30 min, as recommended by SESAME (2004) in Table 2-1.

Processing

The signal processing was performed using the software Geopsy (Wathelet et al., 2020) with the toolbox H/V. The signal processing was conducted in the signal section with stationary noise, avoiding transient noise. The part of the signal selected for processing was divided into windows of the same length. A 60-second window with 5% overlaps was used. A threshold was selected to avoid drastic variations in amplitude. For this analysis, a percentage between 5 to 30% was used as a threshold depending on the variation of amplitudes within the signal. Also, an anti-trigger algorithm was applied to the raw signal. For this purpose, STA and LTA values were defined. The STA and LTA were 5 seconds and 0 seconds, respectively. Also, a minimum ratio between STA and LTA of 0.1 and a maximum ratio of STA and LTA of 10 were selected.

The horizontal components of the signal were square-averaged for the computation of the Fourier amplitude spectrum. Then, the Konno & Ohmachi smoothing function (Konno &

Ohmachi, 1998) was applied to the Fourier amplitude spectrum. For the smoothing function, a constant of 20 and a cosine tapper window was used. Afterward, the HVSR curves were computed for each one of the windows.

Correlations of F_0 with V_{S30} measurements

After the peak of the HVSR curve was identified, the correlations found in the literature review were used to estimate V_{S30}. The correlations used in this study were taken from Ghofrani & Atkinson (2014), Hassani & Atkinson (2016), and Stanko & Markušić (2020).

3.3.3 Rayleigh wave ellipticity

Data Collection

The same data used for the computation of HVSR was used to compute R-wave ellipticity. Therefore, the signal is a single-sensor measurement. From the signal, a two-hour window frame was selected for further processing.

Processing

The R-wave ellipticity was computed using the RayDec method (Hobiger et al., 2009). RayDec is publicly available (ManuelHobiger, 2021) as a MATLAB function to estimate the ellipticity of R-waves from three-component single-station recordings. The signal analysis was performed between a minimum frequency of 0.2 Hz and a maximum frequency between 18-40 Hz, depending on the type of equipment used to record the signal. For equipment with a sampling frequency of 40 Hz, a maximum frequency of 18 Hz was used for the analysis. The rest of the equipment used a maximum frequency of 40 Hz. The signal was divided into 10-minute windows, as suggested by Hobiger et al. (2009). The RayDec code computed ellipticity curves for each one

of the time windows selected. Additionally, the average of the ellipticity curves and standard deviations were calculated.

Joint Inversion of Surface Waves and Ellipticity

The joint inversion of the R-wave ellipticity curve and the dispersion curve of the fundamental mode of the R-waves were performed using Geopsy Software (Wathelet et al., 2020). Depending on the site, the velocity model was defined between 2-4 layers. A wide range of potential velocities was used for the inversion to allow the model to include the overall variation of the velocity profiles. The Poisson's ratio varied from 0.2-0.5, and the density was constant for all the layers, 2,000 kg/m^3. The values of the Poisson's ratio and the density of the soil do not significantly impact the inversion process (Gouveia et al., 2018).

The joint inversion was made considering equal weight for the misfits of the dispersion and the ellipticity curves. The inversion process was repeated until over 100,000 models were computed to verify the stability of the inversion.

3.3.4 Proxy Methods

For this research, the terrain-based, the hybrid slope-geology, and the topographic slope proxy methods were used to estimate V_{S30}. These three methods were selected because they have been reviewed and evaluated for the PEER NGA-East Database (Goulet et al., 2021). The surface geology proxy method proposed by Kottke et al. (2012) could not be used for this study because Alabama is mostly classified as Residual soil from the map (Figure 2-25), and this geology classification does not have a V_{S30} value associated.

A GIS-based engineering geomorphological map was used to implement the terrain-based proxy. The map is publicly available from Iwahashi & Pike (2007). The terrain map was obtained,

and then the location of the stations was imported into the same map to classify each station into the terrain types. Once the terrain type of each station was identified, the correlation proposed by Yong et al. (2012) was used to acquire a value of V_{S30}.

For the application of the hybrid slope-geology proxy method, each station was categorized according to the geologic age of formation. The geologic period and epoch were also identified for the stations in the Cenozoic era. This method proposed 18 groups to classify the geologic formation (Parker et al., 2017). The groups belonging to the Wisconsin glaciation were discarded from this study. After each station was classified into the groups, the correlation proposed by Parker et al. (2017) was used to assign a value of V_{S30}. The results acquired for each one of the stations are presented in Table 5-2.

The topographic slope method was implemented similar to the terrain-based proxy method, using a GIS-based engineering geomorphological map (Wald & Allen, 2007; Allen & Wald, 2009; Yong et al., 2016; Heath et al., 2020) publicly available from the USGS website (https://earthquake.usgs.gov/data/vs30/). The GIS-based map was downloaded, and the location of the seismic stations was imported into the map. The GIS-based map provided the velocity for each location based on the topographic slope.

CHAPTER 4 RESULTS OF DIRECT METHODS

4.1 INTRODUCTION

The collected V_{S30} measurements from the application of direct methods across the state are presented in this Chapter. The Chapter is separated into two main sections. The first section describes all the sites in which this study performed the direct methods. The second section describes all the sites collected with previously published data. All the sites analyzed for this study are shown in Figure 3-1. The methods applied to each site and the seismic station are summarized in Table 3-1. Both sections are separated into subsections according to the site or seismic station where the methods were applied. The first section presents a description of the location, geology, particular details regarding the data collection process (i.e., type of source used, number of receivers, location of the shots performed, among others), and the results for each site. The second section showed profiles adapted from published data and V_{S30} measurements for those profiles.

The results included MASW and seismic refraction methods. For the MASW method, the classical inversion and a non-inversion approach were used. Also, over 100,000 models were generated to develop a wide range of acceptable models. However, only a subset of the best 5,000 V_S profiles is presented. The seismic refraction method generated 2D profiles of V_P using two- and three-layers models. The V_P profiles were transformed into V_S profiles for each site to compute V_{S30}. MASW method could not be applied to the AN01 site. For this site, only seismic refraction results are provided.

A summary of the results from the application of the direct methods to the sites and seismic stations is shown in Table 4-1.

Table 4-1: Summary results from the direct methods applied to the sites and seismic stations

Site/ Station	MASW			Seismic Refraction	Joint Inversion		SASW	Other Method
	V_{S30} (m/s) from Inversion	Std (m/s) from Inversion	V_{S30} (m/s) from non-Inversion	V_{S30} (m/s)	V_{S30} (m/s)	Std (m/s)	V_{S30} (m/s)	V_{S30} (m/s)
ASEL	424	19.8	399	367-551	-	-	-	-
TU01	354	13.9	351	212-304	-	-	-	-
SR-21	396	1.01	349	281-422	-	-	-	-
SR-219	286	1.07	295	204-290	-	-	-	-
AN01	-	-	-	788-1,182	-	-	-	-
BLF1*	-	-	-	-	-	-	-	1,165
AFBM*	323	-	-	-	-	-	-	-
X50B	943	12.1	958	841-1,261	964	21.2	-	-
S1AL	317	0.3	326	221-313	340	1.8	-	-
S2AL	357	1.99	357	193-284	354	3.3	-	-
Y47A	425	1.16	414	339-508	401	0.2	-	-
X48A	501	2.2	490	780-1,170	540	3.4	-	-
B01X	760	3.3	598	855-1,282	734	11	-	-
SWET*	-	-	-	-	-	-	715	840
LRAL*	-	-	-	-	-	-	568	-

* Sites and seismic stations collected from publicly available reports.

4.2 SITES WITH DIRECT METHODS COLLECTED BY THIS STUDY

4.2.1 ASEL Site

Location and Geology

The site is located in Auburn, Alabama, on W. Samford Ave. and Shug Jordan Pkwy (32.60139, -85.50611). At the time of the survey, the site had a sloped surface from northeast to southwest, and there was a road filled with gravel to access the site. The site is now covered by the Advanced Structural Engineering Laboratory (ASEL). The location of the site and the survey array are shown in Figure 4-1.

On this site, two geological units are located, Manchester Schist from the Pine Mountain Group and Tuscaloosa Group undifferentiated. Manchester Schist shows interlayered muscovite-quartz schist and quartzite. Also, the geological unit locally contains garnet, sillimanite, and graphite, which are commonly intensely shared characteristics of weathered soil. Tuscaloosa Group exhibits varicolored clayey, gravelly, gravelly fine to very coarse sand; massive mottled sandy clay; local wood and leaf beds; and some thin beds of indurated sandstone. Gravel consists primarily of quartz and quartzite and range in size from very fine pebbles to large cobbles (Szabo et al., 1988).

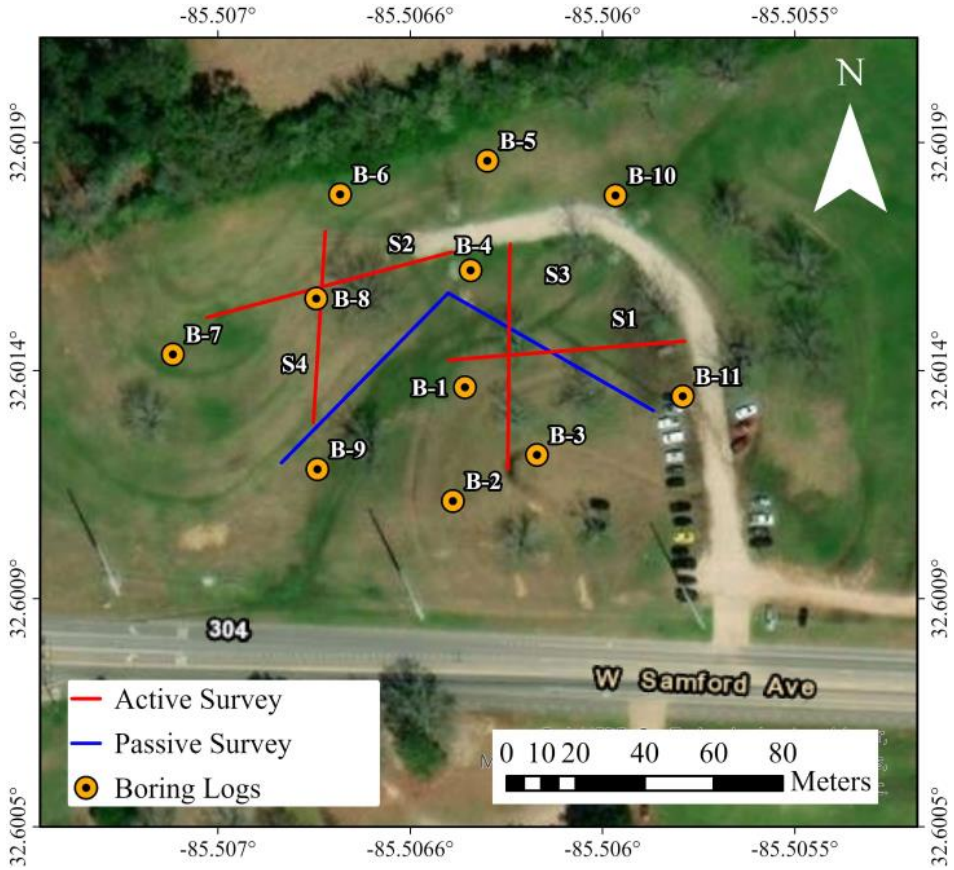

Figure 4-1: Site map with the location of the survey line for the ASEL site

Previous Investigation

A field exploration of the site was performed by Bhate company (Bhate, 2018) between May 8 to 10, 2018. A total of 11 boring logs were drilled at the site reaching different depths. A detail of the boring logs can be found in Appendix A. Boring B-1 reached a depth of 12.2 m (40 ft); boring B-2 was drilled to a depth of 10.4 m (34 ft); borings B-3 and B-4 were extended to 4.7 m (15.5 ft) of depth; borings B-5 and B-6 reached a depth of 6.2 (20.5 ft); borings B-7 and B-8 were drilled until 4.7 m (15.5 ft) of depth; and boring B-9, B-10, and B-11 were extended to 1.7 m (5.5 ft) of depth.

The soil exploration had residual soil or coastal plain sediments immediately below the topsoil. Some locations had a layer of sediments between three and five feet; in others, the residual soil was found immediately below the surface. The sediments consisted of dense, mottled red-brown to gray clayey fine sand. The residual soil contained medium to stiff varicolored elastic, micaceous silt, and fine sand, reaching depths between 7.6 to 9.1 m. The residual soil showed remnant rock structure increasing its consistency with depth. Three boring logs had schist at depths between 7.6 to 9.1 m.

Data collection

Active and passive seismic surveys were performed at the site. The active seismic survey was used for MASW and seismic refraction analysis. The active survey used 48 geophones arranged in a linear array with a spacing of 1 m, obtaining a survey line of 47 m. Active data were recorded with a sampling frequency of 2,000 Hz for 1.5 s, and a delay of -0.1 s was used for recording. No acquisition filters were used. For MASW analysis, the active source was located at the beginning of the survey line, and five shots were recorded in the same position. For seismic refraction analysis, five shots were performed from the beginning until the end of the survey line,

at 3 m each. The passive seismic survey was performed using 24 vertical geophones using an L shape array with an angle of 90 degrees, as shown in Figure 4-1. The geophones were spaced 5 m between each other, obtaining a total length of 115 m. Passive data were acquired with a sampling frequency of 250 Hz for 260 s. A total of 7 files of 260 s duration were recorded to reach 30 min total.

The inversion of the active data was developed using the dispersion curve extracted from line S2. Line S2 was selected because it showed a clear fundamental mode in a wide range of frequencies. The other lines provided similar results in a smaller frequency range. The dispersion curve from the active survey was joined with the passive data collected at the site.

MASW Results

The *Vs* profiles and the dispersion curves for 5,000 of the profiles generated with the lowest misfit are shown in Figure 4-2. The V_S profile with the lower misfit is shown in black and the field dispersion curve is drawn in dark gray, while the corresponding curves from each of the profiles are colored according to their misfit value. A four-layer model was used to generate the profiles. However, the stiffer fourth layer transition for most of the profiles occurs over 45 m depth. Therefore, it is not possible to observe that layer for the best profile. The shallow layer of the V_S profile had a velocity of 199 m/s until 1.3 m in depth. The second layer had velocities of 249 m/s until a depth of 8 m. Then, the V_S profile increases the velocity to 490 m/s for the best fit. The rest of the profiles showed velocities between 500 and 650 m/s. The V_S profile showed a transition to a fourth layer for some of the profiles after 23 m depth, reaching velocities near 1,500 m/s. The mean V_{S30} value computed for this site was 424 m/s with a standard deviation of 19.8 m/s.

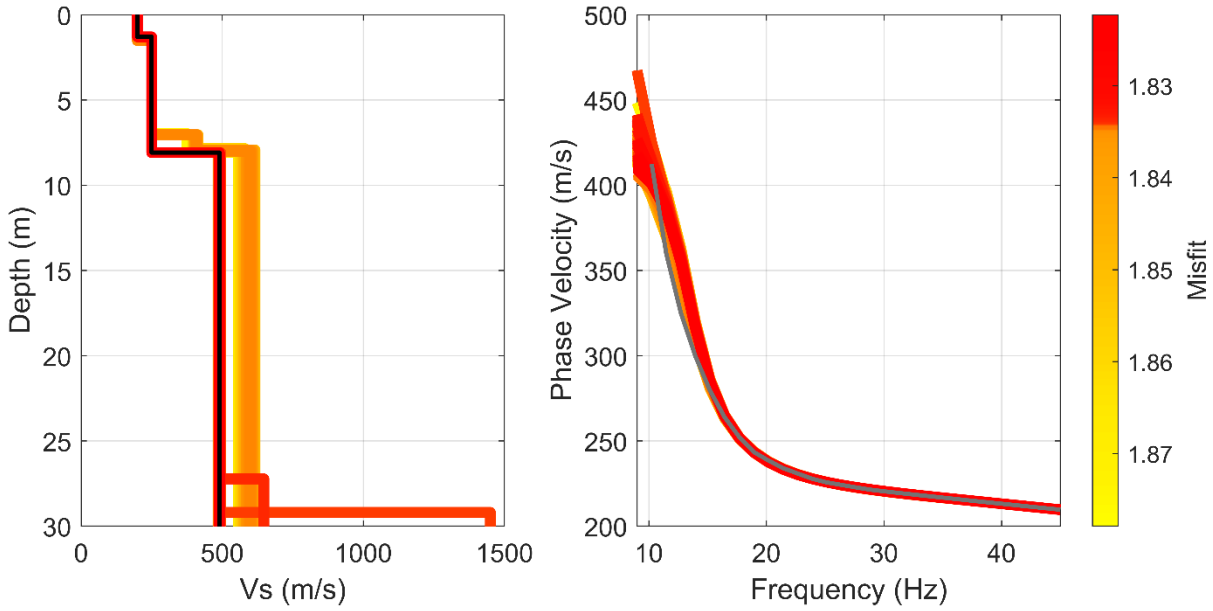

Figure 4-2: V_S profiles (left) and dispersion curves (right) for ASEL site using inversion. The *Vs* profile with the best fit is shown in black. The dispersion curve from the field is shown in dark gray.

The non-inversion method was used to generate a V_S profile until 30 m, as shown in Figure 4-3. The figure also shows the dispersion curves generated by the software. The V_S profiles showed a first layer of 200 m/s of velocity until 2 m depth. Then, the V_S profile constantly increases the velocities until it reaches 588 m/s at 20 m. The V_{S30} computed by the non-inversion method is 399 m/s.

The V_S profile acquired using the non-inversion showed similarities to the profiles computed using the inversion. The range of velocities observed in the profiles from both approaches is very similar. Both profiles showed a constant increment in the velocity with depth. The V_{S30} computed by the non-inversion method is 5.9 % lower than the results acquired using the inversion.

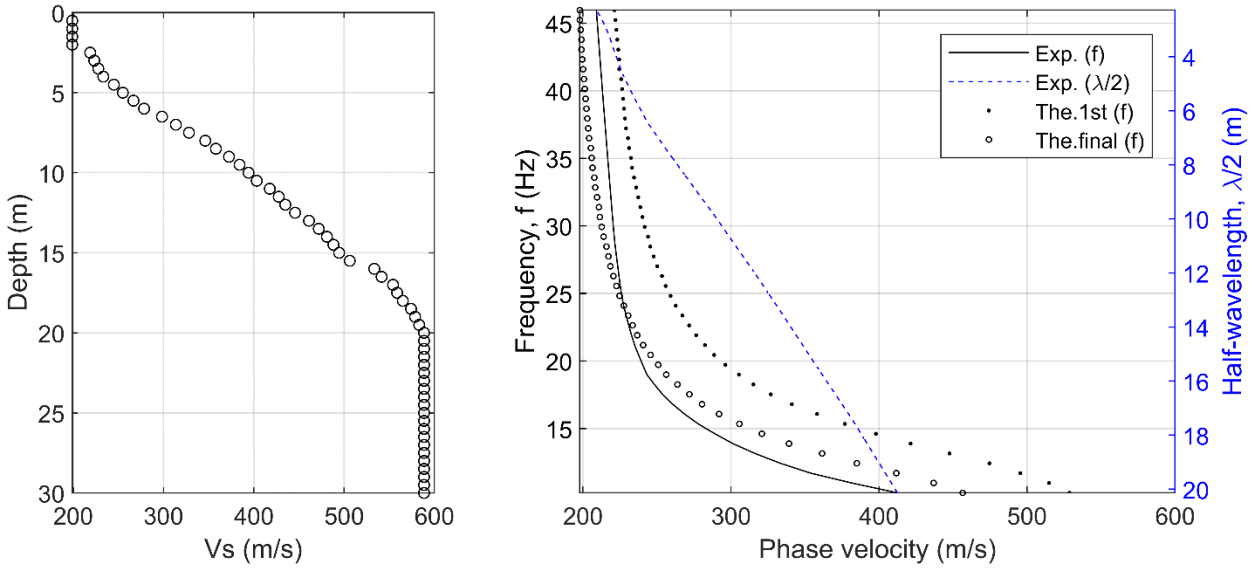

Figure 4-3: V_S profiles (left) and dispersion curves (right) for ASEL site using the non-inversion method.

Seismic Refraction Results

The 2D V_P profile using the seismic refraction method is shown in Figure 4-4. For the seismic refraction analysis, a three-layer model was selected for this site. The results showed velocities of 459 m/s for the first layer until an average depth of 0.89 m. The second layer had a velocity of 597 m/s until an average depth of 7.7 m. The third layer had a velocity of 1,158 m/s.

The V_P profile was transformed into a V_S profile using a range of 0.4 to 0.6 V_P. Using this range, the first layer of the V_S profile has velocities between 183-229 m/s. The second layer of the V_S profile reaches velocities in the range of 238-298 m/s. The third layer of the V_S profile reaches velocities in the range of 463-579 m/s. Assuming the third layer until 30 m depth, the V_{S30} value would be 367-551 m/s for this site, using the seismic refraction method. This extrapolation is very close to the MASW results for the V_S profile for each layer, providing a reasonable estimate for

V_{S30}. The average V_{S30} result from the seismic refraction is 8.4% higher than the V_{S30} results using MASW.

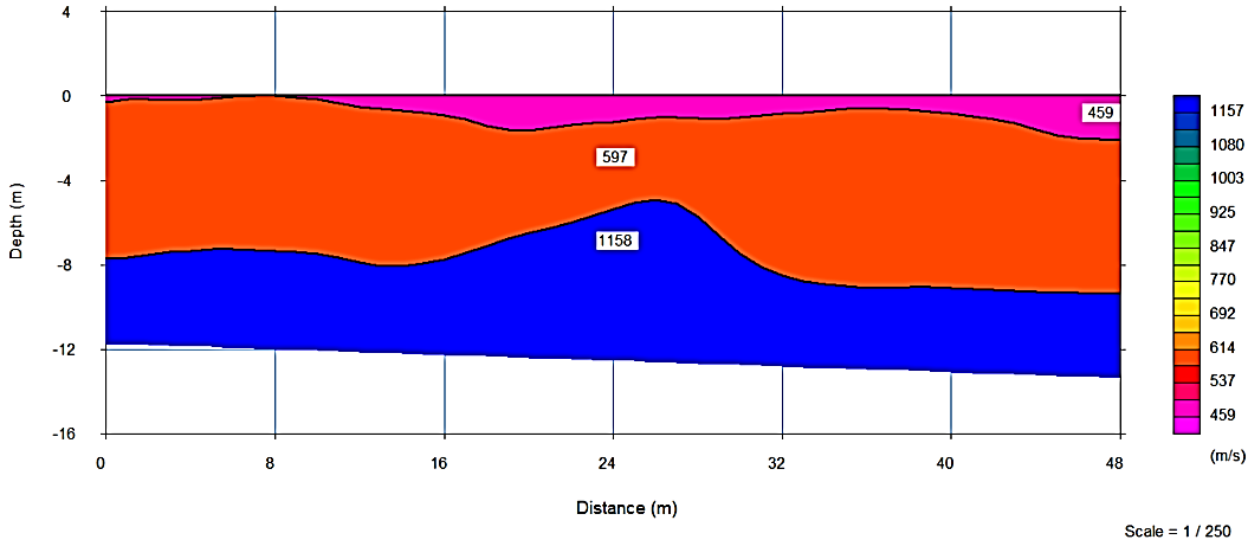

Figure 4-4: 2D V_P profile for ASEL site using seismic refraction method.

4.2.2 TU01 Site

Location and Geology

The seismic survey was performed under and adjacent to a bridge on Highway US-29 (Martin Luther King Hwy) over the Chewacla Creek river, as shown in Figure 4-5. The bridge is located 29.3 miles northeast of Tuskegee, Macon County, Alabama (32.44488°, -85.64729°). The survey line was located on flat topography with minimal vegetation at the time of the survey.

The site is located on an Alluvial coastal and low terrace deposit. The formation belongs to the Holocene epoch from the Quaternary period. It consists of fine to coarse sand with clay lenses and gravel in some locations (Szabo et al., 1988).

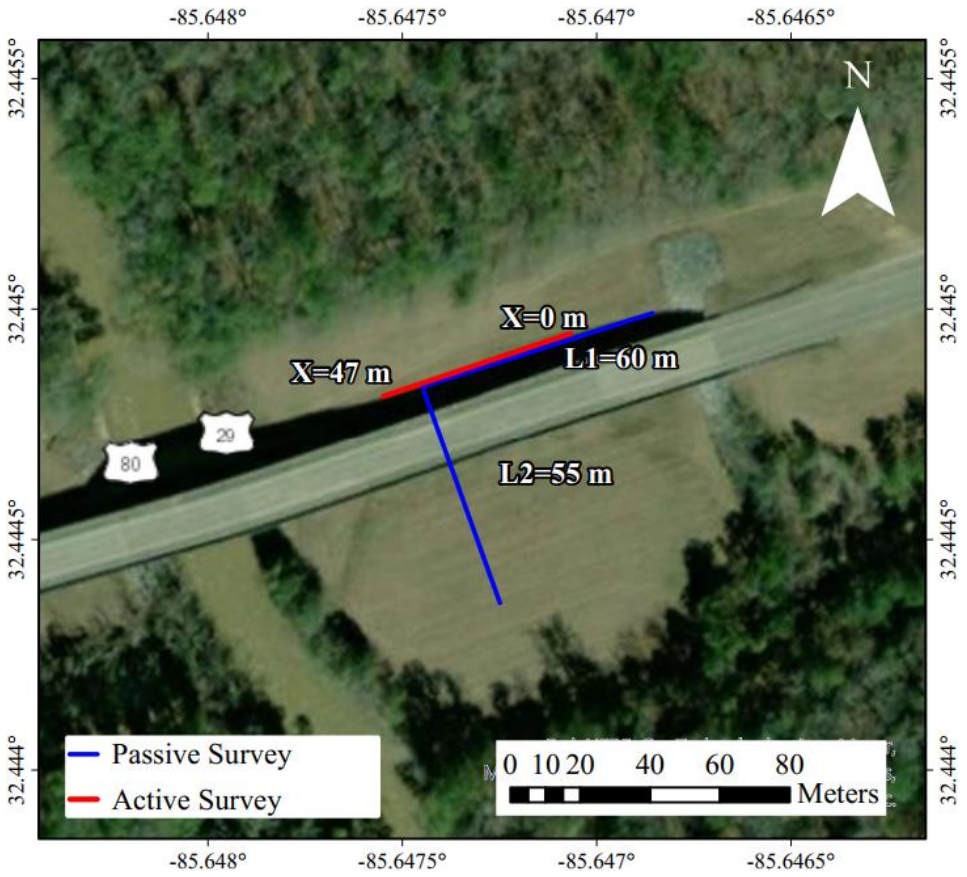

Figure 4-5: Site map with the location of the survey line for the TU01 site

Data Collection

Active and passive seismic surveys were performed at the site. The active seismic survey was used for MASW and seismic refraction analysis. The active seismic survey used 48 geophones arranged in a linear array with a spacing of 1 m between each other, obtaining a survey line of 47 m. Active data were recorded with a sampling frequency of 2,000 Hz for 1.5 s, and a delay of -0.1 s was used for recording. No acquisition filters were used. For MASW analysis, the active source was located 20 m from the end of the survey line, and three shots were recorded in the same position. For seismic refraction analysis, three shots were performed from the beginning until the end of the survey line, at 5 m each. The passive seismic survey was performed using an L shape array with 24 geophones spaced at 5 m with a total length of 115 m, as shown in Figure 4-5. Passive

data were acquired with a sampling frequency of 250 Hz for 240 s. A total of 7 files of 240 s were recorded, reaching 28 min of recording.

MASW Results

The V_S profiles and the dispersion curves computed using the inversion are shown in Figure 4-6 for 5,000 of the profiles generated with the lowest misfit. The V_S profile with the lower misfit is shown in black and the field dispersion curve is drawn in dark gray, while the corresponding curves from each of the profiles are colored according to their misfit value. A fourth layer model was used to generate the profiles. However, the stiffer fourth layer transition occurs at a depth of more than 50 m. Therefore, it is not presented in Figure 4-6. The first layer had a velocity of 170 m/s until 5.8 m in depth. The second layer has velocities of 358 m/s until a depth of 17.9 m. Then, the profile increases the velocity to 541 m/s for the best fit. The rest of the profiles showed velocities between 500 and 700 m/s. The mean V_{S30} value computed for this site was 354 m/s with a standard deviation of 13.9 m/s.

The non-inversion method was used to generate a V_S profile until 30 m, as shown in Figure 4-7. The figure also shows the dispersion curves generated by the software. The profiles showed the first layer between 153 m/s and 169 until 3.5 m depth. Then, the profile increases the velocities constantly until 26 m depth reaches 550 m/s. Between 27 and 30 m depth, the profile displays a constant velocity of 560 m/s. The V_{S30} computed using this method is 351 m/s.

The V_S profile acquired using the non-inversion showed a constant increment in velocity with depth as the profiles computed using the inversion. The range of velocities observed in the profiles from both approaches is very similar. The V_{S30} computed by the non-inversion method is 0.5% lower than the results acquired using the inversion.

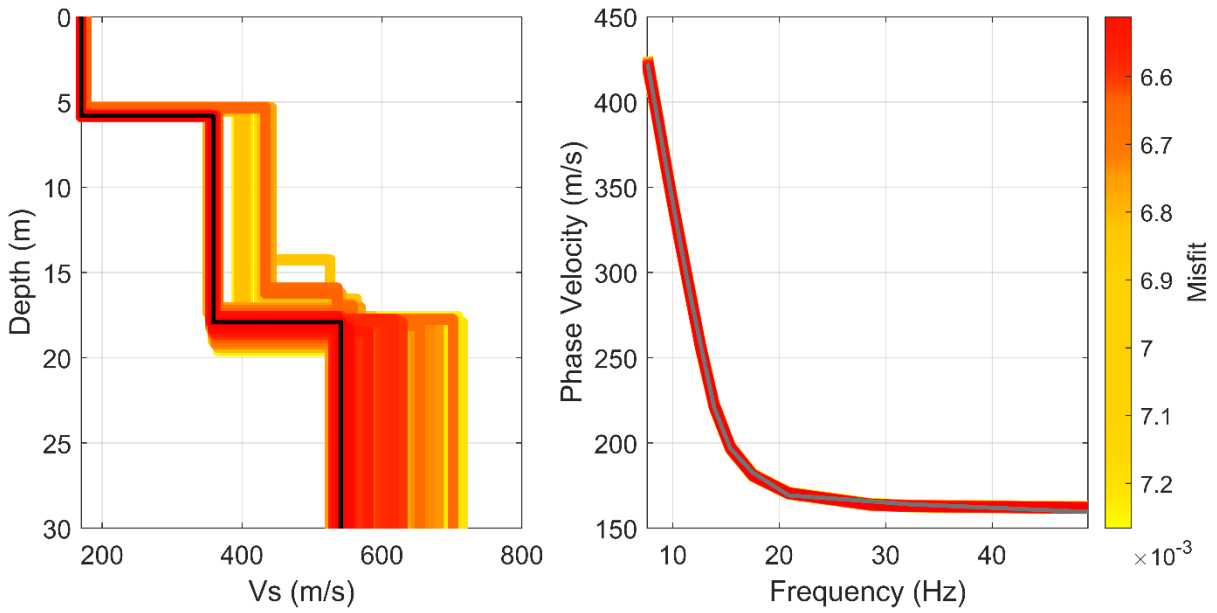

Figure 4-6: V_S profiles (left) and dispersion curves (right) for TU01 site using inversion. The V_S profile with the best fit is shown in black. The dispersion curve from the field is shown in dark gray.

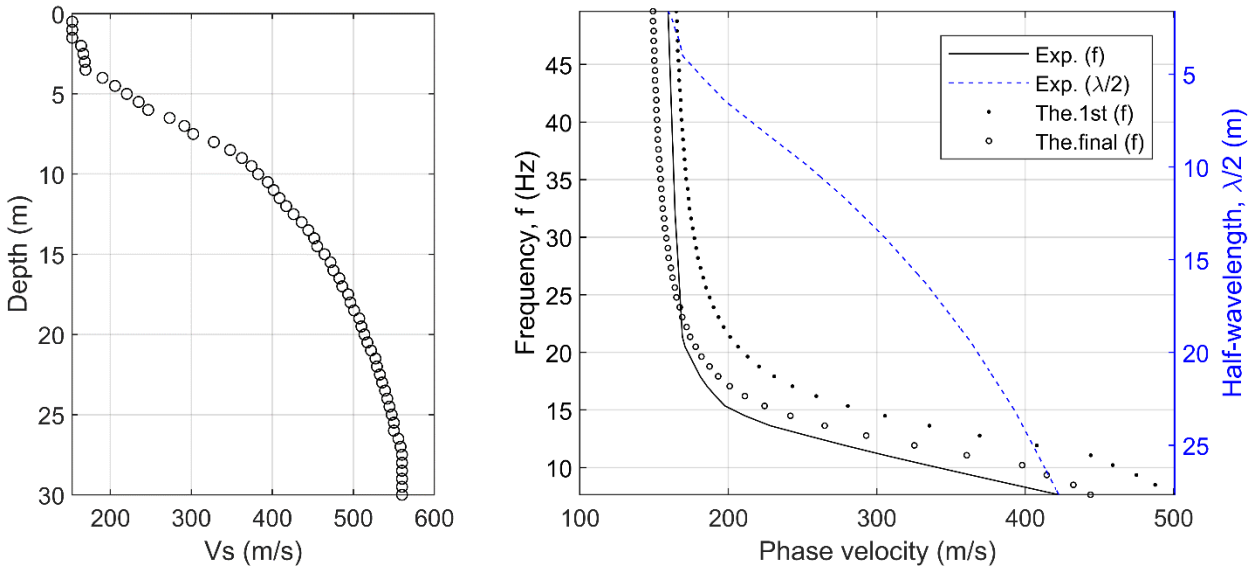

Figure 4-7: V_S profiles (left) and dispersion curves (right) for the TU01 site using the non-inversion method.

Seismic Refraction Results

The 2D V_P profile using the seismic refraction method is shown in Figure 4-8. For the seismic refraction analysis, a three-layer model was selected for this site. The results showed velocities of 257 m/s for the first layer until an average depth of 4.12 m. The second layer had a velocity of 668 m/s until an average depth of 6.9 m. The third layer had a velocity of 1,782 m/s.

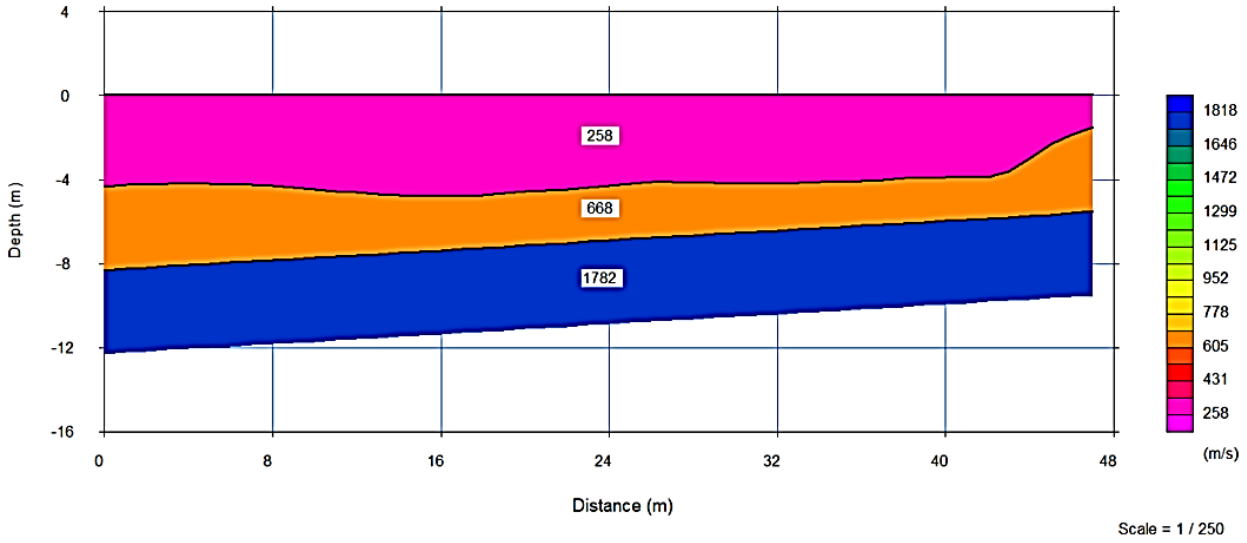

Figure 4-8: 2D V_P profile for TU01 site using seismic refraction method.

The V_P profile was transformed into a V_S profile using a range of 0.4 to 0.6 V_P for the first and second layer. This site is located next to Chewacla Creek river and a sharp increment of velocity is found in the third layer. Therefore, the third layer used a range of 0.14 to 0.2 V_P to correct for the saturation of water in the profile. Using these ranges, the first layer of the V_S profile has velocities between 103-154 m/s. The second layer of the V_S profile reaches velocities in the range of 267-401 m/s. The third layer of the V_S profile reaches velocities in the range of 254-356 m/s. Assuming the third layer until 30 m depth, the V_{S30} value would be 212-304 m/s for this site, using the seismic refraction method. This extrapolation likely underestimates the velocity at these shallower depths. The results from the seismic refraction are in reasonable agreement with the

MASW results in the upper 18 meters. However, the velocities in the third layer are lower than the best estimate results from MASW. However, the second layer for the seismic refraction underestimates the velocity at higher depths leading to a lower V_{S30} estimate than the MASW results. The average V_{S30} result from the seismic refraction is 26.9% lower than the V_{S30} results using MASW.

4.2.3 SR-21 Site

Location and Geology

The geophysical seismic survey was performed on the side of SR-21 at 9.64 km southwest of the city of Talladega, in Talladega County, Alabama (33.36719, -86.17013). The location of the site and the survey array are shown in Figure 4-9. The terrain was clear of vegetation at the time of the survey. The survey line was positioned on the side slope parallel to the highway.

The geology of the site is Knox Group undifferentiated. This formation is part of the Ordovician-Cambrian period from the Paleozoic Era. The Knox Group undifferentiated locally presents sandy dolomite, dolomitic limestone, and limestone. Ample amounts of light-colored chert also characterize the group. (Szabo et al. 1988)

Data Collection

An active seismic survey was performed on the site. The active seismic survey was used for MASW and seismic refraction analysis. The active data were collected with 48 geophones arranged in a linear array with a spacing of 2 m between each other, obtaining a survey line of 94 m. The active data were recorded with a sampling frequency of 2,000 Hz for 1.5 s, and a delay of -0.1 s was used for recording. No acquisition filters were used. For MASW analysis, the active source was located 20 m from the end of the line; five shots were recorded in the same position.

For seismic refraction analysis, five shots were performed from the beginning until the end of the survey line, at 6 m each.

Figure 4-9: Site map with the location of survey line and boreholes for SR-21 site

MASW Results

The V_S profiles and the dispersion curves computed using the inversion are shown in Figure 4-10 for 5,000 of the profiles generated with the lowest misfit. The V_S profile with the lower misfit is shown in black and the field dispersion curve is drawn in dark gray, while the corresponding curves from each of the profiles are colored according to their misfit value. The profiles show similar velocity values for the first two layers before 18 m and then a stiffer layer with higher velocities. The first two layers slightly change in velocity from 189 m/s to 278 m/s at 3 m. After

18 m, the profile with the best fit shows a higher velocity layer of 3,600 m/s. The mean V_{S30} value computed for this site was 396 m/s with a standard deviation of 1.01 m/s.

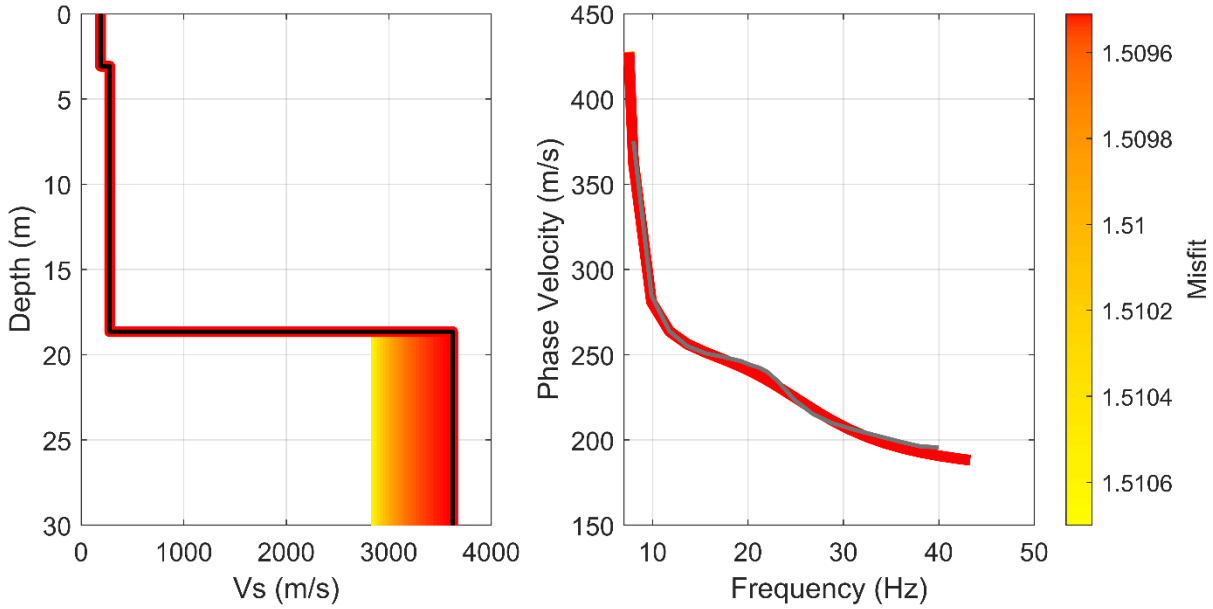

Figure 4-10: V_S profiles (left) and dispersion curves (right) for SR-21 site using inversion. The V_S profile with the best fit is shown in black. The dispersion curve from the field is shown in dark gray.

The non-inversion method was used to generate a V_S profile to 30 m, as shown in Figure 4-11. The figure also shows the dispersion curves generated by the software. The profile shows the first layer around 186 m/s until 2 m depth. Then, the profile increases the velocities, indicating a stiffer layer between 4 and 14 m, ranging from 250 to 350 m/s. Another layer is shown below 15 m depth velocities from 451 m/s to 532 m/s. After 23 m, the profile showed a constant velocity of 532 m/s. The V_{S30} computed the non-inversion method is 349 m/s.

The V_S profile acquired using the non-inversion showed similarities to the profiles computed using the inversion until 15 m. After, the profile calculated using the inversion exhibit higher velocities. The V_{S30} computed by the non-inversion method is 11.8% lower than the results acquired utilizing the inversion.

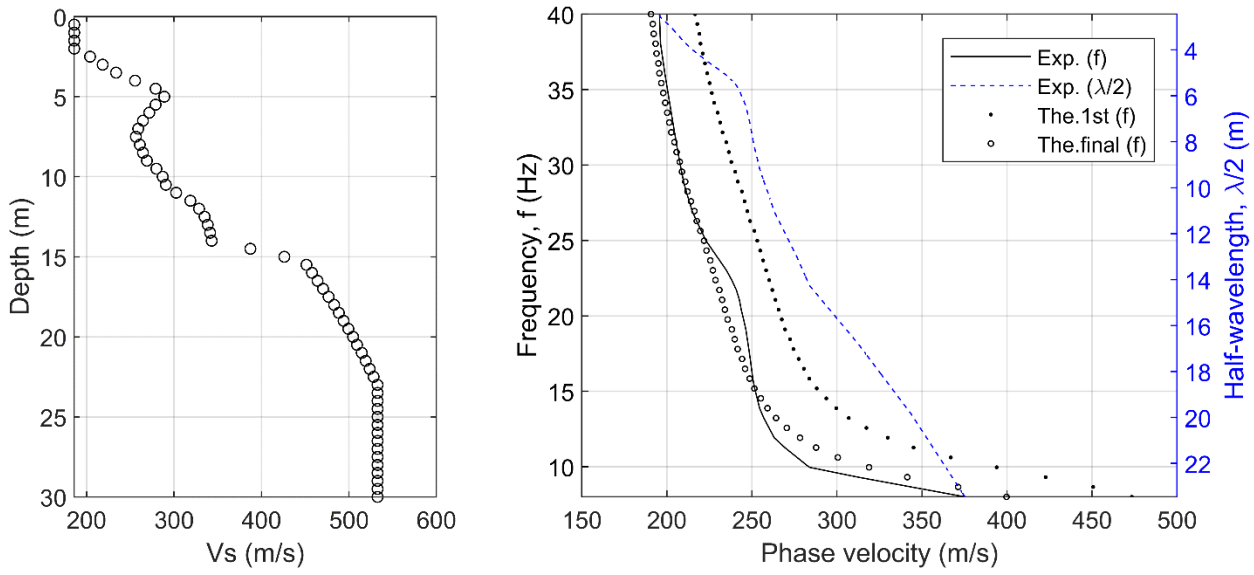

Figure 4-11: V_S profiles (left) and dispersion curves (right) for SR-21 site using the non-inversion method.

Seismic Refraction Results

The 2D V_P profile using the seismic refraction method is shown in Figure 4-12. For the seismic refraction analysis, a two-layer model was selected for this site. The results showed a shallow V_P of 371 m/s until an average depth of 2.2 m. Then, the V_P profile shows a stiffer layer of 759 m/s.

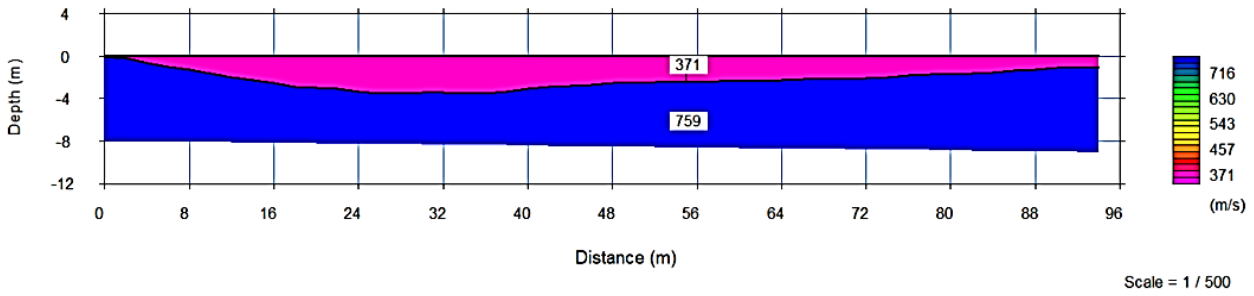

Figure 4-12: 2D V_P profile for SR-21 site station using seismic refraction method.

The V_P profile was transformed into a V_S using a range of 0.4 to 0.6 V_P. Using this range, the first layer of the V_S profile has velocities between 148-222 m/s. The second layer of the V_S profile reaches velocities in the range of 303-422 m/s. Assuming the second layer until 30 m depth, the V_{S30} value would be in a range of 281-422 m/s for this site, using the seismic refraction method. The results from the seismic refraction are very close to the velocities results of MASW for the first and second layers. However, there was not a third layer that the seismic refraction could identify. The V_{S30} values computed using this method are 11% lower than those computed using MASW.

4.2.4 SR-219 Site

Location and Geology

A seismic-based geophysical survey was performed on August 1, 2019, along SR-219 in Bibb County near Centreville, Alabama (32.87841, -87.10224). The locations of the geophysical surveys and borings are shown in Figure 4-13. The image shows that the survey line was centered between boreholes B1 and B2. A slow-moving landslide was reported on the west side of the road in 2010.

The geology of the site belongs to the Gordo formation of the Tuscaloosa group (Szabo et al. 1988), and it is very close to the boundary with the Coker formation. Coker formation usually underlies the Gordo formation. The Gordo formation is characterized by massive beds of cross-bedded sand, gravelly sand, and lenticular beds of locally carbonaceous partly mottled moderate-red and pale-red-purple clay. The lower part of the Gordo formation is predominantly gravelly sand consisting chiefly of chert and quartz pebbles, while the Coker formation contains micaceous sand and clay with a few thin gravel beds containing quartz and chert pebbles (Szabo et al., 1988).

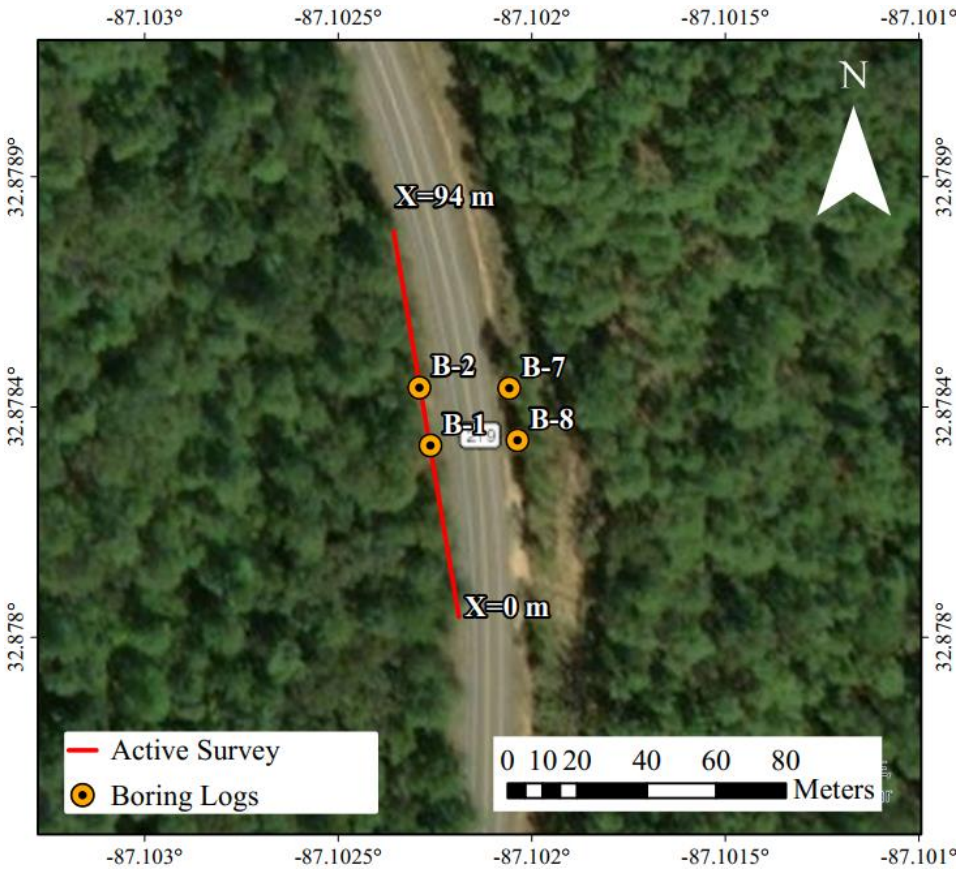

Figure 4-13: Site map with the location of survey line and boreholes for SR-219

Previous Investigations

ALDOT performed a previous investigation in July of 2010, which contemplated eight boreholes, SPTs, and installation of inclinometers and wells. The location of the boring logs close to the data collected is shown in Figure 4-13. Borings B1-B4 were located inside the landslide and were equipped with inclinometers to monitor the landslide stability. The borings B6-B8 were situated outside the slide mass. The borings B1-B4 showed mainly sandy soils in the upper 3-6 m transitioning to clayey soils below. Inside borings B1- B4, inclinometers were installed with data available for the years 2014, 2018, and 2019, depending on the borehole. According to the information provided by the inclinometers in B1, B2, and B3, the slide plane is located around

119-120 m in elevation. The water table elevation inside the slide mass varies between about 122-123 m of elevation (depths of 2-2.5 m).

Data Collection

The seismic data were acquired using a set of 48 geophones with a natural frequency of 4.5-Hz connected to two Geometrics Geode seismograms. No acquisition filters were used. A 45 Newton sledgehammer was used as a source, and the geophones were paced at 1 meter.

The seismic data were processed using the multichannel analysis of surface waves (MASW) technique. Note that only a subset of the collected seismic data were used for this processing technique. For this site, the files chosen had the shots at 5 m from the beginning of the survey line. The files selected showed a clearer dispersion curve of the fundamental mode. Once the dispersion curve was picked, the inversion process was performed in Geopsy (Wathelet et al., 2020). A three-layer profile was selected for this site to show agreement with the information provided by the bore logs.

Results MASW

The V_S profiles and the dispersion curves are shown in Figure 4-14 for 5,000 of the profiles generated with the lowest misfit. The V_S profile with the lower misfit is shown in black and the field dispersion curve is drawn in dark gray, while the corresponding curves from each of the profiles are colored according to their misfit value. The profiles show consistent results with a low-velocity surface layer, an intermediate layer, and a significantly stiffer deep layer. The upper, low-velocity layer with velocities around 147 m/s, while the middle layer had velocities around 250 m/s. The transition to the more rigid layer occurred over 10 m of depth, with velocity values of about 389.9 m/s. The mean V_{S30} value computed for this site was 286 m/s with a standard deviation of 1.07 m/s showing a good convergence of the solution.

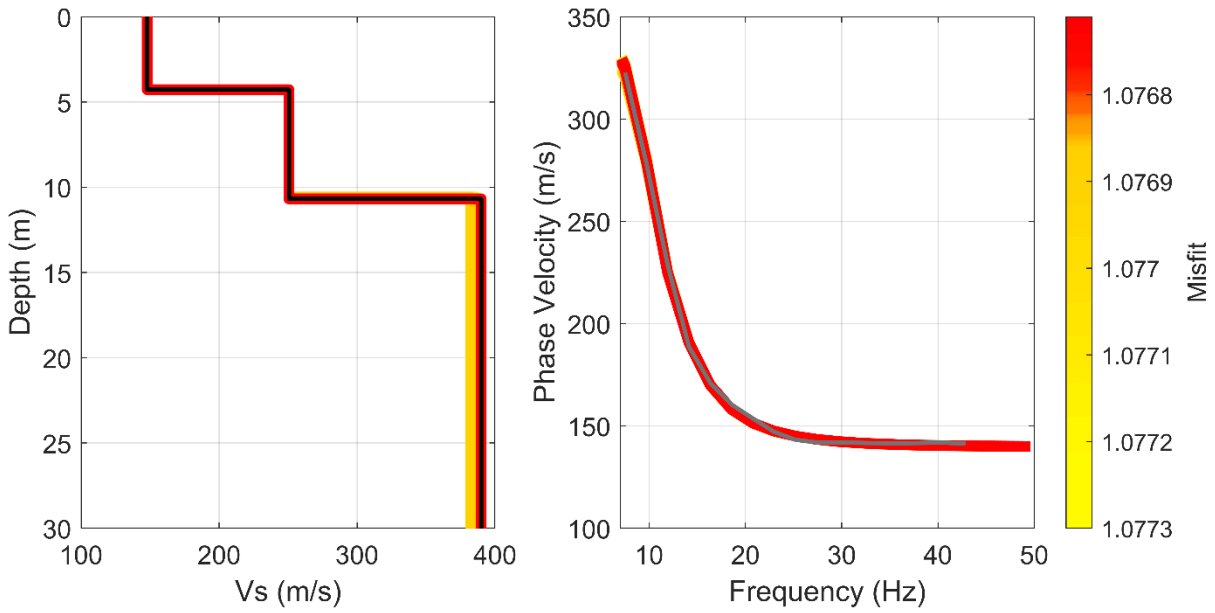

Figure 4-14: V_S profiles (left) and dispersion curves (right) for SR-219 site using inversion. The V_S profile with the best fit is shown in black. The dispersion curve from the field is shown in dark gray.

The non-inversion method was used to generate a V_S profile until the 30 m, as shown in Figure 4-15. The figure also shows the dispersion curves generated by the software. The profiles showed the first layer around 134 m/s until 2 m depth. Then, the profile increases the velocities, indicating a stiffer layer between 12 and 22 m, ranging from 350 to 400 m/s. A final layer showed a velocity of 401 m/s after 21.5 m depth. The V_{S30} computed by the non-inversion method is 295 m/s.

The V_S profile acquired using the non-inversion showed similarities to the profiles computed using the inversion. Both profiles showed a three-layer system, even though the transition of velocities to another layer occurs at different depths. The velocities calculated for the non-inversion method are slightly higher for the second and third layers. The V_{S30} computed by the non-inversion method is 3.1% higher than the results acquired using the inversion.

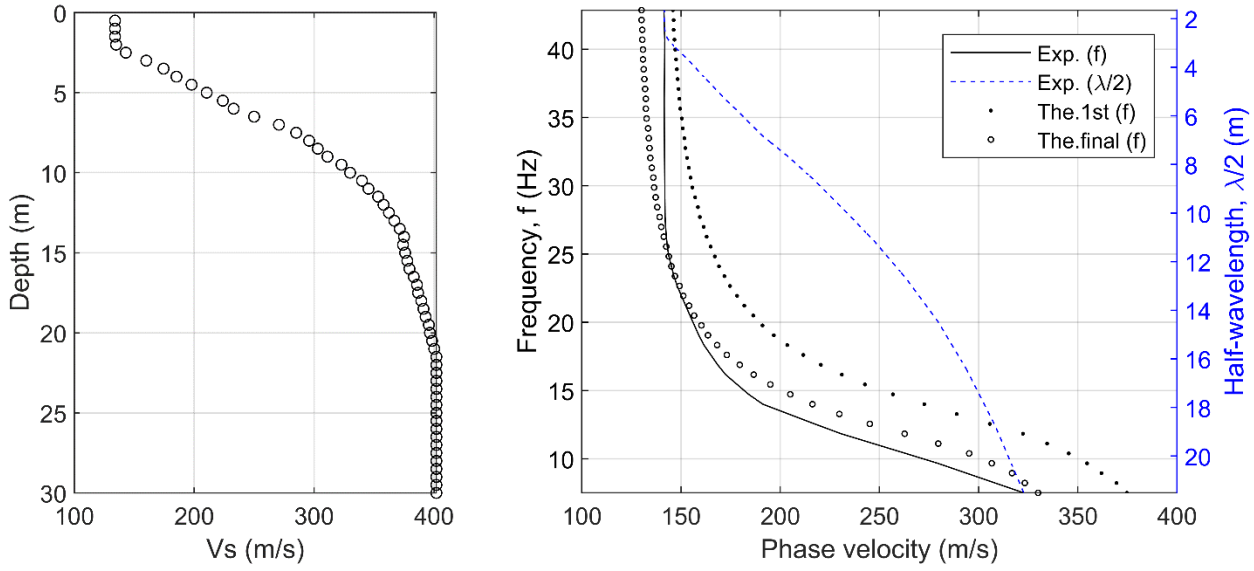

Figure 4-15: V_S profiles (left) and dispersion curves (right) for SR-219 site using the non-inversion method.

The results provided by the seismic profiles are consistent with boring logs, which generally show increasing N-values with depth. The borings show low consistency soils near the surface, corresponding to the low-velocity surficial layer observed in the seismic profiles. The borings also show much higher N-values at depths of 10 m, corresponding to the stiff, deep layer detected by the seismic profile. However, the other transitions in the boring logs are not necessarily captured well by the seismic velocity profiles due to the inherent averaging in the MASW technique. This can cause the seismic profiles to miss local heterogeneities and shift the layer transitions to an average depth across the length of the geophone array.

Seismic Refraction Results

The 2D V_P profile using the seismic refraction method is shown in Figure 4-16. For the seismic refraction analysis, a two-layer model was selected for this site. The results showed a

shallow V_P of 299 m/s until an average depth of 3.5 m. Then, the V_P profile shows a stiffer layer of 1,580 m/s.

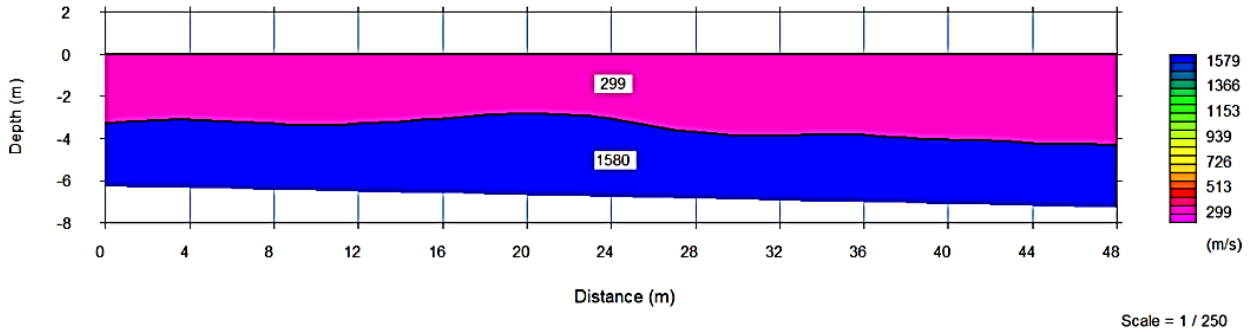

Figure 4-16: 2D V_P profile for SR-219 site using seismic refraction method.

The V_P profile was transformed into a V_S profile using a range of 0.4 to 0.6 V_P for the first layer, while for the second layer a range of 0.14 to 0.2 V_P was used to correct for the saturation of water in the profile, due to the shallow water table indicated in the boring logs. Using these ranges, the first layer of the V_S profile has velocities between 119-179 m/s. The second layer of the V_S profile reaches velocities in the range of 225-315 m/s. Assuming the second layer until 30 m depth, the V_{S30} value would be in a range of 204-290 m/s for this site, using the seismic refraction method. This extrapolation likely provides a good agreement between seismic refraction and MASW for the first layer of velocity. However, the second layer for the seismic refraction underestimates the velocity at higher depths leading to a lower V_{S30} estimate than the MASW results. The average V_{S30} result from the seismic refraction is 13% lower than the V_{S30} results using MASW.

4.2.5 AN01 Site

Location and Geology

The site AN01 is located in the northeast of Anniston in Calhoun County (33.71678, -85.78344). The geophysical survey was performed on the 25th of November 2019, using active and

passive MASW methods on the site. The terrain was flat in topography and clear of vegetation at the time of the survey. The location of the survey lines used to collect the data are shown in Figure 4-17.

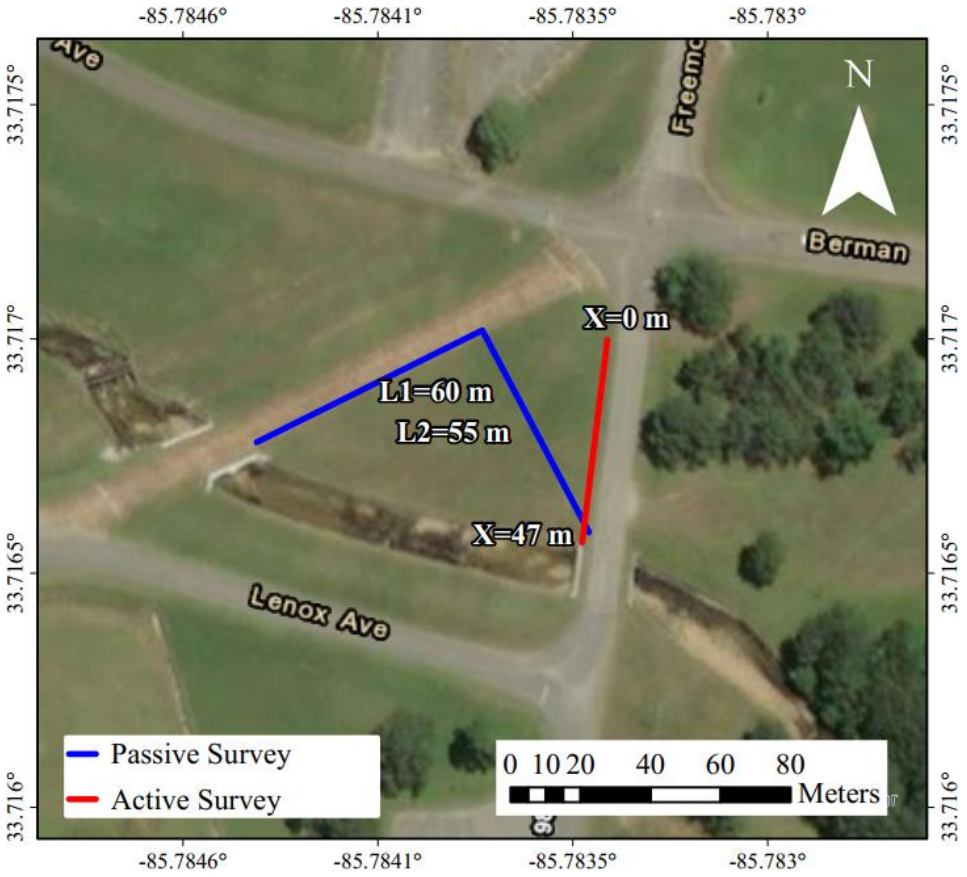

Figure 4-17: Site map with the location of survey line for AN01 site

The site is located in Paleozoic shale undifferentiated and little oak and Newala limestones undifferentiated. The Paleozoic shale is characterized by shale and mudstone. Locally, it contains interbeds lenses of sandstone. Near Anniston, it includes Athens shale and probable Floyd Shale. On the other hand, the little oak Limestone is characterized by clayey to silty limestone that contains chert nodules. Locally, it has thin beds of bentonite. (Szabo et al., 1988).

Data Collection

An active and passive seismic survey was performed on the site. Unfortunately for this site, the MASW method did not provide reliable dispersion curves for further analysis. Therefore, the analysis on this site was performed only using the seismic refraction method. The active data for seismic refraction analysis used 48 geophones. The geophones were arranged in a linear array with a spacing of 1 m between each other, obtaining a survey line of 47 m. Active data were recorded with a sampling frequency of 2,000 Hz for 1.5 s, and a delay of -0.1 s was used for recording. No acquisition filters were used. From the beginning until the end of the survey line, three shots were performed at 5 m each.

Seismic Refraction Results

The 2D V_P profile using the seismic refraction method is shown in Figure 4-18. A two-layer model was selected for this site. The results showed a shallow V_P 335m/s until an average depth of 4.14 m. Then, the V_P profile shows a stiffer layer of 3,323 m/s.

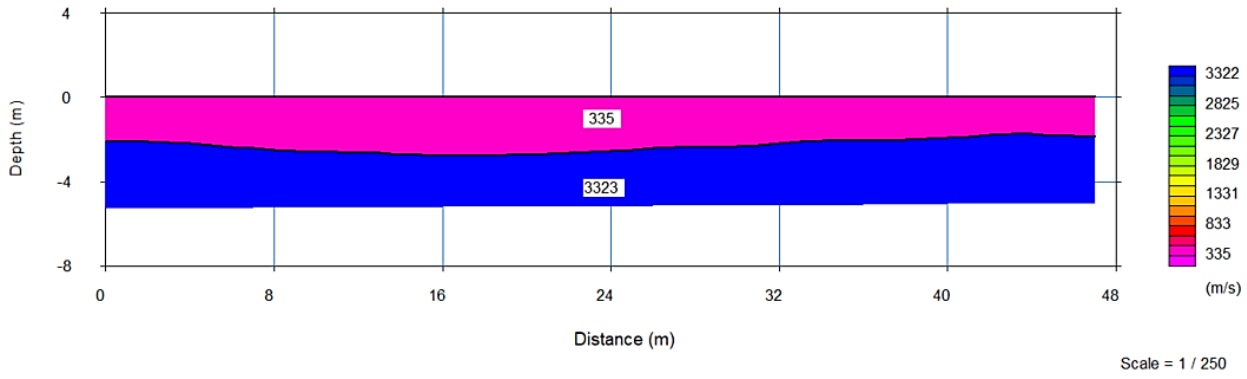

Figure 4-18: 2D V_P profile for AN01 site using seismic refraction method.

The V_P profile was transformed into a V_S profile using a range of 0.4 to 0.6 V_P. Using this range, the first layer of the V_S profile has velocities between 134-201 m/s, while the second stiffer layer of velocity would be between 1329-1993 m/s. Assuming the second layer until 30 m depth,

the V_{S30} value would be in a range of 788-1182 m/s for this site, using the seismic refraction method.

4.2.6 X50B Seismic Station

Location and Geology

The seismic station X50B is located in the northeast of Alabama in Fort Payne, DeKalb County (34.46110, -85.64990). The geophysical survey was performed on the 6th of December 2021 using active and passive MASW methods on the site. The terrain was flat in topography and clear of vegetation at the time of the survey. The location of the survey lines used to collect the data are shown in Figure 4-19.

The geology of the site is Pottsville Formation from the Pennsylvanian age of the Paleozoic era. Pottsville Formation is characterized by light-gray thin to thick-bedded quartzose sandstone and conglomerate containing interbedded dark-gray shale, siltstone, and coal (Szabo et al., 1988).

Data Collection

An active and passive seismic survey was performed on the site. The active seismic survey was used for MASW and seismic refraction analysis. For the active survey, 48 geophones were used arranged in a linear array with a spacing of 2 m between each other, obtaining a survey line of 94 m. Active data were recorded with a sampling frequency of 2,000 Hz for 1.5 s, and a delay of -0.1 s was used for recording. No acquisition filters were used. For MASW analysis, the active source was located 25 m from the beginning of the survey line, and five shots were recorded in the same position. For seismic refraction analysis, three shots were performed from the beginning until the end of the survey line, at 10 m each. The passive survey was performed using 24 geophones spaced 5 m in an L-shape array, with a total length of 115 m, as shown in Figure 4-19. Passive

data were acquired with a sampling frequency of 250 Hz for 240 s. A total of 9 files of 240 s were recorded, reaching 36 min of recording. Passive data collected did not show precise results of the fundamental mode. Therefore, it could not be used to select the dispersion curve. A four-layer profile was chosen for this site.

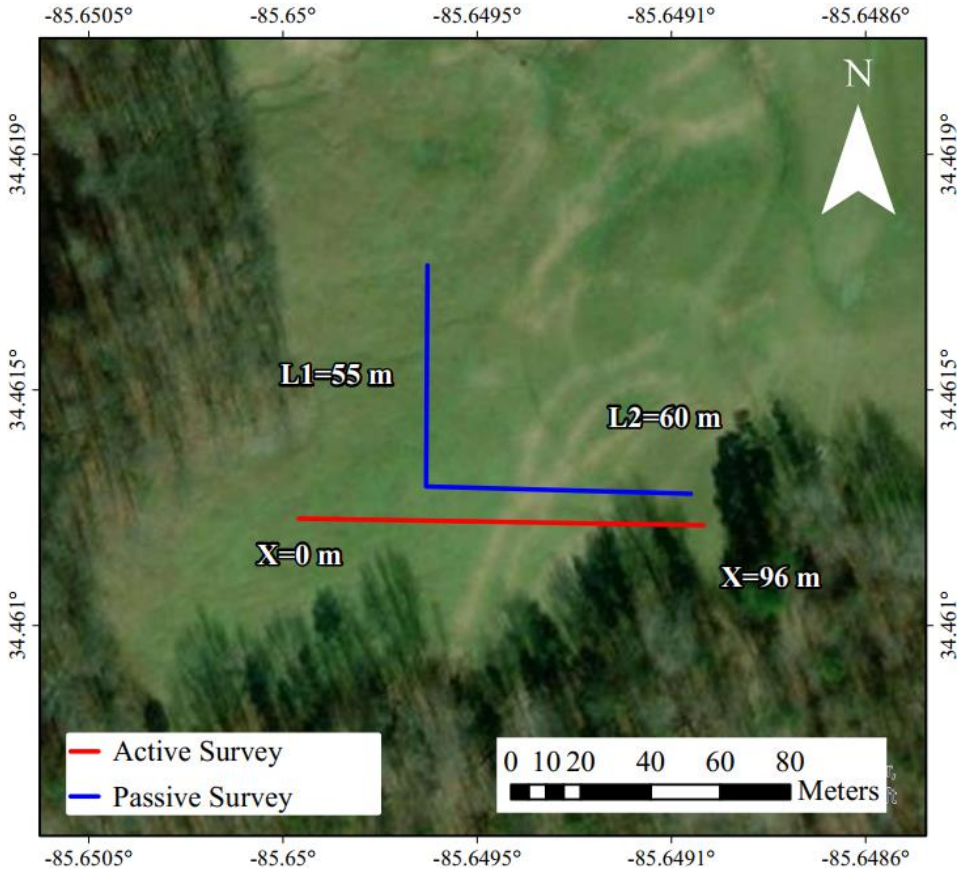

Figure 4-19: Site map with the location of survey line for X50B seismic station

MASW Results

The V_S profiles and the dispersion curves using inversion are shown in Figure 4-20 for 5,000 of the profiles generated with the lowest misfit. The V_S profile with the lower misfit is shown in black and the field dispersion curve is drawn in dark gray, while the corresponding curves from each of the profiles are colored according to their misfit value. The profiles show consistent results with increments in velocities with depth. The fourth layer of the model is not shown in the image

because the transition to the stiffer layer occurs over 30 m. The shallow layer showed velocities around 626 m/s until 1.4 m depth. The second layer had velocities around 840 m/s between 1.4-15.6 m. The third layer showed velocities around 1,776 m/s. Then, the profile transition to a stiffer layer occurred over 34.5 m of depth, with velocity values of about 1,900 m/s. The V_{S30} for this site was computed with a median value of 943 m/s and a standard deviation of 12.1 m/s.

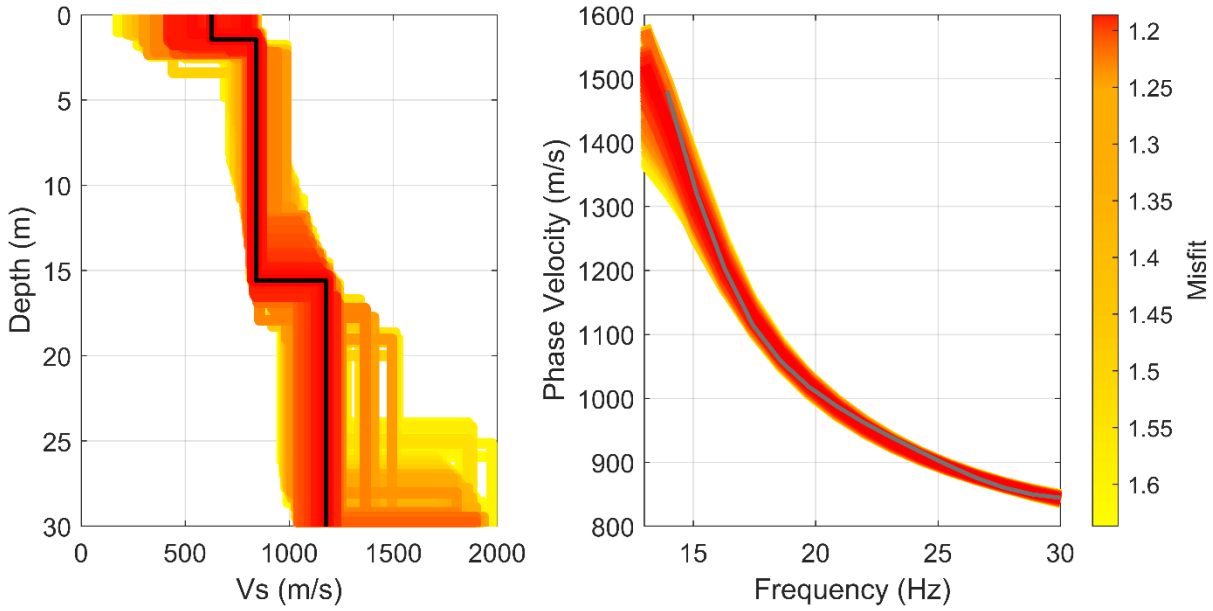

Figure 4-20: V_S profiles (left) and dispersion curves (right) for X50B seismic station using inversion. The V_S profile with the best fit is shown in black. The dispersion curve from the field is shown in dark gray.

The non-inversion method was used to generate a V_S profile until the 30 m, as shown in Figure 4-21. The figure also shows the dispersion curves generated by the software. The profiles showed the first continuous layer around 780 m/s until 13 m. Then, the profile increases the velocities indicating another layer between 17 and 30 m with velocities ranging from 1,057 to 1,436 m/s. A final velocity of 1,842 m/s is shown at 30 m depth, suggesting a stiffer layer. However, only one point of velocity is not enough to confirm it. The V_{S30} computed using this method is 958 m/s.

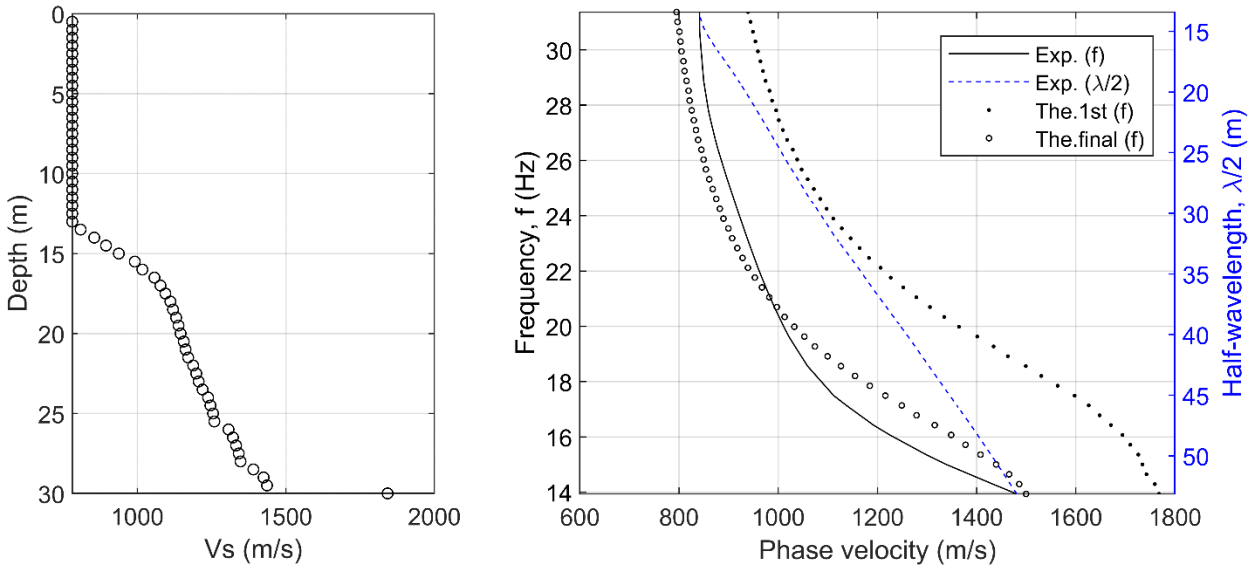

Figure 4-21: V_S profiles (left) and dispersion curves (right) for X50B seismic station using the non-inversion method.

The V_S profile acquired using the non-inversion showed a constant increment in velocity with depth as the profiles computed using the inversion. The range of velocities observed in the profiles from both approaches is very similar. The V_{S30} computed by the non-inversion method is 1.6% higher than the results acquired using the inversion.

Seismic Refraction Results

The 2D V_P profile using the seismic refraction method is shown in Figure 4-22. For the seismic refraction analysis, a two-layer model was selected for this site. The results showed a shallow V_P of 413 m/s until an average depth of 2.5 m. Then, the V_P profile shows a stiffer layer of 3,380 m/s.

The V_P profile was transformed into a V_S profile using a range of 0.4 to 0.6 V_P. Using this range, the first layer of the V_S profile has velocities between 165-274 m/s. The second layer of the V_S profile reaches velocities of 1,351-2,027 m/s. Assuming the second layer until 30 m depth, the

V_{S30} value would be in a range of 841-1,261 m/s for this site, using the seismic refraction method. This extrapolation likely underestimates the velocity at shallower depths while overestimating the velocity in the deeper layers. The average V_{S30} result from the seismic refraction is 11.4% higher than the V_{S30} result using MASW. Therefore, the results from the seismic refraction for V_{S30} are in reasonable agreement with the MASW results.

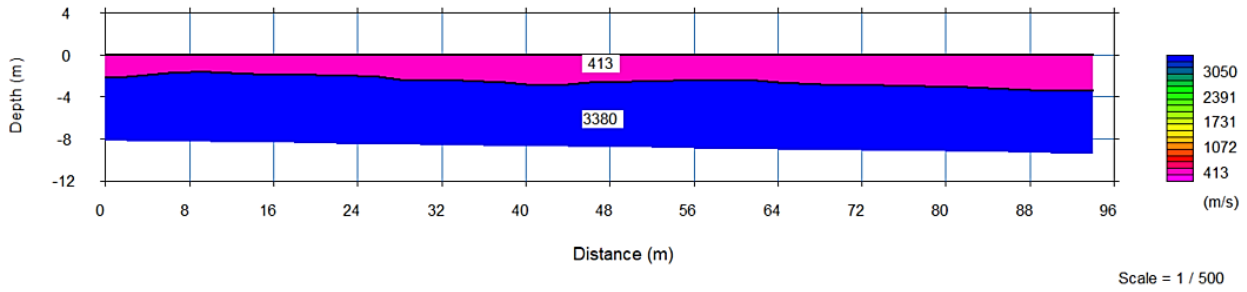

Figure 4-22: 2D V_P profile for X50B seismic station using seismic refraction method.

4.2.7 S1AL Seismic Station

Location and Geology

The seismic station S1AL is located 6 km northeast of Flomaton in Escambia County (31.0368, -87.21011). The geophysical survey was performed on the 3rd of March 2022 using active and passive MASW methods on the site. The terrain was flat in topography and clear of vegetation at the time of the survey. The location of the survey lines used to collect the data are shown in Figure 4-23.

The geology of the site is Miocene Series undifferentiated from the Miocene epoch from the Cenozoic era. The Miocene Series contains moderate- yellowish-orange thin-bedded to massive fine to coarse and gravelly sand. This formation can have thin-bedded to massive clay and sandy clay (Szabo et al., 1988).

Figure 4-23: Site map with the location of survey line for S1AL seismic station

Data Collection

An active and passive seismic survey was performed on the site. The active seismic survey was used for MASW and seismic refraction analysis. For the active survey, 48 geophones were arranged in a linear array with a spacing of 2 m between each other, obtaining a survey line of 94 m. Active data were recorded with a sampling frequency of 2,000 Hz for 1.5 s, and a delay of -0.1 s was used for recording. No acquisition filters were used. For MASW analysis, the active source was located 25 m from the beginning of the survey line, and five shots were recorded in the same position. For seismic refraction analysis, three shots were performed from the beginning until the end of the survey line, at 10 m each. The passive survey was performed using 24 geophones spaced 5 m in an L-shape array, with a total length of 115 m, as shown in Figure 4-23. Passive data were

acquired with a sampling frequency of 250 Hz for 240 s. A total of 10 files of 240 s were recorded, reaching 40 min of recording. For this site, passive data did not provide good results; therefore, the inversion was performed using only the active data acquired in the field.

MASW Results

The V_S profiles and the dispersion curves using inversion are shown in Figure 4-24 for 5,000 of the profiles generated with the lowest misfit. The V_S profile with the lower misfit is shown in black and the field dispersion curve is drawn in dark gray, while the corresponding curves from each of the profiles are colored according to their misfit value. The profiles showed an increment of velocity with depth. A two-layer profile was the best fit for this site. The shallow layer had velocities around 271 m/s until 15.5 m depth. The profile then transitions to a stiffer layer of velocities around 390.8 m/s. The V_{S30} for this site was computed with a median value of 317 m/s and a standard deviation of 0.3 m/s.

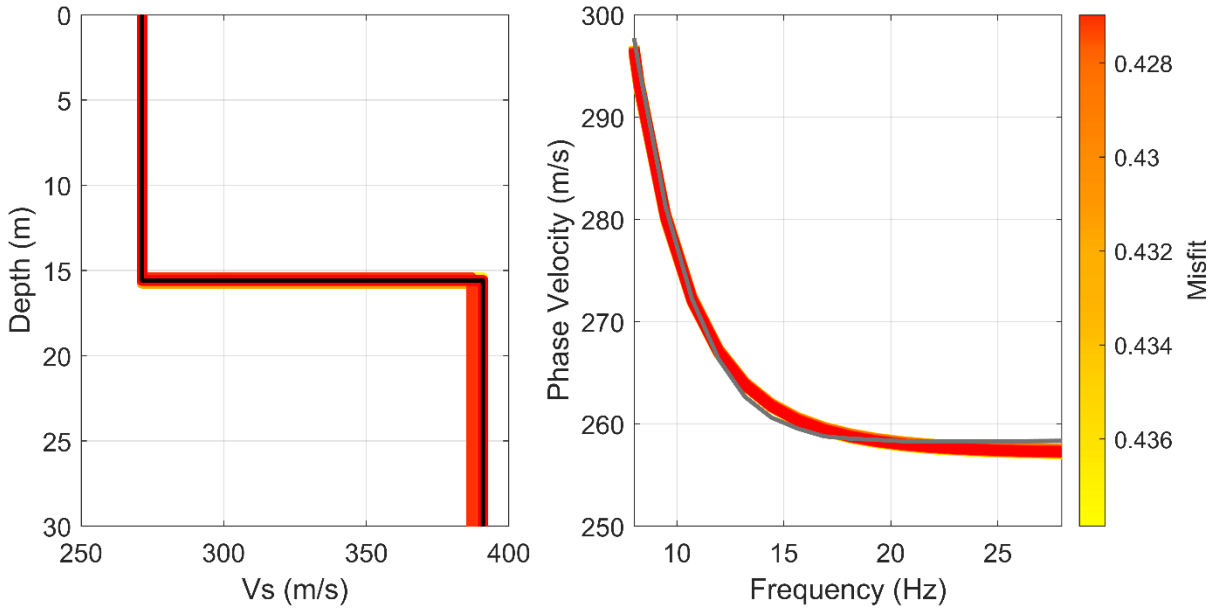

Figure 4-24: V_S profiles (left) and dispersion curves (right) for S1AL seismic station using inversion. The V_S profile with the best fit is shown in black. The dispersion curve from the field is shown in dark gray.

The non-inversion method was used to generate a V_S profile until 30 m, as shown in Figure 4-25. The figure also shows the dispersion curves generated by the software. The profiles showed a layer of constant velocity with 258 m/s until 5.5 m of depth. Then the velocity of the profile increases to 400 m/s at 26.5 m depth, suggesting a stiffer layer. After 26.5 m, the profile shows a constant velocity layer of 441 m/s. The V_{S30} computed using this method is 326 m/s.

The V_S profile acquired using the non-inversion showed, in general, an increment of velocity with depth, starting with a continuous layer of velocity that transitions to a stiffer layer between 6 m and 25 m depth. The range of velocities observed in the profiles from both approaches is very similar. The V_{S30} computed by the non-inversion method is 2.8% higher than the results acquired using the inversion.

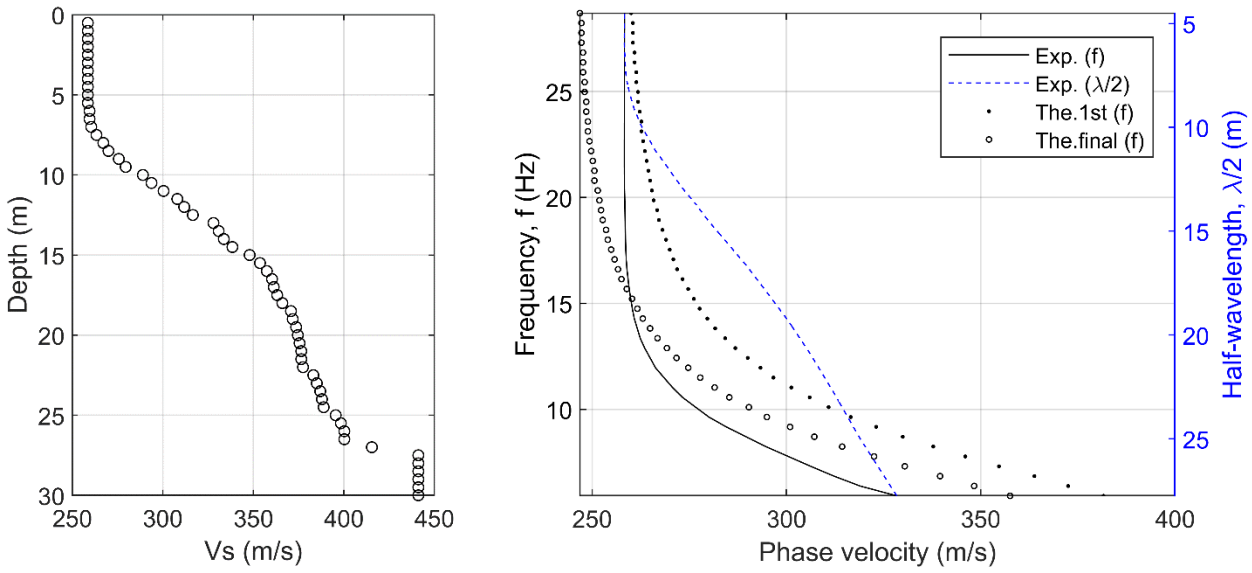

Figure 4-25: V_S profiles (left) and dispersion curves (right) for S1AL seismic station using the non-inversion method.

Seismic Refraction Results

The 2D V_P profile using the seismic refraction method is shown in Figure 4-26. For the seismic refraction analysis, a two-layer model was selected for this site. The results showed a shallow V_P of 396 m/s until an average depth of 4.14 m. Then, the V_P profile shows a stiffer layer of 1,654 m/s.

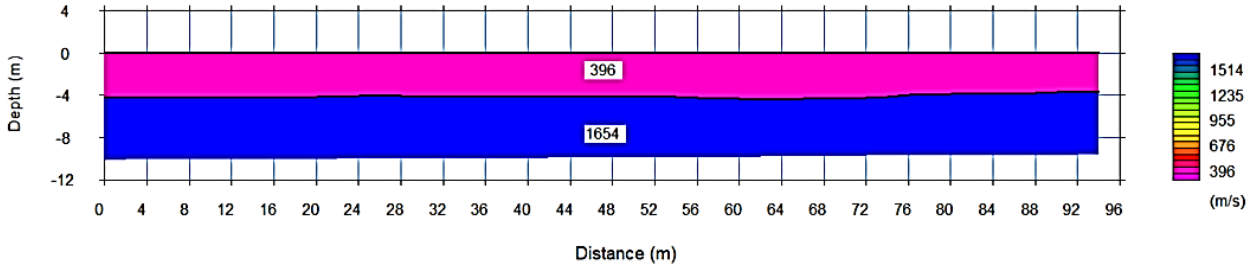

Figure 4-26: 2D V_P profile for S1AL seismic station using seismic refraction method.

The V_P profile was transformed into a V_S profile using a range of 0.4 to 0.6 V_P for the first layer, and a range of 0.14 to 0.2V_P for the second layer to correct for the saturation of water in the profile. The saturation of the profile is indicated by the sharp increment in velocity in profile characterized by sediments. Using this range, the first layer of the V_S profile has velocities between 158-237 m/s. The second layer of the V_S profile reaches velocities in the range of 236-330 m/s. Assuming the second layer until 30 m depth, the V_{S30} value would be in a range of 221-313 m/s for this site, using the seismic refraction method. This extrapolation likely underestimates the velocity computed using seismic refraction. The average V_{S30} result from the seismic refraction is 16% lower than the V_{S30} results using MASW.

4.2.8 S2AL Seismic Station

Location and Geology

The seismic station S1AL is located 3.5 km northeast of Flomaton in Escambia County (31.0079, -87.22488). The geophysical survey was performed on the 3rd of March 2022 using active and passive MASW methods on the site. The terrain was flat in topography and clear of vegetation at the time of the survey. The location of the survey lines used to collect the data are shown in Figure 4-27.

The geology of the site is Alluvial, Coastal, and low terrace deposits from the Holocene epoch from the Cenozoic era. The deposits are characterized by varicolored fine to coarse quartz sand material that contains clay lenses and gravel in some places (Szabo et al., 1988).

Data Collection

An active and passive seismic survey was performed on the site. The active seismic survey was used for MASW and seismic refraction analysis. For the active seismic survey, 48 geophones were used arranged in a linear array with a spacing of 2 m between each other, obtaining a survey line of 94 m. Active data were recorded with a sampling frequency of 2,000 Hz for 1.5 s, and a delay of -0.1 s was used for recording. No acquisition filters were used. For MASW analysis, the active source was located 25 m from the beginning of the survey line, and five shots were recorded in the same position. For seismic refraction analysis, three shots were performed from the beginning until the end of the survey line, at 10 m each. The passive survey was performed using 24 geophones spaced 5 m in an L-shape array, with a total length of 115 m, as shown in Figure 4-27. Passive data were acquired with a sampling frequency of 250 Hz for 240 s. A total of 10 files of 240 s were recorded, reaching 40 min of recording.

Figure 4-27: Site map with the location of survey line for S2AL seismic station

MASW Results

The V_S profiles and the dispersion curves using inversion are shown in Figure 4-27 for 5,000 of the profiles generated with the lowest misfit. The V_S profile with the lower misfit is shown in black and the field dispersion curve is drawn in dark gray, while the corresponding curves from each of the profiles are colored according to their misfit value. The profiles showed an increment of velocity with depth. A two-layer profile was the best fit for this site. The shallow layer had velocities around 231 m/s until 11.3 m depth. The profile then transitions to a stiffer layer with a velocity of 542 m/s. The V_{S30} for this site was computed with a median value of 356.9 m/s and a standard deviation of 1.99 m/s.

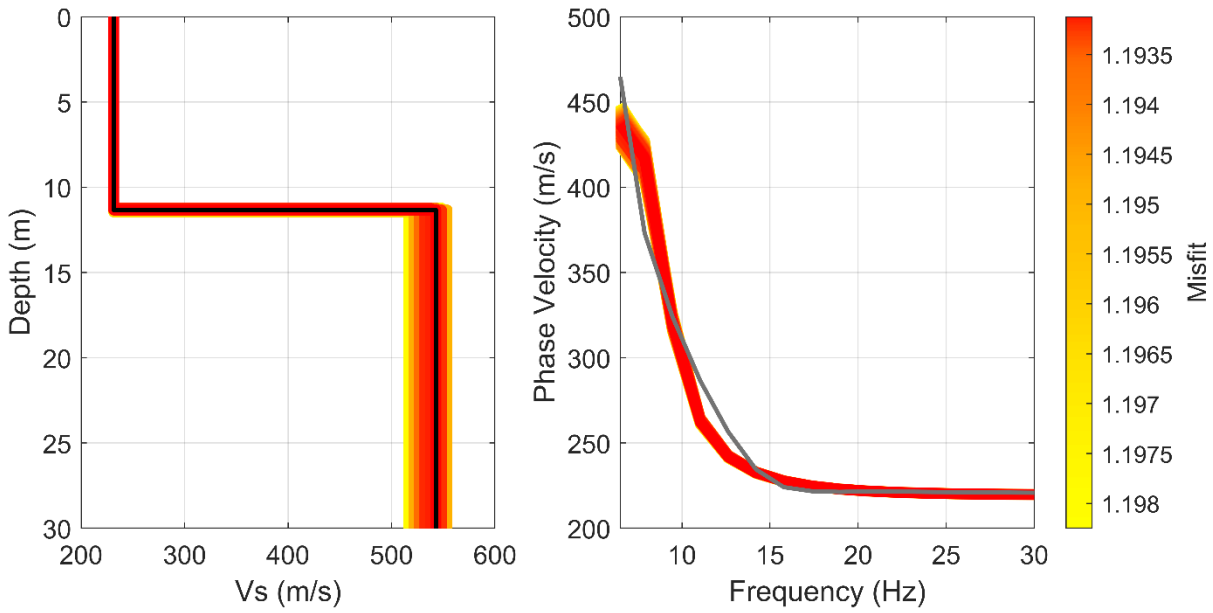

Figure 4-28: V_S profiles (left) and dispersion curves (right) for S2AL seismic station using inversion. The V_S profile with the best fit is shown in black. The dispersion curve from the field is shown in dark gray.

The non-inversion method was used to generate a V_S profile until the 30 m, as shown in Figure 4-29. The figure also shows the dispersion curves generated by the software. The profiles showed a layer of constant velocity with 214 m/s until 5.5 m of depth. Then the velocity of the profile increases to 498 m/s at 23.5 m depth, suggesting a transition to a stiffer layer. After 25 m depth, the profile shows velocities between 583 to 647 m/s. The V_{S30} computed using this method is 357 m/s.

The V_S profile acquired using the non-inversion showed an increment of velocity with depth, starting with a continuous layer of velocity that transition to a stiffer layer between 6 m and 25 m depth. The range of velocities observed in the profiles from both approaches is very similar. The V_{S30} computed by the non-inversion method is 0.03% higher than the results acquired using the inversion.

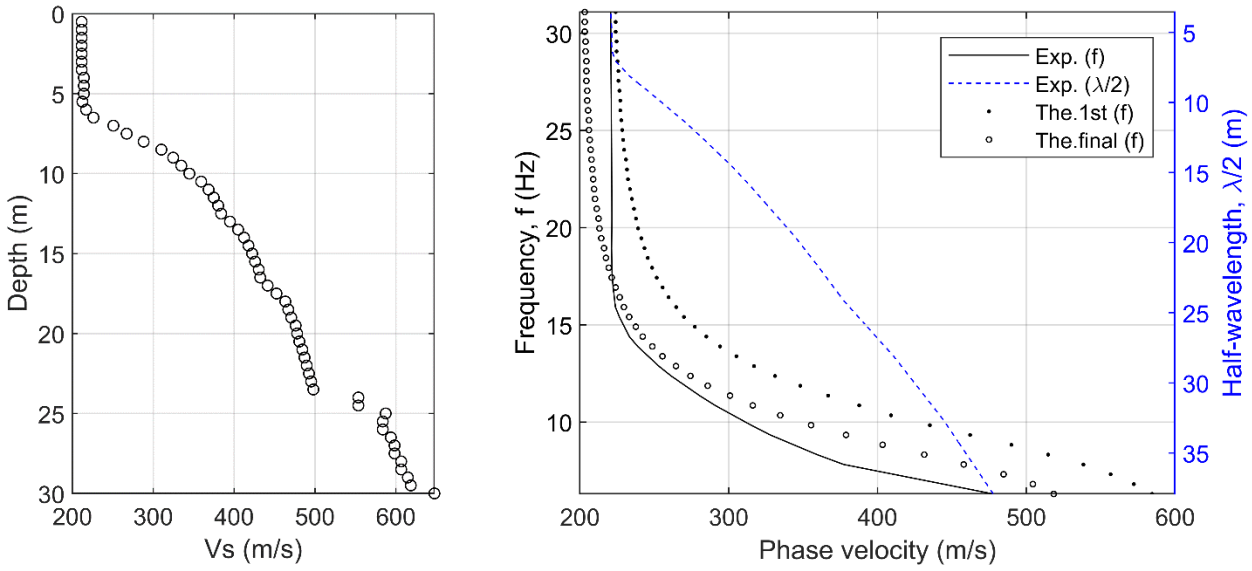

Figure 4-29: V_S profiles (left) and dispersion curves (right) for S2AL seismic station using the non-inversion method.

Seismic Refraction Results

The 2D V_P profile using the seismic refraction method is shown in Figure 4-30. For the seismic refraction analysis, a two-layer model was selected for this site. The results showed a shallow V_P 363m/s until an average depth of 3.95 m. Then, the V_P profile shows a stiffer layer of 1,423 m/s.

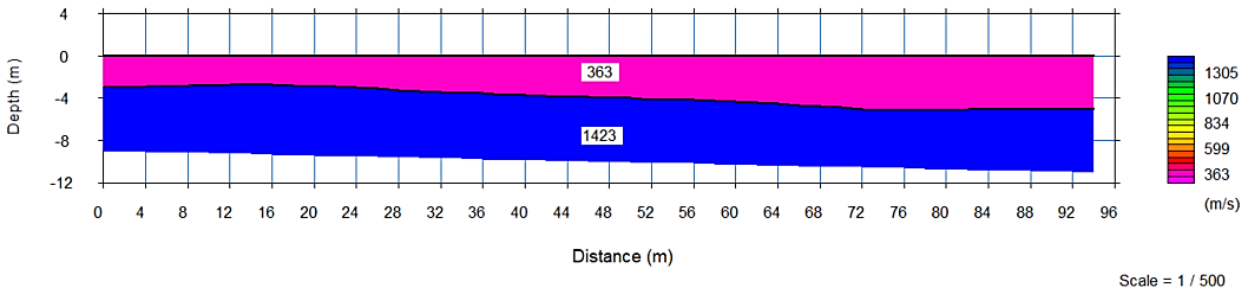

Figure 4-30: 2D V_P profile for S2AL seismic station using seismic refraction method.

The V_P profile was transformed into a V_S profile using a range of 0.4 to 0.6 V_P for the first layer, and a range of 0.14 to 0.2V_P for the second layer to correct for the saturation of water in the

profile. The saturation of the profile is indicated by the sharp increment in velocity in profile characterized by sediments. Using this range, the first layer of the V_S profile has velocities between 145-218 m/s. The second layer of the V_S profile reaches velocities in the range of 203-284 m/s. Assuming the second layer until 30 m depth, the V_{S30} value would be in a range of 193-284 m/s for this site, using the seismic refraction method. This extrapolation likely underestimates the velocity computed using the seismic refraction method. The average V_{S30} result from the seismic refraction is 33% lower than the V_{S30} results using MASW.

4.2.9 Y47A Seismic Station

Location and Geology

The seismic station Y47A is located approximately 4 km of southwest of Winfield in Fayette County, Alabama (33.9025, -87.84940). The geophysical survey was performed on the 9th of April 2022 using active and passive MASW methods on the site. The terrain was flat in topography and clear of vegetation at the time of the survey. The location of the survey lines used to collect the data are shown in Figure 4-31.

The geology of the site is Alluvial, Coastal, and low terrace deposits from the Holocene epoch from the Cenozoic era. The deposits are characterized by varicolored fine to coarse quartz sand material that contains clay lenses and gravel in some places (Szabo et al., 1988).

Data Collection

An active and passive seismic survey was performed on the site. The active seismic survey was used for MASW and seismic refraction analysis. For the active survey, 48 geophones were arranged in a linear array with a spacing of 2 m between each other, obtaining a survey line of 94 m. Active data were recorded with a sampling frequency of 2,000 Hz for 1.5 s, and a delay of -0.1

s was used for recording. No acquisition filters were used. For MASW analysis, the active source was located 25 m from the beginning of the survey line, and five shots were recorded in the same position. For seismic refraction analysis, three shots were performed from the beginning until the end of the survey line, at 10 m each. The passive survey was performed using 24 geophones spaced 5 m in an L-shape array, with a total length of 115 m, as shown in Figure 4-31. Passive data were acquired with a sampling frequency of 250 Hz for 240 s. A total of 9 files of 240 s were recorded, reaching 36 min of recording.

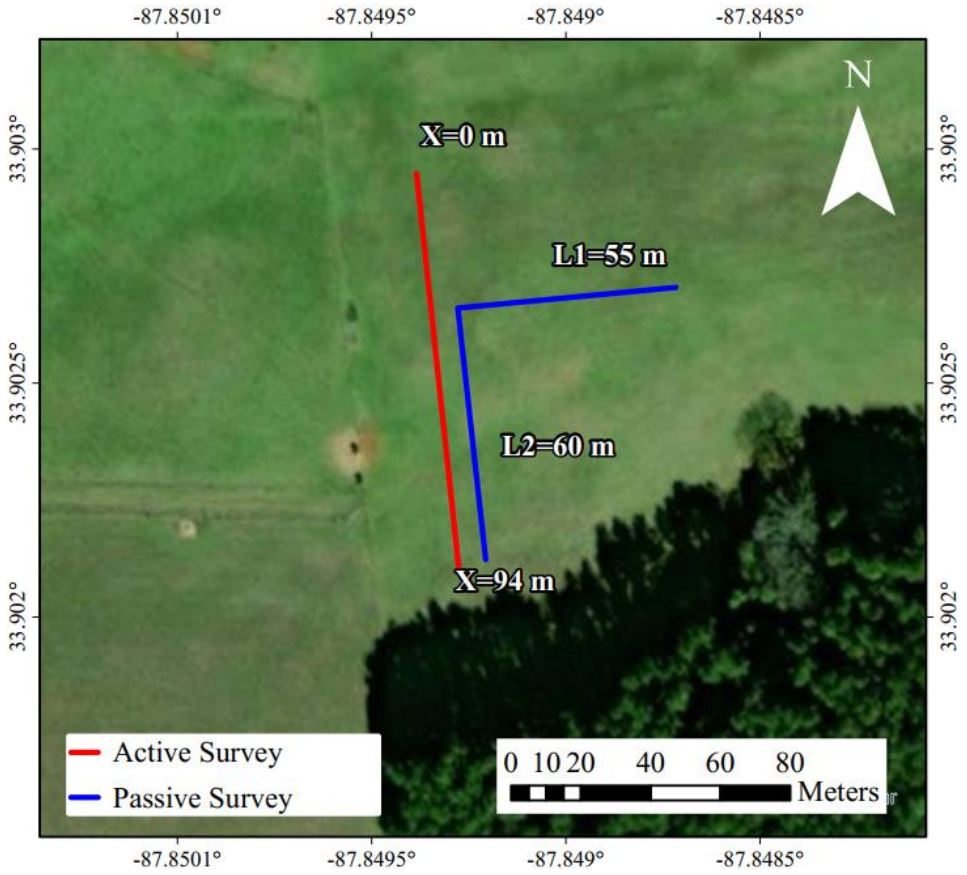

Figure 4-31: Site map with the location of survey line for Y47A seismic.

MASW Results

The V_S profiles and the dispersion curves using inversion are shown in Figure 4-32 for 5,000 of the profiles generated with the lowest misfit. The V_S profile with the lower misfit is shown

in black and the field dispersion curve is drawn dark gray, while the corresponding curves from each of the profiles are colored according to their misfit value. The profiles showed an increment of velocity with depth. A three-layer profile showed the best fit for this site. The shallow layer of the velocity profile had velocities around 324 m/s until 9.4 m depth. The profile then transitions to velocities of 444 m/s until 26.6 m depth. After 26.6 m, the profile shows a stiffer third layer of velocities of 1,248 m/s. The V_{S30} for this site was computed with a median value of 425 m/s and a standard deviation of 1.16 m/s.

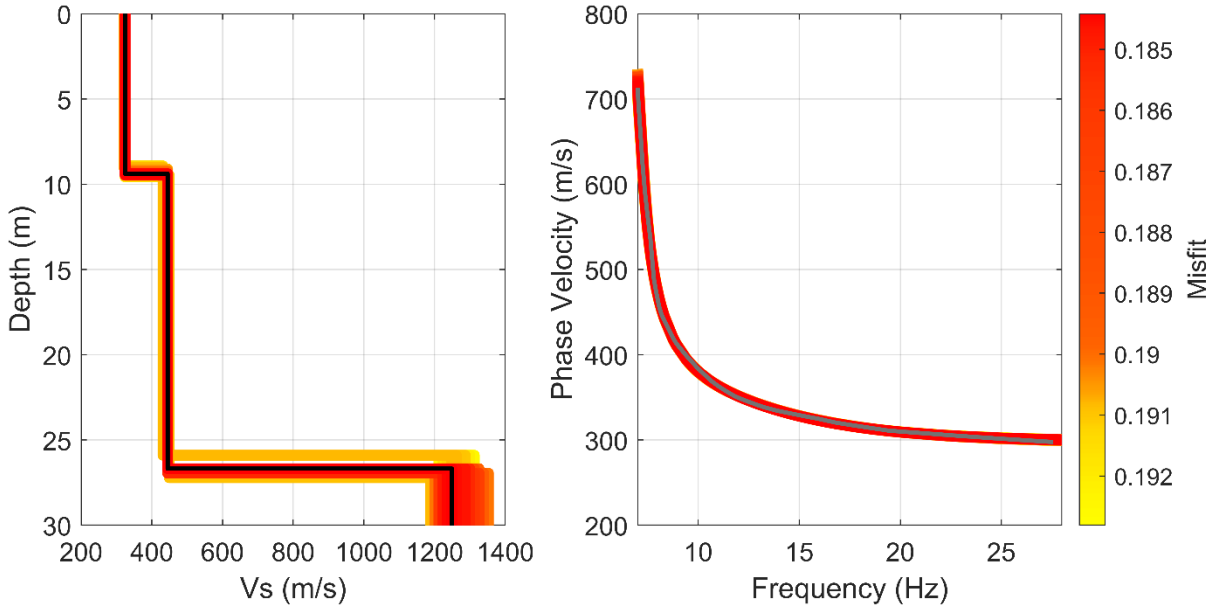

Figure 4-32: V_S profiles (left) and dispersion curves (right) for Y47A seismic station using inversion. The V_S profile with the best fit is shown in black. The dispersion curve from the field is shown in dark gray.

The non-inversion method was used to generate a V_S profile until the 30 m, as shown in Figure 4-33. The figure also shows the dispersion curves generated by the software. The profiles showed a layer of constant velocity with 282 m/s until 5 m of depth. Then the velocity of the profile increases until 27.5 m depth, reaching 627 m/s, suggesting a stiffer layer. After 27.5 m, the profile

shows a second layer of velocities between 690 m/s and 744 m/s. A last point of velocity is located at 30 m depth with 1,096 m/s. The V_{S30} computed using this method is 414 m/s.

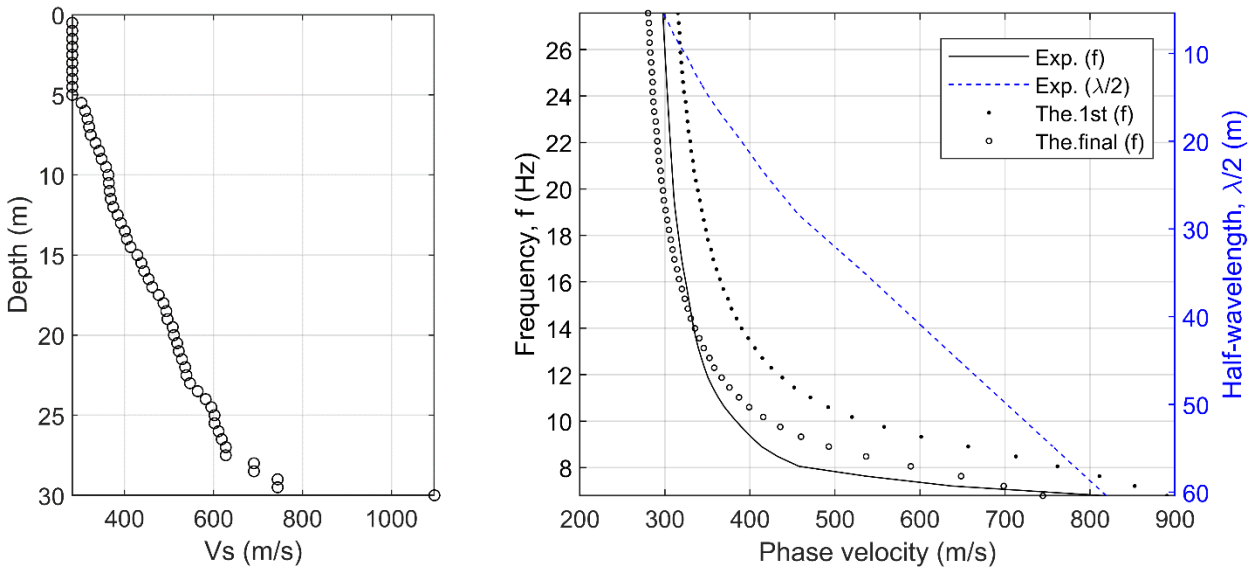

Figure 4-33: V_S profiles (left) and dispersion curves (right) for Y47A seismic station using the non-inversion method.

The V_S profile acquired using the non-inversion showed, in general, an increment of velocity with depth, starting with a continuous layer of velocity that transition to a stiffer layer between 6 m and 27.5 m depth. The range of velocities observed in the profiles from both approaches is very similar after 25 m depth. After this depth, the profile using the inversion method reached higher velocities than the profile calculated with the non-inversion technique. The V_{S30} computed by the non-inversion method is 2.6% lower than the results acquired using the inversion.

Seismic Refraction Results

The 2D V_P profile using the seismic refraction method is shown in Figure 4-34. For the seismic refraction analysis, a two-layer model was selected for this site. The V_P profile showed a

shallow layer of V_P 530 m/s until an average depth of 10.7 m. Followed by a second stiffer velocity layer of 1,268 m/s.

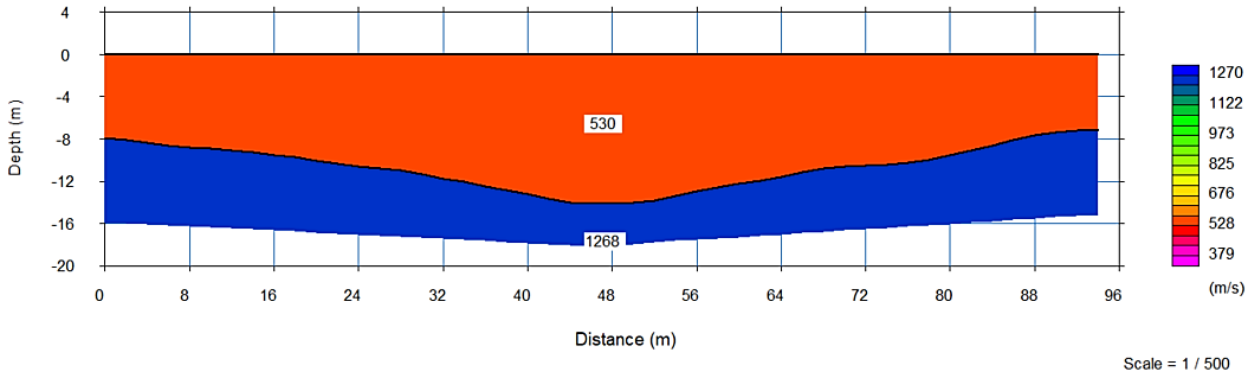

Figure 4-34: 2D V_P profile for Y47A seismic station using seismic refraction method.

The V_P profile was transformed into a V_S profile using a range of 0.4 to 0.6 V_P. Using this range, the first layer of the V_S profile has velocities between 211-317 m/s. The second layer of the V_S profile reaches velocities in the range of 507-760 m/s. Assuming the second layer until 30 m depth, the V_{S30} value would be in a range of 339-508 m/s for this site, using the seismic refraction method. This extrapolation is very close to the MASW results for the V_S profile for each layer, providing a reasonable estimate for V_{S30}. The average V_{S30} result from the seismic refraction is 0.3% lower than the V_{S30} result using MASW, showing a good agreement between the methods.

4.2.10 X48A Seismic Station

Location and Geology

The seismic geophysical survey was located approximately 9 km west of Hartselle in Morgan County (34.4517, -87.04523). The survey was located in the same geologic unit at 940 m southeast of the seismic station. Unfortunately, access to the seismic station site is private, and the owner could not be reached. The survey was performed on the 9th of April 2022 using active and passive MASW methods on the site. The terrain was flat in topography and clear of vegetation at

the time of the survey. The location of the survey lines used to collect the data are shown in Figure 4-35.

The geology of the site is Hartselle Sandstone and low terrace deposits from the Mississippian period from the Paleozoic era. The formation is characterized by light-colored thick-bedded to massive quartzose sandstone. It also contains interbeds of shale with a dark-grey color (Szabo et al., 1988).

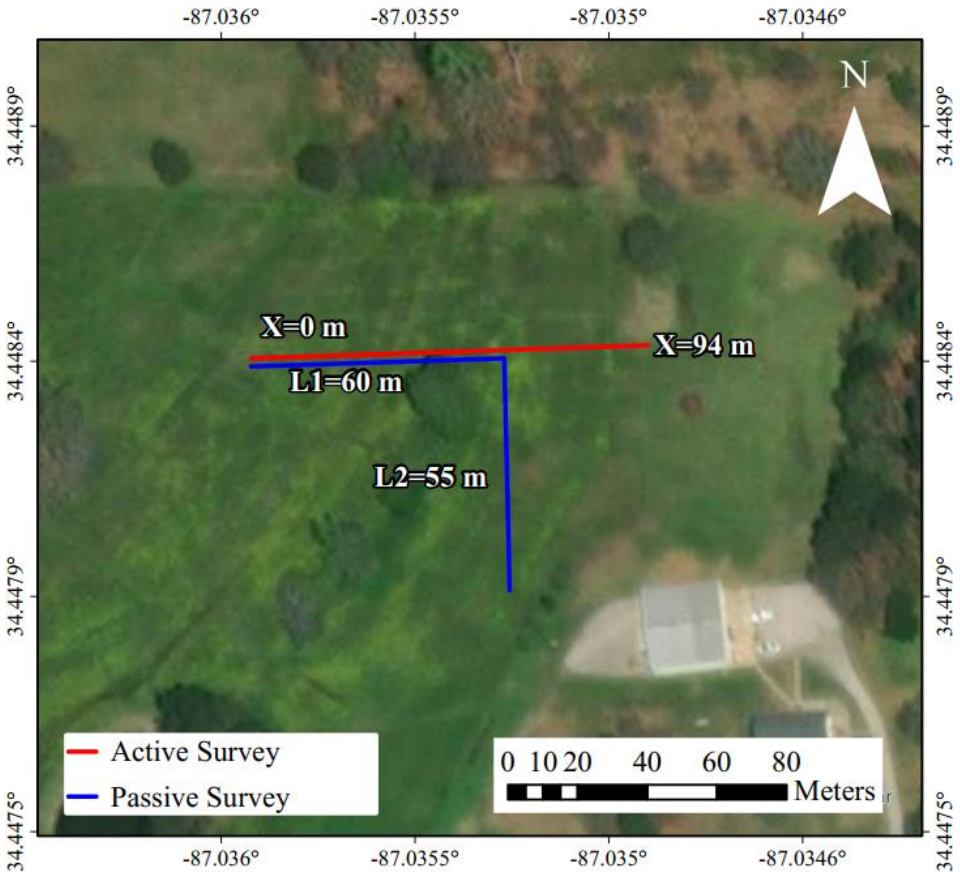

Figure 4-35: Site map with the location of survey line for X48A seismic station

Data Collection

An active and passive seismic survey was performed on the site. The active seismic survey was used for MASW and seismic refraction analysis. For the active seismic survey, 48 geophones

were used arranged in a linear array with a spacing of 2 m between each other, obtaining a survey line of 94 m. The data were recorded with a sampling frequency of 2,000 Hz for 1.5 s, and a delay of -0.1 s was used for recording. No acquisition filters were used. The active source was located 25 m from the end of the line; five shots were recorded in the same position. For seismic refraction analysis, three shots were performed from the beginning until the end of the survey line, at 10 m each. The passive survey was performed using 24 geophones spaced 5 m in an L-shape array, with a total length of 115 m, as shown in Figure 4-35. Passive data were acquired with a sampling frequency of 250 Hz for 240 s. A total of 9 files of 240 s were recorded, reaching 36 min of recording. For this site, passive data did not provide good results; therefore, the inversion was performed using only the active data acquired in the field.

MASW Results

The V_S profiles and the dispersion curves using inversion are shown in Figure 4-36 for 5,000 of the profiles generated with the lowest misfit. The V_S with the lower misfit is shown in black and the field dispersion curve is drawn in dark gray, while the corresponding curves from each profile are colored according to their misfit value. The profiles showed an increment of velocity with depth. A three-layer profile showed the best fit for this site. The shallow layer had velocities around 187 m/s until 2.9 m depth. The profile then transitions to velocities of 410 m/s until 11.4 m depth. After 11.4 m, the profile shows a stiffer third layer of velocities of 790 m/s. The V_{S30} for this site was computed with a median value of 501 m/s and a standard deviation of 2.2 m/s.

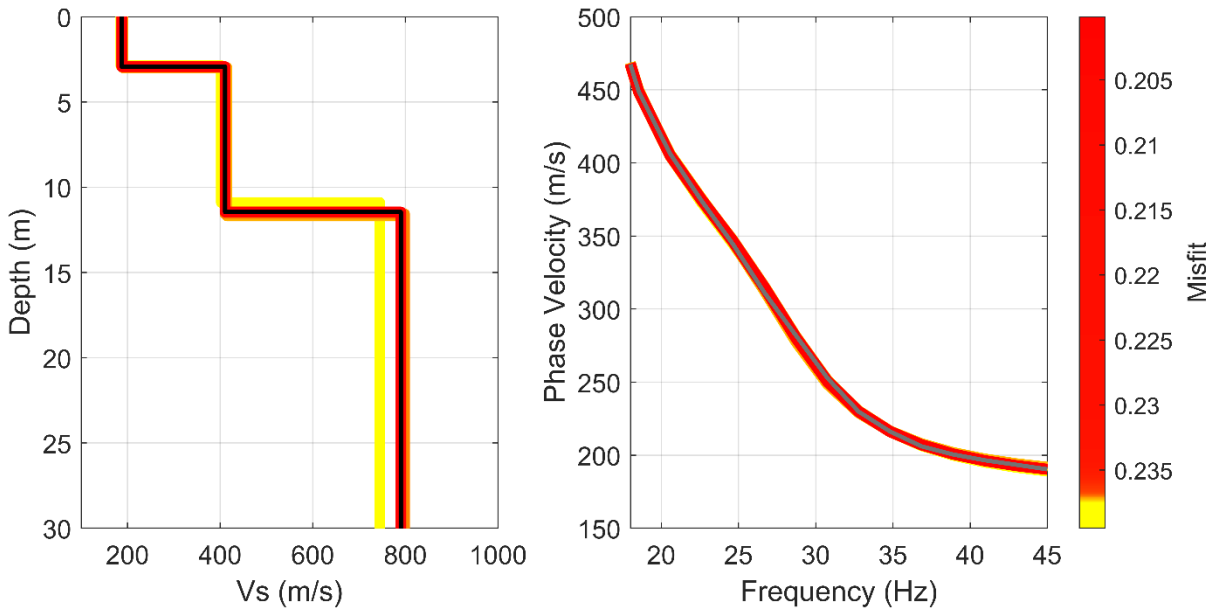

Figure 4-36: V_S profiles (left) and dispersion curves (right) for X48A seismic station using inversion. The V_S profile with the best fit is shown in black. The dispersion curve from the field is shown in dark gray.

The non-inversion method was used to generate a V_S profile until the 30 m, as shown in Figure 4-37. The figure also shows the dispersion curves generated by the software. The profiles showed a thin shallow layer of constant velocity with 171 m/s until 2 m depth. Then, the velocity of the profile increases, reaching a stiffer layer with a velocity of 702 m/s at 15.5 m depth. The V_{S30} computed using this method is 490 m/s.

The V_S profiles acquired using both techniques showed, in general, an increment of velocity with depth. Both profiles show a transition to a stiffer layer between 2 m and 15 m depth. The range of velocities observed in the profiles computed using the non-inversion approach is very similar to the first two layers shown in the profiles calculated using the inversion method. However, the profile computed using the inversion approach reaches higher velocities than the profile calculated using the non-inversion technique. The V_{S30} computed by the non-inversion method is 4.1% lower than the results acquired using the inversion.

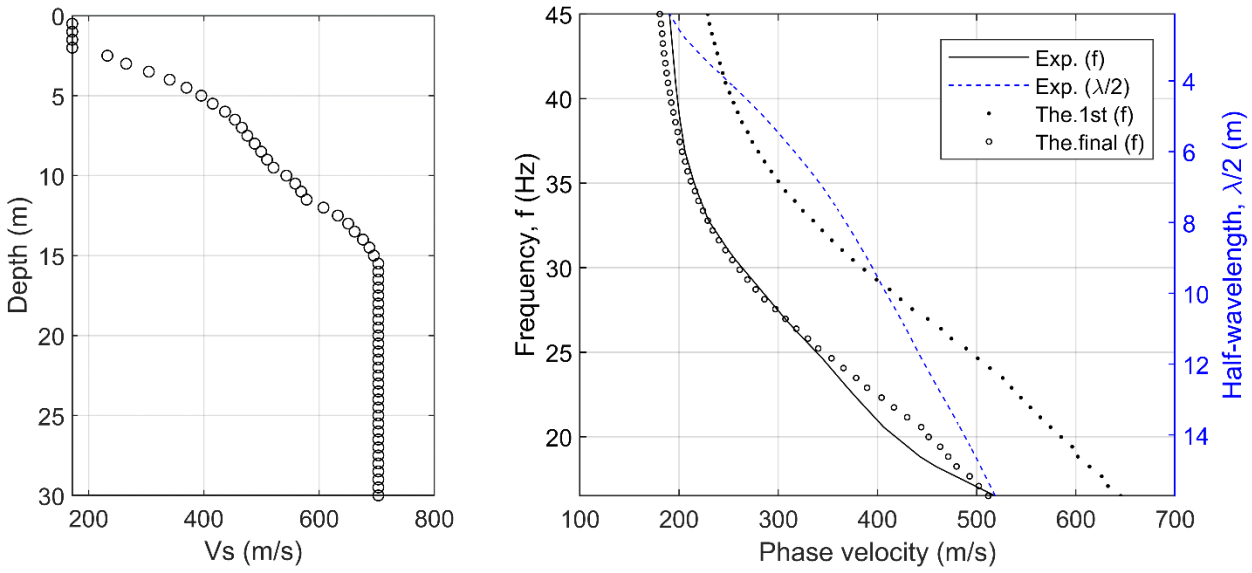

Figure 4-37: V_S profiles (left) and dispersion curves (right) for X48A seismic station using the non-inversion method.

Seismic Refraction Results

The 2D V_P profile using the seismic refraction method is shown in Figure 4-38. For the seismic refraction analysis, a two-layer model was selected for this site. The V_P profile showed a shallow layer of V_P 418 m/s until an average depth of 10.7 m. Followed by a second stiffer velocity layer of 3,168 m/s.

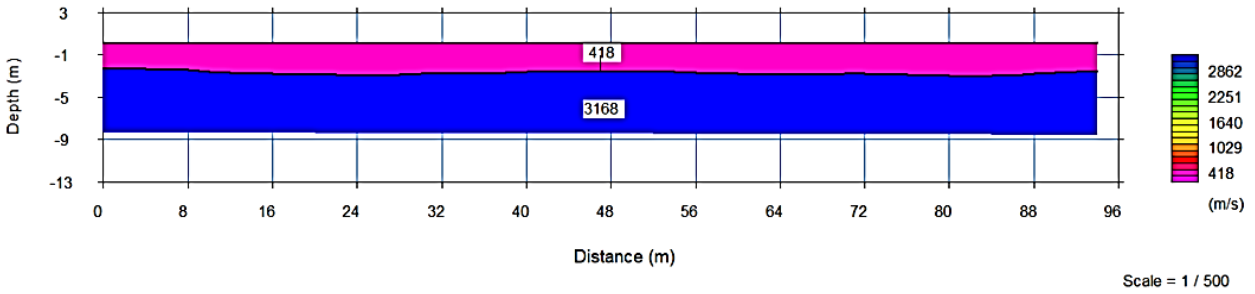

Figure 4-38: 2D V_P profile for X48A seismic station using seismic refraction method.

The V_P profile was transformed into a V_S profile using a range of 0.4 to 0.6 V_P. Using this range, the first layer of the V_S profile has velocities between 167-250 m/s. The second layer of the V_S profile reaches velocities in the range of 1,267-1,901 m/s. Assuming the second layer until 30 m depth, the V_{S30} value would be in a range of 780-1,170 m/s for this site, using the seismic refraction method. This extrapolation likely overestimates the velocity for both layers. The average V_{S30} result from the seismic refraction is 94% higher than the V_{S30} results using MASW.

4.2.11 B01X Seismic Station

Location and Geology

The seismic station B01X is located approximately 6 km southeast of Russellville in Franklin County (34.45390, -87.76700). The geophysical survey was performed on the 9th of April 2022 using active and passive MASW methods on the site. The terrain was relatively flat in topography with clear vegetation at the time of the survey. The location of the survey lines used to collect the data are shown in Figure 4-39.

The geology of the site belongs to the Pottsville Formation (upper part) from the Pennsylvanian period of the Paleozoic era. The formation is characterized by interbedded dark-gray shale, siltstone, medium-gray sandstone, and coal in repeated sequences (Szabo et al., 1988).

Data Collection

An active and passive seismic survey was performed on the site. The active seismic survey was used for MASW and seismic refraction analysis. For the active seismic survey, 48 geophones were used arranged in a linear array with a spacing of 2 m between each other, obtaining a survey line of 94 m. The data were recorded with a sampling frequency of 2,000 Hz for 1.5 s, and a delay of -0.1 s was used for recording. No acquisition filters were used. For MASW analysis, the active

source was located 25 m from the end of the line; five shots were recorded in the same position. For seismic refraction analysis, three shots were performed from the beginning until the end of the survey line, at 10 m each. The passive survey was performed using 24 geophones spaced 5 m in an L-shape array, with a total length of 115 m, as shown in Figure 4-39. Passive data were acquired with a sampling frequency of 250 Hz for 240 s. A total of 10 files of 240 s were recorded, reaching 40 min of recording. For this site, passive data did not provide good results; therefore, the inversion was performed using only the active data acquired in the field.

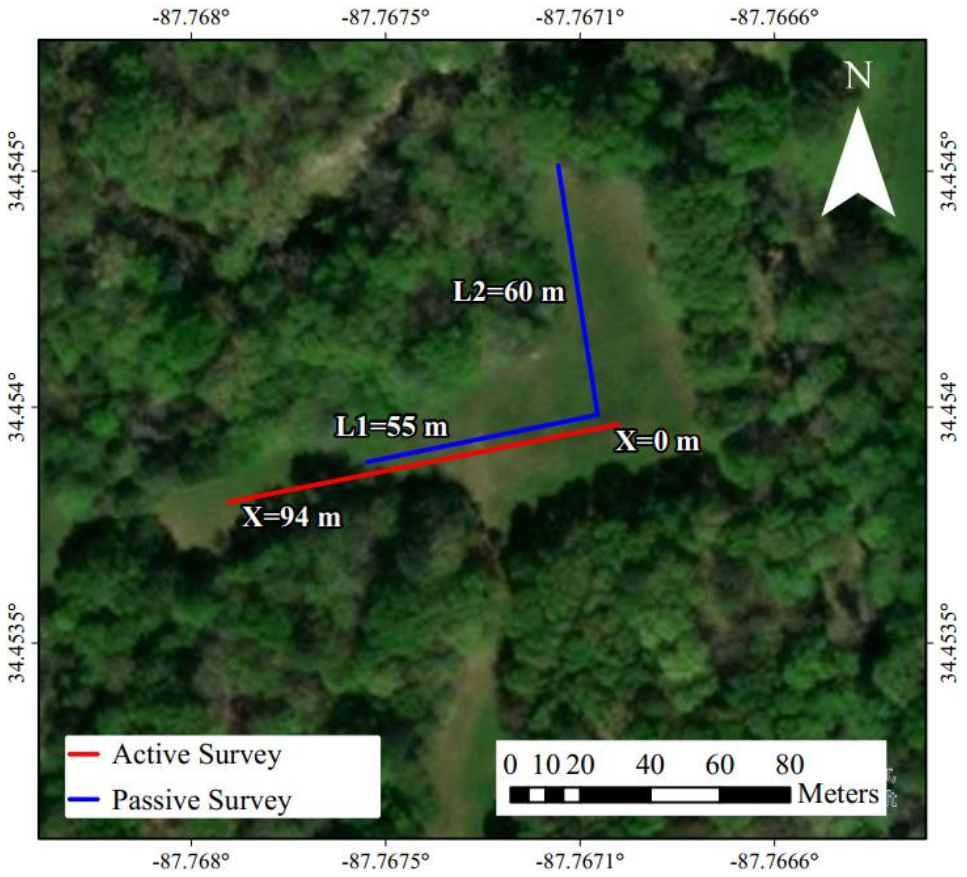

Figure 4-39: Site map with the location of survey line for B01X seismic station

MASW Results

The V_S profiles and the dispersion curves using inversion are shown in Figure 4-40 for 5,000 of the profiles generated with the lowest misfit. The V_S profile with the lower misfit is shown

in black and the field dispersion curve is drawn in dark gray, while the corresponding curves from each of the profiles are colored according to their misfit value. The profiles showed an increment of velocity with depth. A three-layer profile showed the best fit for this site. The shallow layer had velocities around 279 m/s until 2.44 m depth. The profile then transitions to velocities of 431 m/s until 7.5 m depth. After 7.5 m, the profile shows a stiffer third layer with a velocity of 1,164 m/s. The V_{S30} for this site was computed with a median value of 760 m/s and a standard deviation of 3.3 m/s.

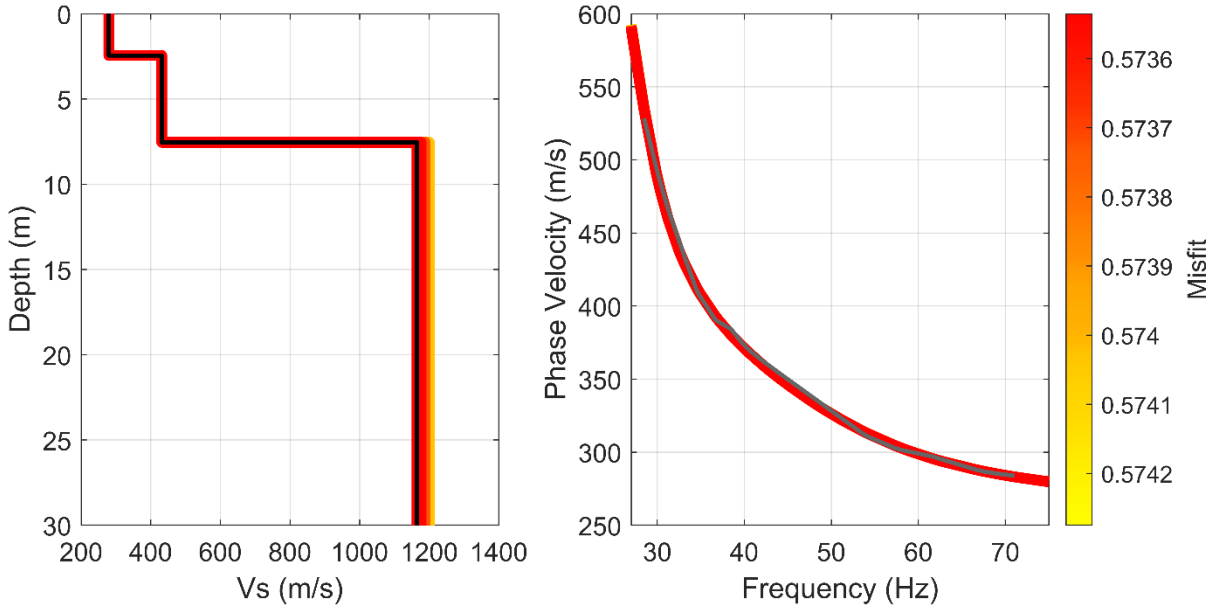

Figure 4-40: V_S profiles (left) and dispersion curves (right) for B01X seismic station using inversion. The V_S profile with the best fit is shown in black. The dispersion curve from the field is shown in dark gray.

The non-inversion method was used to generate a V_S profile until the 30 m, as shown in Figure 4-41. The figure also shows the dispersion curves generated by the software. The profiles showed a thin shallow layer of constant velocity with 260 m/s until 2 m of depth. Then, the velocity of the profile increases to 729 m/s at 9 m depth and remains constant until 30m, suggesting a stiffer layer. The V_{S30} computed using this method is 598 m/s.

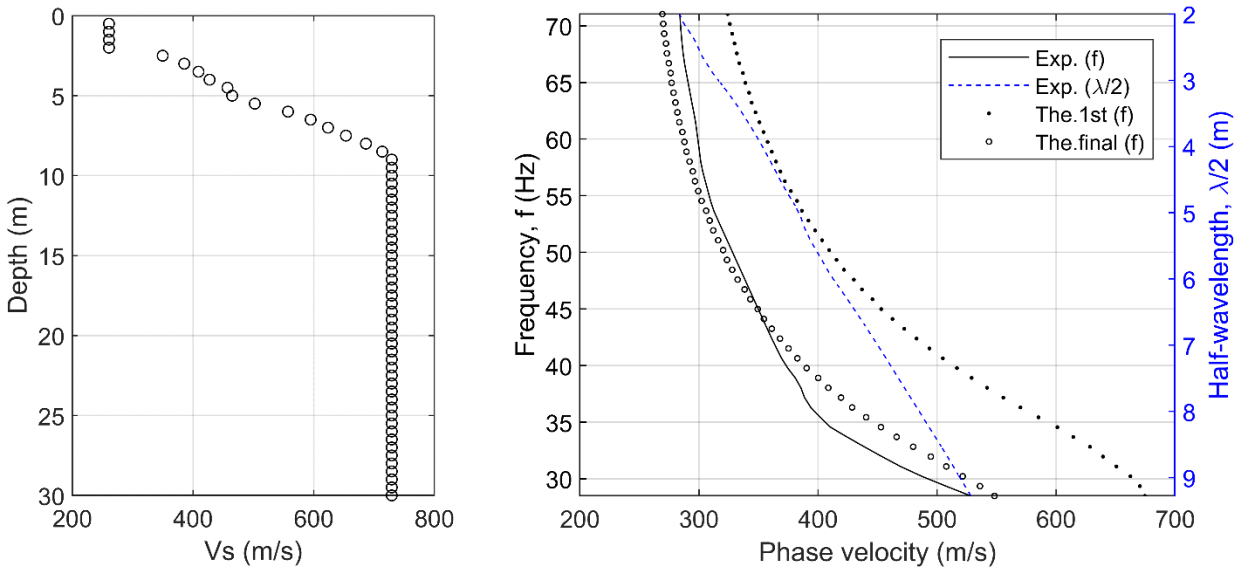

Figure 4-41: V_S profiles (left) and dispersion curves (right) for B01X seismic station using the non-inversion method.

The V_S profiles acquired using both techniques showed, in general, an increment of velocity with depth. Both profiles show a transition to a stiffer layer between 2 m and 11 m depth. The range of velocities observed in the profiles computed using the non-inversion approach is very similar to the first layer. However, the profile computed using the inversion approach reaches higher velocities than the profile calculated using the non-inversion technique. This generates that the V_{S30} computed using the non-inversion method is 21.3% lower than the results acquired using the inversion.

Seismic Refraction Results

The 2D V_P profile using the seismic refraction method is shown in Figure 4-42. For the seismic refraction analysis, a two-layer model was selected for this site. The results showed a shallow V_P of 377 m/s until an average depth of 2.7 m. Then, the V_P profile shows a stiffer layer of 4,055 m/s.

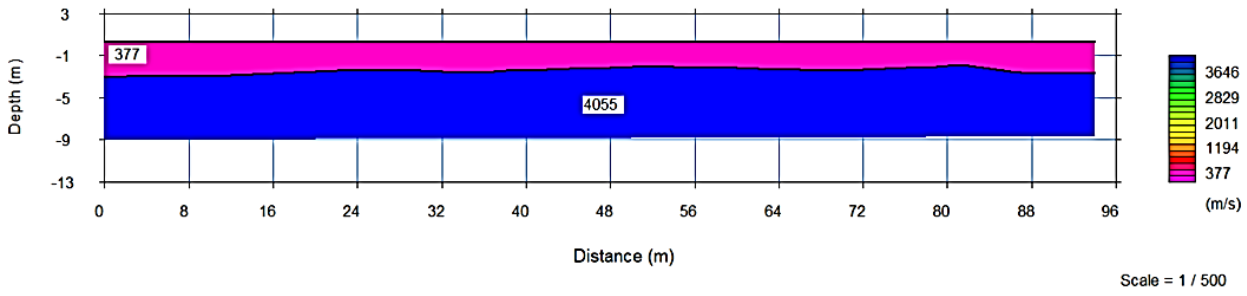

Figure 4-42: 2D V_P profile for B01X seismic station using seismic refraction method.

The V_P profile was transformed into a V_S profile using a range of 0.4 to 0.6 V_P. Using this range, the first layer of the V_S profile has velocities between 150-225 m/s. The second layer of the V_S profile reaches velocities in the range of 1,622-2,432 m/s. Assuming the second layer until 30 m depth, the V_{S30} value would be in a range of 855-1,282 m/s for this site, using the seismic refraction method. This extrapolation likely underestimates the velocity at shallower depths while overestimating the velocity in the deeper layers. The average V_{S30} result from the seismic refraction is 41% higher than the V_{S30} results using MASW.

4.3 SITES WITH PREVIOUSLY PUBLISHED DATA

4.3.1 SWET Seismic Station

The information provided for SWET seismic station is based on the "Ground-Motion Model Review Project: Shear Wave Velocity Measurements at Seismic Recording Stations in the Central and Eastern United States" developed by EPRI (2013).

Location and Geology

The seismic station SWET is in Sewanee, Franklin County, in Tennessee. It was located in the University of the South Horse Pasture with coordinates of 35°12'58.5"N and 85°55'54.6"W. The station is located in a rural area, and there is undulating topography in the vicinity of the site.

Two different surveys were performed on the site. One of them was executed by the University of Texas at Austin and the second one by the company Geovision Geophysical Services. The investigations were performed between May 15th and July 19th of, 2012. The University of Texas at Austin conducted a seismic survey using the SASW method to analyze the data. At the same time, Geovision used MALW.

The site is in the Crab Orchard Mountain Group, a Paleozoic geologic unit specifically in the Pennsylvanian period. The site is characterized by conglomerate, sandstone, siltstone, shale, and coal (Hardeman et al., 1996; Greene & Wolfe, 2000).

Results

The data collected could not be processed using the MASW method due to dominant higher modes at the site that prevented observing the fundamental frequency of the site. The velocity profiles and dispersion curves generated using both methods are shown in Figure 4-43. The dispersion curves and the profiles computed for this site showed consistency in the results for both techniques. Both techniques showed an agreement in the first meters of the profile showing several velocity layers with velocities between 100 and 400 m/s. Then, the profiles showed a transition to a higher velocity of 650 m/s after 5 m of depth. The discrepancy in the profiles occurs between 10 and 35 m, where MALW shows more layers in this region with a faster transition to higher velocities. After 36 m of depth, the profiles showed agreement in the layer velocity around 2,100 m/s. The dispersion curve selected using SASW showed slightly higher phase velocities for wavelengths from 8 m and above.

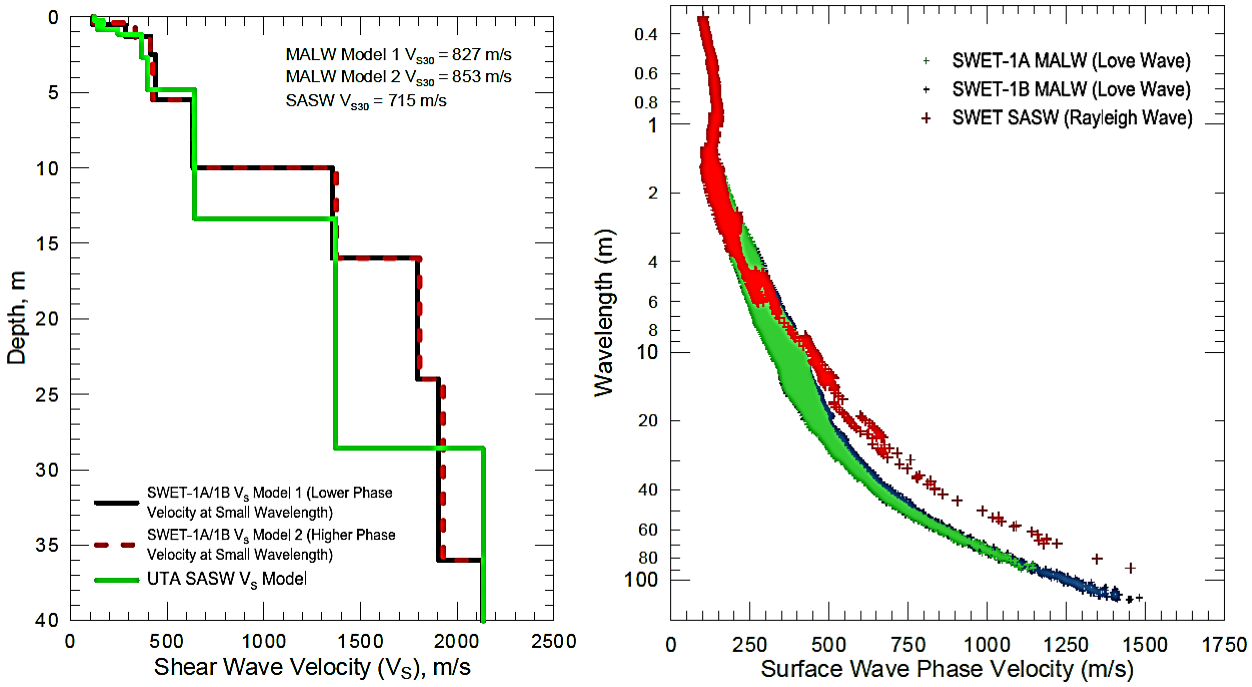

Figure 4-43: V_S profiles (left) and dispersion curves (right) for SWET seismic station. The profile computed by the University of Texas at Austin is shown in green, while the dispersion curve is shown in red color. The profiles calculated by Geovision are shown in red and black, while the dispersion curves are shown in green and blue (EPRI, 2013)

The V_{S30} values computed using the different techniques show a difference of around 15% in the results. SASW method calculated V_{S30} of 715 m/s, while the average V_{S30} computed through MALW was 840 m/s.

4.3.2 LRAL Seismic Station

The information provided for LRAL seismic station is based on the "Ground-Motion Model Review Project: Shear Wave Velocity Measurements at Seismic Recording Stations in the Central and Eastern United States" developed by EPRI (2013).

Location and Geology

The seismic station LRAL is in Sewanee, Franklin County, in Tennessee. The seismic station is located at the Lakeview Retreat Golf Course, Brierfield, in Bibb County, Alabama

(33.0399,-86.9978). The site investigations were performed on May 15^{h} of 2012. The station is located at the top of a small hill. The University of Texas at Austin conducted a seismic survey using the SASW method to analyze the data.

The site is in the Conasauga Formation, a Cambrian geologic. This formation is characterized by medium to thick beds of dolomite. The dolomite varies from light to dark-grey color in finely to coarse crystalline form. The formation also contains greenish-gray shale and light-bluish chert. In Bibb County, where the seismic station is located, the formation consists of fine-grained argillaceous limestone in thin-bedded and interbedded shale (Szabo et al., 1988).

Results

The V_S profile for the LRAL seismic station recommended by the University of Texas at Austin is shown in Figure 4-44. The V_S profile showed variation in velocity from 450 to 650 m/s in the first 20 m. Then the profile increases the velocity to 914 m/s. The V_{S30} value computed for this site is 568 m/s.

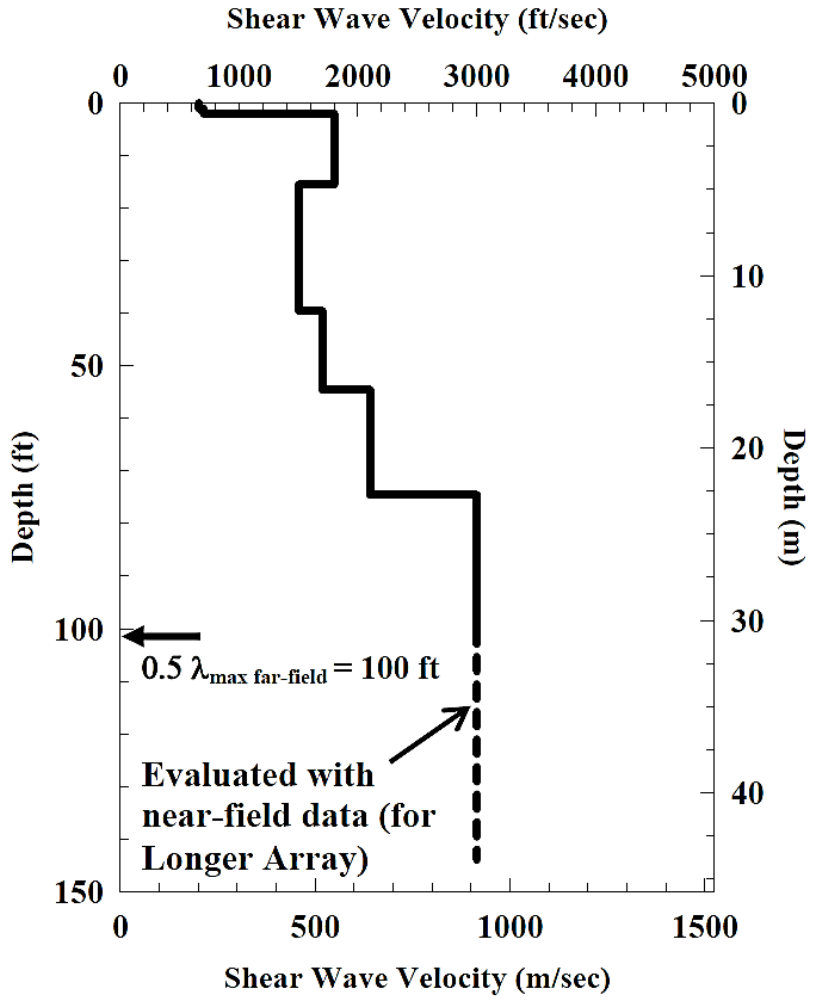

Figure 4-44: V_S profile for LRAL seismic station recommended by the University of Texas at Austin EPRI (2013).

4.3.3 BLF1 Site

The information provided for the BLF1 site is based on the report "*Bellefonte Nuclear Plant, Units 3 & 4 COL Application Part 2, FSAR"* by the Tennessee Valley Authority (TVA, 2007)

Location and Geology

Site characterization was performed for the Bellefonte Nuclear Plant project (TVA, 2007). The site is located in the northeast part of Alabama, in Jackson County (34.71370, -85.92622). The

site characterization at this site included five types of geophysical surveys (Seismic refraction, SCPT, suspension and downhole logging test, microgravity, and natural gamma borehole).

The geologic unit of the site is the Stones River Groups, undifferentiated in part from the Paleozoic era. This group consists of thick to thins-bedded limestone of medium to dark-grey color. The limestone can be argillaceous in part or fossiliferous (Szabo et al., 1988).

Results

The profile selected to compute V_{S30} is from Boring B-1032PS (34.71370, -85.92622), shown in Figure 4-45. This profile was performed on the 10th of June 2006, and the coordinates used for this site are for this boring. The V_S profile from Boring B-1032PS was acquired using P-S suspension logging. As shown on the image, this profile was simplified to a two-layers profile. The first layer reached a depth of 6.1 m (20ft) with a velocity of 347 m/s (1,139 ft/s). The second layer had a velocity around 2,925 m/s (9,595 ft/s). The V_{S30} value computed for this site is 1,165 m/s.

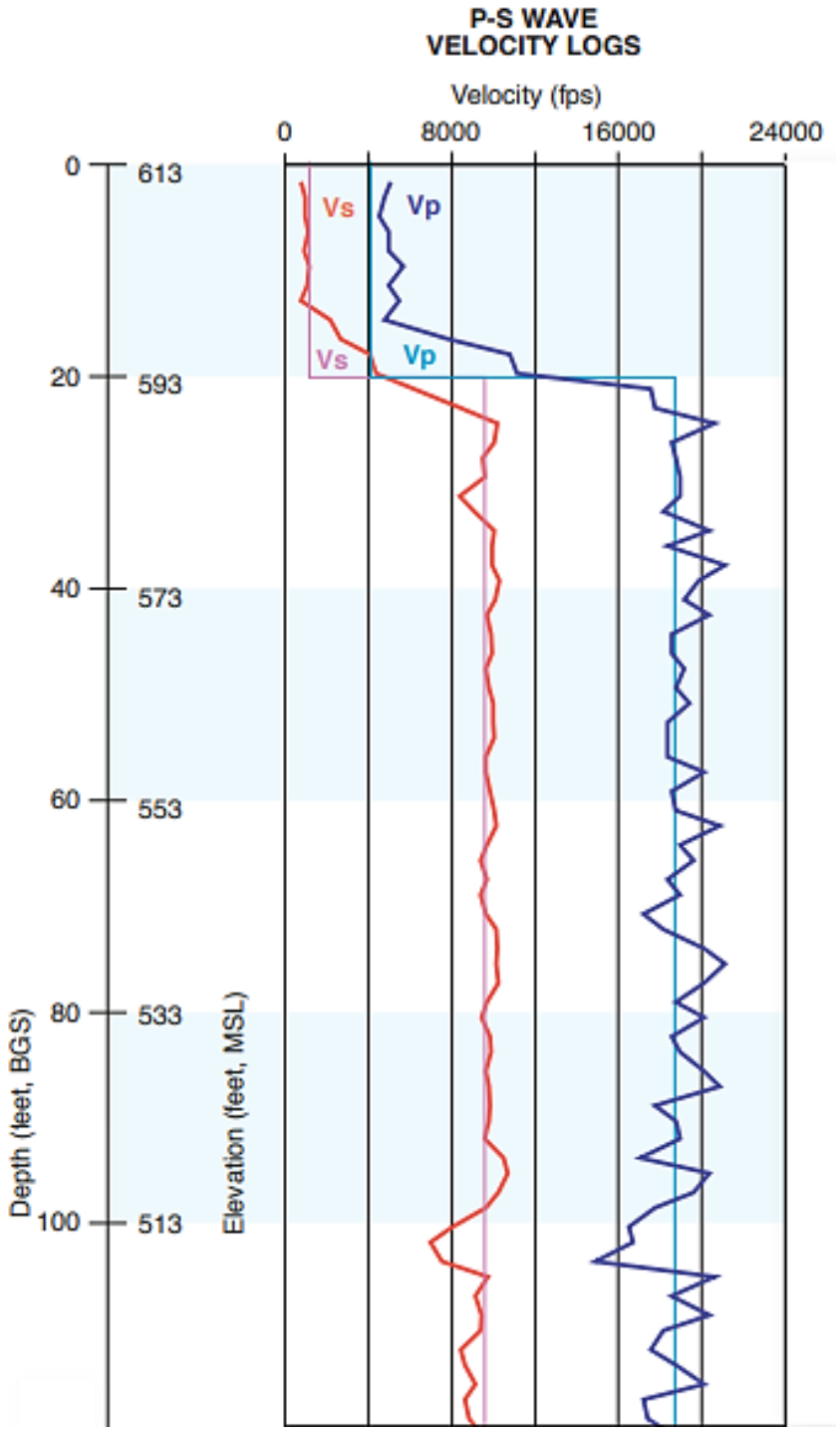

Figure 4-45: V_S and V_P profile for BLF1 site at B-1032PS (TVA, 2007)

4.3.4 AFBM Site

The information provided for the AFBM site is based on the report "Delineating Subsurface Features with the MASW Method at Maxwell AFB in Montgomery, Alabama," developed by Xia (2022).

Location and Geology

The report was prepared for the Maxwell Air Force Base in Montgomery, Alabama (32.3706545, -86.3530631). The authors used geophysical methods to detect shallow geological features in the site. Among the features discovered on the site is a possible buried channel. For this site, nine survey lines were across the site. Lines 1,2, and 4 do not cross the possible buried channel and have similar velocity profiles. Line 1 was selected to represent the site, and the coordinates provided here are at the center of line 1. The geophysical survey was performed using the MASW method with a roll-along acquisition format.

The geology of the site is Alluvial Coastal and low terrace deposits from the Holocene epoch in the Cenozoic era. The deposits are characterized by varicolored fine to coarse quartz sand material that contains clay lenses and gravel in some places (Szabo et al., 1988).

Results

The author retrieved several profiles along the line to generate a 2D model, as shown in Figure 4-46. The 2D V_S profile for the AFBM site showed the location of well MW-430 at the beginning of the survey line.

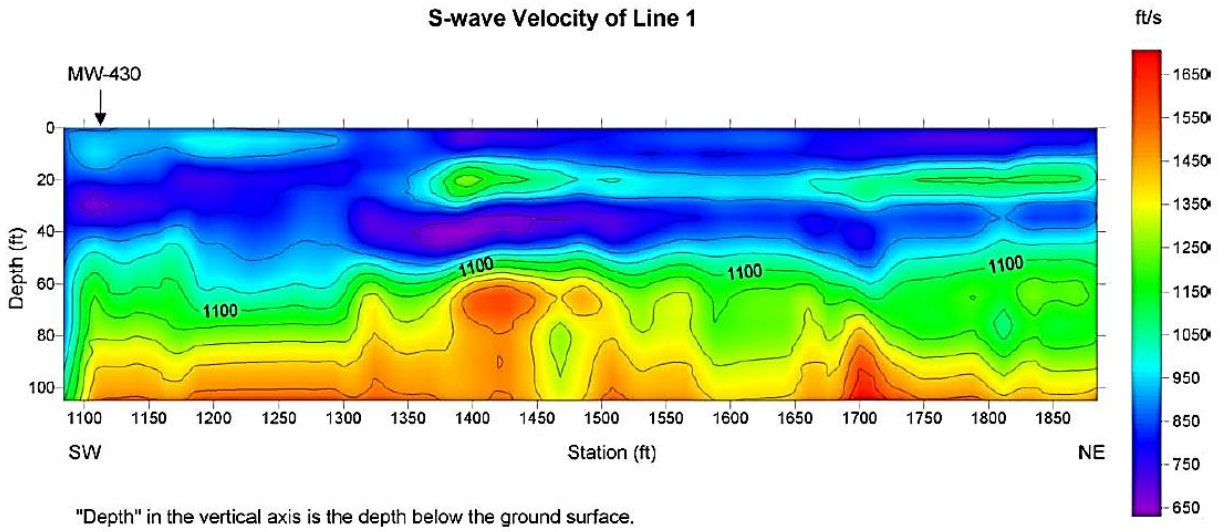

Figure 4-46: 2D V_S profile for AFBM site using MASW method for survey line 1 (Xia, 2022).

V_S profiles for survey line 1 were digitized from Figure 4-46 to compute $V_{S30.}$ The profiles are shown in Figure 4-47. The points in the image are V_S values from the contour map at locations 14+00 and 16+00 of the 2D V_S profile. The profile lines were drawn, estimating the thickness of each layer as the average distance between the V_S points. The V_S profile at 14+00 showed a constant velocity of 274 m/s until 14 m. depth, while V_S profile at 16+00 showed a variation of velocity between 274 to 366 m/s. Then the profiles increase in velocity with the velocity varying from 240 to 330 m/s in the first 15 m. After 15 m depth, the profiles showed another stiffer layer with a velocity between 366 to 427 m/s until 38 m depth. The V_{S30} values computed at location 14+00 and 16+00 were 314.2 m/s and 331.9 m/s, respectively. For further comparison, it will be used an average V_{S30} value of 323 m/s.

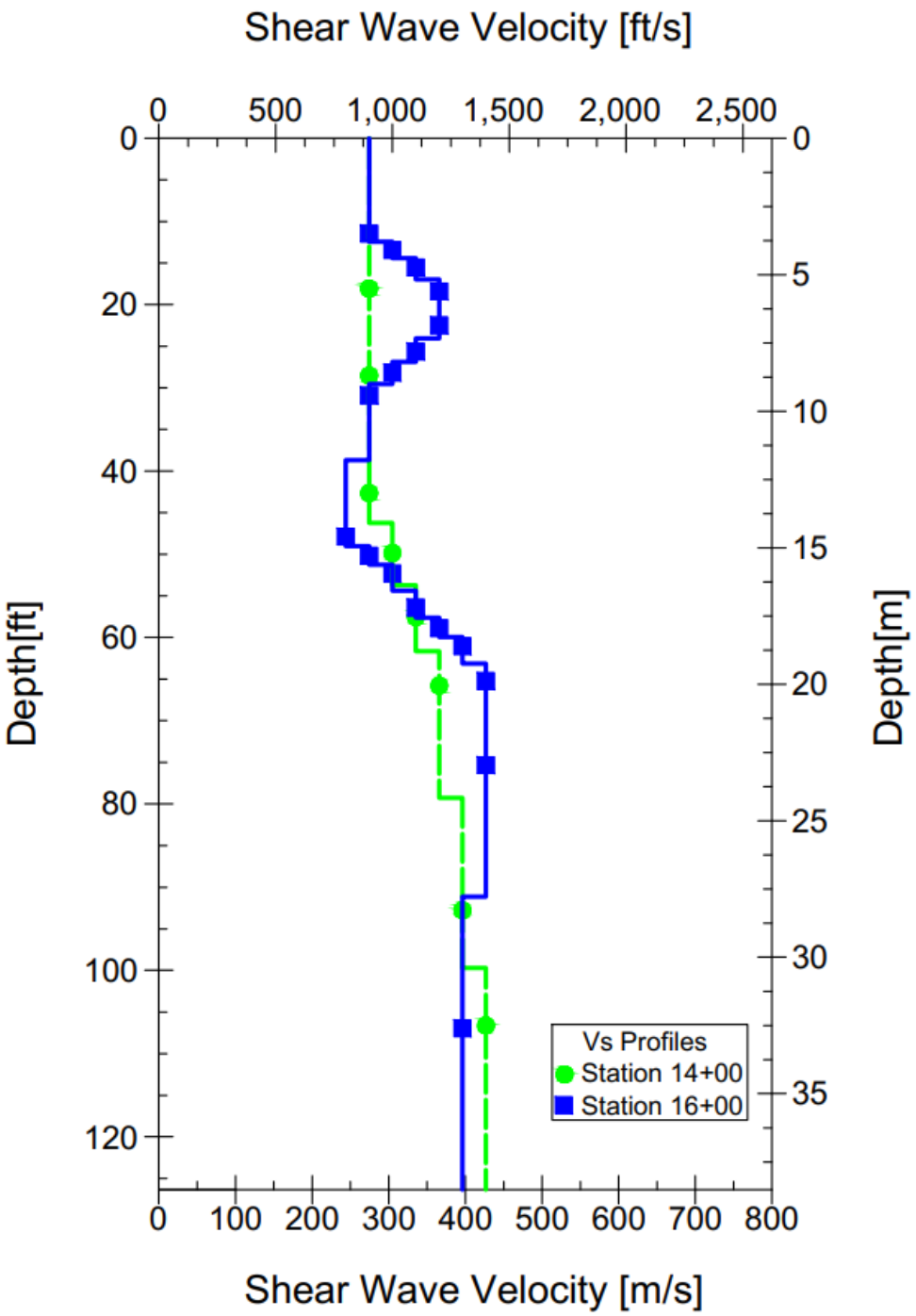

Figure 4-47: V_S profile from station 14+00 for survey line 1 digitalized from Xia (2022).

CHAPTER 5 RESULTS OF INDIRECT METHODS

5.1 INTRODUCTION

The results of the indirect methods used to estimate V_{S30} at the selected sites (Figure 3-1) are presented in this chapter. Each section in this chapter presents a description of the results and summary tables for each of the methods applied (i.e., P-wave, HVSR, R-wave ellipticity, and proxy methods).

The results from the P-wave seismogram method provide estimations for V_{SZ} and V_{S30} using seismic recordings and the correlations from Kim et al. (2016). Also, a sensitivity analysis of the V_{SZ} estimations to the various processing parameters was performed. The HVSR and the R-wave ellipticity methods were used to identify frequency peaks and amplification values for the sites with seismic stations. The HVSR results were used with existing correlations to estimate V_{S30} based on the peak frequency. The R-wave ellipticity curve was used to perform a joint inversion with the dispersion curve from MASW for the sites where the R-wave ellipticity could be computed. Finally, the proxy methods provided V_{S30} estimations for all the sites included in the study.

5.2 P-WAVE SEISMOGRAM METHOD

The P-wave seismogram method was applied successfully to 46 of the 57 seismic stations selected for the study. A total of 8,128 seismic records were processed from these 56 stations. Almost 95% of the recordings could not be used due to low SNR, including all the records for 11 of the stations. The total number of records and the number of records meeting the SNR criteria are listed in Table 5-1:. V_{SZ} values were estimated for 459 seismic records for the 46 seismic stations. The V_{SZ} values calculated for each one of the stations are shown in Figure 5-1. The V_S

value for station 249A could be computed only using amplitude ratio correlation because the depth of the seismic record available with SNR higher than 1.5 was in the first layer of the crustal model, and the ray parameter could not be computed to estimate V_{SZ}.

Table 5-1: Selected stations

Station/ Site	Latitude	Longitude	Start	End	No. Records Available	No. Records SNR>1.5
PWLA	34.98	-88.064	04/02/13	OPEN	565	17
PLAL	34.982	-88.076	03/23/11	OPEN	744	33
N29A	34.9733	-87.2793	05/30/13	10/05/13	0	0
B01	34.7172	-87.9824	08/01/13	12/31/15	62	5
B01X	34.4539	-87.767	07/31/13	12/31/15	56	4
X47A	34.5178	-87.8571	12/10/11	07/29/13	210	20
X48A	34.452	-87.045	12/16/13	OPEN	207	6
X48A-V	34.4517	-87.0452	12/14/11	12/16/13	212	15
SWET	35.216	-85.932	08/04/10	OPEN	432	6
DYTN	35.491	-85.092	08/22/12	OPEN	611	15
W50A	35.2	-85.312	03/01/16	OPEN	201	9
CSTN	35.101	-85.237	11/21/13	OPEN	476	0
X49A	34.5126	-86.326	12/11/11	07/26/13	198	23
X50A	34.4596	-85.6486	12/16/11	04/04/12	1	0
X50B	34.4611	-85.6499	05/04/12	08/04/13	212	31
FPAL	34.54	-85.611	03/30/10	OPEN	411	10
JIM	34.475	-85.526	05/01/03	06/06/03	1	0
TEMP	34.38	-85.714	05/01/03	06/06/03	1	0
DEB	34.4113	-85.6355	04/29/03	06/06/03	1	1
FISH	34.4616	-85.6412	04/29/03	06/06/03	1	1
PAYN	34.5006	-85.6876	04/29/03	06/06/03	1	1
LARR	34.4592	-85.5866	04/29/03	06/06/03	1	0
X51A	34.566	-84.857	03/01/16	OPEN	201	10
Y48A	33.9131	-87.1696	12/17/11	08/06/13	183	55
Y49A	33.858	-86.412	12/16/13	OPEN	162	60
Y49A-V	33.8577	-86.4119	12/18/11	12/16/13	210	40
Y50A	33.8911	-85.7347	12/20/11	08/08/13	202	6
Z48A	33.3764	-87.5556	04/15/11	02/03/13	85	4
Z49A	33.1942	-86.5311	12/19/11	08/06/13	183	0
Z50A	33.254	-85.9226	01/22/13	05/24/14	185	7
Z51A	33.317	-85.175	05/30/14	03/05/18	142	4
Y47A	33.9025	-87.8494	04/13/11	02/03/13	97	2
Z47A	33.199	-88.0696	04/16/11	01/31/13	75	1
Z47B	33.199	-88.07	02/28/14	OPEN	53	7
EUAL	32.97143	-88.08669	03/31/15	09/23/15	3	1
LRAL	33.04	-86.998	05/02/11	OPEN	2	1
147A	32.6738	-88.2708	04/10/11	11/17/13	166	5
148A	32.6469	-87.571	01/16/12	08/07/13	117	1

149A	32.5983	-86.7916	01/17/12	08/07/13	166	1
150A	32.6067	-86.022	01/18/12	08/09/13	133	4
151A	32.5269	-85.3267	01/19/12	08/09/13	109	3
248A	32.094	-87.7393	04/08/11	01/25/13	73	1
249A	31.9752	-87.1225	01/21/12	08/10/13	138	0
250A	31.978	-86.268	12/16/13	OPEN	42	2
250A-V	31.9778	-86.2677	01/22/12	12/16/13	170	10
251A	32.0929	-85.409	01/24/12	08/09/13	154	6
347A	31.4017	-88.5412	03/19/11	12/15/12	32	0
348A	31.4129	-87.9023	03/20/11	01/25/13	67	0
349A	31.3504	-87.1924	01/20/12	08/10/13	138	1
350A	31.4207	-86.3353	01/21/12	08/14/13	137	2
351A	31.2753	-85.6036	02/02/12	08/15/13	56	0
BRAL	31.169	-87.051	05/02/11	OPEN	11	3
S1AL	31.037	-87.21	03/26/19	07/29/19	3	2
S1FL	30.941	-87.2	03/26/19	07/29/19	3	3
S2AL	31.008	-87.225	03/26/19	07/29/19	3	2
S2FL	30.982	-87.145	03/26/19	07/29/19	3	2
448A	30.9309	-87.8608	04/07/11	41376	20	1

5.2.1 V_{SZ} Estimations

Approximately 40% of the study stations have at least five seismic records successfully used with the P-wave seismogram method (Figure 5-1). Y49A station has significantly more estimates (60) than the other stations, while 14 stations have one estimation of V_{SZ}. Median values for the stations range from approximately 287m/s at Z47B station to 3,468 m/s at X49A station. The variability in V_{SZ} is small for some stations, while it is quite large for others. For example, X47A station V_{SZ} estimates are as low as 925 m/s and high as 4,279 m/s, while for Z47B station, V_{SZ} estimates range from 263 m/s to 382 m/s. Kim et al. (2016) suggested that the depth of the profile over which V_{SZ} is averaged could be estimated using the relationship $z = 0.1*V_{SZ}$ to provide an idea of the depth of the profiles. According to this relationship, the stations located in the southern part of the state had V_{SZ} profiles with depths smaller than 100m, while the other stations had depths up to 300-400 m.

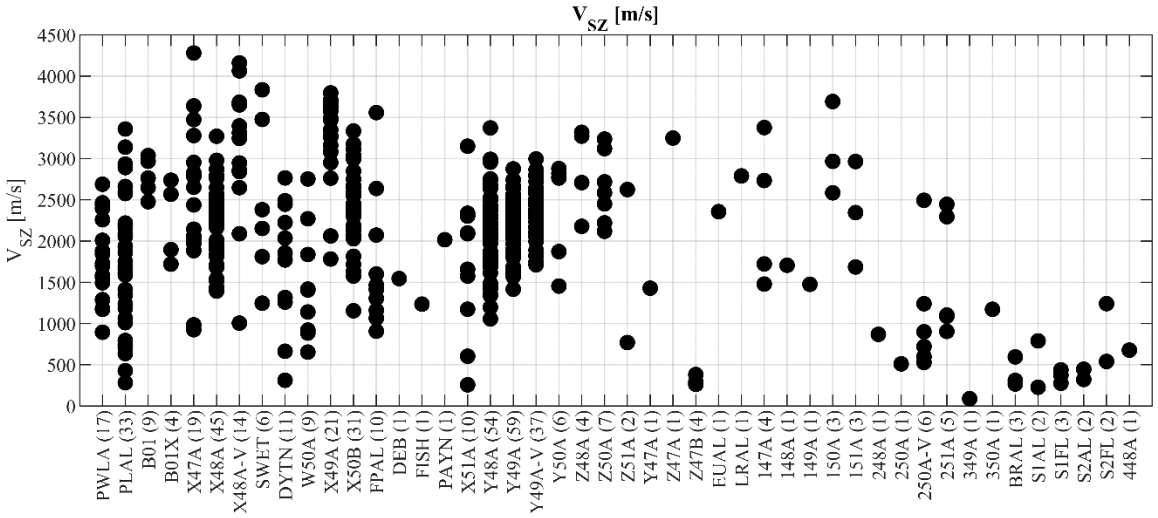

Figure 5-1: V_{SZ} values for the 46 seismic stations using the P-wave seismogram method. Labels indicate seismic identification, and the number in parenthesis is the number of events estimated.

5.2.2 V_{S30} Estimations

The equations proposed by Kim et al. (2016) were used to estimate V_{S30} values. The V_{SZ} correlation was successfully applied to 22 seismic stations with a total of 149 seismic records (Figure 5-2). The V_{SZ} correlation was limited to records with an average depth ($z = 0.1*V_{SZ}$) less than 200 m, based on the recommendations of Kim et al. (2016). Therefore, no estimate of V_{S30} was acquired using V_{SZ} correlation when the depth of the V_{SZ} was larger than 200 m. The amplitude ratio correlation was successfully applied to 444 seismic records from 37 stations (Figure 5-3). The amplitude ratio correlation did not use V_{SZ} and was not subject to the same limitations. Stations with only one usable record or with two records where V_{S30} estimates varied by more than 50% were not used in this study and are not shown in Figure 5-2 and 5.3 as the box and whisker plot is not meaningful for these sites.

The estimates of V_{S30} using V_{SZ} correlations are generally higher and have more scatter than the estimates from amplitude ratio correlation. This is especially true for stations located in the northern part of the study area (SA and CT crustal regions). The median estimates for many of

these stations would have been even higher had the average depth cutoff not been applied. Median V_{S30} values greater than 1,500 m/s also do not seem realistic for the geologic units in the study area, which consist primarily of metamorphic and sedimentary profiles. Based on this comparison, the amplitude ratio correlation appears to be more reasonable. Therefore, the median V_{S30} and 25th and 75th percentiles using the amplitude ratio correlation for each site are shown at the end of this section (Table 5-2) and will be used for further comparison.

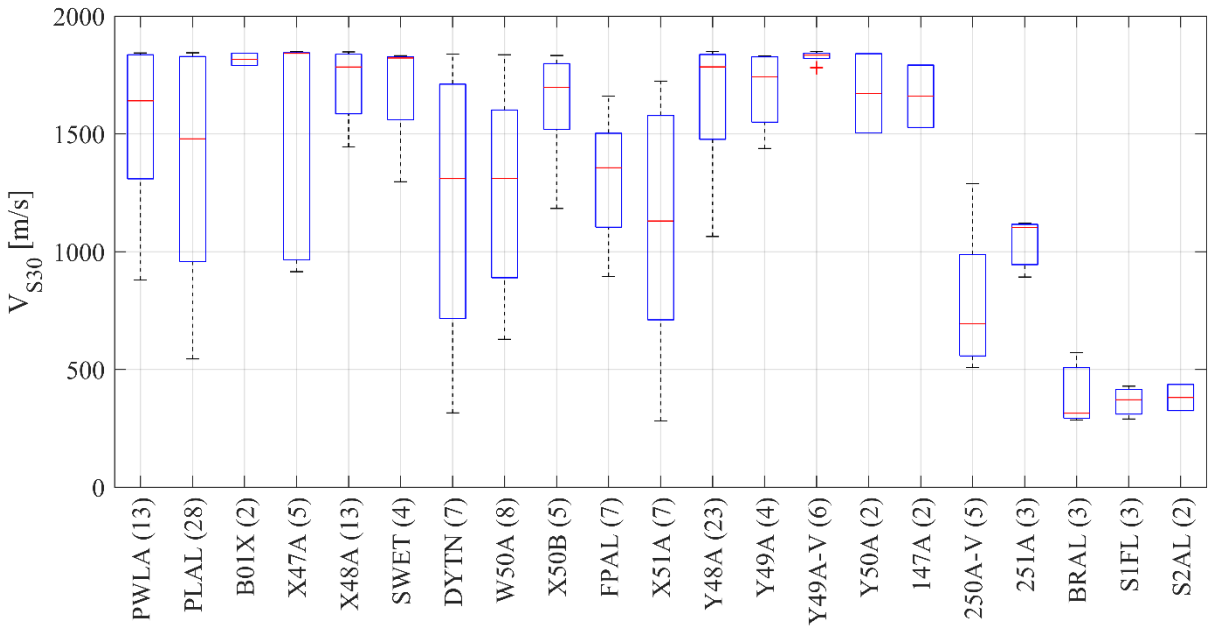

Figure 5-2: V_{S30} values computed using V_{SZ} correlation. Minimum and maximum values for a station are shown as the extremes of dashed lines, and the 25th and 75th percentiles are the lower and upper values within the box plot. Median values are shown as a red horizontal line within the box.

The results acquired using amplitude ratio correlation were geographically plotted in the Alabama map, as shown in Figure 5-4. Generally, the median values of V_{S30} tend to decrease as the stations are located near the south of the state. The highest values of V_{S30} are concentrated in the CT and SA regions, except for the stations W50A and PLAL. The lower values of V_{S30} are

founded in the GC region except for stations 147A and 150A. Station 150A belongs to the GC regions, but it is very close to the transition of crustal models.

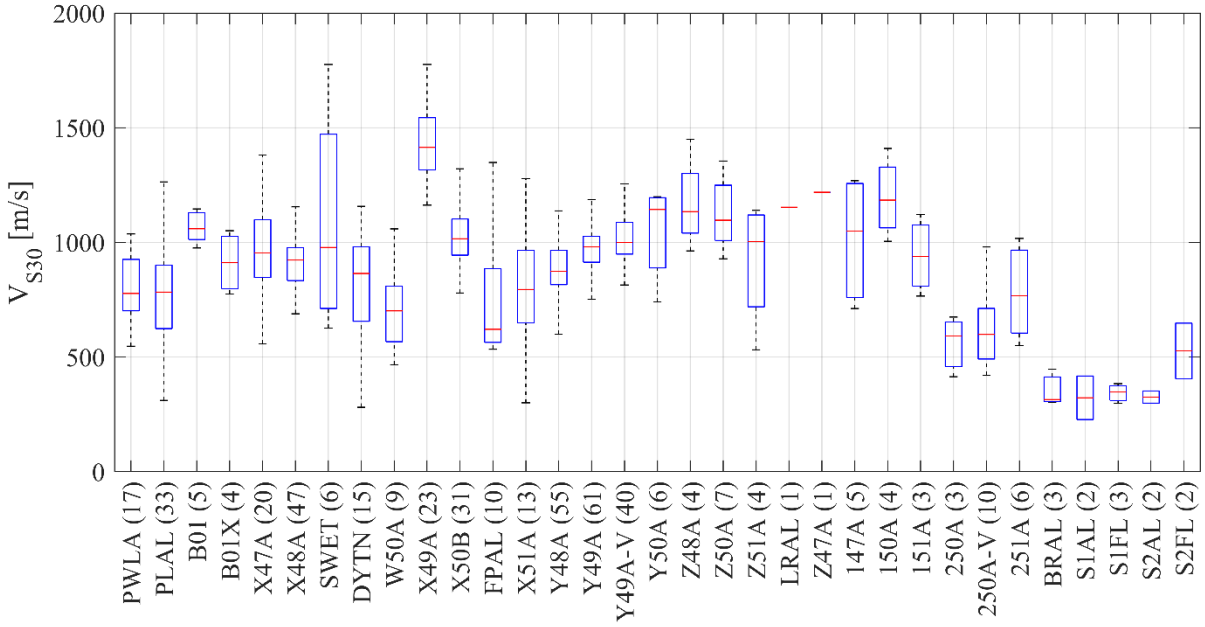

Figure 5-3: V_{S30} values computed using amplitude ratio correlation. Minimum and maximum values for a station are shown as the extremes of dashed lines, and the 25th and 75th percentiles are the lower and upper values within the box plot. Median values are shown as a red horizontal line within the box.

Table 5-2: Summary of V_{S30} estimates using P-wave seismogram method with the amplitude ratio correlation, 25th and 75th percentiles, and the crustal region for each site in the study.

Station/ Site	Crustal Region[a]	*25th Per.* V_{S30} (m/s)	*75th Per.* V_{S30} (m/s)	*Median* V_{S30} (m/s)	*Coeff of Variation*
PWLA	CT	701	926	777	18%
PLAL	CT	624	900	783	33%
B01	CT	1012	1129	1059	7%
B01X	CT	798	1026	911	15%
X47A	CT	847	1098	954	28%
X48A	CT	833	977	922	13%
X48A-V	CT	1039	1295	1218	30%
SWET	SA	712	1472	978	40%
DYTN	SA	656	981	864	42%
W50A	SA	567	808	701	26%
X49A	SA	1315	1544	1414	19%
X50B	SA	944	1102	1016	17%
FPAL	SA	564	885	621	32%
X51A	SA	648	966	836	42%
Y48A	SA	815	966	874	15%
Y49A	SA	914	1026	980	10%
Y49A-V	SA	948	1088	999	10%
Y50A	SA	888	1195	1143	20%
Z48A	SA	1040	1300	1134	17%
Z50A	SA	1008	1249	1097	14%
Z51A	SA	719	1119	1003	35%
Y47A	GC	402	697	549	39%
Z47B	GC	288	325	300	10%
147A	GC	759	1257	1049	27%
150A	GC	1063	1328	1184	14%
151A	GC	809	1075	939	19%
250A	GC	458	653	591	25%
250A-V	GC	491	712	598	26%
251A	GC	604	966	767	28%
350A	GC	629	935	782	28%
BRAL	GC	305	413	315	21%
S1AL	GC	227	418	322	43%
S1FL	GC	310	375	347	13%
S2AL	GC	299	352	326	11%
S2FL	GC	405	647	526	33%

[a] CT: Central Tennessee, SA: South Appalachian, GC: Gulf Coast (Figure 3-6)

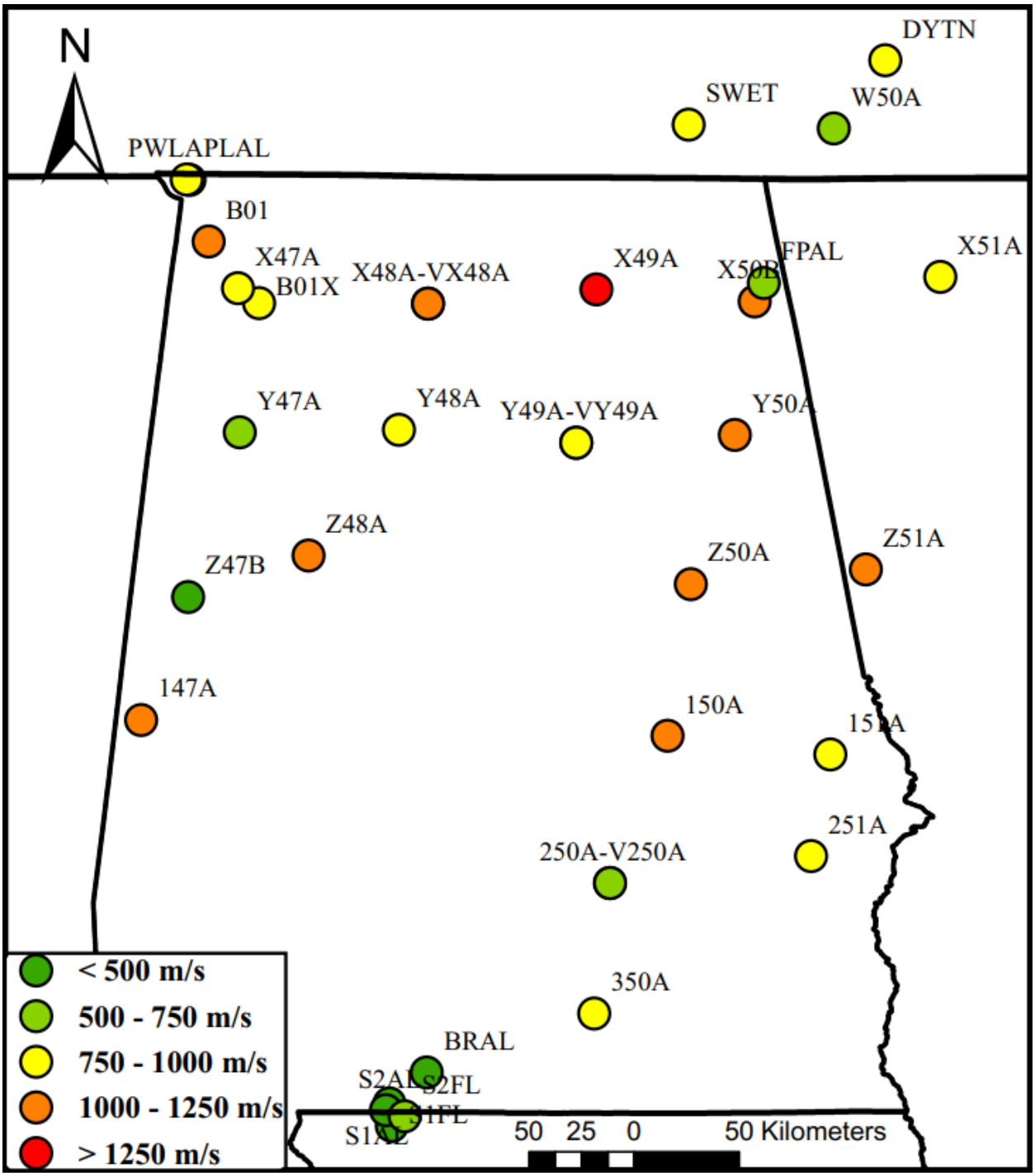

Figure 5-4: Map of V_{S30} estimates for seismic stations in this study using the amplitude ratio correlation.

5.2.3 Sensitivity Analysis of V_{SZ} Estimations

The computation of V_{SZ} through the P-wave seismogram method required parameters such as the hypocenter location of the earthquake, which is associated with horizontal and vertical uncertainty in its determination. To analyze the effect of this uncertainty on the computation of V_{SZ}, the earthquake catalogs from the CERI website were acquired with the standard horizontal and vertical error specified for each event. The uncertainty associated with the events was applied to recompute the values V_{SZ}. Four cases were analyzed to observe the variability of V_{SZ} estimations. Cases A and B studied the horizontal uncertainty by adding and subtracting the standard error provided by the catalog. Cases C and D studied the vertical uncertainty using the same approach. The values computed for all the cases are summarized in Table 5-3. For cases A and B, a variation of less than a 1% was generally computed in the stations analyzed. In general, cases C and D calculated variabilities lower than 4%. The stations with larger variability in the re-computations of V_{SZ} were caused by the lack of events available for those stations and the significant uncertainty of those events. This is the case of station DEB, FISH, and PAYN, with only one event available. These stations had 25.9% and 30% uncertainty for horizontal and vertical, respectively.

A fundamental parameter in the V_{SZ} calculation is the crustal model selected for the computations. Two approaches were investigated in cases E and F to analyze the uncertainty of the crustal model selected. First, Kim et al. (2016) proposed a reduction of 14% of the V_{P2} value used to compute V_{SZ}, to remove bias in the residual computation. This reduction is suggested for CENA stations where no measurement of V_S is available. The suggestion was applied to the calculations of V_{SZ} (case E), lowering the results in a range of 13.4% to 16.9% from the original computations. The maximum variation of 19.7% was reported in station EUAL with only one event. The second approach (case F) considered uncertainty in the crustal model used for the

calculations of V_{SZ}. In some cases, the earthquake was generated in a different crustal model than the station, so it is unclear which crustal model should be used for the calculations. The crustal models of Central Tennessee were exchanged with the Southern Appalachian to observe the variation in the V_{SZ} estimations. The uncertainty generated by the change in the crustal model ranged from -10% to -5% in Central Tennessee stations and 6% to 16% for Southern Appalachian stations.

Table 5-3: Summary of V_{SZ} variation for cases A through F.

Station	Case A	Case B	Case C	Case D	Case E	Case F
PWLA	0.00%	0.00%	0.69%	-1.47%	-14.12%	-9.35%
PLAL	0.00%	0.00%	0.52%	-1.24%	-14.35%	-9.67%
B01	0.00%	0.00%	0.00%	0.00%	-14.12%	-10.65%
B01X	0.00%	0.00%	0.01%	-0.01%	-14.12%	-9.69%
X47A	0.00%	0.00%	0.56%	-0.02%	-14.12%	-9.43%
X48A	-0.01%	0.01%	0.08%	-0.07%	-14.29%	-10.17%
X48A-V	-0.07%	0.07%	0.40%	-0.36%	-14.57%	-5.39%
SWET	-0.17%	0.19%	2.15%	-2.00%	-15.11%	10.77%
DYTN	-1.58%	0.24%	1.11%	-1.92%	-15.83%	10.77%
W50A	-0.64%	0.26%	0.75%	-1.34%	-15.99%	8.17%
X49A	-0.02%	0.02%	0.45%	-4.22%	-15.39%	9.87%
X50B	-0.06%	0.06%	2.07%	-1.94%	-15.85%	9.46%
FPAL	-1.91%	0.49%	2.54%	-2.77%	-15.51%	9.91%
DEB	-3.08%	12.10%	17.16%	-13.20%	-13.44%	13.86%
FISH	-16.97%	31.67%	30.96%	-22.14%	-16.90%	6.14%
PAYN	-6.63%	21.98%	24.31%	-18.45%	-14.83%	16.68%
X51A	-0.01%	0.01%	0.86%	-0.20%	-14.85%	9.31%
Y48A	0.00%	0.00%	3.51%	-14.94%	-14.67%	10.00%
Y49A	0.00%	0.00%	0.59%	-0.35%	-14.67%	10.80%
Y49A-V	0.00%	0.00%	1.10%	-1.80%	-15.63%	9.33%
Y50A	0.00%	0.00%	0.40%	-0.46%	-16.11%	8.02%
Z48A	0.00%	0.00%	3.31%	-	-13.53%	14.95%
Z51A	0.00%	0.00%	0.24%	-0.29%	-14.68%	9.82%
LRAL	-0.01%	0.01%	0.28%	-0.33%	-14.68%	9.82%
Y47A	0.00%	0.00%	0.78%	-0.10%	-15.71%	0.00%
Z47B	-0.38%	0.42%	0.38%	-0.14%	-15.75%	0.00%
EUAL	-29.21%	38.33%	0.71%	-0.71%	-19.77%	0.00%
250A	0.00%	0.00%	0.02%	-0.01%	-16.15%	0.00%
251A	0.00%	0.00%	0.08%	-0.02%	-16.15%	0.00%

These results demonstrate the importance of the crustal model in estimating V_{SZ} values, whereas the uncertainty in estimates due to the hypocenter location was small. Selecting a single crustal model for a station is not straightforward, mainly when earthquakes may be located a long distance from the site. Uncertainties of $\pm$10-20% should be considered to account for this uncertainty in the crustal model.

5.2.4 Sensitivity Analysis of Amplitude Ratio Correlation

The measured V_{S30} and ratios from the 31 stations selected by Kim et al. (2016) for 106 earthquake ground motions are shown in Figure 5-5. The dashed lines in the figure indicate the 95% confidence interval. The regression fit for the data is shown in the equation 5.1 and is very close to the one presented in the study of Kim et al. (2016).

$$\log V_{S30} = 0.4796 \ln\left(\dot{U}_R / \dot{U}_Z\right) + 6.9750 \qquad 5.1$$

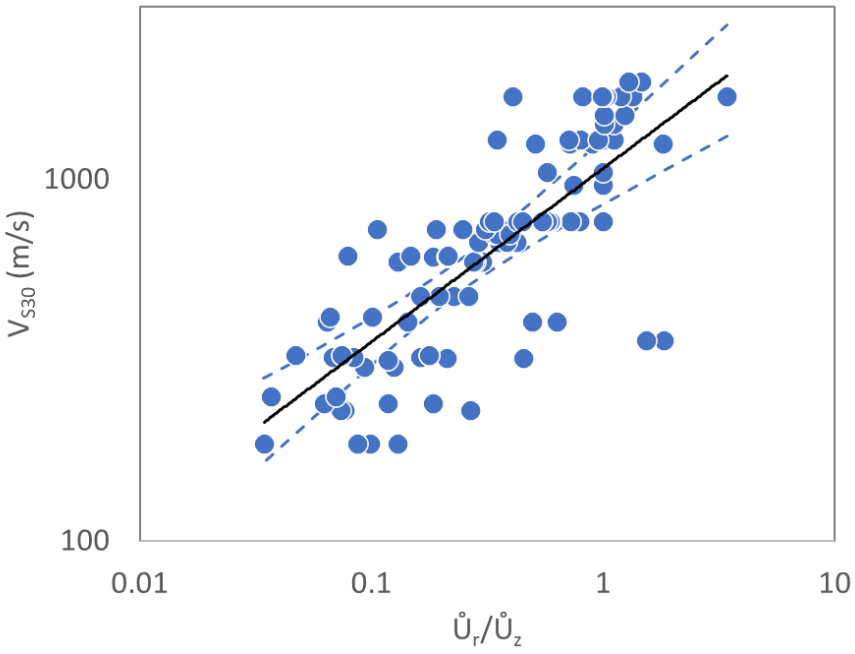

Figure 5-5: Empirical correlation between measured V_{S30} and the amplitude ratio (Kim et al. 2016) with a 95% confidence interval for the correlation shown by the dashed lines.

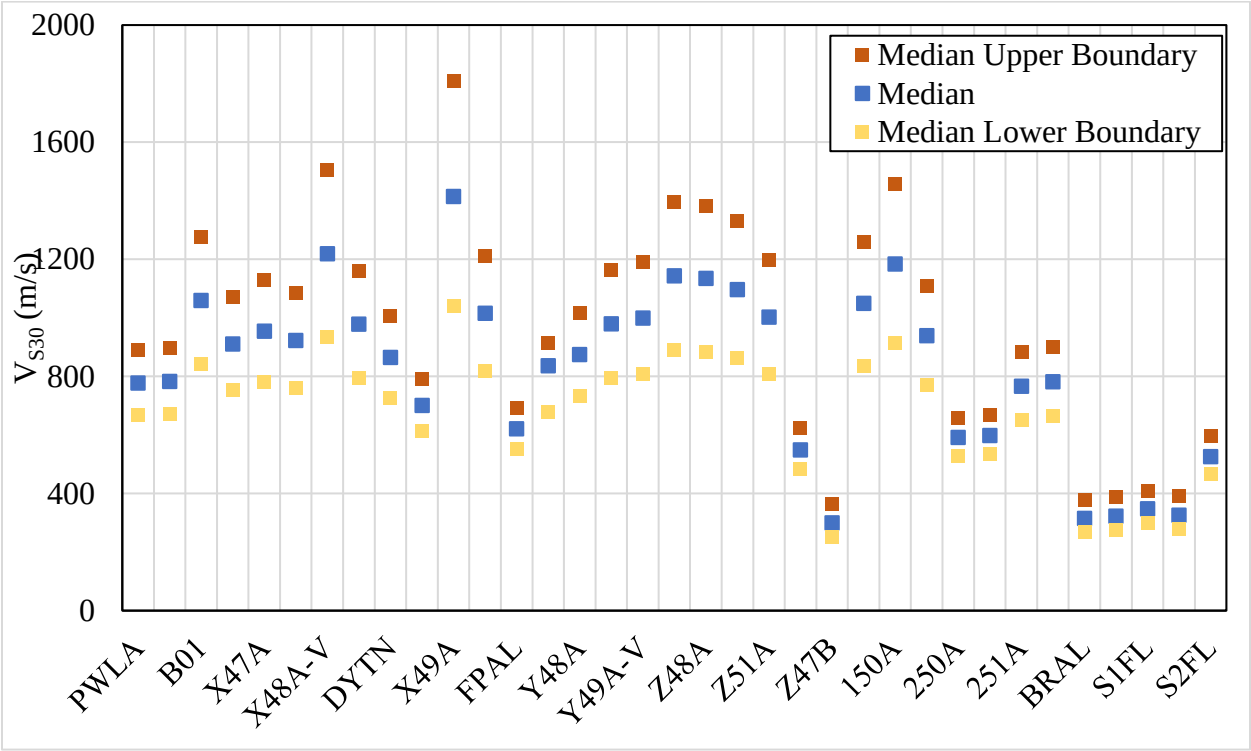

Figure 5-6: P-wave seismogram amplitude ratio correlation using lower and upper confidence intervals.

Table 5-4: Summary of V_{S30} estimates using P-wave seismogram method with the amplitude ratio correlation, 25th and 75th percentiles, for the upper and lower 95% confidence interval

Station	P-wave Lower Boundary			P-wave Upper Boundary		
	Median V_{S30} (m/s)	**25th Per. V_{S30} (m/s)**	**75th Per. V_{S30} (m/s)**	**Median V_{S30} (m/s)**	**25th Per. V_{S30} (m/s)**	**75th Per. V_{S30} (m/s)**
PWLA	667	612	762	889	792	1,088
PLAL	671	556	748	897	697	1,053
B01	842	816	881	1,275	1,208	1,375
B01X	752	681	823	1,070	917	1,227
X47A	780	713	863	1,128	981	1,332
X48A	761	704	794	1,084	964	1,158
X48A-V	935	831	975	1,507	1,246	1,622
SWET	795	620	1,074	1,160	805	1,900
DYTN	725	578	797	1,005	736	1,165
W50A	612	509	688	792	631	930
X49A	1,042	986	1,109	1,808	1,653	2,013
X50B	819	774	865	1,212	1,115	1,337
FPAL	553	508	739	693	627	1,032
X51A	679	576	787	913	726	1,143
Y48A	731	692	787	1,018	942	1,144
Y49A	796	755	824	1,163	1,072	1,227
Y49A-V	808	776	857	1,189	1,121	1,318
Y50A	890	741	920	1,397	1,036	1,472
Z48A	884	830	978	1,383	1,249	1,636
Z50A	862	813	949	1,330	1,202	1,555
Z51A	808	616	875	1,198	827	1,362
Y47A	482	355	609	624	462	786
Z47B	252	240	278	366	355	390
147A	836	654	955	1,260	866	1,567
150A	913	844	994	1,458	1,281	1,676
151A	770	687	850	1,108	932	1,299
250A	529	408	578	659	520	733
250A-V	536	444	620	668	549	805
251A	653	539	787	884	674	1,144
350A	664	559	768	902	702	1,102
BRAL	267	257	367	380	371	474
S1AL	276	181	371	388	299	477
S1FL	300	262	328	410	376	436
S2AL	278	251	305	390	365	415
S2FL	466	358	575	595	465	725

5.3 HORIZONTAL TO VERTICAL SPECTRAL RATIO (HVSR)

The HVSR method was applied to 32 stations that were selected because they also have data from the P-wave seismogram method that could be used. After the HVSR curves were generated, the criteria for reliable and clear HVSR curves (Figure 2-17) proposed by SESAME (2004) were applied to classify the stations. The results of each criterion applied to the station are shown in Table 5-5. All of the reliability criteria needed to be met to have a reliable HVSR curve, but only five of the six clarity criteria need to be achieved to have a clear peak. A reliable HVSR curve was displayed in 27 of the seismic stations, 21 of them showed a clear HVSR peak, and 16 of the stations met both requirements. Only stations with clear and reliable curves were considered in this study. Curves for all of the sites are provided in Appendix C.

The fundamental frequency, the peak amplification, and the respective standard deviations of the stations with reliable and clear HVSR curves are shown in Table 5-6. The fundamental frequencies of the stations range from 0.18 Hz at stations S1FL and S2AL to 23 Hz at station B01X. This range is expected as S1FL is in the coastal plain where very deep sediments are expected, while B01X has very shallow rock. The standard deviation for the fundamental frequency varies from 1.01 Hz to 1.1 Hz in S1AL and S1FL, respectively. The maximum amplification values for the stations range from 2.28 in station 147A to 6.67 in station Z50A. The standard deviation for the maximum amplification ranges from 1.07 at station X48A to 1.473 at S1AL station.

Table 5-5: Reliability and clarity criteria applied to the HVSR curves from the seismic stations

	Station	RELIABILITY			CLARITY						RELIABLE	CLEAR
		C1	C2	C3	C1	C2	C3	C4	C5	C6		
Reliable HVSR Curve and Clear Peak	B01	✓	✓	✓	✓	✓	✓	✓		✓	✓	✓
	B01X	✓	✓	✓	✓	✓	✓	✓		✓	✓	✓
	X48A	✓	✓	✓	✓	✓	✓	✓	✓	✓	✓	✓
	X50B	✓	✓	✓	✓	✓	✓	✓		✓	✓	✓
	Y50A	✓	✓	✓	✓	✓	✓	✓	✓		✓	✓
	Z50A	✓	✓	✓	✓	✓	✓	✓	✓	✓	✓	✓
	Y47A	✓	✓	✓	✓	✓	✓	✓		✓	✓	✓
	Z47B	✓	✓	✓	✓	✓	✓	✓	✓	✓	✓	✓
	147A	✓	✓	✓	✓	✓	✓		✓	✓	✓	✓
	150A	✓	✓	✓	✓	✓	✓	✓	✓	✓	✓	✓
	151A	✓	✓	✓	✓	✓	✓	✓	✓	✓	✓	✓
	250A	✓	✓	✓	✓	✓	✓	✓	✓	✓	✓	✓
	250A-V	✓	✓	✓	✓	✓	✓		✓	✓	✓	✓
	251A	✓	✓	✓	✓	✓	✓	✓	✓	✓	✓	✓
	S1FL	✓	✓	✓	✓	✓	✓	✓	✓	✓	✓	✓
	S2AL	✓	✓	✓	✓	✓	✓	✓	✓	✓	✓	✓
	PWLA	✓	✓	✓	✓	✓			✓	✓	✓	
	PLAL	✓	✓	✓	✓	✓	✓			✓	✓	
	SWET	✓	✓	✓	✓	✓				✓	✓	
	W50A	✓	✓	✓	✓	✓				✓	✓	
	X51A	✓	✓	✓	✓	✓				✓	✓	
	Y49A	✓	✓	✓	✓	✓				✓	✓	
	Y49A-V	✓	✓	✓	✓	✓		✓		✓	✓	
	Z51A	✓	✓	✓	✓	✓				✓	✓	
	350A	✓	✓	✓	✓	✓	✓			✓	✓	
	S1AL	✓	✓	✓	✓	✓				✓	✓	
	S2FL	✓	✓	✓	✓	✓		✓		✓	✓	
	X47A	✓	✓		✓	✓	✓	✓	✓			✓
	X48A-V	✓	✓		✓	✓	✓	✓	✓	✓		✓
	X49A	✓	✓		✓	✓	✓	✓	✓			✓
	Y48A	✓	✓		✓	✓	✓	✓	✓	✓		✓
	Z48A	✓	✓		✓	✓	✓	✓		✓		✓

Table 5-6: Summary of frequency peak, amplification peak, and standard deviation for the HVSR curves of the seismic stations

Station	f_{peak} (Hz)	Std f_{peak}(Hz)	A_{peak}	Std A_{peak}
B01	5.652	1.041	5.355	1.253
B01X	23.809	1.044	2.855	1.392
X48A	11.339	1.013	5.957	1.074
X50B	7.162	1.040	3.603	1.203
Y50A	2.281	1.015	5.316	1.302
Z50A	4.083	1.012	6.668	1.145
Y47A	3.684	1.025	4.624	1.133
Z47B	0.616	1.046	3.178	1.225
147A	0.267	1.055	2.285	1.347
150A	5.933	1.012	6.372	1.107
151A	1.933	1.014	5.892	1.169
250A	0.265	1.033	3.502	1.354
250A-V	0.250	1.045	4.646	1.364
251A	0.317	1.042	4.168	1.367
S1FL	0.183	1.104	2.422	1.522
S2AL	0.183	1.076	2.362	1.473

5.3.1 Correlations of F_0 with V_{S30}

The stations that showed a reliable curve and a clear peak were selected to compute V_{S30} estimates using correlations. The correlations used to estimate V_{S30} shown in Table 5-7 are based on the proposed correlations by: Ghofrani & Atkinson (2014), Hassani & Atkinson (2016), and Stanko & Markušić (2020). The correlation proposed by Ghofrani & Atkinson (2014) used the equation 2.13 considering f_{peak} and A_{peak}. This correlation could not be applied to the stations with a fundamental frequency lower than 1 Hz. The lower estimations are calculated using the correlation proposed by Stanko & Markušić (2020), and the highest values are acquired using Hassani & Atkinson (2016).

The V_{S30} estimations varied from 208 m/s using Stanko & Markušić (2020) at several stations with frequencies under 2 Hz, to 1,167m/s with Hassani & Atkinson (2016) at station

B01X. The best correlation agreement is shown at station Y47A, with an average velocity of 367 m/s. The greatest correlation difference is for station B01X, with almost 570 m/s in difference.

Table 5-7: V_{S30} results from HVSR correlations

Station	V_{S30} (m/s)		
	HVSR1 Ghofrani & Atkinson (2014)	**HVSR2 Hassani & Atkinson (2016)**	**HVSR3 Stanko & Markušić (2020)**
B01	359.74	471.94	462.54
B01X	620.07	1,167.75	600.00
X48A	381.27	731.77	600.00
X50B	455.48	547.88	515.77
Y50A	312.27	266.46	304.70
Z50A	306.03	384.49	398.26
Y47A	361.49	360.40	379.88
Z47B	-	250.00	208.00
147A	-	250.00	208.00
150A	332.35	486.58	472.97
151A	288.86	250.00	282.37
250A	-	250.00	208.00
250A-V	-	250.00	208.00
251A	-	250.00	208.00
S1FL	-	250.00	208.00
S2AL	-	250.00	208.00

5.4 RAYLEIGH WAVE ELLIPTICITY

The R-wave ellipticity was computed for all the stations that meet the reliable curve and clear peak criteria proposed by SESAME (2004) (Figure 2-17). Station S1AL did not meet the requirements; however, it was possible to access the site of the station and take direct measurements, so it was included in this section. The results of the R-wave ellipticity curves are shown in Appendix D.

5.4.1 Joint Inversion of Ellipticity Curve and MASW

A joint inversion was performed at the stations where MASW measurements could be taken. The joint inversion was achieved using the dispersion curve acquired from MASW and the R-wave ellipticity curve. The R-wave ellipticity curve was used entirely for some stations, and for others, a fragment of the curve was used. This section presents the result for each seismic station using the inversion that showed the lowest misfit. Over 100,000 models were generated for the inversion to develop a wide range of acceptable models. However, only the 5,000 models with the lowest misfit were plotted and analyzed.

X50B Seismic Station

The V_S profiles, the dispersion curves, and the R-wave ellipticity curve are shown in Figure 5-7 for 5,000 of the profiles generated with the lowest misfit. The V_S profile with the lowest misfit is shown in black. The field dispersion curve from MASW and the R-wave ellipticity curve from ambient noise are shown in dark gray. The corresponding curves from each profile are colored according to their misfit value. The V_S profiles show relatively consistent results. For this seismic station, a four-layer profile was selected to represent better the conditions of the site. The fourth layer of the model is not shown in the image because the transition to the stiffer layer occurs over 30 m. The shallow layer showed velocities around 626 m/s until 1.5 m depth. The second layer had velocities around 840 m/s between 1.5 and 15.5 m. The third layer showed velocities around 1,776 m/s. Then, the V_S profile transitions to a stiffer layer at approximately 37 m, with velocity values of about 1,900 m/s. The V_{S30} for this site was computed with a median value of 964 m/s and a standard deviation of 21.2m/s. The joint inversion of the R-wave ellipticity curve and MASW provides very similar results to MASW. The V_{S30} value from joint inversion is 2.2% higher than the MASW and the standard deviation increased for the joint inversion.

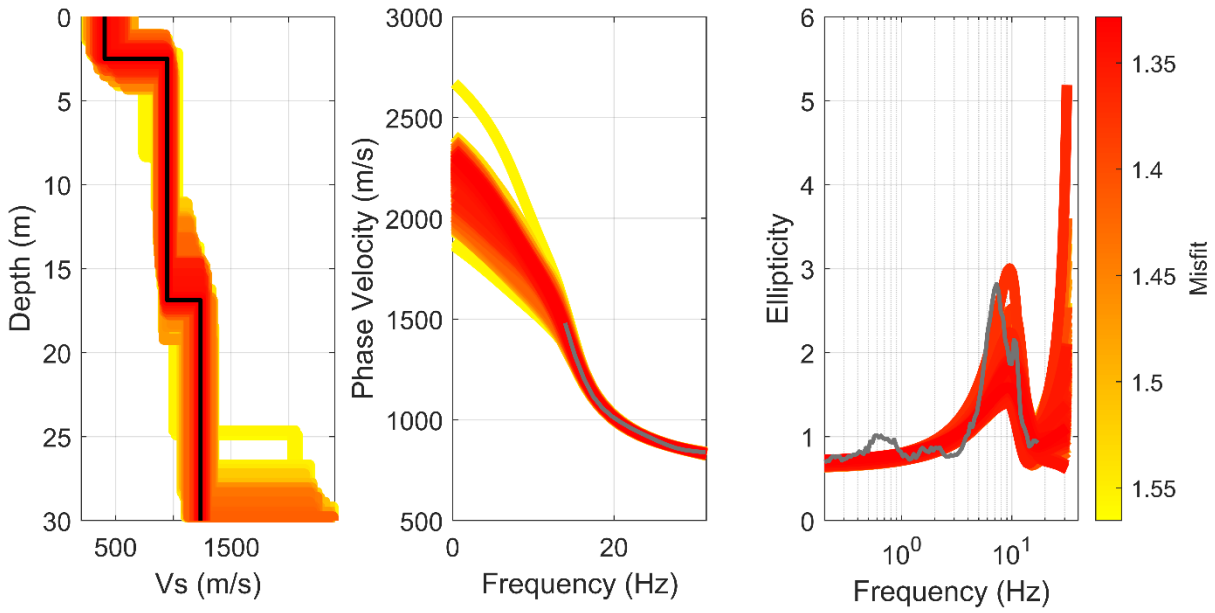

Figure 5-7: V_S profile computed using joint inversion (left), dispersion curve (middle), and R-wave ellipticity (right) for seismic station X50B. The V_S profile with the best fit is shown in black. The dispersion curve from the field and the R-wave ellipticity curve are shown in dark gray.

S1AL Seismic Station

The V_S profiles, the dispersion curves, and the R-wave ellipticity curve are shown in Figure 5-8 for 5,000 of the profiles generated with the lowest misfit. The V_S profile with the lowest misfit is shown in black. The field dispersion curve from MASW and the R-wave ellipticity curve from ambient noise are shown in dark gray. The corresponding curves from each profile are colored according to their misfit value. The V_S profiles show relatively consistent results. Fragments of the curve were extracted to compute this inversion; however, it did not improve the results computed by the models. Then, the entire R-wave ellipticity curve was selected for this inversion, even though there is no good agreement between the R-wave ellipticity curve measured from ambient noise and the ones generated for the model. The V_S profiles show relatively consistent results. For this seismic station, a two-layer profile was selected to better represent the conditions of the site. The shallow layer showed velocities around 282 m/s until 14.5 m depth. The second layer had

velocities around 431 m/s. The V_{S30} for this site was computed with a median value of 340 m/s and a standard deviation of 1.8 m/s. The joint inversion of the R-wave ellipticity curve and MASW provides very similar results to MASW. The V_{S30} value from joint inversion is 7% higher than the MASW and the standard deviation increased for the joint inversion.

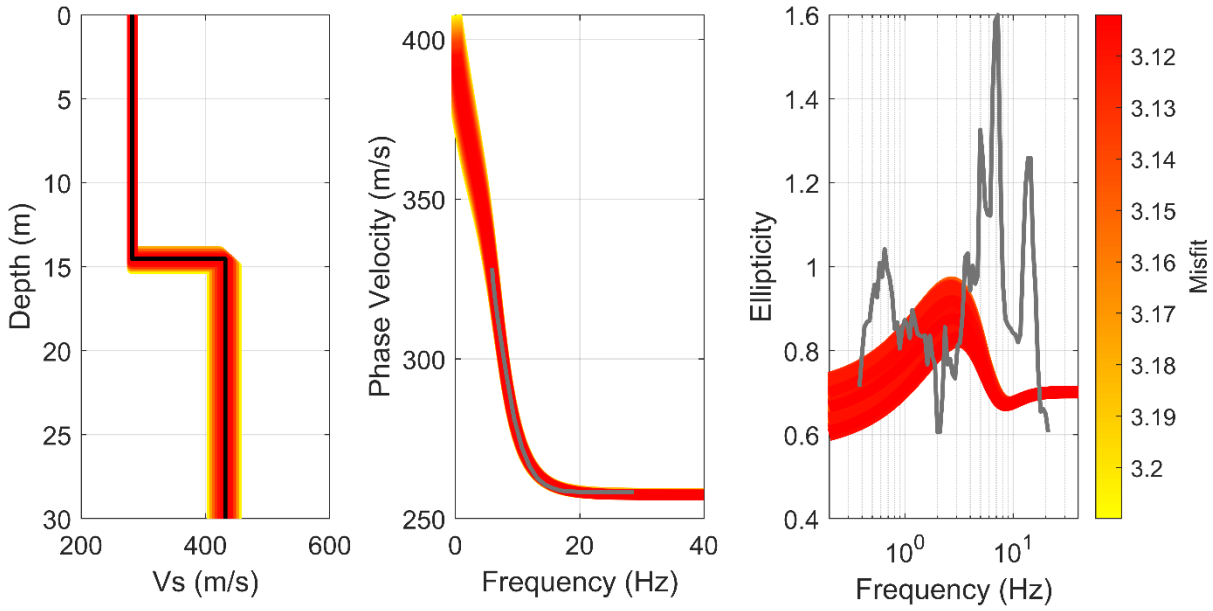

Figure 5-8: V_S profile computed using joint inversion (left), dispersion curve (middle), and R-wave ellipticity (right) for seismic station S1AL. The V_S profile with the best fit is shown in black. The dispersion curve from the field and the R-wave ellipticity curve are shown in dark gray.

S2AL Seismic Station

The V_S profiles, the dispersion curves, and the R-wave ellipticity curve are shown in Figure 5-9 for 5,000 of the profiles generated with the lowest misfit. The V_S profile with the lowest misfit is shown in black. The field dispersion curve from MASW and the R-wave ellipticity curve from ambient noise are shown in dark gray. The corresponding curves from each profile are colored according to their misfit value. Fragments of the curve were extracted to compute this inversion; however, it did not improve results related to the R-wave ellipticity and made worst the agreement

between the dispersion curve from the field and the ones computed by the models. Then, the entire R-wave ellipticity curve was selected for this inversion, even though there is no good agreement between the R-wave ellipticity curve measured from ambient noise and the ones generated for the model. For this seismic station, a two-layer profile was selected to better represent the conditions of the site. The V_S profiles show relatively consistent results. The shallow layer showed velocities around 240 m/s until 10 m depth. The second layer had velocities around 467 m/s. The V_{S30} for this site was computed with a median value of 354 m/s and a standard deviation of 3.3 m/s. The joint inversion of the R-wave ellipticity curve and MASW provides very similar results to MASW. The V_{S30} value from joint inversion is 0.8% lower than the MASW and the standard deviation increased for the joint inversion.

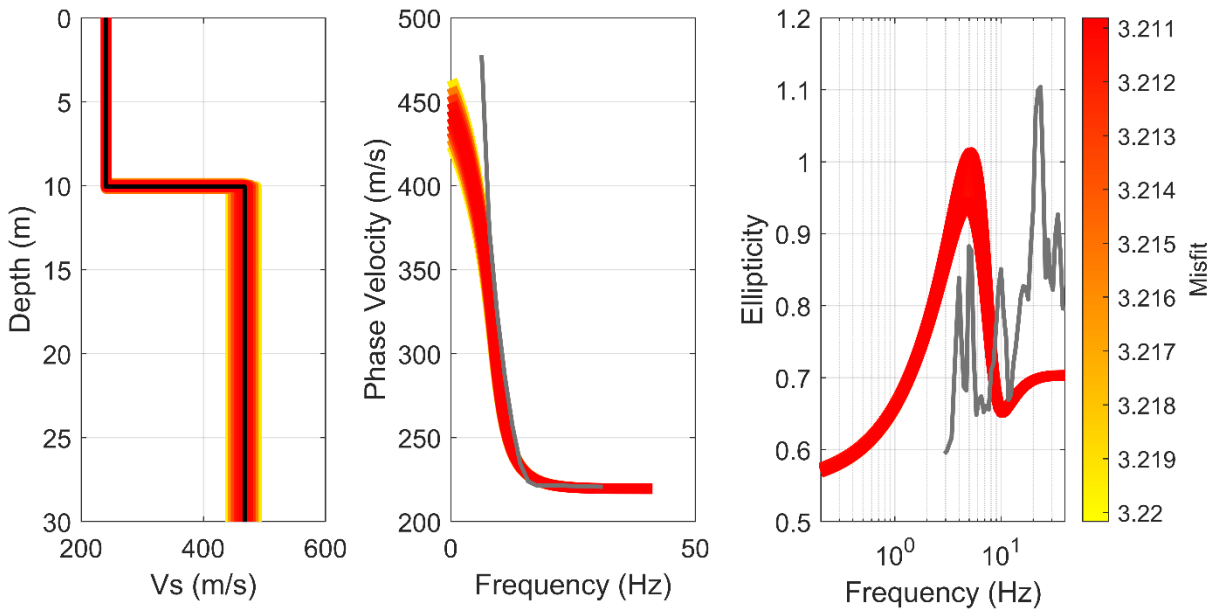

Figure 5-9: V_S profile computed using joint inversion (left), dispersion curve (middle), and R-wave ellipticity (right) for seismic station S2AL. The V_S profile with the best fit is shown in black. The dispersion curve from the field and the R-wave ellipticity curve are shown in dark gray.

Y47A Seismic Station

The V_S profiles, the dispersion curves, and the R-wave ellipticity curve are shown in Figure 5-10 for 5,000 of the profiles generated with the lowest misfit. The V_S profile with the lowest misfit is shown in black. The field dispersion curve from MASW and the R-wave ellipticity curve from ambient noise are shown in dark gray. The corresponding curves from each profile are colored according to their misfit value. A subset of the R-wave ellipticity curve where the peak is located was used to generate the inversion. This fragment of the R-wave ellipticity curve selected showed better agreement between the curve measured from ambient noise and the ones generated for the model.

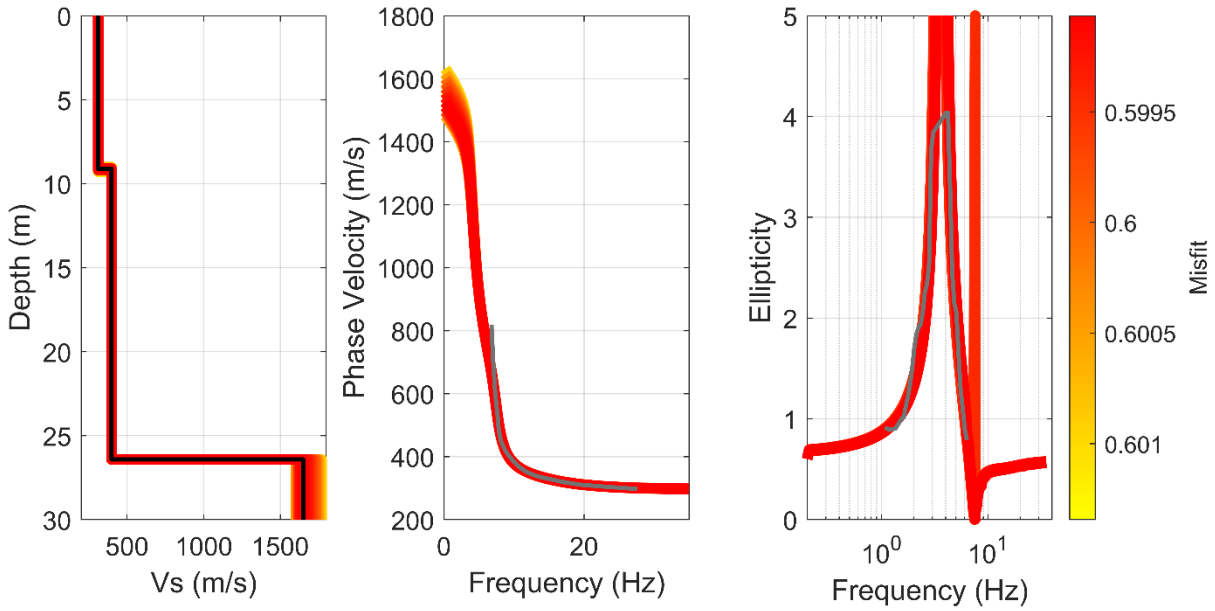

Figure 5-10: V_S profile computed using joint inversion (left), dispersion curve (middle), and R-wave ellipticity (right) for seismic station Y47A. The V_S profile with the best fit is shown in black. The dispersion curve from the field and the R-wave ellipticity curve are shown in dark gray.

The V_S profiles show relatively consistent results. For this seismic station, a three-layer profile was selected to represent better the conditions of the site. The shallow layer showed

velocities around 311 m/s until 9.1 m depth. The second layer had a slight increment in velocity, reaching 398 m/s until 26.4 m depth. The third layer showed a stiffer layer with velocities of 1,650 m/s The V_{S30} for this site was computed with a median value of 401 m/s and a standard deviation of 0.2 m/s. The joint inversion of the R-wave ellipticity curve and MASW provides very similar results to MASW. The V_{S30} value from joint inversion is 5.6% lower than the MASW and the standard deviation increased for the joint inversion.

X48A Seismic Station

The V_S profiles, the dispersion curves, and the R-wave ellipticity curve are shown in Figure 5-11 for 5,000 of the profiles generated with the lowest misfit. The V_S profile with the lowest misfit is shown in black. The field dispersion curve from MASW and the R-wave ellipticity curve from ambient noise are shown in dark gray. The corresponding curves from each profile are colored according to their misfit value. A subset of the R-wave ellipticity curve where the peak is located was used to generate the inversion. This fragment of the R-wave ellipticity curve selected showed better agreement between the curve measured from ambient noise and the ones generated for the model. The V_S profiles show relatively consistent results. For this seismic station, a three-layer profile was selected to represent better the conditions of the site. The shallow layer showed velocities around 197 m/s until 3 m depth. The second layer had a velocity of 453 m/s until 11.9 m depth. The third layer showed a stiffer layer with velocities of 881 m/s. The V_{S30} for this site was computed with a median value of 540 m/s and a standard deviation of 3.4 m/s. The joint inversion of the R-wave ellipticity curve and MASW provides very similar results to MASW. The V_{S30} value from joint inversion is 7.7% higher than the MASW and the standard deviation increased for the joint inversion.

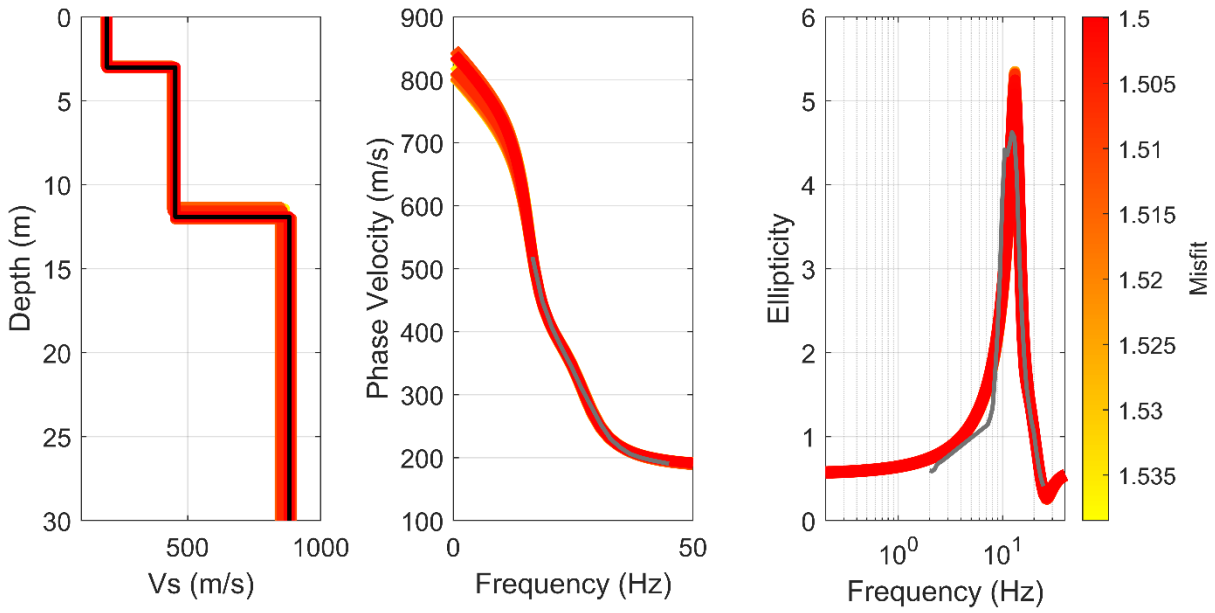

Figure 5-11: V_S profile computed using joint inversion (left), dispersion curve (middle), and R-wave ellipticity (right) for seismic station X48B. The V_S profile with the best fit is shown in black. The dispersion curve from the field and the R-wave ellipticity curve are shown in dark gray.

B01X Seismic Station

The V_S profiles, the dispersion curves, and the R-wave ellipticity curve are shown in Figure 5-12 for 5,000 of the profiles generated with the lowest misfit. The V_S profile with the lowest misfit is shown in black. The field dispersion curve from MASW and the R-wave ellipticity curve from ambient noise are shown in dark gray. The corresponding curves from each profile are colored according to their misfit value. A subset of the R-wave ellipticity curve where the peak is located was used to generate the inversion. This fragment of the R-wave ellipticity curve selected showed better agreement between the curve measured from ambient noise and the ones generated for the model. The V_S profiles show relatively consistent results. For this seismic station, a three-layer profile was selected to represent better the conditions of the site. The shallow layer showed velocities around 288 m/s until 2.1 m depth. The second layer had a slight increment in velocity, reaching 467 m/s until 5.8 m depth. The third layer showed a stiffer layer with velocities of 983

m/s. The V_{S30} for this site was computed with a median value of 734 m/s and a standard deviation of 11 m/s. The joint inversion of the R-wave ellipticity curve and MASW provides very similar results to MASW. The V_{S30} value from joint inversion is 3.4% lower than the MASW and the standard deviation increased for the joint inversion.

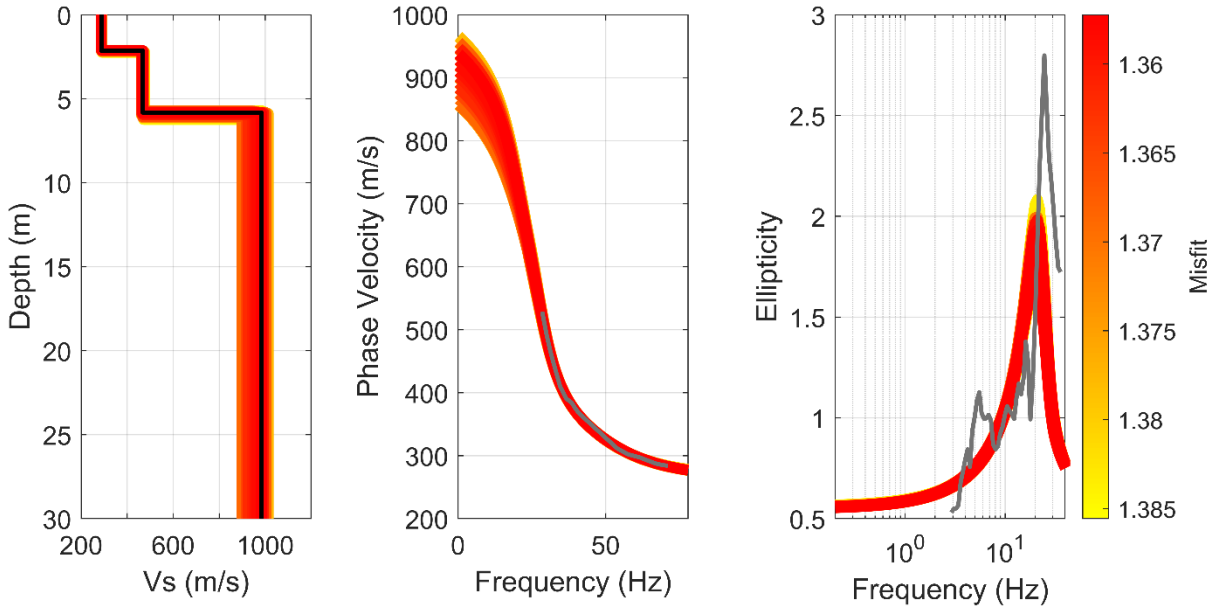

Figure 5-12: V_S profile computed using joint inversion (left), dispersion curve (middle), and R-wave ellipticity (right) for seismic station B01X. The V_S profile with the best fit is shown in black. The dispersion curve from the field and the R-wave ellipticity curve are shown in dark gray.

5.5 PROXY METHODS

The terrain-based, the hybrid slope-geology, and the topographic slope proxy methods were applied to all the sites (both with and without seismic stations) in the study to estimate V_{S30}. The hybrid slope-geology proxy required classifying each site according to their geologic era, period, and epoch. After the V_{S30} estimates were assigned to each site, the topographic slope gradient was computed for the geologic groups. Group 12 was the only group of the sites classified for this study with a topographic slope gradient relationship, as shown in Table 2-2 (Section 2.2.).

Three of the sites (Z50A, Z51A, and ASEL) fell within more than one of the geologic groupings proposed by Parker et al. (2017). The seismic stations were classified into the geologic groups 15-17. ASEL has two geologic formations at the site, with one of the formations spanning two geologic eras. Due to this, the ASEL site was classified into three groups, 13-15-17, with different V_{S30} estimates.

The terrain proxy method classified the seismic stations/sites into 16 different categories based on the slope gradient, local convexity, and surface texture. The terrain classification was mapped by Iwahashi & Pike (2007) for all of the United States, and this map was used to estimate the terrain group for each of the sites in this study area. Each group used in this study had a correlated V_{S30} value provided by Yong et al. (2012) except for group 13, which is the classification for the seismic stations Z47A, Z47B, 148A, 249A, and BRAL. V_{S30} estimates using this method range from 201 m/s for sites classified in geologic group 1, from the Cenozoic era to 822 m/s for sites classified in geologic group 13 from the Mesozoic era.

The topographic proxy method provided V_{S30} estimates for all the sites. The velocities ranged from 219 to 900 m/s.

A summary of the V_{S30} estimates using the hybrid geology-slope, the terrain, and the topographic slope proxy methods for each site in the study area is presented in Table 5-8. In addition to the V_{S30} estimates, the hybrid geology-slope proxy method also provided the geologic era of the site, the geologic group classification, and the topographic slope gradient. The terrain group classification is also included in the table for the terrain proxy method. In general, the V_{S30} estimates were lower when using the terrain proxy method, with an average difference of 191m/s and 108 m/s when compared to the hybrid geology-slope and the topographic proxy methods, respectively.

Table 5-8: Summary of V_{S30} estimates using the hybrid geology-slope and the terrain proxy methods for each seismic station/site in the study.

Station/ Site	Hybrid Geology-Slope Proxy				Terrain Proxy		Topographic Proxy
	Geologic Era [a]	Geol. Group	V_{S30} (m/s)	Topographic Slope Gradient	Terrain Group	V_{S30} (m/s)	V_{S30} (m/s)
PWLA	M	13	822	-	5	402	636
PLAL	P	15	684	-	9	497	693
B01	P	15	684	-	5	402	807
B01X	P	15	684	-	5	402	341
X47A	P	15	684	-	9	497	477
X48A	P	15	684	-	11	328	332
X48A-V	P	15	684	-	11	328	332
SWET	P	15	684	-	1	519	637
DYTN	P	15	684	-	1	519	900
W50A	P	15	684	-	5	402	612
X49A	P	15	684	-	1	519	900
X50B	P	15	684	-	5	402	782
FPAL	P	15	684	-	1	519	694
DEB	P	15	684	-	5	402	716
FISH	P	15	684	-	5	402	572
PAYN	P	15	684	-	9	497	776
X51A	P	15	684	-	7	388	613
Y48A	P	15	684	-	9	497	309
Y49A	P	15	684	-	3	547	900
Y49A-V	P	15	684	-	3	547	900
Y50A	P	15	684	-	7	388	552
Z48A	P	15	684	-	5	402	486
Z50A	Pr-P	15-17	684-699	-	5	402	530
Z51A	Pr-P	15-17	684-699	-	5	402	405
Y47A	C	1	210	-	5	402	436
Z47A	C	1	210	-	13	0	331
Z47B	C	1	210	-	13	0	331
EUAL	M	13	822	-	11	328	469
LRAL	P	15	684	-	9	497	517
147A	M	13	822	-	9	497	366
148A	C	1	210	-	13	0	284
149A	M	13	822	-	5	402	598
150A	M	13	822	-	9	497	427
151A	M	13	822	-	9	497	424
248A	C	12	315	0.98	9	497	383
249A	C	12	315	0.98	13	0	336
250A	M	13	822	-	9	497	382
250A-V	M	13	822	-	9	497	382
251A	M	13	822	-	7	388	368
349A	C	12	315	0.98	9	497	353
350A	C	12	315	0.98	9	497	371

BRAL	C	12	315	0.98	13	0	301
S1AL	C	12	315	0.98	9	497	478
S1FL	C	12	315	0.98	5	402	653
S2AL	C	1	210	-	11	328	339
S2FL	C	12	315	0.98	5	402	478
448A	C	12	315	0.98	5	402	442
ASEL	Pr-P-M	13-15-17	684-699-822	-	5	402	503
TU01	C	1	210	-	5	402	254
SR-21	P	15	684	-	5	402	319
SR-219	M	13	822	-	11	328	672
AN01	P	15	684	-	7	388	547
BLF1	P	15	684	-	9	497	390
AFBM	C	1	210	-	15	363	219

[a] Pr: Precambrian, P: Paleozoic, C: Cenozoic, M: Mesozoic

CHAPTER 6 COMPARISON OF DIFFERENT APPROACHES

6.1 COMPARISON OF DIRECT METHODS

This section compares the V_{S30} results from the direct methods applied to the sites and seismic stations. The direct methods applied to the sites and seismic stations were in reasonable agreement in terms of the V_{S30} values measured. The V_{S30} results computed using the MASW data jointly inverted with ellipticity curves were similar to the results from MASW alone, with a maximum variation of 7.8% between the two approaches. V_{S30} results from the inversion-based MASW (without ellipticity) and non-inversion MASW approaches were in close agreement with the inversion-based approach being 3% higher on average. Three of the sites showed larger disagreements (ASEL, SR-21, and B01X) with B01X showing a difference of more than 20% between the two approaches. The reasons for these larger discrepancies are unclear, but it seems that the non-inversion approach might be providing a good result for the sites with larger changes in the velocity profile. The non-inversion approach is considered an approximate method, so this level of disagreement is not unexpected. Future comparisons will rely on the jointly inverted MASW results when available and the inversion-based MASW results when ellipticity curves are not available. The selected MASW results are shown in Figure 6-1 based on the mean V_{S30} from the 5,000 models with the lowest misfit.

The seismic refraction results were converted to V_S values using an assumed ratio between V_P/V_S which introduces additional uncertainty, and then used to determine a range of V_{S30}. The mean V_{S30} values computed using seismic refraction is shown in Figure 6-1. Generally, seismic refraction estimates of V_{S30} were very close to the results using MASW. Of the 10 sites with MASW and seismic refraction, the MASW V_{S30} fell within the range of seismic refraction results

for 8 sites. The median MASW V_{S30} was on average 5.3% lower than the mean refraction V_{S30} with the largest differences in the seismic station located in the CT region, B01X and X48A. These stations showed higher mode interference in the lower frequencies. Therefore, the average between the seismic refraction and the MASW results was used for further comparisons.

From the V_{S30} results collected from the publicly available reports, the only site with two methods (SASW and MALW) applied is seismic station SWET. For seismic station SWET, the SASW method provided V_{S30} measurement 17.5% lower than the MALW method.

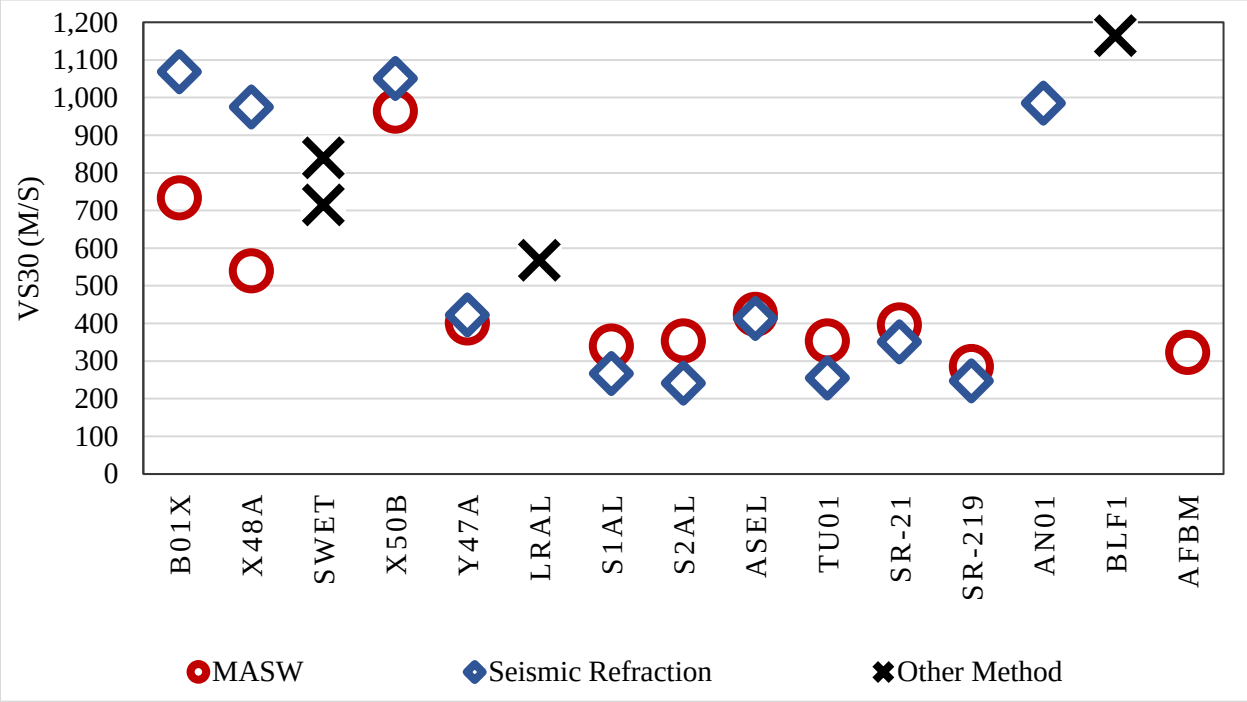

Figure 6-1: V_{S30} values computed using the direct methods. MASW results are the mean V_{S30} from the 5,000 models with the lowest misfit. The results of V_{S30} from the MASW method using joint inversion were preferred when available. V_{S30} results computed from the seismic refraction method are the median of the range.

6.2 COMPARISON OF DIRECT METHODS AND INDIRECT METHODS

This section provides a comparison between the V_{S30} results from the direct methods and the indirect methods. The proxy methods were applied to all the locations selected in the study area, while the P-wave method and HVSR correlations were only applied to seismic stations. Each method was compared separately to the MASW method, and the results are provided in the following sections. When available, the MASW results used in this section are the results from the joint inversion. The plots presented in this section shown 1 to 1 line along with a 30% range. The range selected is the required in the NEHRP *Provisions* (NEHRP, 2020) when correlations are used to estimate V_{S30}.

6.2.1 Comparison of MASW with P-wave Seismogram Method

A comparison between the V_{S30} results from MASW and the P-wave seismogram method using the amplitude ratio correlation is shown in Figure 6-2. The dashed lines in the figure indicate the ± 30% range. As mentioned before, the P-wave seismogram method was only applied to the seismic stations. The stations were classified by the region in which they are located as CT, SA, and GC. MASW results are the mean V_{S30} from the 5,000 models with the lowest misfit. V_{S30} for seismic station SWET was computed using an average of SASW and MALW methods. The range shown for the P-wave seismogram method represents the 25^{th} and 75^{th} percentiles using the amplitude ratio correlation. Figure 6-2 shows the V_{S30} results using the original amplitude ratio correlation (left) and the V_{S30} results using the lower boundary of the amplitude ratio correlation (right), computed in section 5.4.4.

Using the original equation proposed by Kim et al. (2016), the P-wave seismogram method estimated similar or higher V_{S30} results than the MASW method for all stations. All sites had an

agreement within ± 30% except for station X48A, which was significantly overestimated by the P-wave approach. The median V_{S30} from the P-wave results is on average 9% higher than the mean MASW results. When the lower boundary of the 95% of the confidence interval was applied to the seismic stations, the median values were in better agreement with the measured values showing all the stations inside the 30% range. The median V_{S30} from the P-wave using the lower 95% confidence interval is, on average, 9% lower than the mean MASW results. In addition, the range observed between the 25th and 75th percentiles is also reduced when using the lower boundary of the amplitude ratio correlation. Therefore, the agreement within the ± 30% using the lower boundary of the confidence interval seems to work better for the sites with available measurements in Alabama.

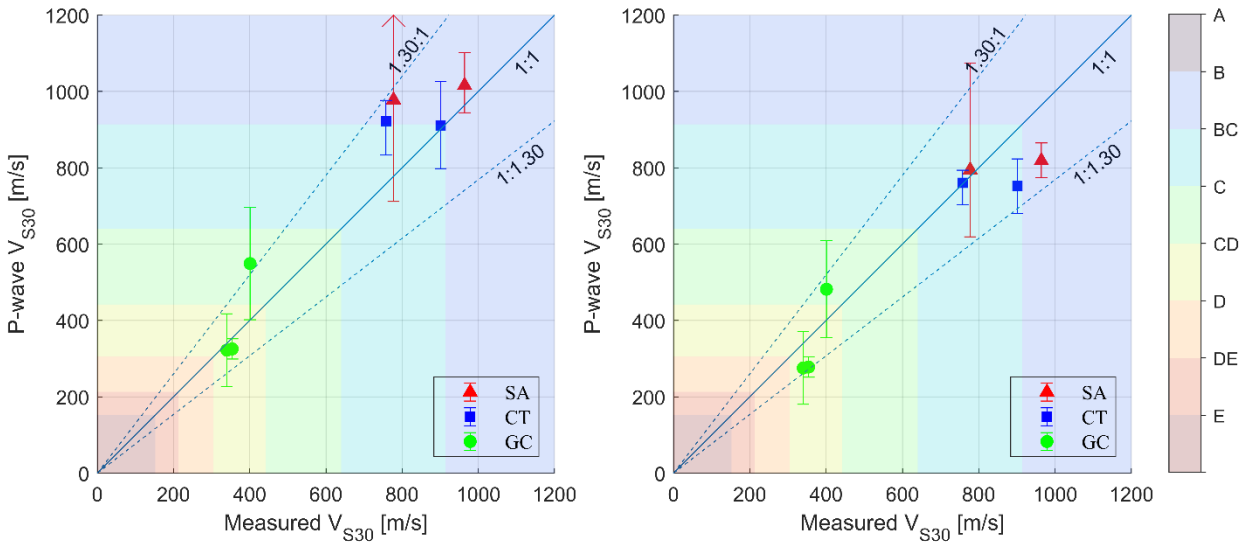

Figure 6-2: Comparison of V_{S30} values computed using the MASW and P-wave seismogram method, one-to-one line, and with a range of ±30%. For the original amplitude ratio correlation (left) and the lower boundary of the 95% confidence interval (right). The results of V_{S30} from the MASW method using joint inversion were preferred when available, and the mean V_{S30} from the 5,000 models with the lowest misfit was used.

6.2.2 Comparison of Direct Methods with HVSR Correlations

A comparison between the V_{S30} results from the MASW method and the HVSR correlations is shown in Figure 6-3. The dashed lines in the figure indicate the ± 30% range. As mentioned before, the HVSR correlations were only applied to seismic stations. The stations were classified by the region in which they are located as CT, SA, and GC. MASW results are the mean V_{S30} from the 5,000 models with the lowest misfit. Seismic stations SWET, LRAL, and S1AL, did not fulfill the requirements for a reliable curve and a clear peak. Therefore, no correlations were computed for these stations. HVSR1, HVSR2, and HVSR3 are the correlations proposed by Ghofrani & Atkinson (2014), Hassani & Atkinson (2016), and Stanko & Markušić (2020) from section 5.3.1.

The HVSR correlations generally provided lower estimates for V_{S30} than the MASW method. The best agreement between the V_{S30} results from MASW and the different HVSR correlations is at seismic station Y47A and the most considerable variability at seismic station X50B. On average, the V_{S30} results for the HVSR1 correlation are 36% lower than the mean MASW result. For correlation HVSR2, the V_{S30} results are on average 11% lower than the mean MASW result; however, only one station fits in the ±30% range indicating poor agreement. Correlation HVSR3 fits three seismic stations in the ±30% range; nevertheless, its results are 29% lower than the mean MASW result on average. Consequently, the HVSR correlations cannot estimate V_{S30} accurately, at least for this region with the available data.

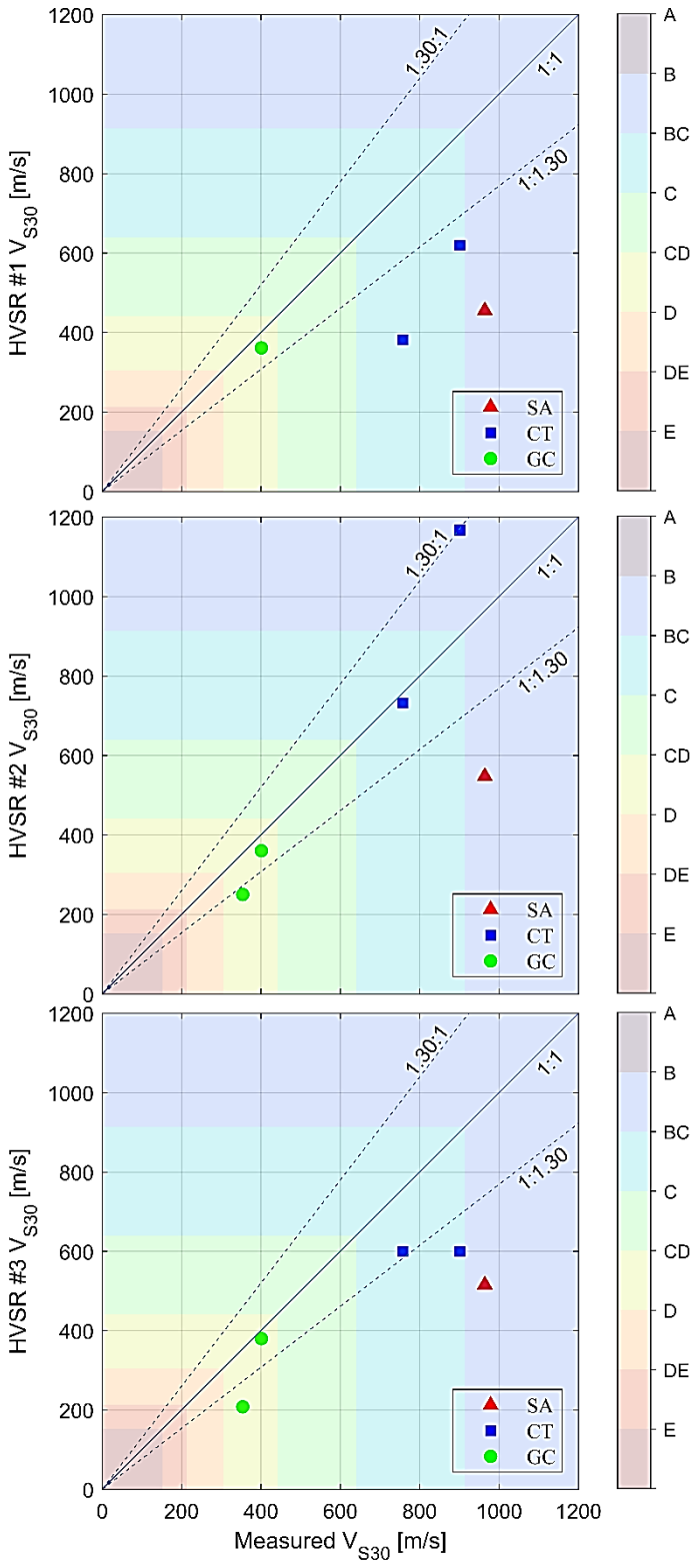

Figure 6-3: Comparison of V_{S30} estimates from the HVSR1 (up), HVSR2 (middle), and HVSR3 (low) correlations with direct methods, one-to-one, and a range of ±30%.

6.2.3 Comparison of Direct Methods with Proxy Methods

A comparison between the V_{S30} results from MASW and proxy methods is shown in Figure 6-4. MASW results are the mean V_{S30} from the 5,000 models with the lowest misfit. V_{S30} for seismic station SWET was computed using an average of SASW and MALW methods. The dashed lines in the figure indicate the ±30% range. The V_{S30} results for seismic station LRAL and BLF1 were computed using SASW and P-S suspension logging methods. For the ASEL site, an average of the V_{S30} estimates from the hybrid geology-slope proxy methods was used for the comparison. The sites were classified by the region in which they are located as CT, SA, and GC. The relative difference between the V_{S30} results from the direct measurement and the proxy estimates is shown in Table 6-1.

In general, proxy methods provided lower V_{S30} estimates than direct methods. Also, the range of velocities estimated from the proxies is very constrained, at least for the terrain and the hybrid geology-slope proxy methods. The range of velocities estimated using the terrain proxy is very narrow for the stations and sites analyzed, ranging from 328 to 529 m/s. At the same time, the hybrid geology-slope proxy method has two velocity ranges, the first between 210 to 315 m/s and the second from 684 to 822 m/s.

The terrain proxy method provided the closest V_{S30} for the sites located in the GC region, fitting most of the stations of this region within the ±30% range. The terrain proxy estimates were an average of 13% higher than the results computed using the direct methods in the CG region. This method showed an average difference of 31% and 56% for the SA and CT regions, respectively. The better agreement in the GC region could be explain by the range of velocities that this method is able to provide, which relates better to the lower velocities computed in this

region. In contrast with the measurement from the SA and CT with V_{S30} much higher than the maximum velocity provided by the method (V_{S30}=547 m/s).

The hybrid geology-slope proxy method showed the best agreement for the CT region, fitting both stations in the ±30% range, but with only two measurements it is difficult to draw conclusions. The proxy estimates from this method had an average difference of 17% from the results of the direct method for the CT region. The other regions computed using this method had an average difference of 13% and 5% from the direct method results for the SA and CG regions, respectively. Even though the average differences computed from this method are lower than for the other proxies, in reality most of the sites are do not fall into the ±30% range. The reason of this greater disagreement between this method and the measurement might be because the hybrid geology-slope classification is grouping the sites mainly by geologic era, which is a very broad parameter and might not be representing the complexity of the geologic formations. In addition, in some parts of the state there are very different geologic ages situated very close from each other which might lead to a misinterpretation of the velocity profile.

The topographic slope proxy method showed better agreement with the results for the sites in the GC and SA regions, fitting most of them within the ±30% range or very close to it. The estimates using this method showed an average of 21% and 13% relative difference from the results computed using the direct methods for the CG and SA regions, respectively. The CT region had an average difference of 59% between the topographic slope estimates and the direct methods. The good agreement in the SA region could be related with the capability of the method to capture effect of mountainous areas in the estimation of velocities in the region

Table 6-1: Summary of the relative difference between the V_{S30} from the direct measurement and the proxy estimates

Region	Station Site	Terrain Proxy	Hybrid Geology-Slope Proxy	Topographic Slope Proxy
CT	B01X	55%	24%	62%
	X48A	57%	10%	56%
SA	SWET	33%	12%	18%
	X50B	59%	29%	21%
	ASEL	5%	-73%	-19%
	SR-21	-2%	-73%	19%
	BLF1	57%	41%	67%
GC	Y47A	0%	48%	-9%
	LRAL	13%	-20%	9%
	S1AL	-46%	7%	-41%
	S2AL	-14%	41%	28%
	TU01	-15%	40%	27%
	SR-219	-15%	-187%	-135%
	AFBM	-12%	35%	32%

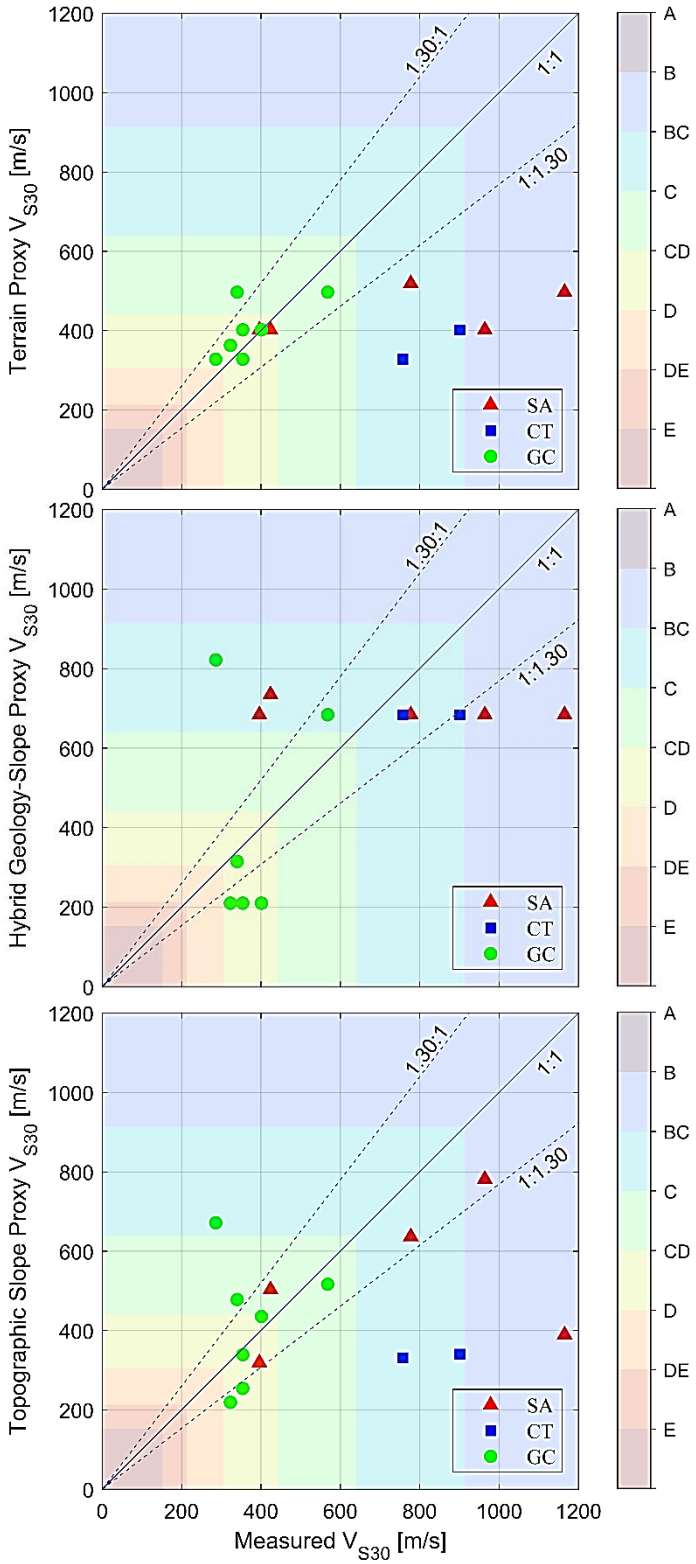

Figure 6-4: Comparison of V_{S30} estimates from the terrain(up), hybrid geology-slope(middle), and topographic slope(low) proxy with direct methods, one-to-one, and a range of ±30%.

6.3 COMPARISON OF INDIRECT METHODS

The indirect methods were applied to a broader range of locations than the direct ones, so a comparison of results from the indirect methods provides more data points. As observed in the previous sections of this chapter, the proxy methods generally provided lower V_{S30} estimates. In comparison, the P-wave seismogram method using the amplitude ratio correlation provided higher estimates than the direct methods. However, when using the lower boundary of the 95% confidence interval of the amplitude ratio correlation, the agreement between the results from the P-wave seismogram method and the direct method was improved. The HVSR correlations could not provide reliable estimates for V_{S30}. Therefore, these HVSR correlations were not included in this section.

A comparison between the V_{S30} estimates from the proxy methods and the P-wave seismogram method using the lower boundary (95% confidence interval) of amplitude ratio correlation is shown in Figure 6-5. The dashed lines in the figure indicate the ± 30% range. The stations were classified by the region in which they are located as CT, SA, and GC. The relative difference between the V_{S30} results from the direct measurement and the proxy estimates is shown in Table 6-2.

The terrain proxy provided the closest V_{S30} for the sites located in the GC region. The terrain proxy estimates had an average difference of 21% with the results computed using the P-wave seismogram method. More considerable differences were encountered when using this method for the other regions. The terrain proxy method shed an average difference of 51% and 55% for the SA and CT regions, respectively.

The hybrid geology-slope proxy method provided the best agreement with the P-wave method for all of the regions in the study area, fitting most of the data within the ± 30% range. The average differences between this method and the P-wave seismogram method are 16%, 27%, and

24% for the GC, SA, and CT regions, respectively. However, the results provided by the hybrid geology slope proxy method have a wide range of uncertainty. As mentioned before, the velocities provided by this method were constrained into two limited ranges.

The topographic slope proxy method showed better agreement with the results for the sites in the GC and SA regions, fitting most of them within or close to the ±30% range with a significant portion also being underestimated using the proxy method. The estimates using this method showed an average of 17% and 30% difference from the results computed using the direct methods for the CG and SA regions, respectively. The CT region had an average difference of 43% between the topographic slope estimates and the P-wave method.

Table 6-2: Summary of the difference between the V_{S30} results from the lower boundary of the amplitude ratio correlation from the P-wave seismogram method and the proxy estimates

Region	Station	Terrain Proxy	Hybrid Geology-slope Proxy	Topographic Slope
CT	PWLA	48%	-6%	18%
	PLAL	37%	13%	12%
	B01	62%	35%	24%
	B01X	56%	25%	63%
	X47A	48%	28%	50%
	X48A	64%	26%	64%
	X48A-V	73%	44%	73%
SA	SWET	47%	30%	35%
	DYTN	40%	21%	-4%
	W50A	43%	2%	13%
	X49A	63%	52%	36%
	X50B	60%	33%	23%
	FPAL	16%	-10%	-12%
	X51A	54%	18%	27%
	Y48A	43%	22%	65%
	Y49A	44%	30%	8%
	Y49A-V	45%	32%	10%
	Y50A	66%	40%	52%
	Z48A	65%	40%	57%
	Z50A	63%	37%	52%
	Z51A	60%	31%	60%
GC	Y47A	27%	62%	21%
	Z47B	-	30%	-11%
	147A	53%	22%	65%
	150A	58%	31%	64%
	151A	47%	12%	55%
	250A	16%	-39%	35%
	250A-V	17%	-37%	36%
	251A	49%	-7%	52%
	350A	36%	60%	53%
	BRAL	-	0%	4%
	S1AL	-54%	2%	-48%
	S1FL	-16%	9%	-88%
	S2AL	-1%	36%	-4%
	S2FL	24%	40%	9%

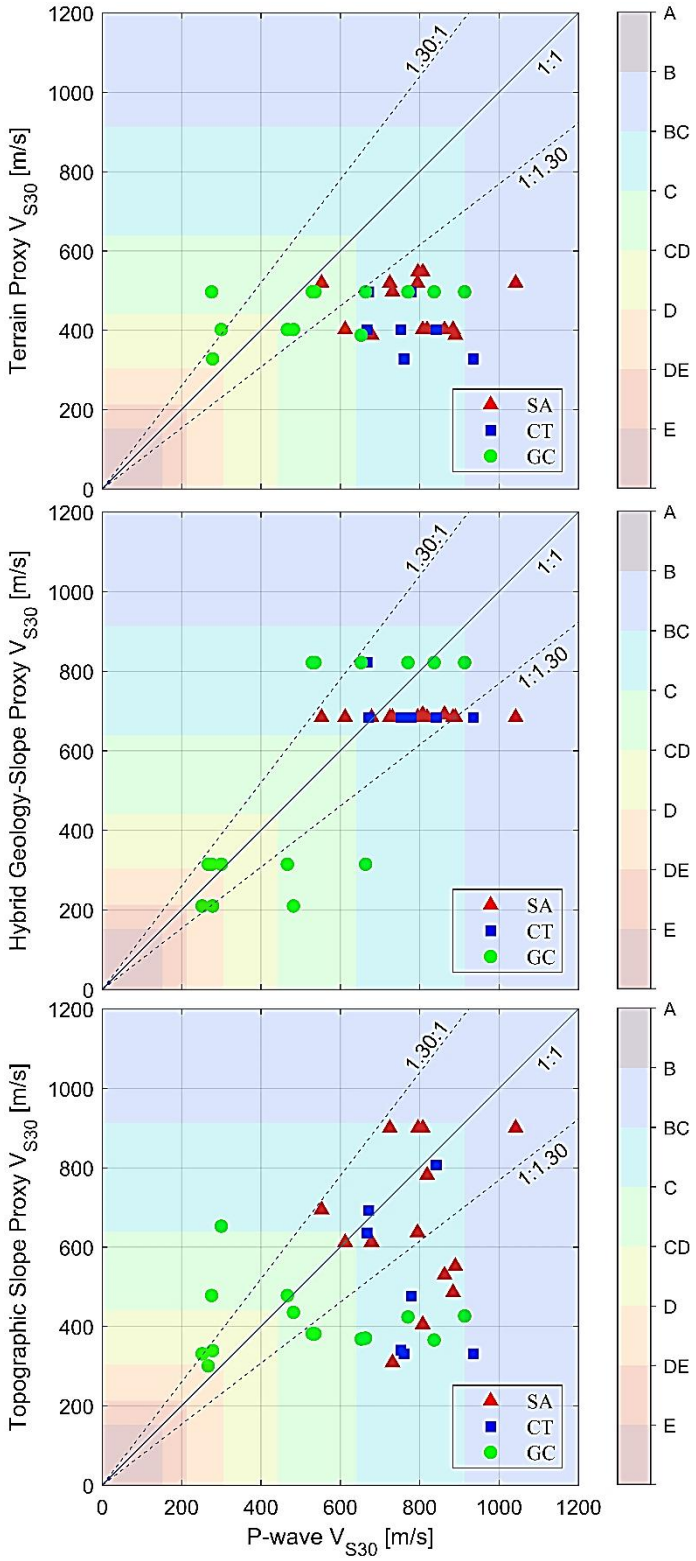

Figure 6-5: Comparison of V_{S30} estimates from the terrain (top), hybrid geology-slope (middle), and topographic slope (bottom) proxy with the P-wave seismogram method, one-to-one, and a range of ±30%.

CHAPTER 7 CONCLUSIONS AND FUTURE RESEARCH

7.1 CONCLUSIONS

V_{S30} values were measured and estimated in Alabama using different direct and indirect methods. MASW and seismic refraction provided direct measurements of velocities at 11 sites for comparison with the indirect methods (P-wave seismogram method, HVSR correlations, joint inversion with R-wave ellipticity, and proxy methods). Another four V_{S30} values were collected from the publicly available profiles. The different approaches were compared to provide recommendations for estimating V_{S30} at sites in Alabama, which are discussed in this section.

MASW was found to be the most reliable direct method at most of the sites, but seismic refraction was an excellent method to compare with the results of the MASW method. Refraction was also able to provide results at sites where MASW could not be applied due to higher mode interference, such as the AN01 site. The 2D V_P profile computed using seismic refraction for the AN01 site showed a sharp velocity contrast and a shallow first layer. The combination of these two factors caused the MASW method to not provide a reliable dispersion curve for the first mode due to the interaction of higher modes. The equipment and data collection for these two methods are very similar, so applying both is a good practice for future sites.

The V_{S30} results computed using the non-inversion approach provided excellent agreement compared to the MASW results using inversion. The results using the non-inversion were generally lower than those acquired using the inversion except for seismic stations S1AL and S2AL. Most stations had a good agreement between the approaches, with an average difference of 3% for most sites. However, the sites with more significant changes in the velocity profile had larger discrepancies with the results from the MASW. The non-inversion approach is considered

an approximate method, so this level of disagreement is not unexpected. The non-inversion method provided a complement to the inversions, but as the two methods provide similar data, the noninversion method did not add significant value to the measurements.

The joint inversion using R-wave ellipticity and MASW method showed excellent agreement compared with the results of only using MASW. R-wave ellipticity helped to constrain the V_S profiles by adding additional information about the site amplification to the inversion process. Therefore, the V_{S30} results from the joint inversion are recommended when sufficient data are available.

The P-wave seismogram method was applied to 56 stations in Alabama and surrounding states, with successful results for 46 stations. Correlations proposed by Kim et al. (2016) were used to estimate V_{S30} values. These results were compared with three proxy estimations and measurements. The amplitude ratio correlation showed to be more reliable for the stations studied, providing, in general, a fair agreement ($\pm$ 30%) with the different methods of comparison when multiple recordings were available. Using the lower boundary of the 95% confidence interval on the original amplitude ratio correlation significantly improved the agreement between the median of the P-wave amplitude results and the direct methods. Therefore, using the both the mean and the lower boundary of the 95% confidence interval of the amplitude ratio correlation is recommended for sites in Alabama. Additional direct measurements at seismic stations are needed to better determine if a new relationship is needed for sites in Alabama.

HVSR curves were computed for the seismic stations with 16 of the stations showing both reliable HVSR curves and clear peaks. Many of the sites showed more than one peak and so selecting a single peak was not possible. HVSR correlations for V_{S30} were applied to the stations that provided reliable curves and clear peaks. The correlations showed significant scatter when

compared with direct measurements and this level of uncertainty makes the use of these relationships unreliable for the sites considered. This result is not unexpected as HVSR peaks are more closely associated with the depth to a significant impedance contrast, which may occur at shallower or deeper depths than 30 meters. The HVSR results are conceptually similar to the R-wave ellipticity and rely on similar data, so joint inversion with R-wave ellipticity is recommended as opposed to using HVSR.

The comparisons of the proxy methods with the P-wave seismogram results and direct measurements showed the terrain proxy worked fairly well in the GC region, but not in the SA or CT regions. The topographic slope methods worked well in the SA regions. The hybrid geology-slope proxy method worked well for some sites and not for others. This method is grouping a large variety of sites in limited geologic groups that cannot consider the complexity and variety of the geology and the geologic formations in the state. On average, the proxy methods tended to underestimate the V_{S30} with this level of underestimation increasing for stiffer sites (>750 m/s). Underestimation would be conservative in terms of the seismic design category, but direct methods or the P-wave seismogram approach should be used when possible.

7.2 RECOMMENDATIONS

This study is a preliminary approach for providing V_{S30} measurements and estimates for Alabama and for regions with low seismicity where direct *in situ* measurements are not available. Future studies seeking to measure V_{S30} at other sites should first consider the possibility of using direct methods as these are the most reliable. MASW and seismic refraction can both be performed using an active survey approach and provide complementary data. Passive MASW can be used to extend the dispersion curve to deeper depths but requires additional time and enough space to

perform the large survey. At sites where seismometer recordings are available, R-wave ellipticity can provide additional constraints on the inversion. This technique uses ambient vibration and so can be applied to temporary recordings, such as those collected from portable seismometers. Sites with permanent or longer-term seismometer installations should consider using the P-wave seismogram method with both the original (mean) amplitude ratio correlation from Kim et al. (2016) and the proposed lower boundary of the 95% confidence interval. Multiple earthquake records are needed, which does limit the usefulness of this method in less seismically active regions like Alabama. Proxy methods can be used at sites without any measurements but tend to underestimate V_{S30} at stiffer sites. All three proxy methods should be considered in the GC region, while the topographic methods should be considered in SA. To provide recommendations in the CT regions more data are required to evaluate the reliability of the different correlations.

Future studies should continue to expand the database of measurements created in this study for Alabama. Having additional sites with direct measurements will allow for more accurate assessment of the reliability of the proxy methods and potential modifications to the amplitude ratio correlation for the P-wave method for use in Alabama. Furthermore, incorporating new earthquake data would allow an expansion of the dataset to compute more accurate V_{S30} estimates from the P-wave method.

7.3 FUTURE RESEARCH

The lower boundary of the 95% confidence interval of the amplitude ratio correlation of the P-wave seismogram method showed more reliable V_{S30} estimations when compared to the direct measurements, but more data were required for further validation of this approach. This is especially important in the north part of the state, which is more subjected to seismic hazards.

Future studies should consider whether region-specific correlations are needed for use with this method. If this is the case, the factors that control which relationship is more applicable should be explored.

The use of both MASW and seismic refraction was found to be the most effective as each provides different information about the subsurface. Techniques that can integrate these two measurements (i.e., joint inversion or full waveform inversion) may be able to provide more reliable estimates but need additional work to be ready to use in practice. This study has provided a database of several sites that could be used to test this more advanced inversion approaches to see what improvements they provide in terms of V_{S30} measurements.

The database of V_{S30} measurements created for this study should continue to be expanded. It would be particularly valuable to collect data in regions and geologic settings that were not explored in this study. This will allow the reliability of the indirect approaches to be more clearly assessed and potentially for new correlations to be developed that more accurately reflect the characteristics of this region.

REFERENCES

AASHTO. (2020). *AASHTO LRFD Bridge Design Specifications, 9th Edition* (LRFDBDS-9). Washington, D.C. American Association of State Highway Officials. https://trid.trb.org/view/1704698

Abrahamson, N., Atkinson, G., Boore, D., Bozorgnia, Y., Campbell, K., Chiou, B., Idriss, I. M., Silva, W., & Youngs, R. (2008). Comparisons of the NGA Ground-Motion Relations. *Earthquake Spectra*, *24*(1), 45-66. https://doi.org/10.1193/1.2924363

Ahdi, S., Shamsher, S., Ilhan, O., Bozorgnia, Y., Hashash, Y., Kwak, D. Y., Park, D., Yong, A., & Stewart, J. (2018). *Development of a United States Community Shear Wave Velocity Profile Database*. *Reston, VA: American Society of Civil Engineers.*, 330-339. https://doi.org/10.1061/9780784481462.032

Aki, K., & Richards, P. G. (2002). Quantitative Seismology, 2nd Ed. *Quantitative Seismology*. https://ui.adsabs.harvard.edu/abs/2002quse.book.....A/abstract

Allen, T. I., & Wald, D. J. (2009). On the Use of High-Resolution Topographic Data as a Proxy for Seismic Site Conditions (VS30). *Bulletin of the Seismological Society of America*, *99*(2A), 935-943. https://doi.org/10.1785/0120080255

Anbazhagan, P., & Sitharam, T. G. (2008). Mapping of Average Shear Wave Velocity for Bangalore Region: A Case Study. *Journal of Environmental and Engineering Geophysics*, *13*(2), 69-84. https://doi.org/10.2113/JEEG13.2.69

Andrus, R. D., Mohanan, N. P., Piratheepan, P., Ellis, B. S., & Holzer, T. L. (2007). *PREDICTING SHEAR-WAVE VELOCITY FROM CONE PENETRATION RESISTANCE*. *2528*, 12.

ASCE/SEI. (2022). *ASCE/SEI 7-22 Minimum Design Loads and Associated Criteria for Buildings and Other Structures* (Vol. 1). American Society of Civil Engineers. https://www.asce.org/publications-and-news/asce-7

Asmussen, J. C. (1997). *Modal Analysis based on the Random Decrement Technique—Application to Civil Engineering Structures* [Department of Building Technology and Structural Engineering]. Denmark. University of Aalborg.

Azhar, A. S. bin, Latiff, A. H. A., Lim, L. H., & Gödeke, S. H. (2019). Groundwater investigation of a coastal aquifer in Brunei Darussalam using seismic refraction. *Environmental Earth Sciences*, *78*(6), 220. https://doi.org/10.1007/s12665-019-8203-6

Aziman, M., Hazreek, Z. A. M., Azhar, A. T. S., & Haimi, D. S. (2016). Compressive and Shear Wave Velocity Profiles using Seismic Refraction Technique. *Journal of Physics: Conference Series*, *710*, 012011. https://doi.org/10.1088/1742-6596/710/1/012011

Baglari, D., Dey, A., & Taipodia, J. (2018). A state-of-the-art review of passive MASW survey for subsurface profiling. *Innovative Infrastructure Solutions*, *3*(1), 66. https://doi.org/10.1007/s41062-018-0171-2

Ballard, R. F. (1976). Method for Crosshole Seismic Testing. *Journal of the Geotechnical Engineering Division*, *102*(12), 1261-1273. https://doi.org/10.1061/AJGEB6.0000355

Bard, P.-Y. (1999). Microtremor measurements: A tool for site effect estimation. *The effects of surface geology on seismic motion*, *3*, 1251-1279.

Bhate, G. C., Inc. (2018). *Report of Subsurface Exploration and Geotechnical Engineering Evaluation for Proposed Advanced Structural Testing Laboratory site, Auburn University, Alabama* (BHATE Project Number 118175).

Boaga, J., Vaccari, F., & Panza, G. F. (2010). Shear wave structural models of Venice Plain, Italy, from Time Cross Correlation of seismic noise. *Engineering Geology*, *116*(3), 189-195. https://doi.org/10.1016/j.enggeo.2010.09.001

Bonnefoy-Claudet, S., Köhler, A., Cornou, C., Wathelet, M., & Bard, P.-Y. (2008). Effects of Love Waves on Microtremor H/V Ratio. *Bulletin of the Seismological Society of America*, *98*(1), 288-300. https://doi.org/10.1785/0120070063

Borcherdt, R. D. (2012). *VS30 – A site-characterization parameter for use in building Codes, simplified earthquake resistant design, GMPEs, and ShakeMaps*. The 15th World Conference on Earthquake Engineering. https://pubs.er.usgs.gov/publication/70041709

Butler, D. K., & Curro, J. R. (1981). Crosshole seismic testing—Procedures and pitfalls. *GEOPHYSICS*, *46*(1), 23-29. https://doi.org/10.1190/1.1441134

Campanella, R. G., Robertson, P. K., & Gillespie, D. (1986). *Seismic Cone Penetration Test*. 116-130. https://cedb.asce.org/CEDBsearch/record.jsp?dockey=0048818

Cardarelli, E., & De Nardis, R. (2001). Seismic refraction, isotropic anisotropic seismic tomography on an ancient monument (Antonino and Faustina temple ad 141). *Geophysical Prospecting*, *49*(2), 228-240. https://doi.org/10.1046/j.1365-2478.2001.00251.x

Cauchie, L., & Saccorotti, G. (2013). Probabilistic inversion of Rayleigh-wave dispersion data: An application to Mt. Etna, Italy. *Journal of Seismology*, *17*(2), 335-346. https://doi.org/10.1007/s10950-012-9323-6

Chapman, M. C., Powell, C. A., Vlahovic, G., & Sibol, M. S. (1997). *A Statistical Analysis of Earthquake Focal Mechanisms and Epicenter Locations in the Eastern Tennessee Seismic Zone*. *87*(6), 15.

Chávez-García, F. J., & Kang, T.-S. (2014). Lateral heterogeneities and microtremors: Limitations of HVSR and SPAC based studies for site response. *Engineering Geology*, *174*, 1-10. https://doi.org/10.1016/j.enggeo.2014.02.007

Chen, S.-E., & Liu, Y. (2018). Geophysical Monitoring of CO2 Injection at Citronelle Field, Alabama. En *Carbon Capture, Utilization and Sequestration*. IntechOpen. https://doi.org/10.5772/intechopen.78386

Clark, J., Johnson, W., & Milled, W. (1994). *The Application of High Resolution Shear Wave Seismic Reflection Surveying to Hydrogeological and Geotechnical Investigations* (p. 245). https://doi.org/10.4133/1.2922067

Cole, H. A. (1971). *FAILURE DETECTION OF A SPACE SHUTTLE WING FLUTTER MODEL BY RANDOM DECREMENT* (NASA TM X-62,041; Nasa Technical Memorandum, p. 12). Ames Research Field.

Comina, C., Foti, S., Boiero, D., & Socco, L. V. (2011). Reliability of VS,30 Evaluation from Surface-Wave Tests. *Journal of Geotechnical and Geoenvironmental Engineering*, *137*(6), 579-586. https://doi.org/10.1061/(ASCE)GT.1943-5606.0000452

Di Fiore, V., Cavuoto, G., Tarallo, D., Punzo, M., & Evangelista, L. (2016). Multichannel Analysis of Surface Waves and Down-Hole Tests in the Archeological "Palatine Hill" Area (Rome, Italy): Evaluation and Influence of 2D Effects on the Shear Wave Velocity. *Surveys in Geophysics*, *37*(3), 625-642. https://doi.org/10.1007/s10712-015-9350-2

Dobry, R., Borcherdt, R. D., Crouse, C. B., Idriss, I. M., Joyner, W. B., Martin, G. R., Power, M. S., Rinne, E. E., & Seed, R. B. (2000). New Site Coefficients and Site Classification System Used in Recent Building Seismic Code Provisions. *Earthquake Spectra*, *16*(1), 41-67. https://doi.org/10.1193/1.1586082

Dreiling, J., Isken, M. P., Mooney, W. D., Chapman, M. C., & Golbee, R. W. (2014). *"NGA-East regionalization report: Comparison of four crustal regions within central and eastern North America using waveform modeling and 5%-damped pseudo-spectral acceleration response.* (N.º 15). PEER Report.

Dunn, M. M., & Chapman, M. C. (2006). Fault Orientation in the Eastern Tennessee Seismic Zone: A Study Using the Double-Difference Earthquake Location Algorithm. *Seismological Research Letters*, *77*(4), 494-504. https://doi.org/10.1785/gssrl.77.4.494

EPRI. (1993). *Guidelines for Determining Design Basis Ground Motions* (TR-102293). Palo Alto, CA. Electric Power Research Institute.

EPRI. (2013). *Ground-motion model (GMM) review project: Shear wave velocity measurements at seismic recording stations* (EPRI 3002000719). Palo Alto, CA. Electric Power Research Institute.

Fäh, D., Wathelet, M., Kristekova, M., Havenith, H., Endrun, B., Stamm, G., Poggi, V., Burjanek, J., & Cornou, C. (2009). *Using Ellipticity Information for Site Characterisation* (NERIES JRA4; Geotechnical Site Characterisation). NEtwork of Research Infrastructures for European Seismology.

Farr, T. G., & Kobrick, M. (2000). Shuttle radar topography mission produces a wealth of data. *Eos, Transactions American Geophysical Union*, *81*(48), 583-585. https://doi.org/10.1029/EO081i048p00583

Forte, G., Chioccarelli, E., De Falco, M., Cito, P., Santo, A., & Iervolino, I. (2019). Seismic soil classification of Italy based on surface geology and shear-wave velocity measurements. *Soil Dynamics and Earthquake Engineering*, *122*, 79-93. https://doi.org/10.1016/j.soildyn.2019.04.002

Foti, S. (2000). *Multistation Methods for Geotechnical Characterization using Surface Waves*. https://doi.org/10.6092/POLITO/PORTO/2497212

Foti, S., Comina, C., Boiero, D., & Socco, L. V. (2009). *Non-uniqueness in surface-wave inversion and consequences on seismic site response analyses*. *29*(6), 982-993. https://doi.org/10.1016/j.soildyn.2008.11.004

Foti, S., Hollender, F., Garofalo, F., Albarello, D., Asten, M., Bard, P.-Y., Comina, C., Cornou, C., Cox, B., Di Giulio, G., Forbriger, T., Hayashi, K., Lunedei, E., Martin, A., Mercerat, D., Ohrnberger, M., Poggi, V., Renalier, F., Sicilia, D., & Socco, V. (2018). Guidelines for the good practice of surface wave analysis: A product of the InterPACIFIC project. *Bulletin of Earthquake Engineering*, *16*(6), 2367-2420. https://doi.org/10.1007/s10518-017-0206-7

Foti, S., Parolai, S., Albarello, D., & Picozzi, M. (2011). Application of Surface-Wave Methods for Seismic Site Characterization. *Surveys in Geophysics*, *32*(6), 777-825. https://doi.org/10.1007/s10712-011-9134-2

Foti, S., Sambuelli, L., Socco, V. L., & Strobbia, C. (2003). Experiments of joint acquisition of seismic refraction and surface wave data. *Near Surface Geophysics*, *1*(3), 119-129. https://doi.org/10.3997/1873-0604.2003002

Fotouhimehr, M., Shabani, E., Cornou, C., & Azmi, P. (2021). Ambient noise wavefield decomposition and shear-wave velocity retrieval in the south of Tehran, Iran and in the Colfiorito basin, Italy. *Journal of Applied Geophysics*, *184*, 104224. https://doi.org/10.1016/j.jappgeo.2020.104224

Gabriels, P., Snieder, R., & Nolet, G. (1987). *IN SITU MEASUREMENTS OF SHEAR-WAVE VELOCITY IN SEDIMENTS WITH HIGHER-MODE RAYLEIGH WAVES**. 10.

Garofalo, F., Foti, S., Hollender, F., Bard, P. Y., Cornou, C., Cox, B. R., Dechamp, A., Ohrnberger, M., Perron, V., Sicilia, D., Teague, D., & Vergniault, C. (2016). InterPACIFIC project: Comparison of invasive and non-invasive methods for seismic site characterization. Part II: Inter-comparison between surface-wave and borehole methods. *Soil Dynamics and Earthquake Engineering*, *82*, 241-254. https://doi.org/10.1016/j.soildyn.2015.12.009

Garofalo, F., Foti, S., Hollender, F., Bard, P. Y., Cornou, C., Cox, B. R., Ohrnberger, M., Sicilia, D., Asten, M., Di Gulio, G., Forbriger, T., Guillier, B., Hayashi, K., Martin, A., Matsushima, S., Mercerat, D., Poggi, V., & Yamanaka, H. (2016). *InterPACIFIC project: Comparison of invasive and non-invasive methods for seismic site characterization. Part I: Intra-comparison of surface wave methods*. *82*, 222-240. https://doi.org/10.1016/j.soildyn.2015.12.010

Geometrics, I. (2009). *SeisImager/2D Seismic Refraction Data Analysis Software Manual and Examples Booklet (ver 3.3)*.

Ghofrani, H., & Atkinson, G. M. (2014). Site condition evaluation using horizontal-to-vertical response spectral ratios of earthquakes in the NGA-West 2 and Japanese databases. *Soil Dynamics and Earthquake Engineering*, *67*, 30-43. https://doi.org/10.1016/j.soildyn.2014.08.015

Goulet, C. A., Kishida, T., Ancheta, T. D., Cramer, C. H., Darragh, R. B., Silva, W. J., Hashash, Y. M., Harmon, J., Parker, G. A., Stewart, J. P., & Youngs, R. R. (2021). PEER NGA-East database. *Earthquake Spectra*, *37*(1_suppl), 1331-1353. https://doi.org/10.1177/87552930211015695

Gouveia, F., Viana da Fonseca, A., Gomes, R. C., & Teves-Costa, P. (2018). Deeper Vs profile constraining the dispersion curve with the ellipticity curve: A case study in Lower Tagus

Valley, Portugal. *Soil Dynamics and Earthquake Engineering*, *109*, 188-198. https://doi.org/10.1016/j.soildyn.2018.03.010

Greene, D. C., & Wolfe, W. J. (2000). *Superfund GIS - 1:250,000 Geology of Tennessee* (USGS Unnumbered Series) [Report]. Reston, VA. U.S. Geological Survey; Dataset. https://pubs.er.usgs.gov/publication/70046618

Grelle, G., & Guadagno, F. M. (2009). Seismic refraction methodology for groundwater level determination: "Water seismic index". *Journal of Applied Geophysics*, *68*(3), 301-320. https://doi.org/10.1016/j.jappgeo.2009.02.001

Griffiths, S. C., Cox, B. R., Rathje, E. M., & Teague, D. P. (2016). Surface-Wave Dispersion Approach for Evaluating Statistical Models That Account for Shear-Wave Velocity Uncertainty. *Journal of Geotechnical and Geoenvironmental Engineering*, *142*(11), 04016061. https://doi.org/10.1061/(ASCE)GT.1943-5606.0001552

Hagedoorn, J. G. (1959). The Plus-Minus Method of Interpreting Seismic Refraction Sections*. *Geophysical Prospecting*, *7*(2), 158-182. https://doi.org/10.1111/j.1365-2478.1959.tb01460.x

Haque, D. M. E., & Kamal, A. S. M. (2013). *Comparison of Shear Wave Velocity Derived from PS Logging and MASW –A Case Study of Mymensingh Pourashava, Bangladesh*. *26*, 84-97.

Hardeman, W. D., Miller, R. A., & Swingle, G. D. (1996). *Geologic map of Tennessee: Division of Geology, Tennessee Department of Environment and Conservation* [Geology Geol. Map]. Nashville, TN.

Hassani, B., & Atkinson, G. M. (2016). Applicability of the Site Fundamental Frequency as a VS30 Proxy for Central and Eastern North America. *Bulletin of the Seismological Society of America*, *106*(2), 653-664. https://doi.org/10.1785/0120150259

Heath, D. C., Wald, D. J., Worden, C. B., Thompson, E. M., & Smoczyk, G. M. (2020). A global hybrid VS30 map with a topographic slope–based default and regional map insets. *Earthquake Spectra*, *36*(3), 1570-1584. https://doi.org/10.1177/8755293020911137

Hepton, P. (1988). Shear wave velocity measurements during penetration testing. Penetration Testing in the UK. *Thomas Telford, London*, 275-278.

Herath, P., Stern, T., Savage, M., Bassett, D., Henrys, S., Barker, D., Avendonk, H. V., Bangs, N., Arnulf, A., Arai, R., Kodaira, S., & Mochizuki, K. (2020). *Using P- to S- wave conversions from controlled sources to determine the shear-wave velocity structure along Hikurangi Margin Forearc, New Zealand* (N.º EGU2020-11940). EGU2020. Copernicus Meetings. https://doi.org/10.5194/egusphere-egu2020-11940

Herrmann, R. B. (1987). *Computer programs in seismology*. St. Louis, MO. Saint Louis University.

Hobiger, M. (2011). *Polarization of surface waves: Characterization, inversion and application to seismic hazard assessment* [Phdthesis, Université de Grenoble]. https://tel.archives-ouvertes.fr/tel-00577887

Hobiger, M., Bard, P.-Y., Cornou, C., & Le Bihan, N. (2009). Single station determination of Rayleigh wave ellipticity by using the random decrement technique (RayDec). *Geophysical Research Letters*, *36*(14). https://doi.org/10.1029/2009GL038863

Hobiger, M., Cornou, C., Wathelet, M., Giulio, G. D., Knapmeyer-Endrun, B., Renalier, F., Bard, P.-Y., Savvaidis, A., Hailemikael, S., Le, B. N., Ohrnberger, M., & Theodoulidis, N.

(2013). Ground structure imaging by inversions of Rayleigh wave ellipticity: Sensitivity analysis and application to European strong-motion sites. *Geophysical Journal International*, *192*(1), 207-229. https://doi.org/10.1093/gji/ggs005

Hobiger, M., Le Bihan, N., Cornou, C., & Bard, P.-Y. (2009). Rayleigh wave ellipticity estimation from ambient seismic noise using single and multiple vector-sensor techniques. *2009 17th European Signal Processing Conference*, 2037-2041.

Hobiger, M., Le Bihan, N., Cornou, C., & Bard, P.-Y. (2012). Multicomponent Signal Processing for Rayleigh Wave Ellipticity Estimation: Application to Seismic Hazard Assessment. *IEEE Signal Processing Magazine*, *29*(3), 29-39. https://doi.org/10.1109/MSP.2012.2184969

Hollender, F., Cornou, C., Dechamp, A., Oghalaei, K., Renalier, F., Maufroy, E., Burnouf, C., Thomassin, S., Wathelet, M., Bard, P.-Y., Boutin, V., Desbordes, C., Douste-Bacqué, I., Foundotos, L., Guyonnet-Benaize, C., Perron, V., Régnier, J., Roullé, A., Langlais, M., & Sicilia, D. (2018). Characterization of site conditions (soil class, VS30, velocity profiles) for 33 stations from the French permanent accelerometric network (RAP) using surface-wave methods. *Bulletin of Earthquake Engineering*, *16*(6), 2337-2365. https://doi.org/10.1007/s10518-017-0135-5

Holzer, T. L., Padovani, A. C., Bennett, M. J., Noce, T. E., & Tinsley, J. C. (2005). Mapping NEHRP VS30 Site Classes. *Earthquake Spectra*, *21*(2), 353-370. https://doi.org/10.1193/1.1895726

Hosseini, M., Somerville, P., Skarlatoudis, A., Thio, H. K., & Bayless, J. (2016). *Constraining shallow subsurface S wave velocities with the initial portion of local P waves recorded at*

multiple seismic networks including ANSS and EarthScope Transportable Array in the CEUS. (G14AP00110; p. 58).

Hunter, J. A., & Crow, H. L. (2012). *Shear wave velocity measurement guidelines for Canadian seismic site characterization in soil and rock* (Natural Resources Canada). Canada. doi:10.4095/291753

ICC. (2015). *2015 IBC: International Building Code* (3rd ed., Vol. 1-2). Country Club Hills, IL : ICC, International Code Council, Inc., 2015. ©2014.

IRIS. (s. f.). *IRIS: IRISWS: Timeseries: Docs: v. 1: Builder*. Recuperado 16 de mayo de 2021, de https://service.iris.edu/irisws/timeseries/docs/1/builder/

Ivanov, J., Park, C. B., Miller, R. D., Xia, J., Hunter, J. A., Good, R. L., & Burns, R. A. (2000). Joint analysis of surface-wave and refraction events from river-bottom sediments. *SEG Technical Program Expanded Abstracts 2000,* 1307-1310. https://doi.org/10.1190/1.1815636

Iwahashi, J., & Pike, R. (2007). *Automated classifications of topography from DEMs by an unsupervised nested-means algorithm and a three-part geometric signature*. *86,* 409-440. https://doi.org/10.1016/j.geomorph.2006.09.012

Jung, J., & Kim, K. Y. (2014). Site Characterization using Shear-Wave Velocities Inverted from Rayleigh-Wave Dispersion in Chuncheon, Korea. *Geophysics and Geophysical Exploration*, *17*(1), 1-10. https://doi.org/10.7582/GGE.2014.17.1.001

Kalkan, E. (2016). An Automatic *P* -Phase Arrival-Time Picker. *Bulletin of the Seismological Society of America*, *106*(3), 971-986. https://doi.org/10.1785/0120150111

Kaneko, F., Kanemori, T., & Tonouchi, K. (1990). Low-Frequency Shear Wave Logging in Unconsolidated Formations for Geotechnical Applications. *ASTM Special Technical Publication 1101, ASTM*, 79-98.

Kang, S., Kim, B., Park, H.-J., & Lee, J. (2020). *Automated procedure for estimating VS30 utilizing P-wave seismograms and its application to Japan*. *264*. https://doi.org/10.1016/j.enggeo.2019.105388

Kang, S. Y., Kim, K.-H., & Kim, B. (2021). Assessment of seismic vulnerability using the horizontal-to-vertical spectral ratio (HVSR) method in Haenam, Korea. *Geosciences Journal*, *25*(1), 71-81. https://doi.org/10.1007/s12303-020-0040-9

Kanlı, A. I., Tildy, P., Prónay, Z., Pınar, A., & Hermann, L. (2006). VS30 mapping and soil classification for seismic site effect evaluation in Dinar region, SW Turkey. *Geophysical Journal International*, *165*(1), 223-235. https://doi.org/10.1111/j.1365-246X.2006.02882.x

Kearey, P., Brooks, M., & Hill, I. (2002). *An Introduction to Geophysical Exploration*. John Wiley & Sons.

Kim, B., Hashash, Y. M. A., Rathje, E. M., Stewart, J. P., Ni, S., Somerville, P. G., Kottke, A. R., Silva, W. J., & Campbell, K. W. (2016). Subsurface Shear Wave Velocity Characterization Using P-Wave Seismograms in Central and Eastern North America. *Earthquake Spectra*, *32*(1), 143-169. https://doi.org/10.1193/123013EQS299M

Kim, J., Kim, B., & Cho, H. (2020). Shear Wave Velocity Estimation in Korea Using P-Wave Seismograms. *KSCE Journal of Civil Engineering*, *24*(12), 3650-3658. https://doi.org/10.1007/s12205-020-0752-4

King, E. R., & Zietz, I. (1978). The New York-Alabama lineament: Geophysical evidence for a major crustal break in the basement beneath the Appalachian basin. *Geology*, *6*(5), 312. https://doi.org/10.1130/0091-7613(1978)6<312:TNYLGE>2.0.CO;2

Kircher, C. A., Rezaeian, S., & Luco, N. (2019). Proposed Multi-Period Response Spectra and Ground Motion Requirements of the 2020 NEHRP Recommended Provisions and ASCE 7-22. *2019 SEAOC convention proceedings*.

Kirkpatrick, S., Gelatt, C. D., & Vecchi, M. P. (1983). *Optimization by Simulated Annealing*. *220*(4598), 671-680.

Konno, K., & Ohmachi, T. (1998). Ground-motion characteristics estimated from spectral ratio between horizontal and vertical components of microtremor. *Bulletin of the Seismological Society of America*, *88*(1), 228-241. https://doi.org/10.1785/BSSA0880010228

Kottke, A. (2012). *Development of Geologic Site Classes for Seismic Site*. 11.

Kramer, S. L. (1996). *Geotechnical Earthquake Engineering*. Upper Saddle River, New Jersey. Prentice-Hall. https://books.google.com/books/about/Geotechnical_Earthquake_Engineering.html?id=sC22QgAACAAJ

Kwak, D. Y., Brandenberg, S. J., Mikami, A., & Stewart, J. P. (2015). Prediction Equations for Estimating Shear-Wave Velocity from Combined Geotechnical and Geomorphic Indexes Based on Japanese Data Set. *Bulletin of the Seismological Society of America*, *105*(4), 1919-1930. https://doi.org/10.1785/0120140326

Lachetl, C., & Bard, P.-Y. (1994). Numerical and Theoretical Investigations on the Possibilities and Limitations of Nakamura's Technique. *Journal of Physics of the Earth*, *42*(5), 377-397. https://doi.org/10.4294/jpe1952.42.377

Lee, J., Kim, K.-H., Kang, S. Y., Son, M., & Kim, B. (2022). Shear-wave velocity map for Pohang Basin, South Korea, based on the P-wave seismogram method. *Earthquake Spectra*, 87552930221076530. https://doi.org/10.1177/87552930221076532

Leong, E. C., & Cheng, Z. Y. (2016). Effects of Confining Pressure and Degree of Saturation on Wave Velocities of Soils. *International Journal of Geomechanics*, *16*(6). https://doi.org/10.1061/(ASCE)GM.1943-5622.0000727

Lin, C.-P., Chang, C.-C., & Chang, T.-S. (2004). The use of MASW method in the assessment of soil liquefaction potential. *Soil Dynamics and Earthquake Engineering*, *24*(9), 689-698. https://doi.org/10.1016/j.soildyn.2004.06.012

Lin, S., Gucunski, N., Shams, S., & Wang, Y. (2021). Seismic Site Classification from Surface Wave Data to Vs,30 without Inversion. *Journal of Geotechnical and Geoenvironmental Engineering*, *147*(6), 04021029. https://doi.org/10.1061/(ASCE)GT.1943-5606.0002526

Liu, L., & Zoback, M. D. (1997). Lithospheric strength and intraplate seismicity in the New Madrid seismic zone. *Tectonics*, *16*(4), 585-595. https://doi.org/10.1029/97TC01467

Lomax, A., & Snieder, R. (1994). Finding sets of acceptable solutions with a genetic algorithm with application to surface wave group dispersion in Europe. *Geophysical Research Letters*, *21*(24), 2617-2620. https://doi.org/10.1029/94GL02635

Luco, N., Rezaeian, S., Rukstales, K. S., Powers, P. M., Shumway, A. M., Martinez, E. M., & Smoczyk, G. M. (2021). *Gridded earthquake ground motions for the 2020 NEHRP Recommended Seismic Provisions and 2022 ASCE/SEI 7 Standard* [Data set]. U.S. Geological Survey. https://doi.org/10.5066/P9I0R4O6

Malischewsky, P. G., & Scherbaum, F. (2004). Love's formula and H/V-ratio (ellipticity) of Rayleigh waves. *Wave Motion*, *40*(1), 57-67. https://doi.org/10.1016/j.wavemoti.2003.12.015

ManuelHobiger. (2021). *ManuelHobiger/RayDec: RayDec 2.0*. Zenodo. https://doi.org/10.5281/zenodo.5534777

Maranò, S., Reller, C., Loeliger, H.-A., & Fäh, D. (2012). Seismic waves estimation and wavefield decomposition: Application to ambient vibrations: Seismic waves estimation. *Geophysical Journal International*, *191*(1), 175-188. https://doi.org/10.1111/j.1365-246X.2012.05593.x

Martínez-Pagán, P., Navarro, M., Pérez-Cuevas, J., Alcalá, F. j., García-Jerez, A., & Sandoval-Castaño, S. (2014). Shear-wave velocity based seismic microzonation of Lorca city (SE Spain) from MASW analysis. *Near Surface Geophysics*, *12*(6), 739-750. https://doi.org/10.3997/1873-0604.2014032

Martínez-Pagán, P., Navarro, M., Pérez-Cuevas, J., Alcalá, F. J., García-Jerez, A., & Vidal, F. rancisco. (2018). Shear-wave velocity structure from MASW and SPAC methods: The case of Adra town, SE Spain. *Near Surface Geophysics*, *16*(3), 356-371. https://doi.org/10.3997/1873-0604.2018012

Matsuoka, M., Wakamatsu, K., Fujimoto, K., & Midorikawa, S. (2006). *AVERAGE SHEAR-WAVE VELOCITY MAPPING USING JAPAN ENGINEERING GEOMORPHOLOGIC CLASSIFICATION MAP*. *23*(1), 57s-68s.

McDonald, F. J., Angona, F. A., Mills, R. L., Sengbush, R. L., Van Nostrand, R. G., & White, J. E. (1958). *Attenuation of Shear and Compressional Waves in Pierre Shale*. *23*(3), 421-439.

Mcmechan, G. (1981). Analysis of dispersive waves by wave field transformation. *Geophysics*, *46*. https://doi.org/10.1190/1.1441225

McPhillips, D. F., Herrick, J. A., Ahdi, S., Yong, A. K., & Haefner, S. (2020). *Updated Compilation of VS30 Data for the United States* [Data set]. U.S. Geological Survey. https://doi.org/10.5066/P9H5QEAC

Mhaske, S. Y., & Choudhury, D. (2011). Geospatial contour mapping of shear wave velocity for Mumbai city. *Natural Hazards*, *59*(1), 317-327. https://doi.org/10.1007/s11069-011-9758-z

Miao, Y., Shi, Y., & Wang, S.-Y. (2018). Estimating Near-Surface Shear Wave Velocity Using the P-Wave Seismograms Method in Japan. *Earthquake Spectra*, *34*(4), 1955-1971. https://doi.org/10.1193/011818EQS015M

Michel, C., Edwards, B., Poggi, V., Burjánek, J., Roten, D., Cauzzi, C., & Fäh, D. (2014). Assessment of Site Effects in Alpine Regions through Systematic Site Characterization of Seismic Stations. *Bulletin of the Seismological Society of America*, *104*(6), 2809-2826. https://doi.org/10.1785/0120140097

Miller, R. D., Xia, J., Park, C. B., & Ivanov, J. M. (1999). Multichannel analysis of surface waves to map bedrock. *The Leading Edge*, *18*(12), 1392-1396. https://doi.org/10.1190/1.1438226

Nakamura, Y. (2019). What Is the Nakamura Method? *Seismological Research Letters*. https://doi.org/10.1785/0220180376

NEHRP. (2020). *NEHRP Recommended Seismic Provisions for New Buildings and Other Structures: Vol. Volume I: Part 1 Provisions, Part 2 Commentary* (FEMA P-2082-1). United States of America: National Earthquake Hazard Reduction Programs.

Ni, S., Li, Z., & Somerville, P. (2014). *Estimating Subsurface Shear Velocity with Radial to Vertical Ratio of Local P Waves*. *85*(1), 82-90. https://doi.org/10.1785/0220130128

Nishida, K., Kawakatsu, H., & Obara, K. (2008). Three-dimensional crustal *S* wave velocity structure in Japan using microseismic data recorded by Hi-net tiltmeters. *Journal of Geophysical Research*, *113*(B10), B10302. https://doi.org/10.1029/2007JB005395

Nolet, G. (1981). Linearized Inversion of (Teleseismic) Data. En R. Cassinis (Ed.), *The Solution of the Inverse Problem in Geophysical Interpretation* (pp. 9-37). Springer US. https://doi.org/10.1007/978-1-4684-3962-5_2

Ohya, S., Ogura, K., & Imai, T. (1984, mayo 7). *The Suspension PS Velocity Logging System*. Offshore Technology Conference. https://doi.org/10.4043/4680-MS

Palmer, D. (1980). The Generalized Reciprocal Method of Seismic Refraction Interpretation. *General Series*. https://library.seg.org/doi/abs/10.1190/1.9781560802426

Palmer, M. W. (1990). SPATIAL SCALE AND PATTERNS OF SPECIES-ENVIRONMENT RELATIONSHIPS IN HARDWOOD FOREST OF THE NORTH CAROLINA PIEDMONT. *Coenoses*, *5*(2), 79-87.

Pamuk, E., Özdağ, Ö. C., & Akgün, M. (2019). Soil characterization of Bornova Plain (Izmir, Turkey) and its surroundings using a combined survey of MASW and ReMi methods and Nakamura's (HVSR) technique. *Bulletin of Engineering Geology and the Environment*, *78*(4), 3023-3035. https://doi.org/10.1007/s10064-018-1293-7

Pamuk, E., Özdağ, Ö. C., Özyalın, Ş., & Akgün, M. (2017). Soil characterization of Tınaztepe region (İzmir/Turkey) using surface wave methods and nakamura (HVSR) technique. *Earthquake Engineering and Engineering Vibration*, *16*(2), 447-458. https://doi.org/10.1007/s11803-017-0392-y

Park, C. B., Miller, R. D., Xia, J., & Ivanov, J. (2000). Multichannel seismic surface-wave methods for geotechnical applications. *In: Proceedings of the First Int. Conf. on the App. of Geophys. : Methodologies to Transportation Facilities and Infrastructure*, 11-15.

Park, S., & Elrick, S. (1998). Predictions of shear-wave velocities in southern California using surface geology. *Bulletin of the Seismological Society of America*, *88*(3), 677-685. https://doi.org/10.1785/BSSA0880030677

Parker, G. A., Harmon, J. A., Stewart, J. P., Hashash, Y. M. A., Kottke, A. R., Rathje, E. M., Silva, W. J., & Campbell, K. W. (2017). Proxy-Based V_{S30} Estimation in Central and Eastern North America. *Bulletin of the Seismological Society of America*, *107*(1), 117-131. https://doi.org/10.1785/0120160101

Pickett, G. R. (1963). Acoustic Character Logs and their Applications in Formation Evaluation. *Jour. of petroleum Technology*, *15*, 659-667.

Poggi, V., & Fäh, D. (2010). Estimating Rayleigh wave particle motion from three-component array analysis of ambient vibrations. *Geophysical Journal International*, *180*(1), 251-267. https://doi.org/10.1111/j.1365-246X.2009.04402.x

Poggi, V., Fäh, D., Burjanek, J., & Giardini, D. (2012). The use of Rayleigh-wave ellipticity for site-specific hazard assessment and microzonation: Application to the city of Lucerne, Switzerland. *Geophysical Journal International*, *188*(3), 1154-1172. https://doi.org/10.1111/j.1365-246X.2011.05305.x

Powell, C. A., Bollinger, G. A., Chapman, M. C., Sibol, M. S., Johnston, A. C., & Wheeler, R. L. (1994). A Seismotectonic Model for the 300-Kilometer-Long Eastern Tennessee Seismic Zone. *Science*, *264*(5159), 686-688.

Powell, C. A., & Thomas, W. A. (2016). Grenville basement structure associated with the Eastern Tennessee seismic zone, southeastern USA. *Geology*, *44*(1), 39-42. https://doi.org/10.1130/G37269.1

Rahman, Md. Z., Kamal, A. S. M. M., & Siddiqua, S. (2018). Near-surface shear wave velocity estimation and Vs30mapping for Dhaka City, Bangladesh. *Natural Hazards*, *92*(3), 1687-1715. https://doi.org/10.1007/s11069-018-3266-3

Rahman, Md. Z., Siddiqua, S., & Kamal, A. S. M. M. (2016). Shear wave velocity estimation of the near-surface materials of Chittagong City, Bangladesh for seismic site characterization. *Journal of Applied Geophysics*, *134*, 210-225. https://doi.org/10.1016/j.jappgeo.2016.09.006

Raikes, S. A., & White, R. E. (1984). Measurements of Earth Attenuation from Downhole and Surface Seismic Recordings*. *Geophysical Prospecting*, *32*(5), 892-919. https://doi.org/10.1111/j.1365-2478.1984.tb00745.x

Redpath, B. B. (1973). *Seismic refraction exploration for engineering site investigation* (EERL-TR-E-73-4; Army Engineer Waterways Experiment Station, Livermore, p. 70). Explosive Excavation Research Lab.

Reynolds, J. M. (2011). *An Introduction to Applied and Environmental Geophysics*. John Wiley & Sons.

Richart, F. E., Hall, J. R., & Woods, R. D. (1970). *VIBRATIONS OF SOILS AND FOUNDATIONS*. https://trid.trb.org/view/123341

Rix, G. J., Hebeler, G. L., & Orozco, M. C. (2002). *Near-surface VsProfi/ing in the New Madrid Seismic Zone Using Surface-wave Methods*. *73*(3), 380-392.

Robertson, P. K., Campanella, R. G., Gillespie, D., & Rice, A. (1986). *Seismic CPT to Measure in Situ Shear Wave Velocity*. *112(8)*, 791-803.

Rosa-Cintas, S., Clavero, D., Delgado, J., López-Casado, C., Galiana-Merino, J. J., & Garrido, J. (2017). Characterization of the shear wave velocity in the metropolitan area of Málaga (S Spain) using the H/V technique. *Soil Dynamics and Earthquake Engineering, 92*, 433-442. https://doi.org/10.1016/j.soildyn.2016.10.016

Sahadewa, A., Zekkos, D., & Woods, R. D. (2012). *Observations from the Implementation of a Combined Active and Passive Surface Wave Based Methodology*. 2786-2795. https://doi.org/10.1061/9780784412121.285

Sambridge, M. (1999). Geophysical inversion with a neighbourhood algorithm—I. Searching a parameter space. *Geophysical Journal International*, *138*(2), 479-494. https://doi.org/10.1046/j.1365-246X.1999.00876.x

Sambridge, M., & Drijkoningen, G. (1992). Genetic algorithms in seismic waveform inversion. *Geophysical Journal International*, *109*(2), 323-342. https://doi.org/10.1111/j.1365-246X.1992.tb00100.x

Science Learning Hub – Pokapū Akoranga Pūtaiao. (2014). *Earth waves* [Retieved from]. Science Learning Hub. https://www.sciencelearn.org.nz/images/353-earth-waves

Sen, M. K., Datta-Gupta, A., Stoffa, P. L., Lake, L. W., & Pope, G. A. (1995). Stochastic Reservoir Modeling Using Simulated Annealing and Genetic Algorithms. *SPE Formation Evaluation*, *10*(01), 7.

SESAME. (2004). *Guidelines for the Implementation of the H/V Spectral Ratio Technique on Ambient Vibrations: Measurements, Processing, and Interpretation.* (European

Commission – Research General Directorate N.º EVG1-CT-2000-00026 SESAME; WP12 – Deliverable D23.12). SESAME European Research Project.

Sexton, J. L., & B, P. (1986). Evidence for recurrent faulting in the New Madrid seismic zone from Mini-Sosie high-resolution reflection data. *Geophysics*, 1760-1788.

Singh, M., Duggal, S. K., & Singh, V. P. (2021). A Study to Establish Regression Correlation Between Shear Wave Velocity and "N"-Value for Varanasi City, India. *Proceedings of the National Academy of Sciences, India Section A: Physical Sciences*, *91*(2), 405-417. https://doi.org/10.1007/s40010-020-00686-w

Socco, L. V., Foti, S., & Boiero, D. (2010). Surface-wave analysis for building near-surface velocity models—Established approaches and new perspectives. *GEOPHYSICS*, *75*(5), 75A83-75A102. https://doi.org/10.1190/1.3479491

Stanko, D., & Markušić, S. (2020). An empirical relationship between resonance frequency, bedrock depth and VS30 for Croatia based on HVSR forward modelling. *Natural Hazards*, *103*(3), 3715-3743. https://doi.org/10.1007/s11069-020-04152-z

Stoffa, P. L., & Sen, M. K. (1991). *Nonlinear multiparameter optimization using genetic algorithms: Inversion of plane-wave seismograms*. *56*(11), 1794-1810.

Stokoe, K. H., & Santamarina, J. C. (2000, noviembre 19). *Seismic-Wave-Based Testing In Geotechnical Engineering*. ISRM International Symposium. https://onepetro.org/ISRMIS/proceedings/IS00/All-IS00/ISRM-IS-2000-038/50787

Stümpel, H., Kähler, S., Meissner, R., & Milkereit, B. (1984). The Use of Seismic Shear Waves and Compressional Waves for Lithological Problems of Shallow Sediments*. *Geophysical Prospecting*, *32*(4), 662-675. https://doi.org/10.1111/j.1365-2478.1984.tb01712.x

Suemoto, Y., Ikeda, T., Tsuji, T., & Iio, Y. (2020). Identification of a nascent tectonic boundary in the San-in area, southwest Japan, using a 3D S-wave velocity structure obtained by ambient noise surface wave tomography. *Earth, Planets and Space*, *72*(1), 15. https://doi.org/10.1186/s40623-020-1139-y

SurfSeis. (2010). *User's Manual v 3.05*. Kansas Geological Survey.

Symes, W. W. (2009). The seismic reflection inverse problem. *Inverse Problems*, *25*(12), 123008. https://doi.org/10.1088/0266-5611/25/12/123008

Szabo, M. W., Osborne, E. W., Coperland Jr., C. W., & Neathery, T. L. (1988). *Geologic Map of Alabama* [Special Map 220]. Geological Survey of Alabama.

Tanimoto, T., Yano, T., & Hakamata, T. (2013). An approach to improve Rayleigh-wave ellipticity estimates from seismic noise: Application to the Los Angeles Basin. *Geophysical Journal International*, *193*(1), 407-420. https://doi.org/10.1093/gji/ggs123

Tarantola, A. (1984). Linearized Inversion of Seismic Reflection Data*. *Geophysical Prospecting*, *32*(6), 998-1015. https://doi.org/10.1111/j.1365-2478.1984.tb00751.x

Teague, D. P., & Cox, B. R. (2016). *Site response implications associated with using non-unique Vs profiles from surface wave inversion in comparison with other commonly used methods of accounting for Vs uncertainty*. *91*, 81-103. https://doi.org/10.1016/j.soildyn.2016.07.028

Tuttle, M. P. (2002). The Earthquake Potential of the New Madrid Seismic Zone. *Bulletin of the Seismological Society of America*, *92*(6), 2080-2089. https://doi.org/10.1785/0120010227

TVA, T. V. A. (2007). *Bellefonte Nuclear Plant, Units 3 & 4 COL Application Part 2, FSAR*.

USGS. (2018). *2018 Long-term National Seismic Hazard Map | U.S. Geological Survey*. U.S. Geological Survey. https://www.usgs.gov/media/images/2018-long-term-national-seismic-hazard-map

USGS. (2022). *The New Madrid Seismic Zone | U.S. Geological Survey*. https://www.usgs.gov/programs/earthquake-hazards/new-madrid-seismic-zone?qt-science_center_objects=0

van Ginkel, J., Ruigrok, E., & Herber, R. (2020). Using horizontal-to-vertical spectral ratios to construct shear-wave velocity profiles. *Solid Earth*, *11*(6), 2015-2030. https://doi.org/10.5194/se-11-2015-2020

Vidale, R. F. (1964). *The Dispersion of Stress Waves in Layered Media Overlaying a Half Space of Lesser Acoustic Rigidity* [Ph.D., The University of Wisconsin - Madison]. United States -- Wisconsin. https://www.proquest.com/docview/302279023/citation/72388E7723904234PQ/1

Wald, D. J., & Allen, T. I. (2007). Topographic Slope as a Proxy for Seismic Site Conditions and Amplification. *Bulletin of the Seismological Society of America*, *97*(5), 1379-1395. https://doi.org/10.1785/0120060267

Wang, P., Zimmaro, P., Ahdi, S. K., & Kwak, D. Y. (2019). *Shear Wave Velocity Database and Its Application for Analysis of Non-Ergodic Site Amplification Effects* (p. 126). University of California.

Wang, R., Schurr, B., Milkereit, C., Shao, Z., & Jin, M. (2011). An Improved Automatic Scheme for Empirical Baseline Correction of Digital Strong-Motion Records. *Bulletin of the Seismological Society of America*, *101*(5), 2029-2044. https://doi.org/10.1785/0120110039

Wathelet. (2005). *Array recordings of ambient vibrations:surface-wave inversion* [Ph.D Thesis]. Belgium. Liege University.

Wathelet, M. (2008). An improved neighborhood algorithm: Parameter conditions and dynamic scaling. *Geophysical Research Letters*, *35*(9), L09301. https://doi.org/10.1029/2008GL033256

Wathelet, M., Chatelain, J., Cornou, C., Giulio, G. D., Guillier, B., Ohrnberger, M., & Savvaidis, A. (2020a). Geopsy: A User-Friendly Open-Source Tool Set for Ambient Vibration Processing. *Seismological Research Letters*, *91*(3), 1878-1889. https://doi.org/10.1785/0220190360

Wathelet, M., Chatelain, J., Cornou, C., Giulio, G. D., Guillier, B., Ohrnberger, M., & Savvaidis, A. (2020b). Geopsy: A User-Friendly Open-Source Tool Set for Ambient Vibration Processing. *Seismological Research Letters*, *91*(3), 1878-1889. https://doi.org/10.1785/0220190360

Wathelet, M., Jongmans, D., & Ohrnberger, M. (2004). Surface-wave inversion using a direct search algorithm and its application to ambient vibration measurements. *Near Surface Geophysics*, *2*(4), 211-221. https://doi.org/10.3997/1873-0604.2004018

Wei-Jun W., Qi-Fu C., Cheng Q. I., Yi-Pei T. a. N., Xiang Z., & Qing-Yun Z. (2011). The feasibilities and limitations to explore the near-surface structure with microtremor HVSR method—A case in baoding area of Hebei Province, China. *Chinese Journal of Geophysics*, *54*(7), 1783-1797. https://doi.org/10.3969/j.issn.0001-5733.2011.07.012

Wills, C. J., Gutierrez, C. I., Perez, F. G., & Branum, D. M. (2015). A Next Generation VS30 Map for California Based on Geology and Topography. *Bulletin of the Seismological Society of America*, *105*(6), 3083-3091. https://doi.org/10.1785/0120150105

Workman, E., Lin, F.-C., & Koper, K. D. (2017). Determination of Rayleigh wave ellipticity across the Earthscope Transportable Array using single-station and array-based processing of ambient seismic noise. *Geophysical Journal International*, *208*(1), 234-245. https://doi.org/10.1093/gji/ggw381

Xia, J. (2022). *Delineating Subsurface Features with the MASW Method at Maxwell AFB in Montgomery, Alabama*.

Yaghmaei-Sabegh, S., & Rupakhety, R. (2020). A new method of seismic site classification using HVSR curves: A case study of the 12 November 2017 Mw 7.3 Ezgeleh earthquake in Iran. *Engineering Geology*, *270*, 105574. https://doi.org/10.1016/j.enggeo.2020.105574

Yilar, E., Baise, L. G., & Ebel, J. E. (2017). Using H/V measurements to determine depth to bedrock and Vs30 in Boston, Massachusetts. *Engineering Geology*, *217*, 12-22. https://doi.org/10.1016/j.enggeo.2016.12.002

Yong, A., Hough, S. E., Iwahashi, J., & Braverman, A. (2012). A Terrain-Based Site-Conditions Map of California with Implications for the Contiguous United States. *Bulletin of the Seismological Society of America*, *102*(1), 114-128. https://doi.org/10.1785/0120100262

Yong, A., Thompson, E. M., Wald, D. J., Knudsen, K. L., Odum, J. K., Stephenson, W. J., & Haefner, S. (2016). Compilation of VS30 Data for the United States. En *Compilation of VS30 Data for the United States* (USGS Numbered Series N.º 978; Data Series, Vol. 978, p. 16). U.S. Geological Survey. https://doi.org/10.3133/ds978

Zalachoris, G., Rathje, E. M., & Paine, J. G. (2017). VS30 Characterization of Texas, Oklahoma, and Kansas Using the P-Wave Seismogram Method. *Earthquake Spectra*, *33*(3), 943-961. https://doi.org/10.1193/102416eqs179m

Zhao, D., Hasegawa, A., & Horiuchi, S. (1992). Tomographic imaging of P and S wave velocity structure beneath northeastern Japan. *Journal of Geophysical Research: Solid Earth*, *97*(B13), 19909-19928. https://doi.org/10.1029/92JB00603

APPENDIX A: BORING LOGS INFORMATION

ASEL (B-1)

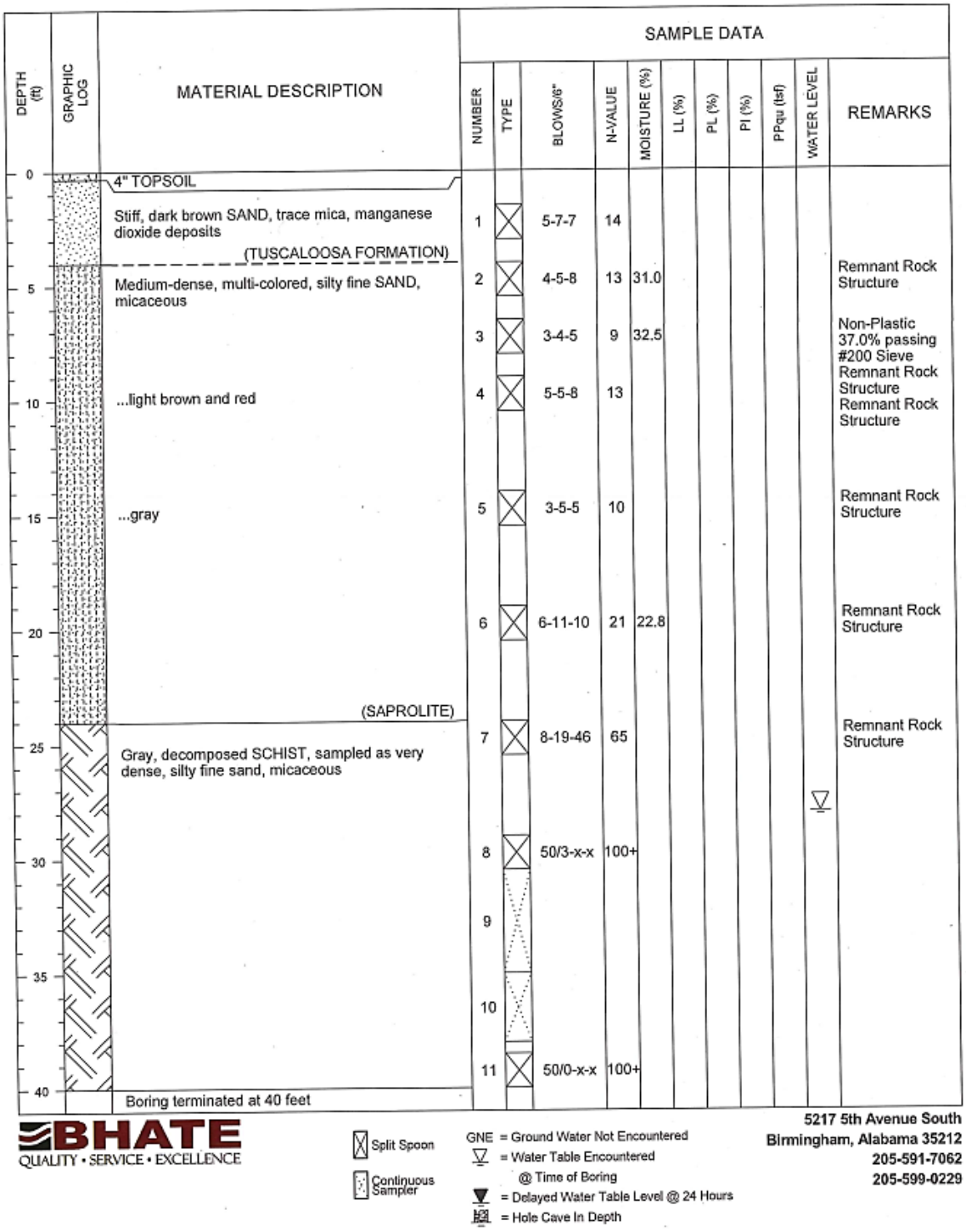

ASEL (B-8)

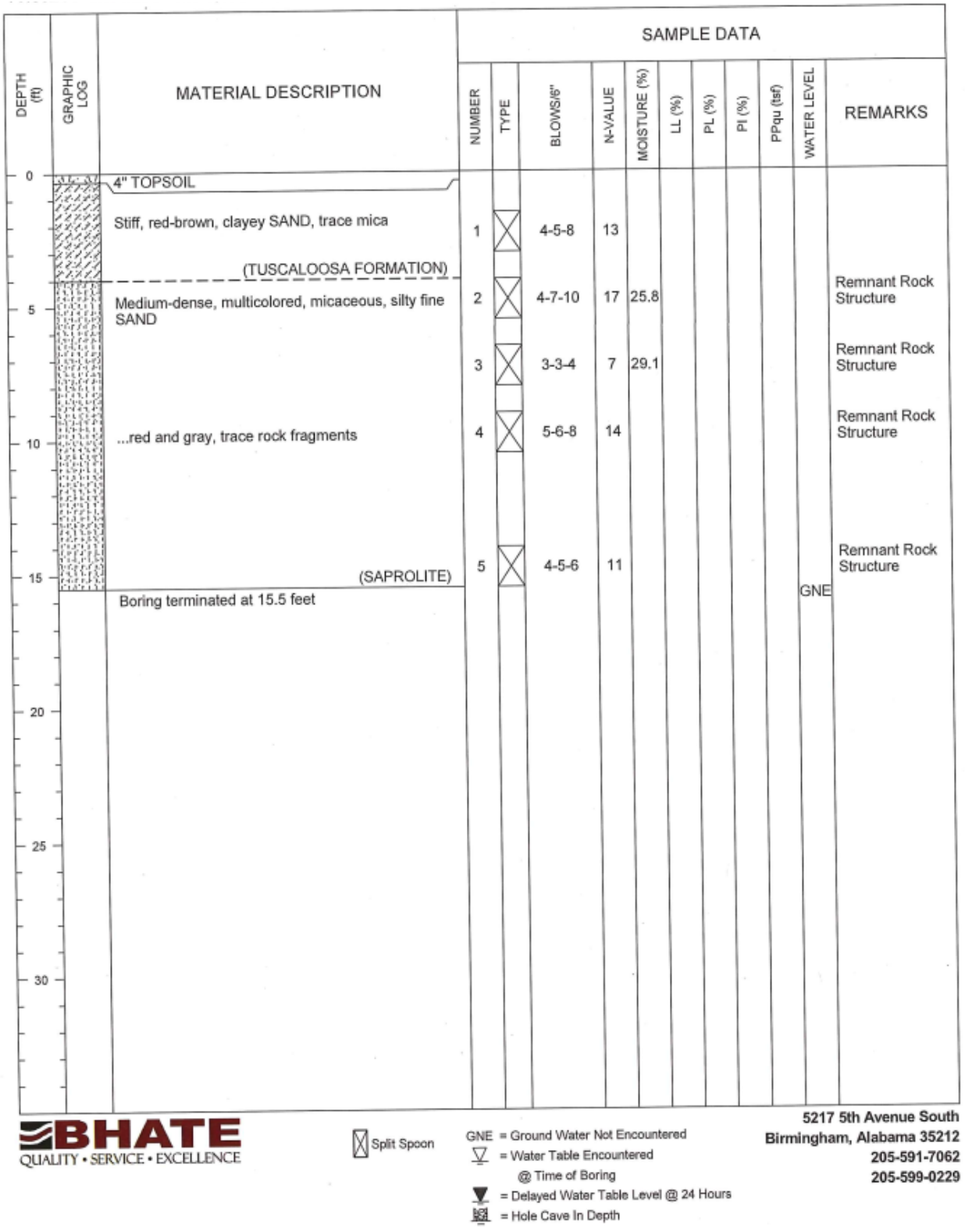
SAMPLE DATA
DEPTH (ft)
GRAPHIC LOG
MATERIAL DESCRIPTION
NUMBER
TYPE
BLOWS/6"
N-VALUE
MOISTURE (%)
LL (%)
PL (%)
PI (%)
PPqu (tsf)
WATER LEVEL
REMARKS
0
4" TOPSOIL
Stiff, red-brown, clayey SAND, trace mica
1
4-5-8
13
(TUSCALOOSA FORMATION)
Medium-dense, multicolored, micaceous, silty fine SAND
2
4-7-10
17
25.8
Remnant Rock Structure
5
3
3-3-4
7
29.1
Remnant Rock Structure
...red and gray, trace rock fragments
4
5-6-8
14
Remnant Rock Structure
10
(SAPROLITE)
5
4-5-6
11
Remnant Rock Structure
15
GNE
Boring terminated at 15.5 feet
20
25
30
BHATE
QUALITY • SERVICE • EXCELLENCE
Split Spoon
GNE = Ground Water Not Encountered
= Water Table Encountered @ Time of Boring
= Delayed Water Table Level @ 24 Hours
= Hole Cave In Depth
5217 5th Avenue South
Birmingham, Alabama 35212
205-591-7062
205-599-0229

B-2

STA 169+65, 42.5 FEET LEFT OF SR-219 SURVEY CL

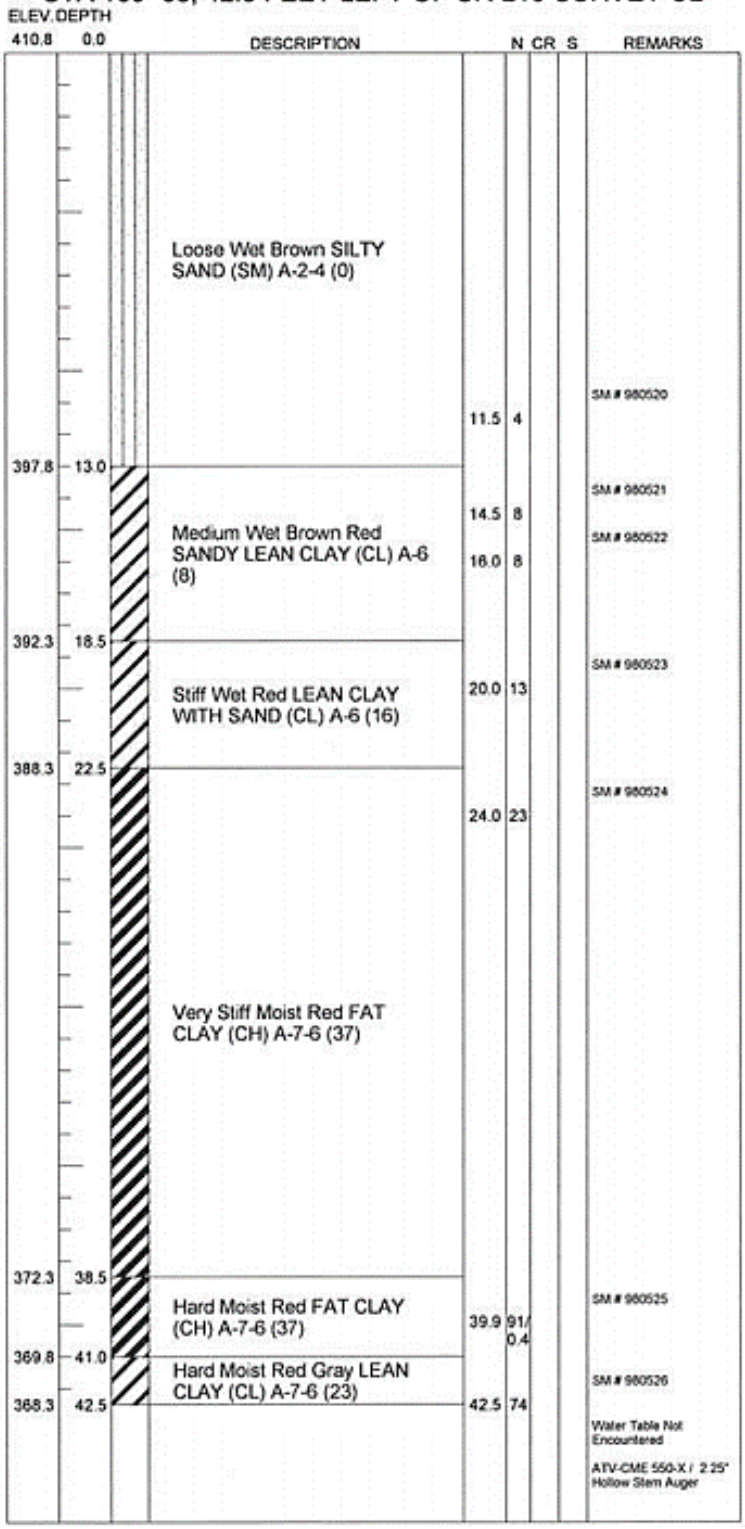

B-1-100

STA 168+19, 33 FEET LEFT OF SR-219 SURVEY CL

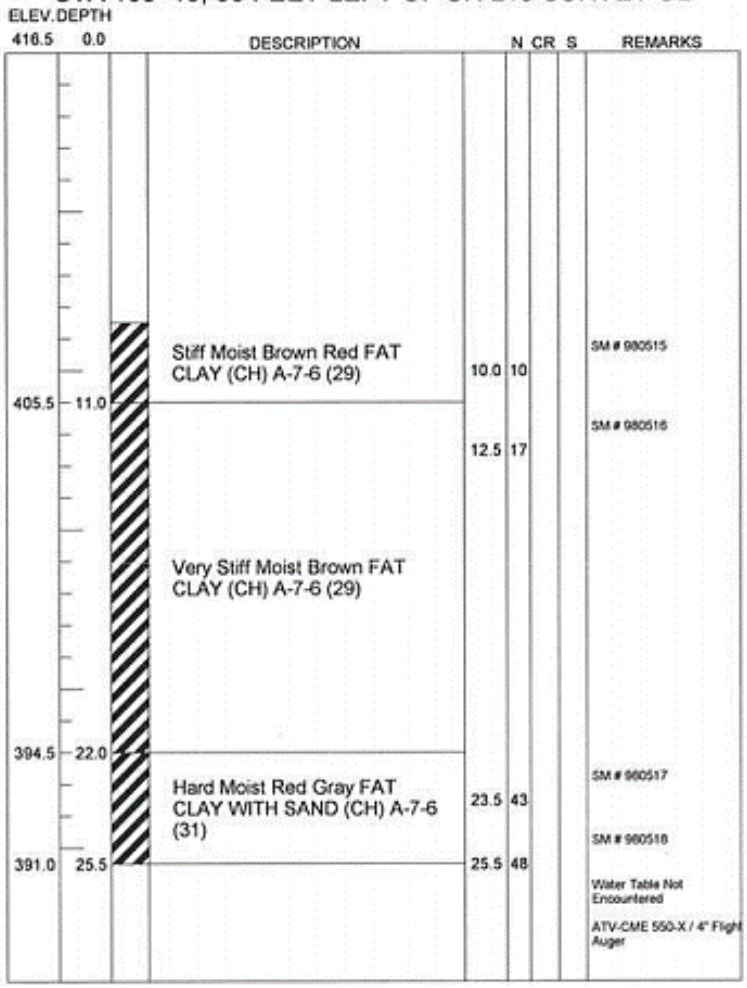

APPENDIX B: NON-INVERSION ITERATIONS

ASEL

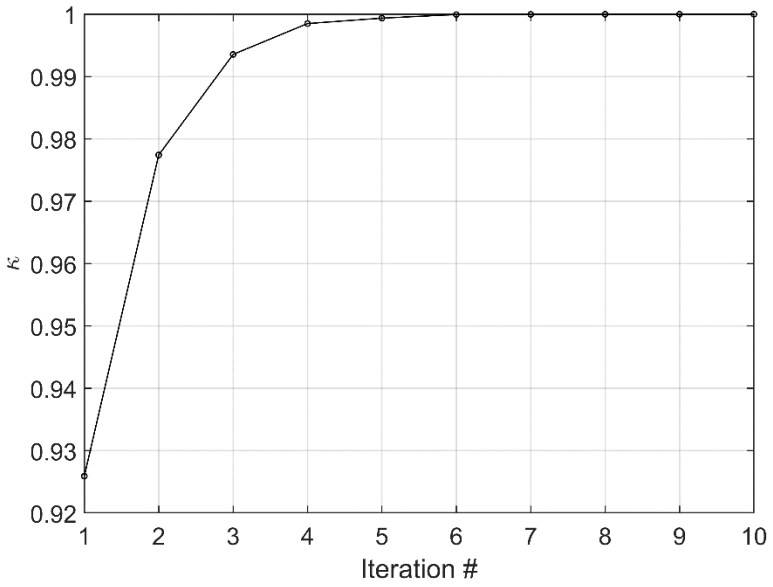

TU01

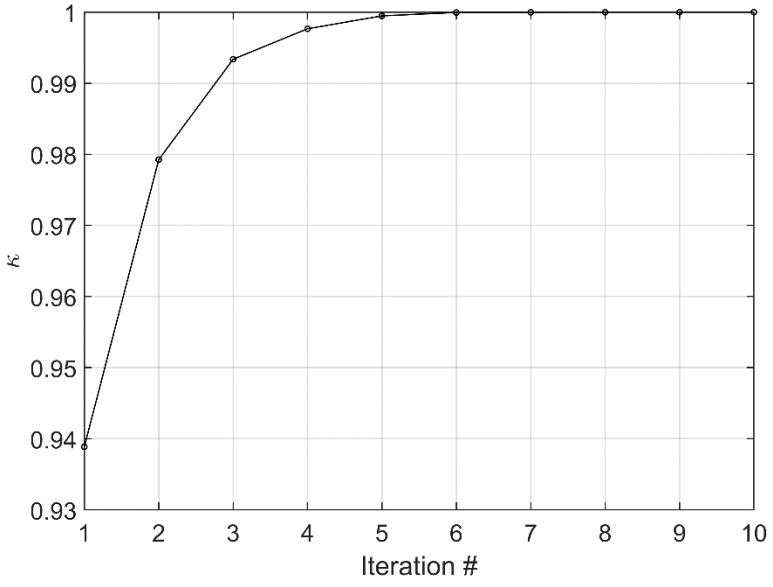

SR-21

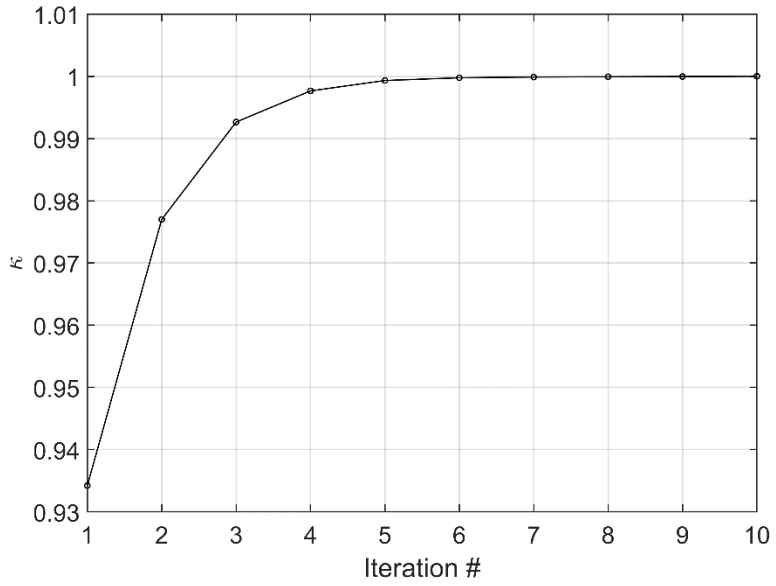
1.01
1
0.99
0.98
0.97
0.96
0.95
0.94
0.93
κ
1
2
3
4
5
6
7
8
9
10
Iteration #

SR-219

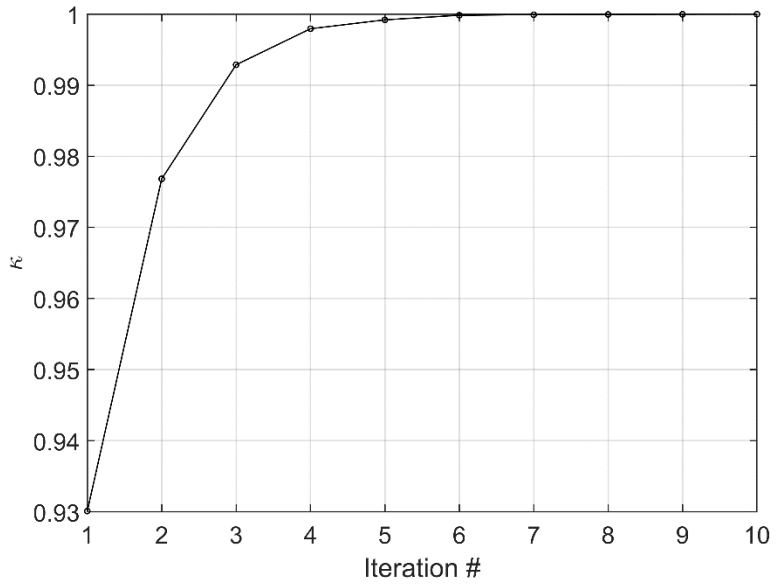
1
0.99
0.98
0.97
0.96
0.95
0.94
0.93
κ
1
2
3
4
5
6
7
8
9
10
Iteration #

Station X50B

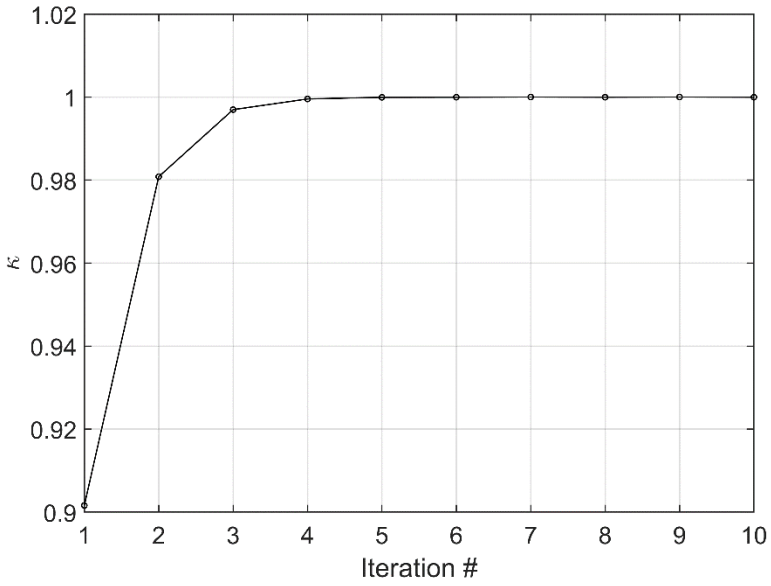

251A

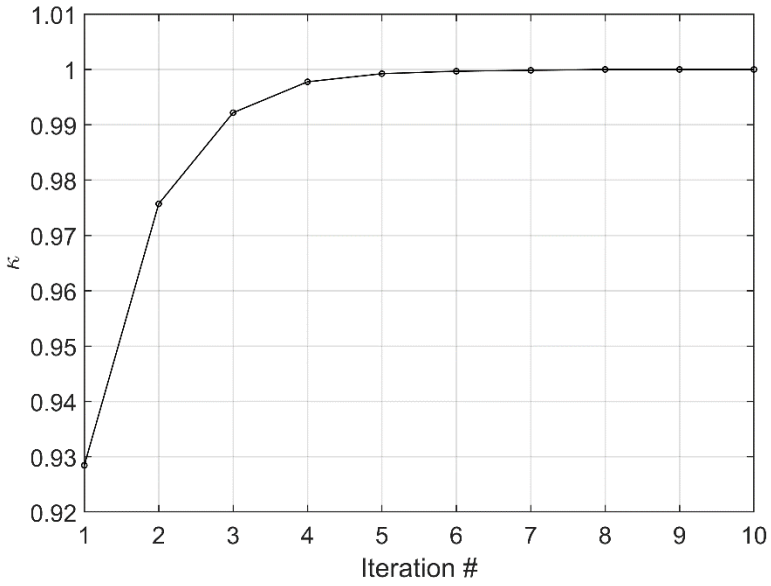

S1AL

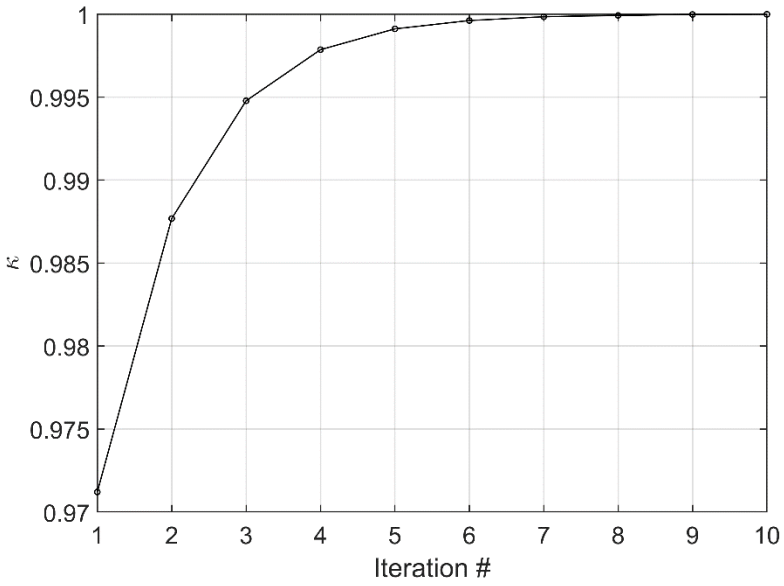
1
0.995
0.99
0.985
0.98
0.975
0.97
κ
1 2 3 4 5 6 7 8 9 10
Iteration #

S2AL

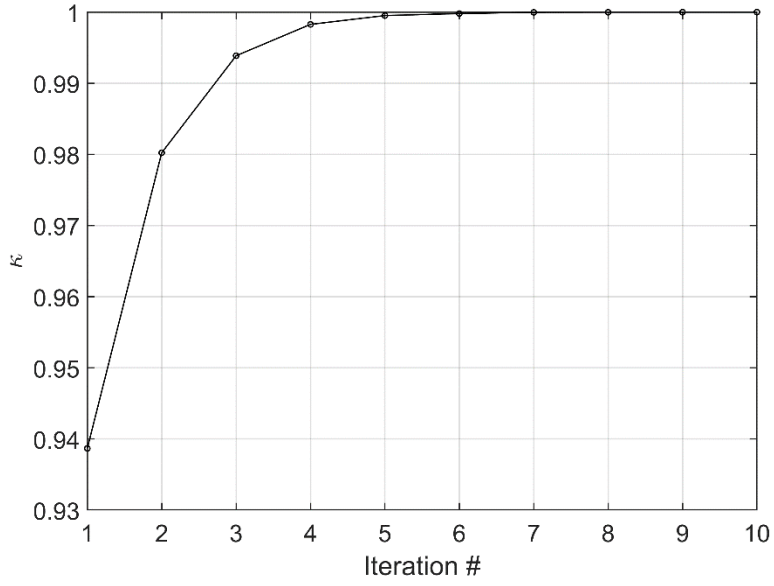
1
0.99
0.98
0.97
0.96
0.95
0.94
0.93
κ
1 2 3 4 5 6 7 8 9 10
Iteration #

Y47A

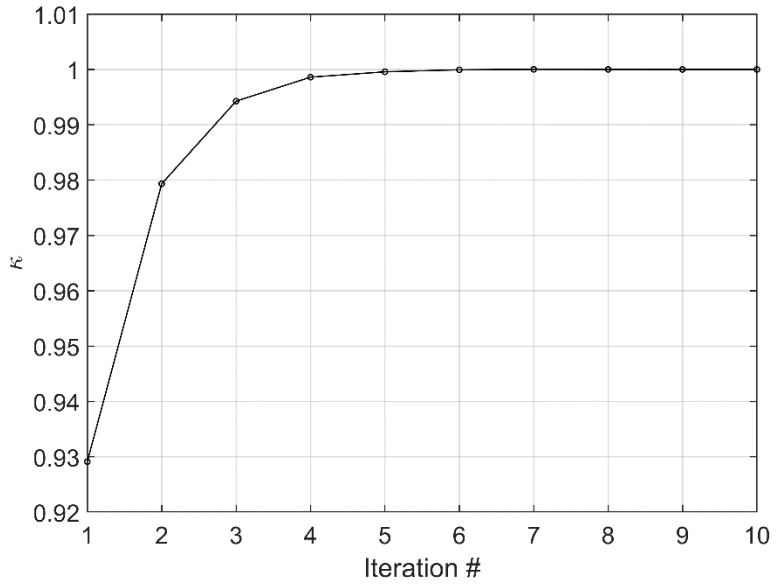
1.01
1
0.99
0.98
0.97
0.96
0.95
0.94
0.93
0.92
κ
1
2
3
4
5
6
7
8
9
10
Iteration #

X48A

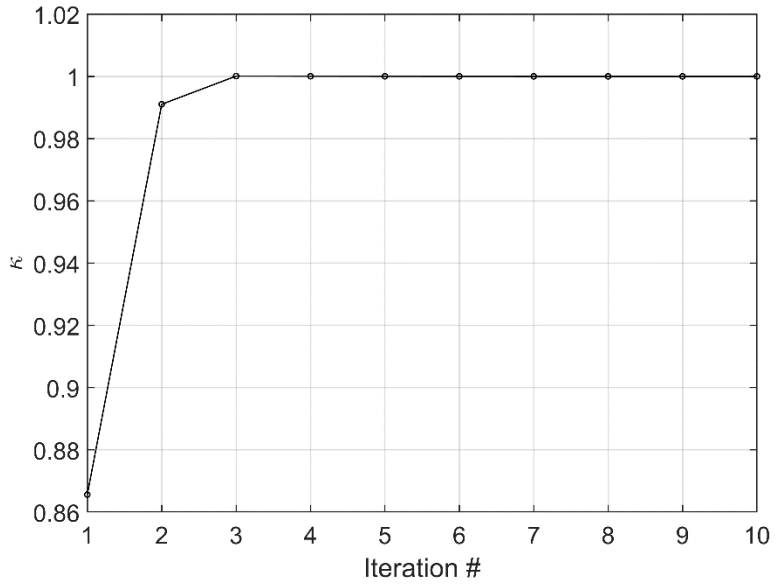
1.02
1
0.98
0.96
0.94
0.92
0.9
0.88
0.86
κ
1
2
3
4
5
6
7
8
9
10
Iteration #

B01X

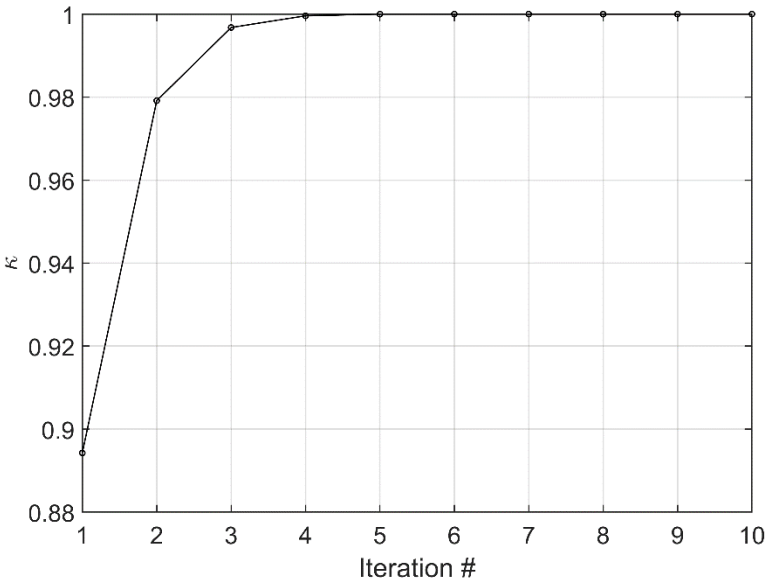

APPENDIX C: HVSR PLOTS

The next section shows the results computed for each one of the stations. The HVSR curves were classified according to the reliability of the curve and the clarity of the peak. From the results, 16 stations provided reliable HVSR curves and a clear peak, 11 stations had reliable HVSR curves without a clear peak, 5 of the stations showed a clear peak without a reliable curve, and three of them could not provide either of these characteristics.

STATIONS WITH A RELIABLE CURVE AND A CLEAR PEAK

The stations that presented a clear peak and a reliable HVSR curve are shown in Figures C-1to C-17. As mentioned before, to have a reliable HVSR curve, the stations needed to meet all three criteria, while the clarity on the HVSR peak needed to fulfill only five of the six criteria. All of the stations meeting the criteria satisfied the first three criteria for the clear peak. These criteria are related to the amplification conditions of the HVSR curve. Specifically, 9 of the stations meet all the criteria required, while the rest meet only five of the six criteria to have a clear peak.

Generally, the stations with a reliable HVSR curve and a clear peak showed one prominent frequency peak. However, some of them also showed other smaller peaks at larger frequencies. Figures C-1 to C-10 showed HVSR curves of stations with a clear peak. All these stations had peaks located at frequencies greater than 1 Hz. Stations with only one significant peak showed a large impedance contrast. If the peak amplification is higher than four it is certain that in this site exists a large velocity contrast causing a sharp discontinuity (SESAME, 2004). The higher the frequency peaks observed in some stations, such as B01X, could indicate a shallower stiff structure.

On the other hand, the stations that showed more than one peak, Figures C-11 to C-17, can be associated with more than one mode of vibration for the HVSR curve. For these stations, the prominent peak was located under 1 Hz, which could indicate a deeper stiff layer in the substructure. The mean amplification of these sites with multiple peaks is generally lower than for the sites with only one peak. Multiple peaks at the HVSR curve could be generated by: shallow soft deposits, thick stiff sediments or soft rock, or very hard underlying bedrock at depth (SESAME, 2004).

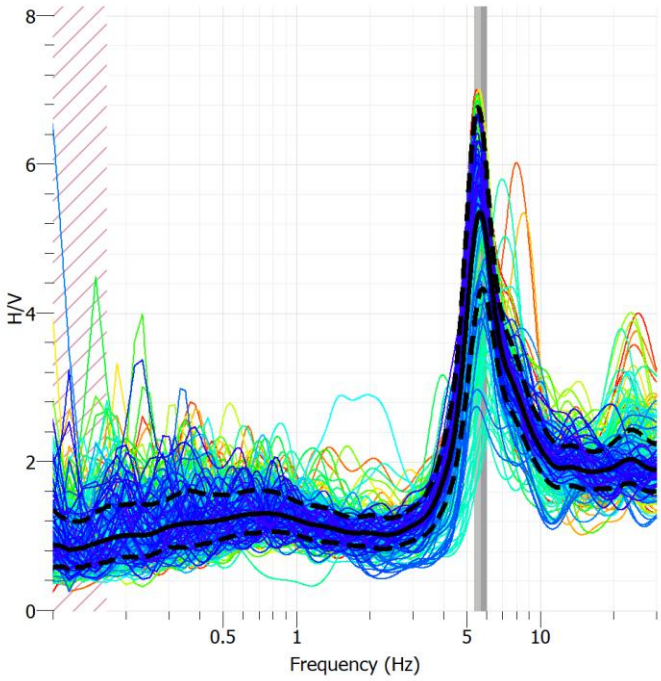

Figure C-1: HVSR curves for B01 seismic station. Frequency peak is marked in gray color, average HVSR curve is shown in black line, and the standard deviation is in dashed black line.

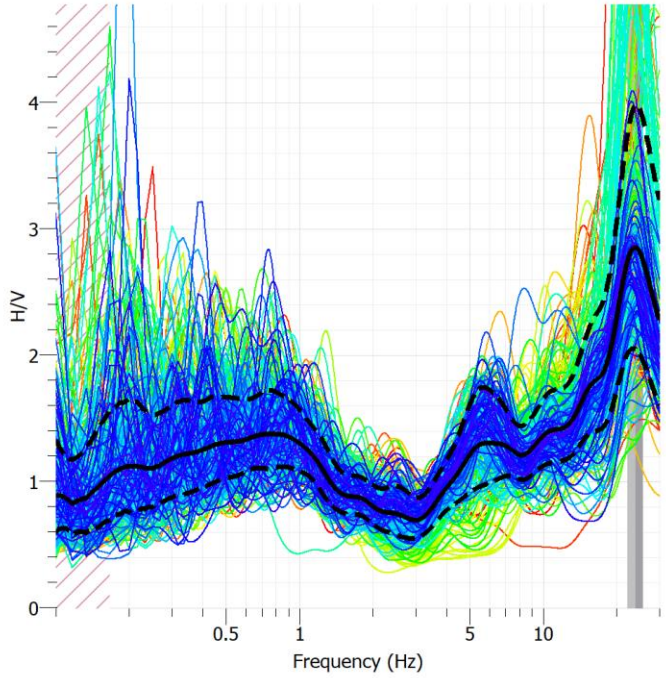

Figure C-2: HVSR curves for B01X seismic station. Frequency peak is marked in gray color, average HVSR curve is shown in black line, and the standard deviation is in dashed black line.

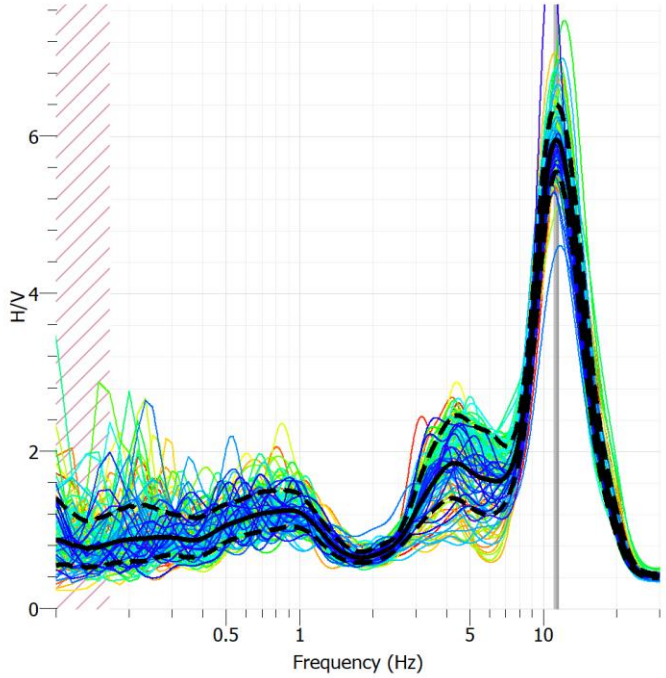

Figure C-3: HVSR curves for X48A seismic station. Frequency peak is marked in gray color, average HVSR curve is shown in black line, and the standard deviation is in dashed black line.

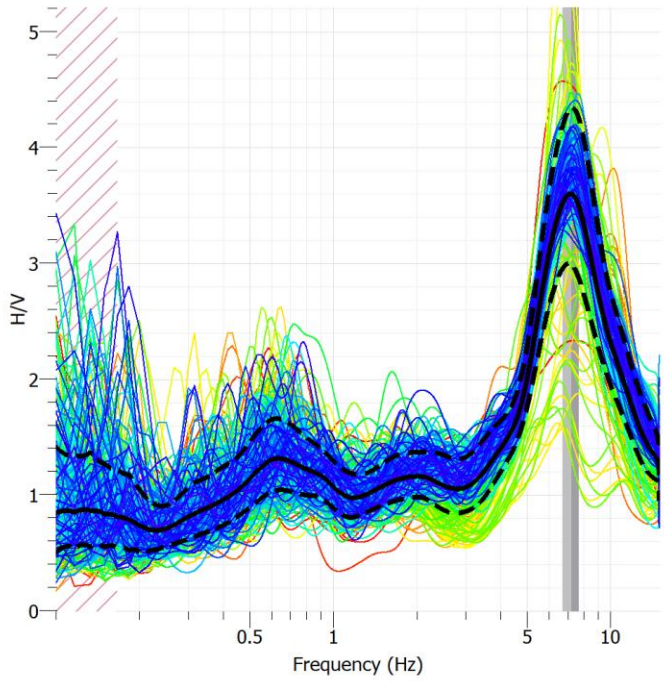

Figure C-4: HVSR curves for X50B seismic station. Frequency peak is marked in gray color, average HVSR curve is shown in black line, and the standard deviation is in dashed black line.

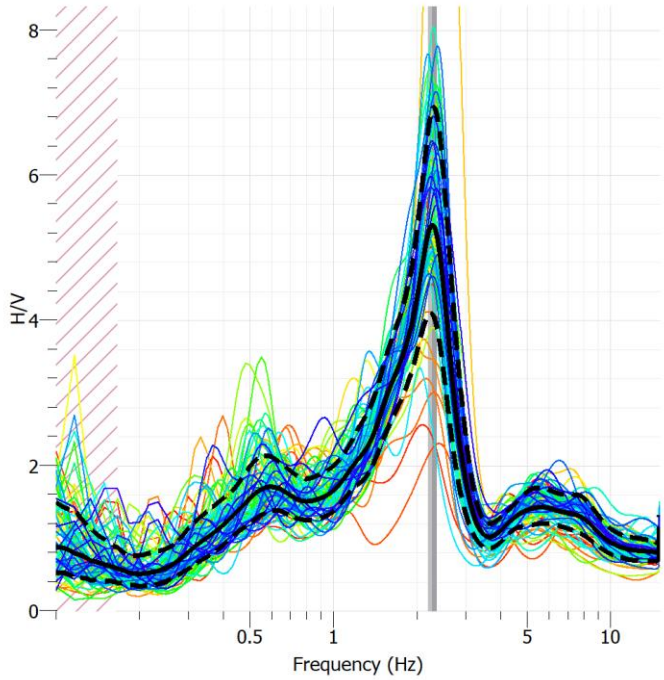

Figure C-5: HVSR curves for Y50A seismic station. Frequency peak is marked in gray color, average HVSR curve is shown in black line, and the standard deviation is in dashed black line.

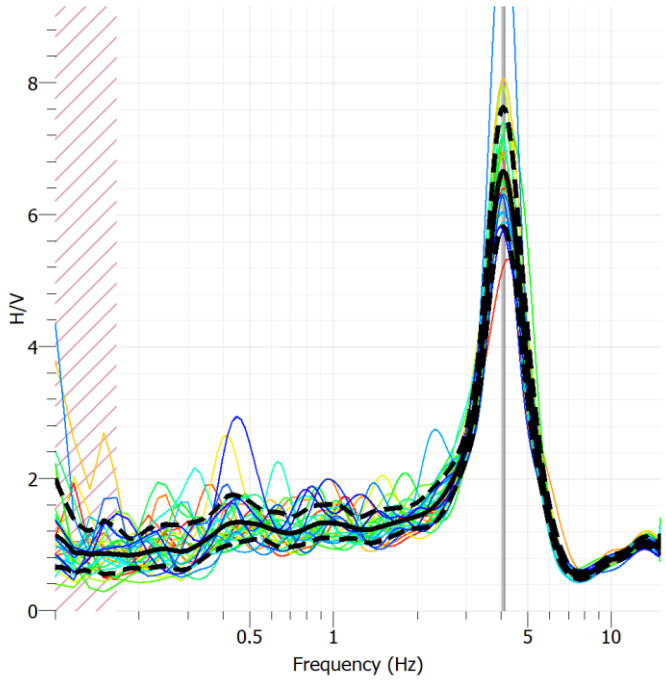

Figure C-6: HVSR curves for Z50A seismic station. Frequency peak is marked in gray color, average HVSR curve is shown in black line, and the standard deviation is in dashed black line.

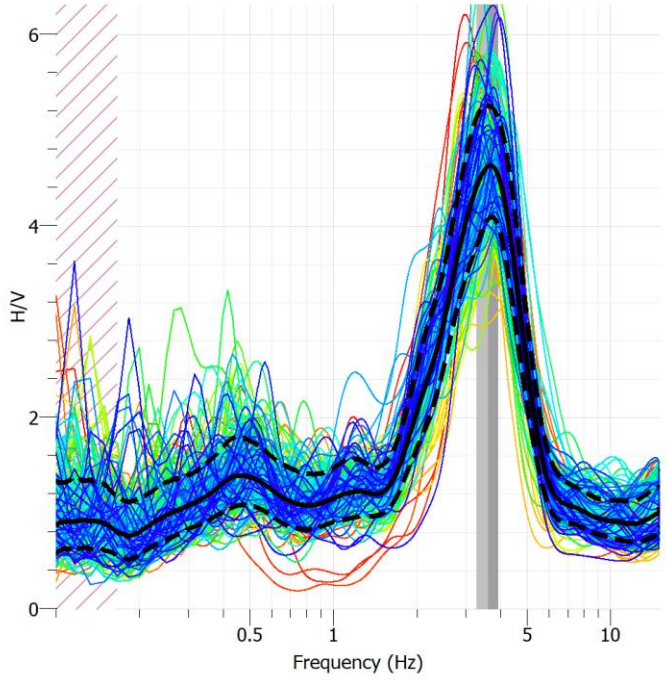

Figure C-7: HVSR curves for Y47A seismic station. Frequency peak is marked in gray color, average HVSR curve is shown in black line, and the standard deviation is in dashed black line.

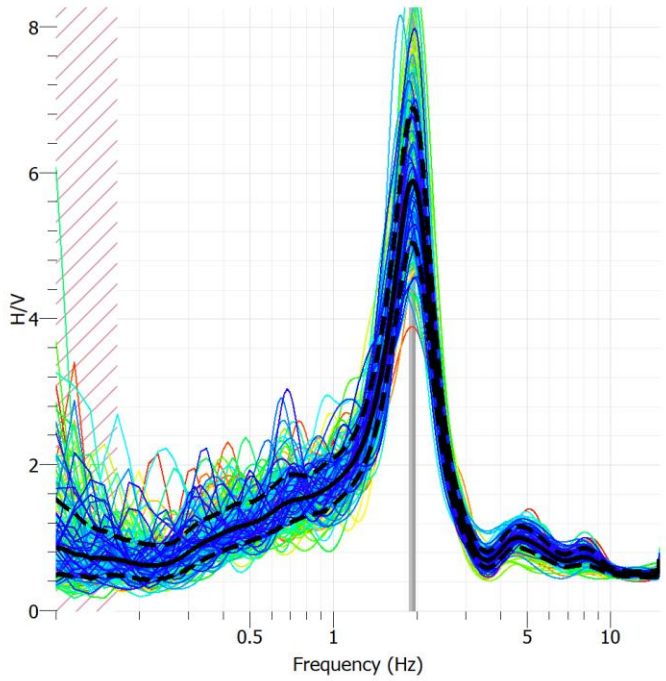

Figure C-8: HVSR curves for 151A seismic station. Frequency peak is marked in gray color, average HVSR curve is shown in black line, and the standard deviation is in dashed black line.

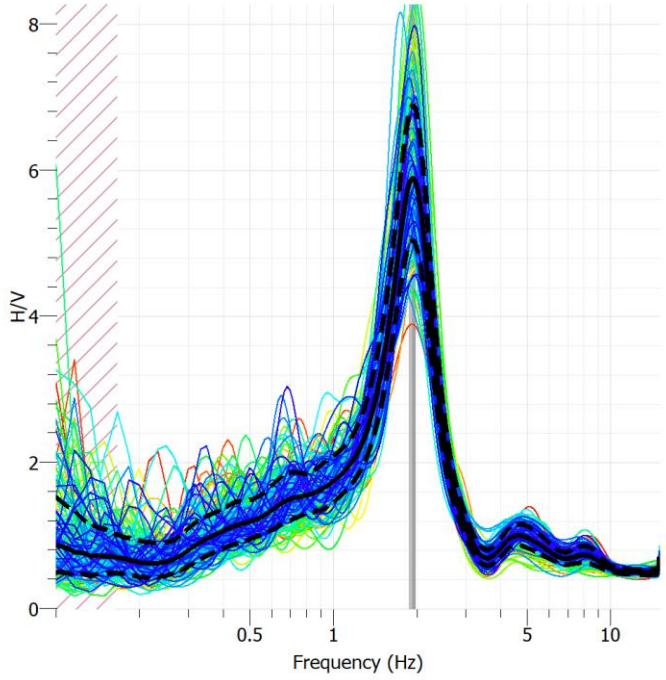

Figure C-9: HVSR curves for 151A seismic station. Frequency peak is marked in gray color, average HVSR curve is shown in black line, and the standard deviation is in dashed black line.

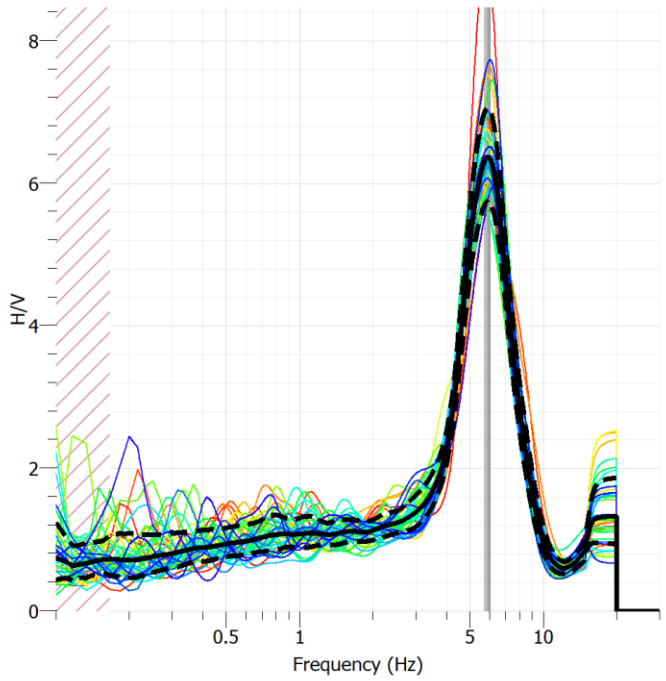

Figure C-10: HVSR curves for 150A seismic station. Frequency peak is marked in gray color, average HVSR curve is shown in black line, and the standard deviation is in dashed black line.

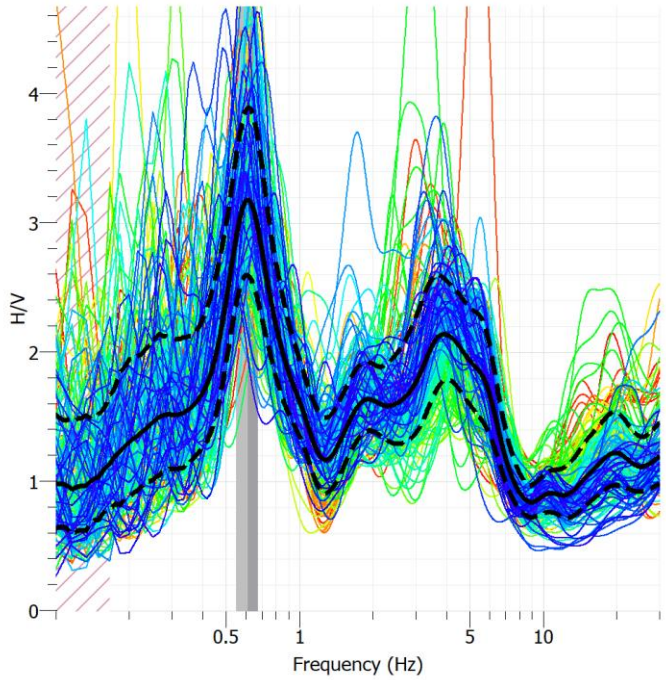

Figure C-11: HVSR curves for Z47B seismic station. Frequency peak is marked in gray color, average HVSR curve is shown in black line, and the standard deviation is in dashed black line.

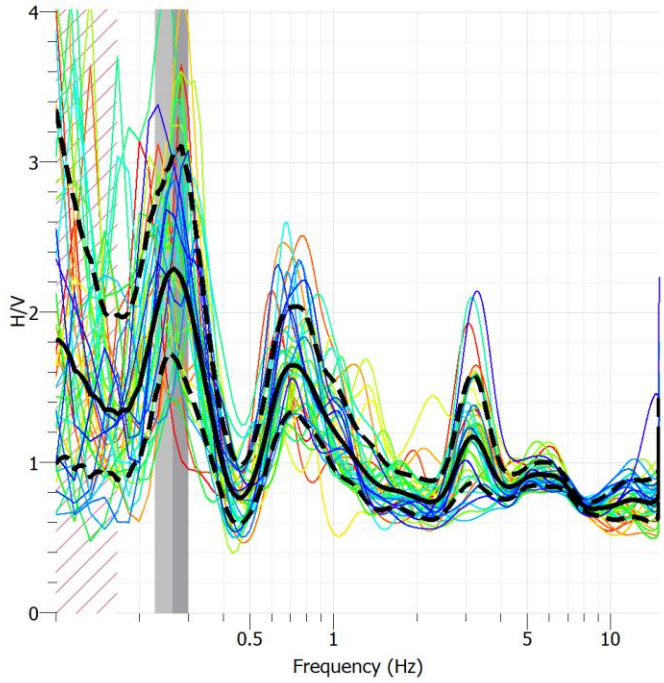

Figure C-12: HVSR curves for 147A seismic station. Frequency peak is marked in gray color, average HVSR curve is shown in black line, and the standard deviation is in dashed black line.

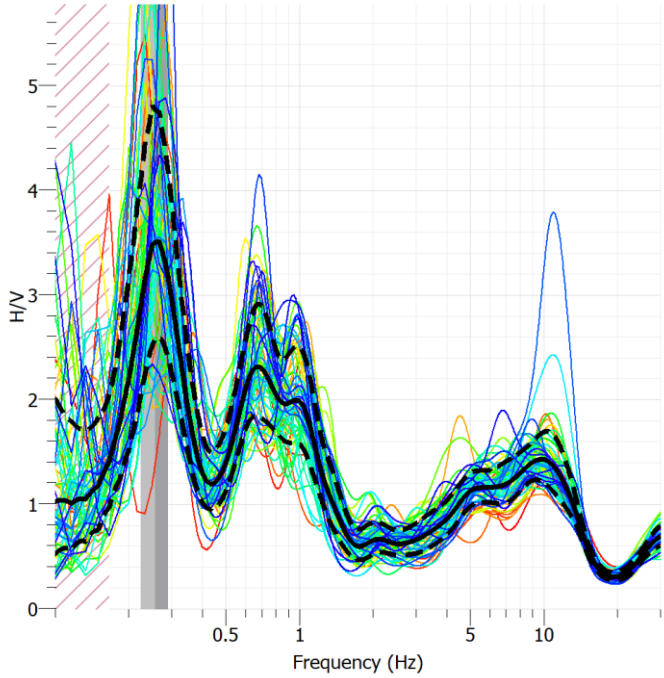

Figure C-13: HVSR curves for 250A seismic station. Frequency peak is marked in gray color, average HVSR curve is shown in black line, and the standard deviation is in dashed black line.

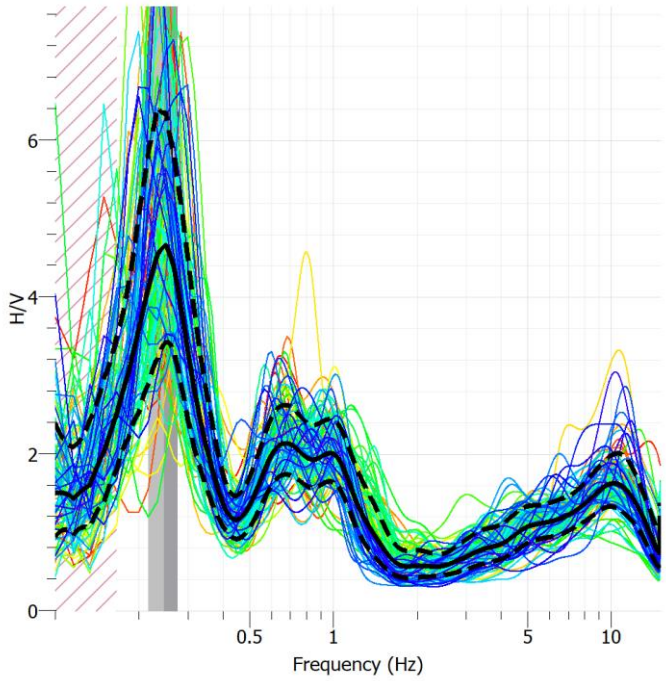

Figure C-14: HVSR curves for 250A-V seismic station. Frequency peak is marked in gray color, average HVSR curve is shown in black line, and the standard deviation is in dashed black line.

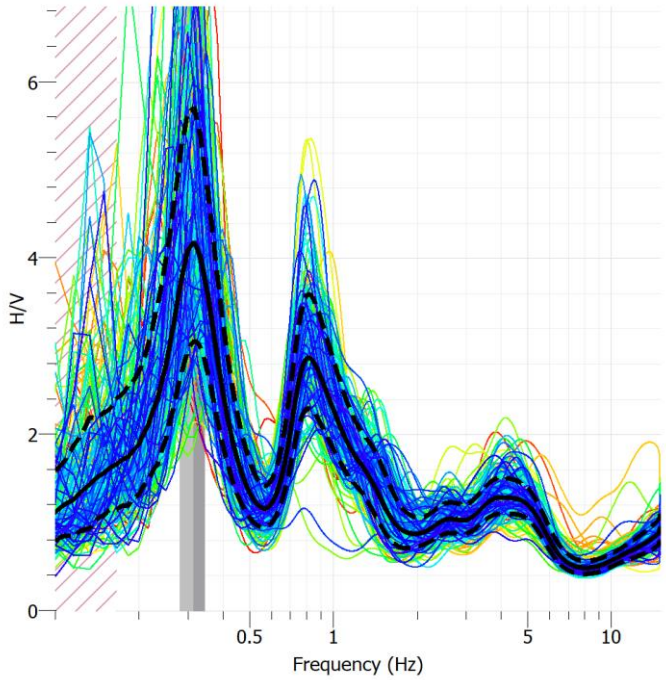

Figure C-15: HVSR curves for 251A seismic station Frequency peak is marked in gray color, average HVSR curve is shown in black line, and the standard deviation is in dashed black line.

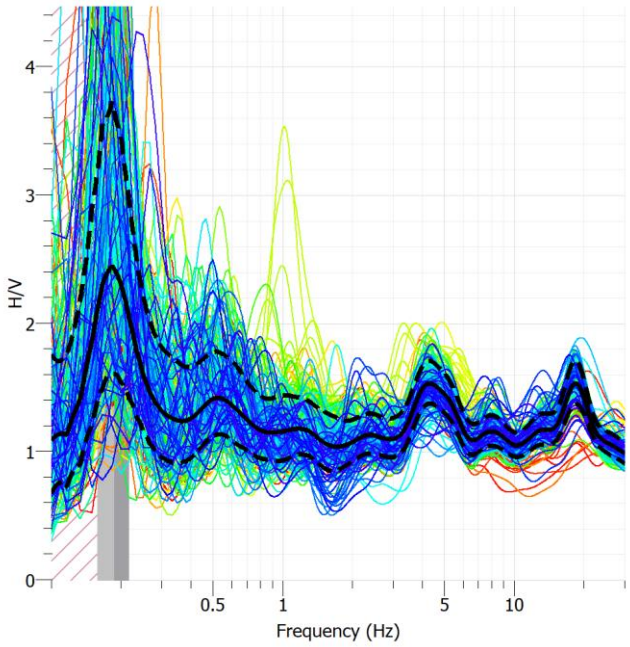

Figure C-16: HVSR curves for S1FL seismic station. Frequency peak is marked in gray color, average HVSR curve is shown in black line, and the standard deviation is in dashed black line.

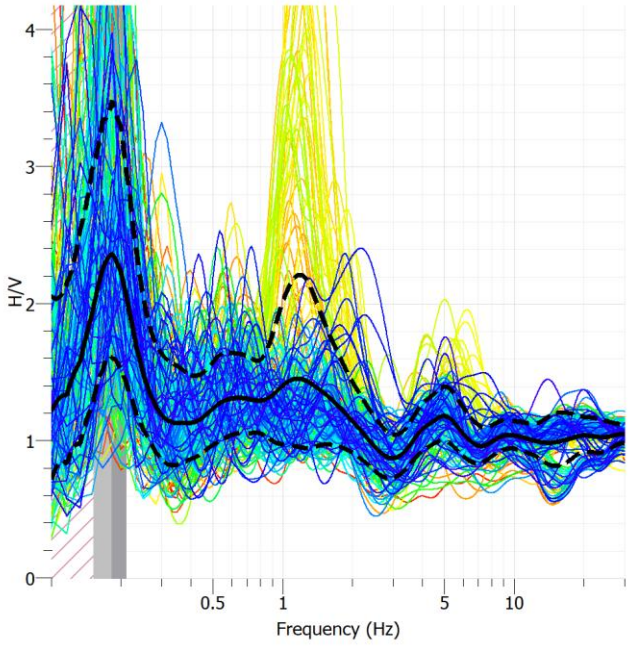

Figure C-17: HVSR curves for S2AL seismic station Frequency peak is marked in gray color, average HVSR curve is shown in black line, and the standard deviation is in dashed black line.

STATIONS WITHOUT FULFILLMENT OF THE CRITERIA

The stations shown in this section did not fulfill the requirements for a reliable HVSR curve and or clear peak. Stations that only met the criteria for a reliable curve are shown in Figures C-18 to C-28. Most of these stations did not meet the clarity criteria between C3 to C5. Additionally, the stations had, in general, lower values of amplification. The stations with only a clear peak are shown in Figures C-29 to C-33. All these stations did not meet reliable criteria C3, which ensures lower standard deviation values to maintain an acceptable level of scattering between analyzed windows of data. The stations with only the clarity criteria met showed higher values of amplification.

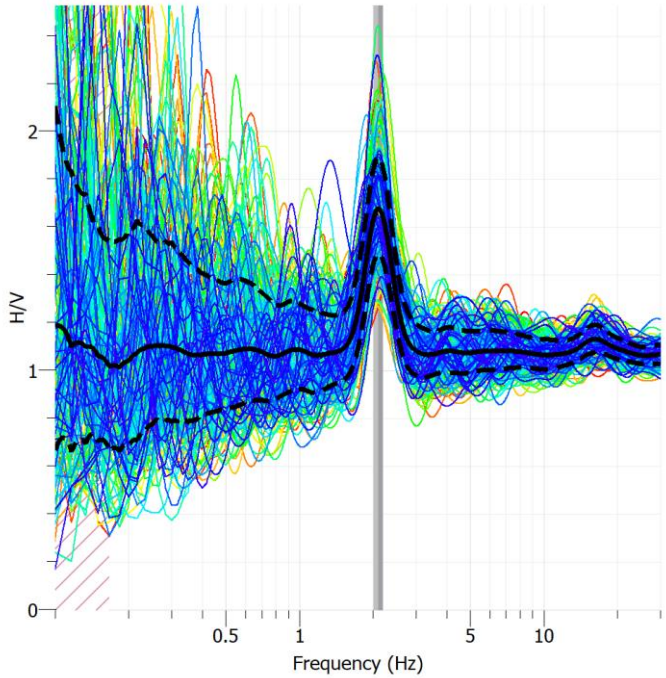

Figure C-18: HVSR curves for PWLA seismic station. Frequency peak is marked in gray color, average HVSR curve is shown in black line, and the standard deviation is in dashed black line.

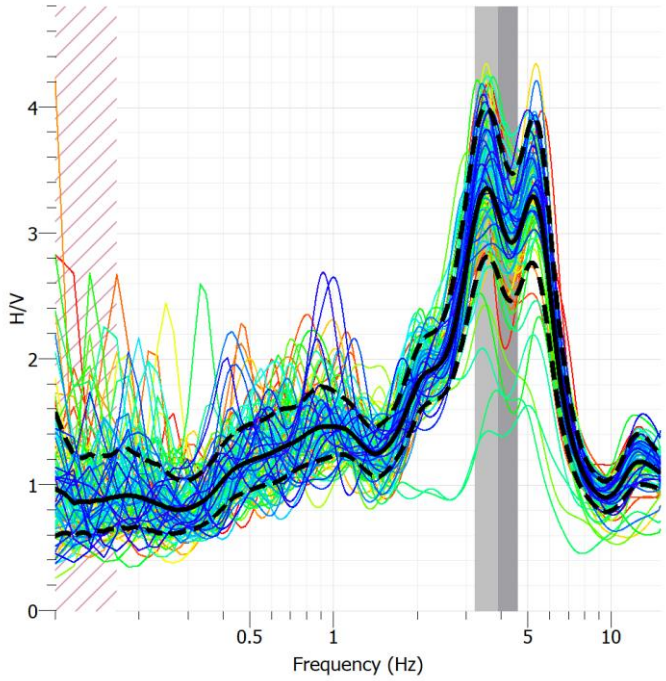

Figure C-19: HVSR curves for PLAL seismic station. Frequency peak is marked in gray color, average HVSR curve is shown in black line, and the standard deviation is in dashed black line.

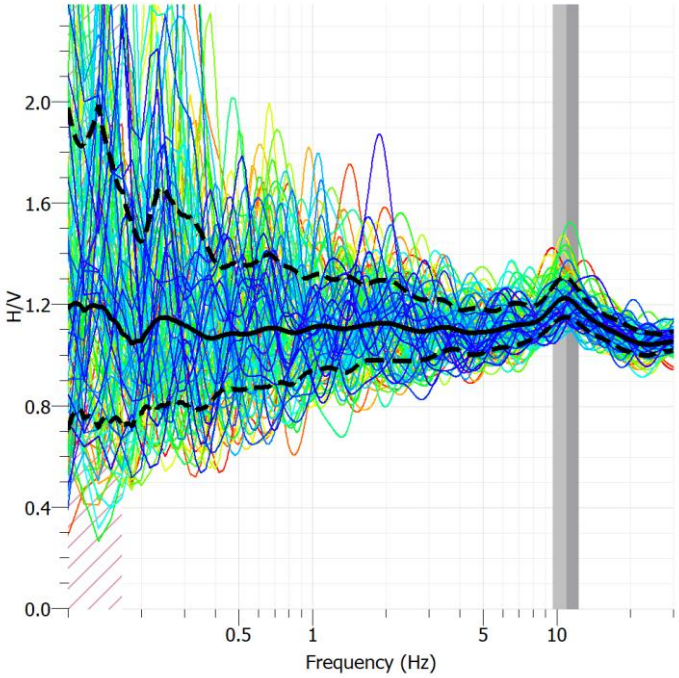

Figure C-20: HVSR curves for SWET seismic station. Frequency peak is marked in gray color, average HVSR curve is shown in black line, and the standard deviation is in dashed black line.

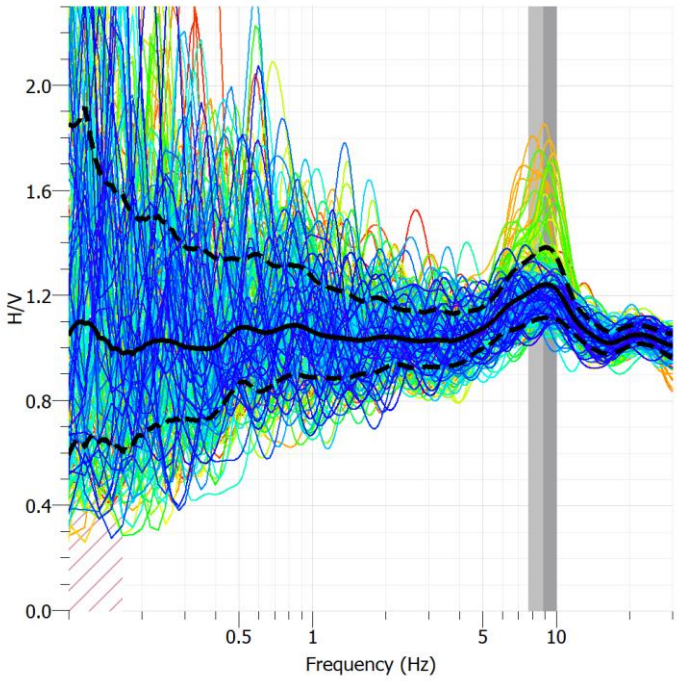

Figure C-21: HVSR curves for W50A seismic station. Frequency peak is marked in gray color, average HVSR curve is shown in black line, and the standard deviation is in dashed black line.

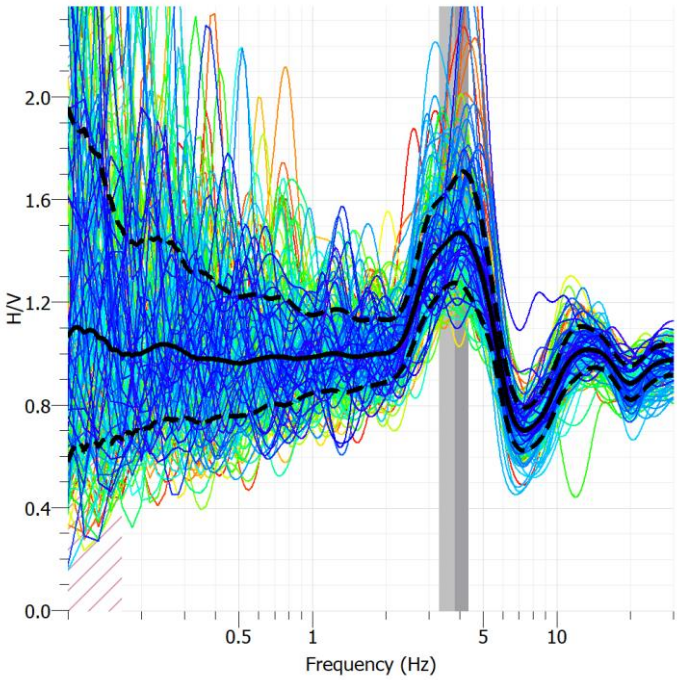

Figure C-22: HVSR curves for X51A seismic station. Frequency peak is marked in gray color, average HVSR curve is shown in black line, and the standard deviation is in dashed black line.

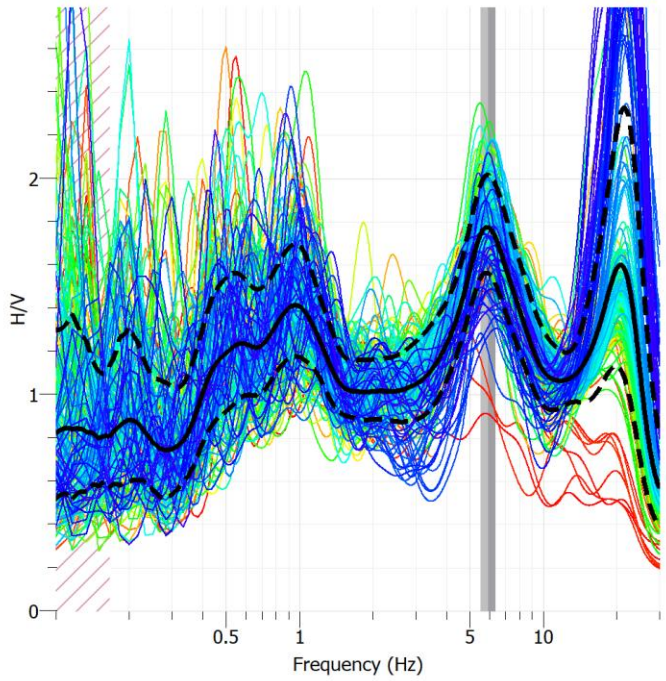

Figure C-23: HVSR curves for Y49A seismic station. Frequency peak is marked in gray color, average HVSR curve is shown in black line, and standard deviation is in dashed black line.

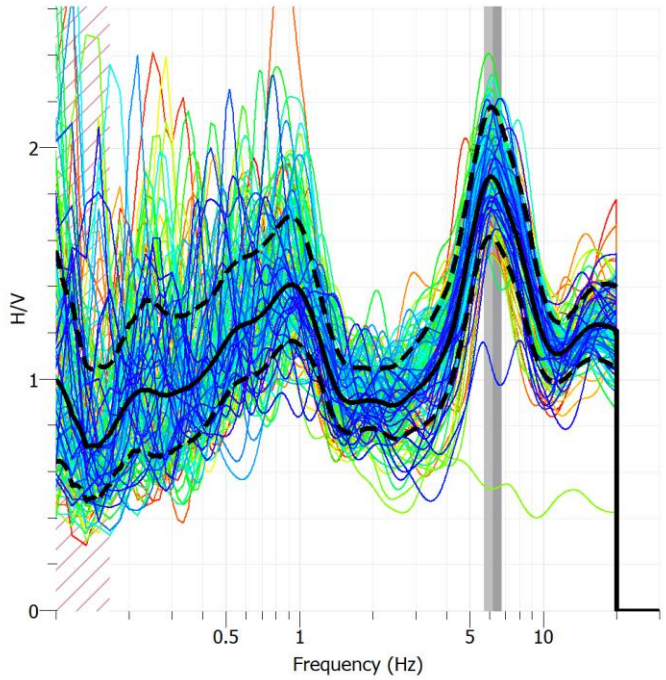

Figure C-24: HVSR curves for Y49A-V seismic station. Frequency peak is marked in gray color, average HVSR curve is shown in black line, and standard deviation is in dashed black line.

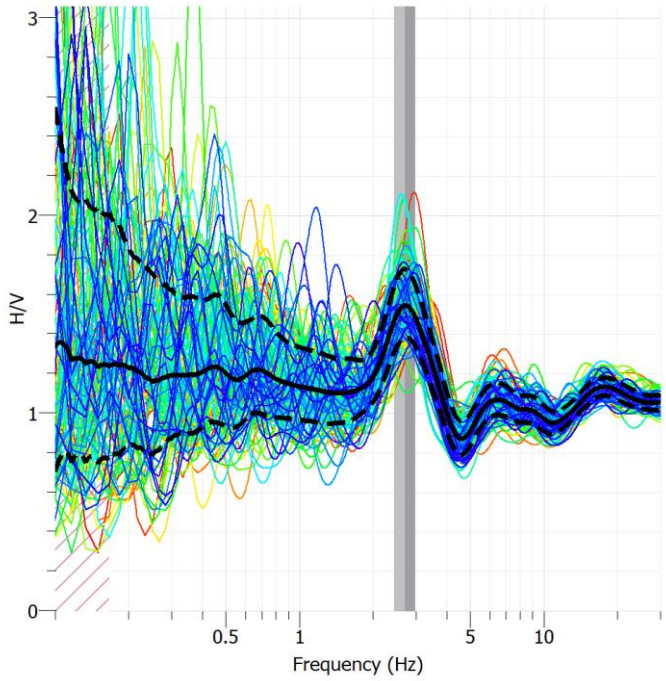

Figure C-25: HVSR curves for Z51A seismic station. Frequency peak is marked in gray color, average HVSR curve is shown in black line, and standard deviation is in dashed black line.

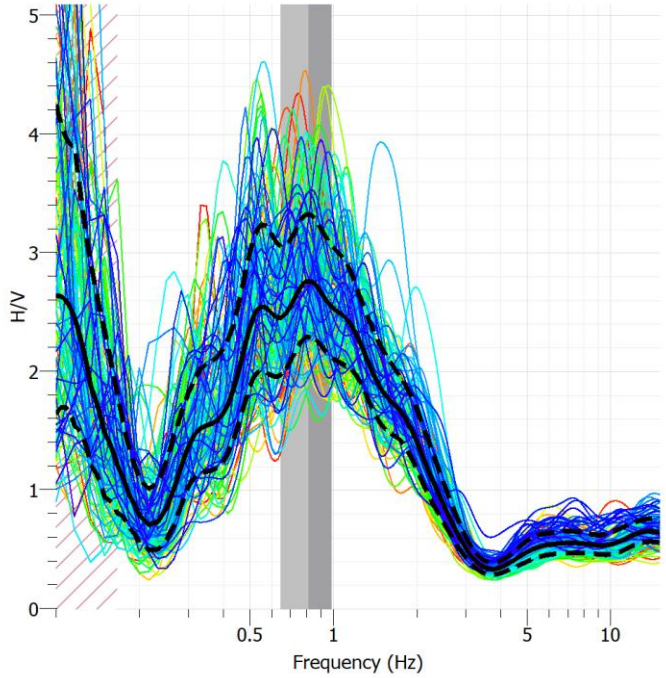

Figure C-26: HVSR curves for 350A seismic station. Frequency peak is marked in gray color, average HVSR curve is shown in black line, and standard deviation is in dashed black line.

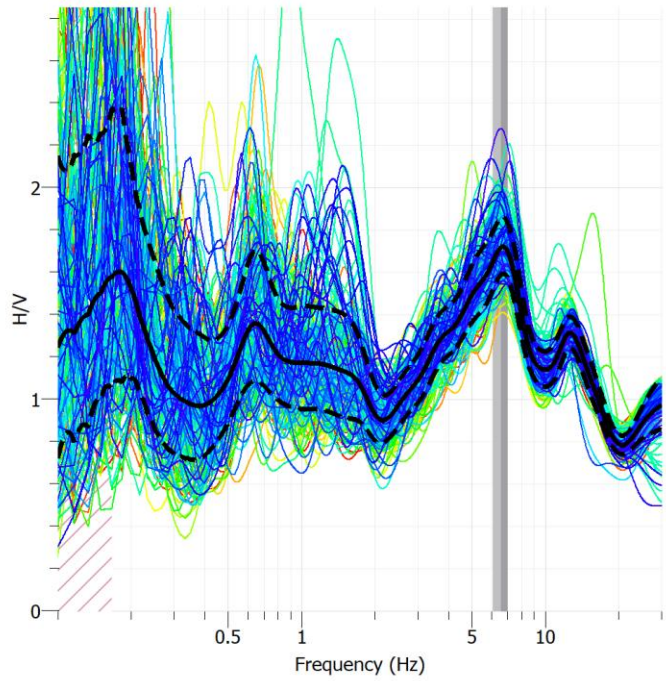

Figure C-27: HVSR curves for S1AL seismic station. Frequency peak is marked in gray color, average HVSR curve is shown in black line, and standard deviation is in dashed black line.

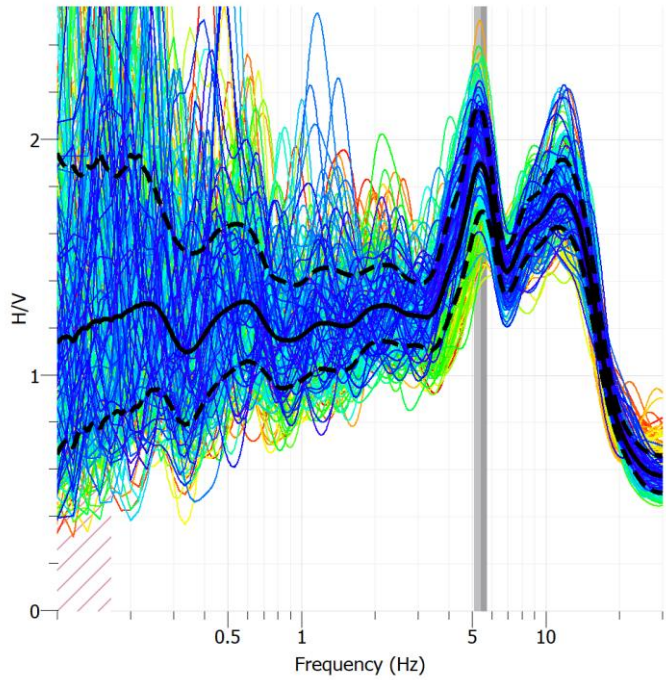

Figure C-28: HVSR curves for S2FL seismic station. Frequency peak is marked in gray color, average HVSR curve is shown in black line, and standard deviation is in dashed black line.

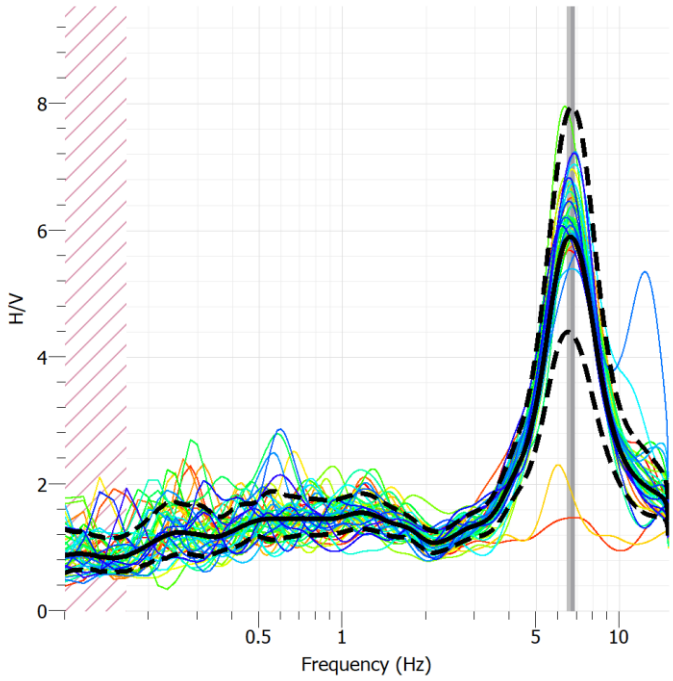

Figure C-29: HVSR curves for X47A seismic station. Frequency peak is marked in gray color, average HVSR curve is shown in black line, and standard deviation is in dashed black line.

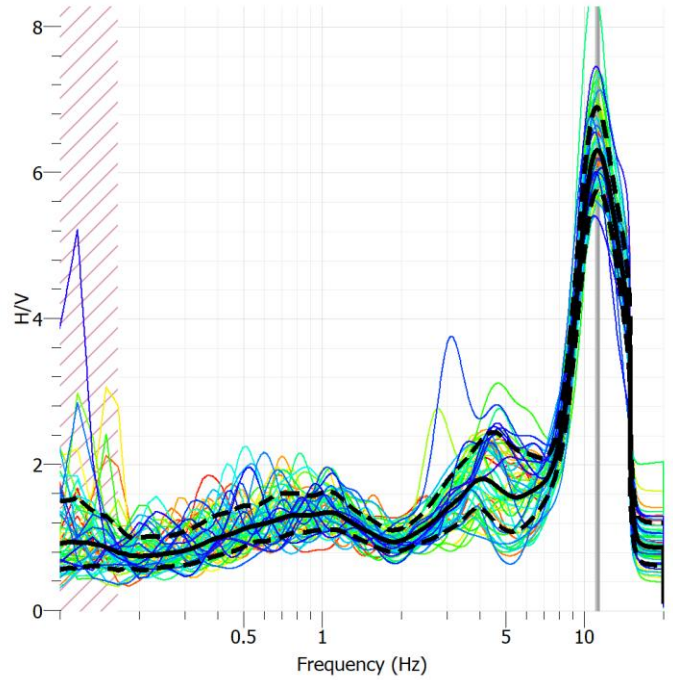

Figure C-30: HVSR curves for X48A-V seismic station. Frequency peak is marked in gray color, average HVSR curve is shown in black line, and standard deviation is in dashed black line.

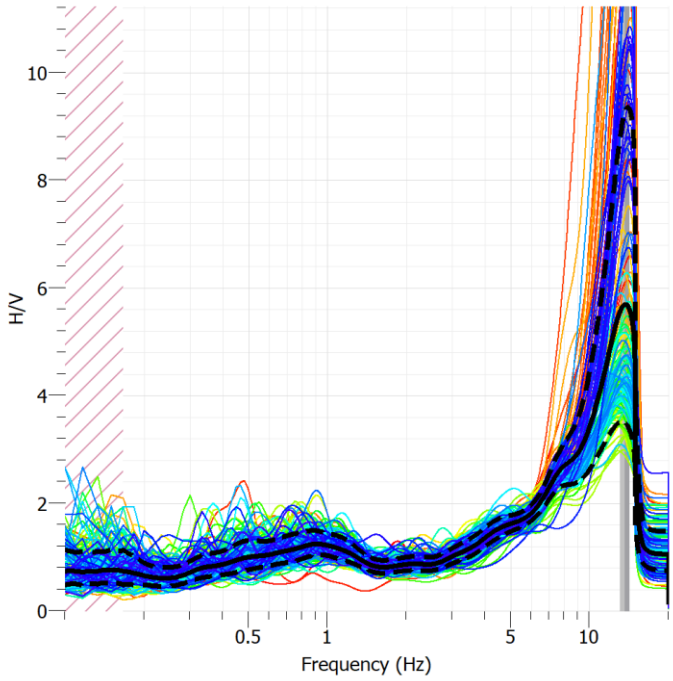

Figure C-31: HVSR curves for X49A seismic station. Frequency peak is marked in gray color, average HVSR curve is shown in black line, and standard deviation is in dashed black line.

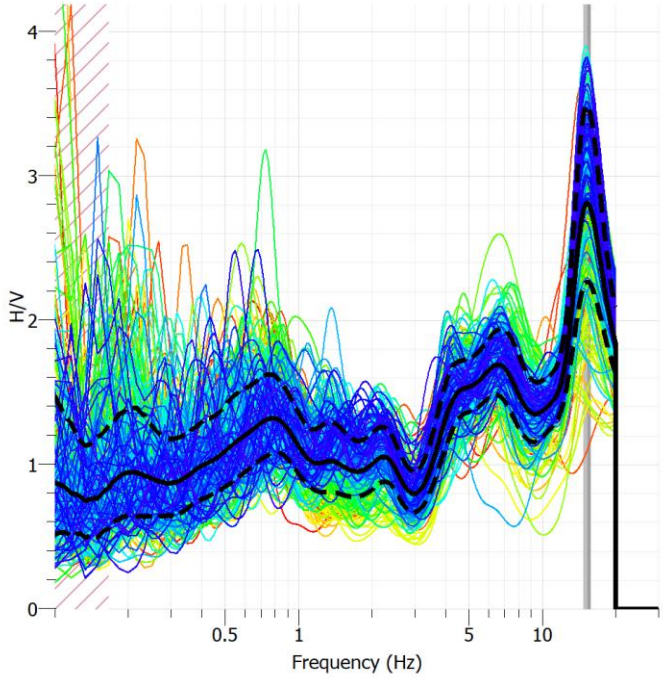

Figure C-32: HVSR curves for Y48A seismic station. Frequency peak is marked in gray color, average HVSR curve is shown in black line, and standard deviation is in dashed black line.

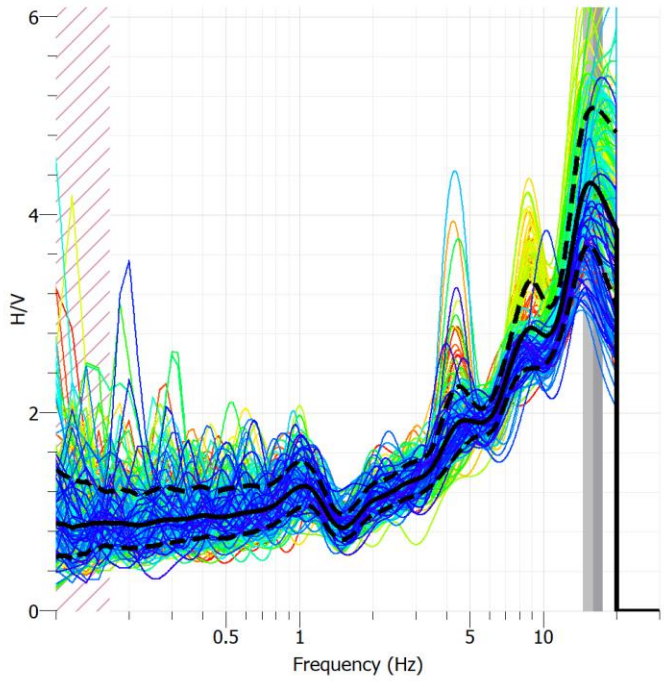

Figure C-33: HVSR curves for Z48A seismic station. Frequency peak is marked in gray color, average HVSR curve is shown in black line, and standard deviation is in dashed black line.

APPENDIX D: R-WAVE ELLIPTICITY PLOTS

The results of the R-wave ellipticity curves are shown in Figures D-1 to D-17. The R-wave ellipticity curves of seismic stations 150A, 151A, and Z50A showed singularities with a clear peak followed by a trough. The shape of the R-wave ellipticity curve for these seismic stations showed a strong impedance contrast in the subsoil. The rest of the seismic stations did not show singularities; in some seismic stations, more than one peak was identified. The multiples peaks in the seismic stations can be interpreted as higher modes or layers with low velocity.

A summary of the frequency peaks and amplification of the R-wave ellipticity curve for the seismic stations is shown in Table D-1. Additionally, the table shows the standard deviation for the amplitude of the R-wave ellipticity curve. The frequency ranges between 0.24 to 24.71 Hz for seismic stations 250A-V and B01X, respectively. The amplification values varied from 2.8 to 10.3 for seismic stations B01X and B01, respectively. Stations F1AL, S1AL, and S2AL were excluded from the table due to the difficulty of identifying a clear peak in the R-wave ellipticity curve.

The frequency peaks identified in the R-wave ellipticity curve are very similar to the ones calculated using the HVSR method for most of the stations. The main difference occurs in seismic station Y47A, where the peak frequency from the R-wave ellipticity curve was 14.1% higher than in the HVSR curve. Generally, the peak amplifications from the R-wave ellipticity curves are lower than the values computed using the HVSR method. The main difference between these values occurs in seismic station B01, in which the amplification from the R-wave ellipticity curve is 92% higher than the amplification peak of the HVSR curve.

Table D-1: Summary of frequency peak, amplification peak, and standard deviation for the R-wave ellipticity curves for the seismic stations

Station	f_{peak} (Hz)	A_{peak}	Std A_{peak}
B01	5.52	10.30	1.37
B01X	24.71	2.80	1.27
X48A	12.32	4.62	1.05
X50B	7.25	2.82	1.18
Y50A	2.33	4.17	1.29
Z50A	4.02	6.97	1.06
Y47A	4.20	4.04	1.14
Z47B	0.65	2.83	1.10
147A	0.25	3.00	1.25
150A	5.52	7.73	1.10
151A	1.94	5.02	1.13
250A	0.26	4.09	1.36
250A-V	0.24	3.80	1.22
251A	0.33	3.85	1.09

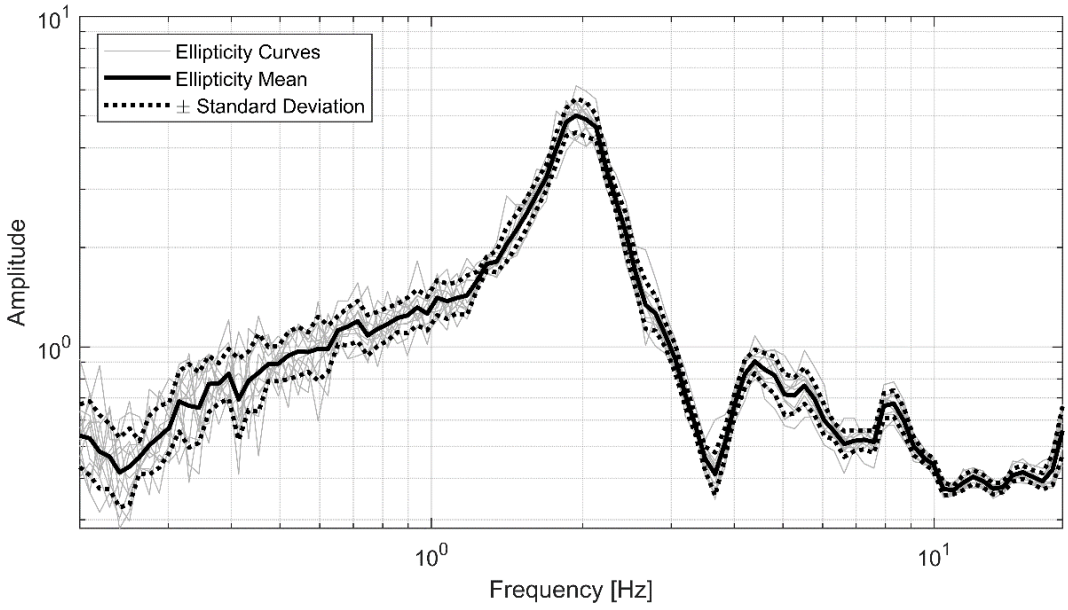

Figure D-1: R-wave ellipticity curve of seismic station 151A

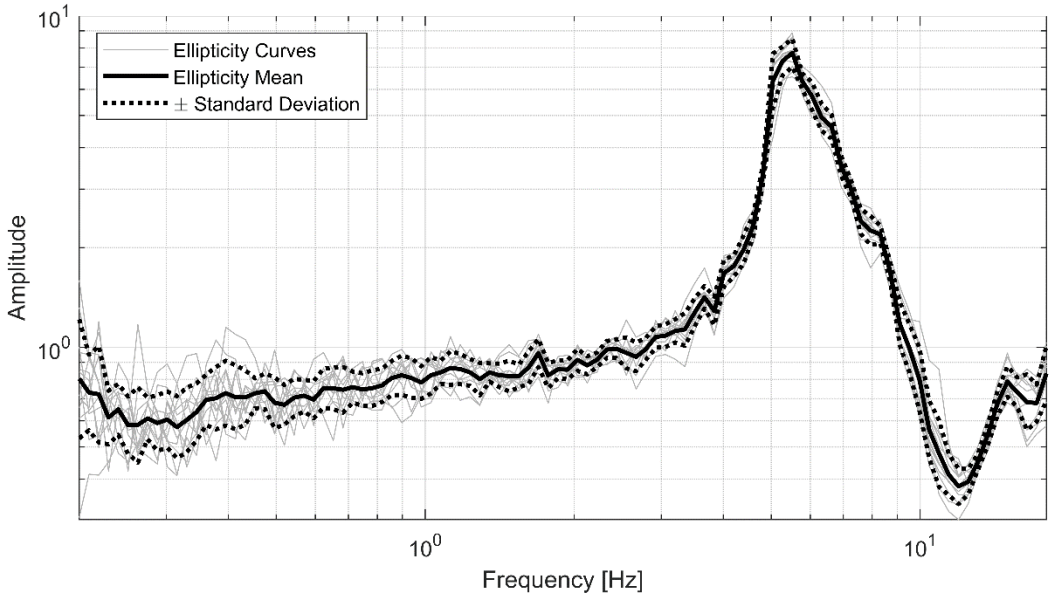

Figure D-2: R-wave ellipticity curve of seismic station 150A

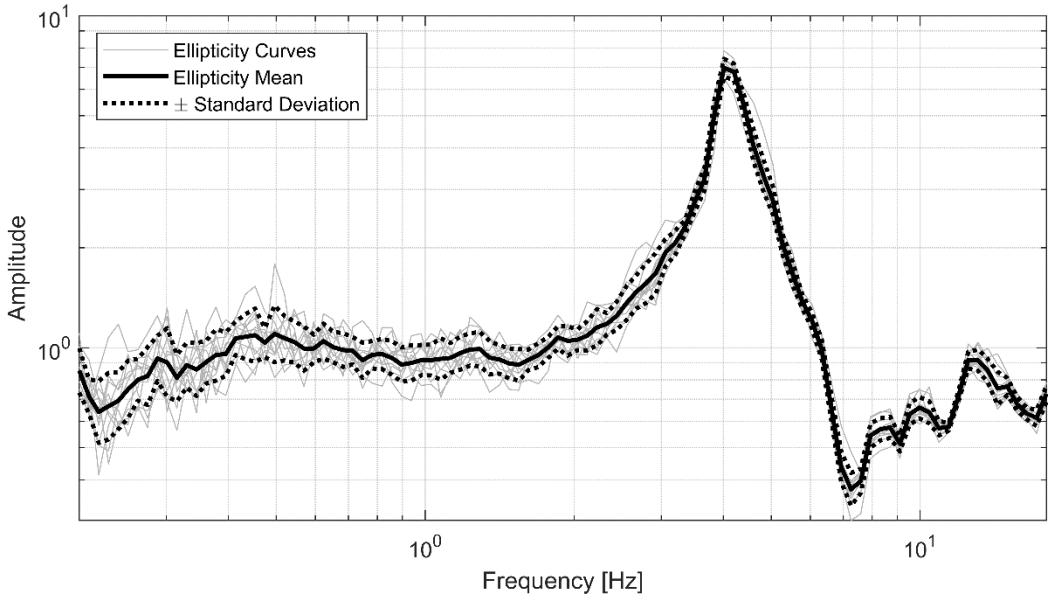

Figure D-3: R-wave ellipticity curve of seismic station Z50A

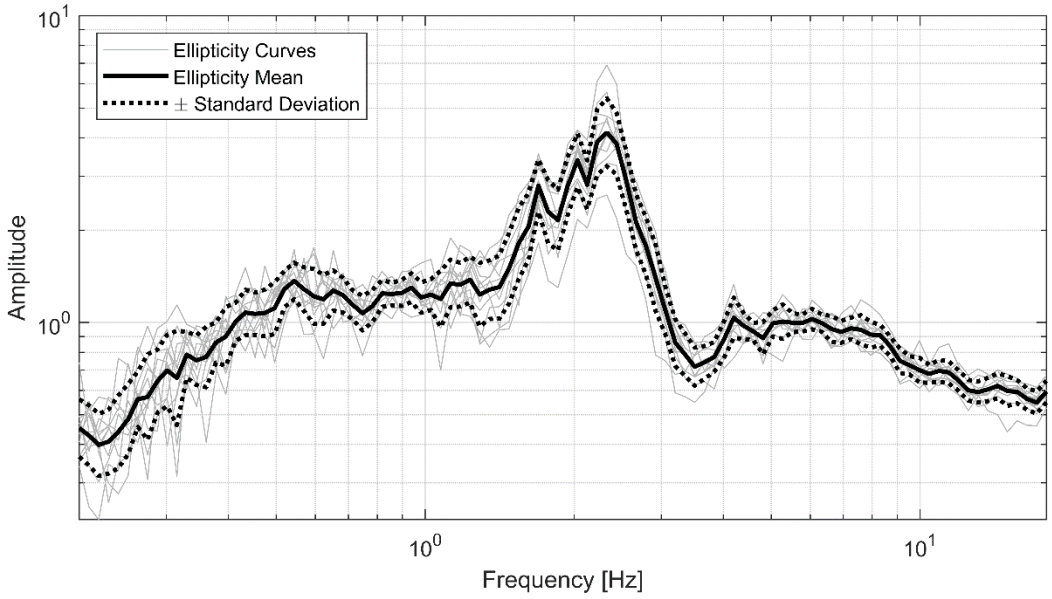

Figure D-5: R-wave ellipticity curve of seismic station Y50A

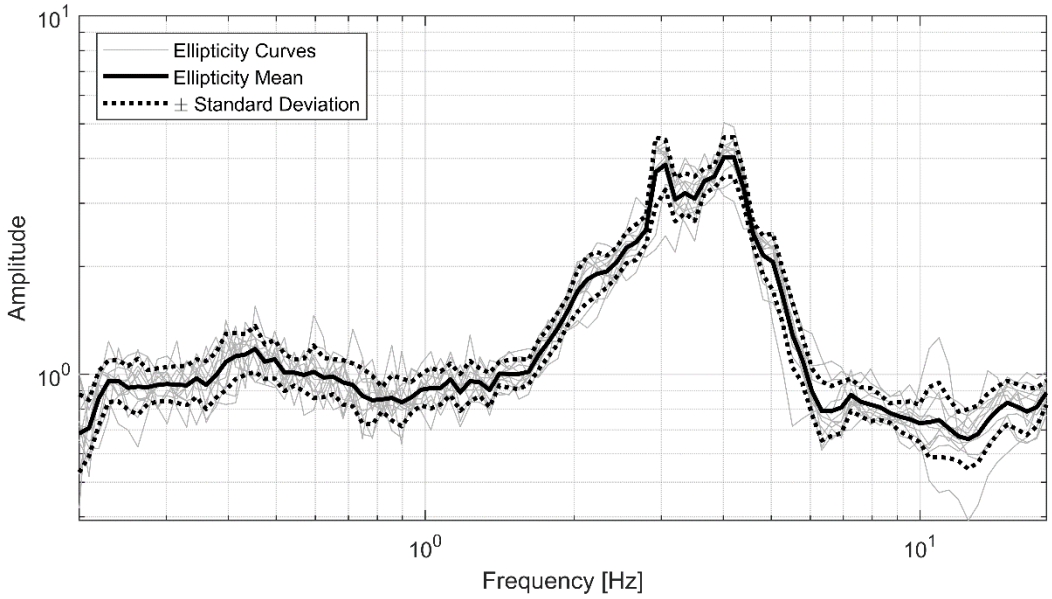

Figure D-6: R-wave ellipticity curve of seismic station Y47A

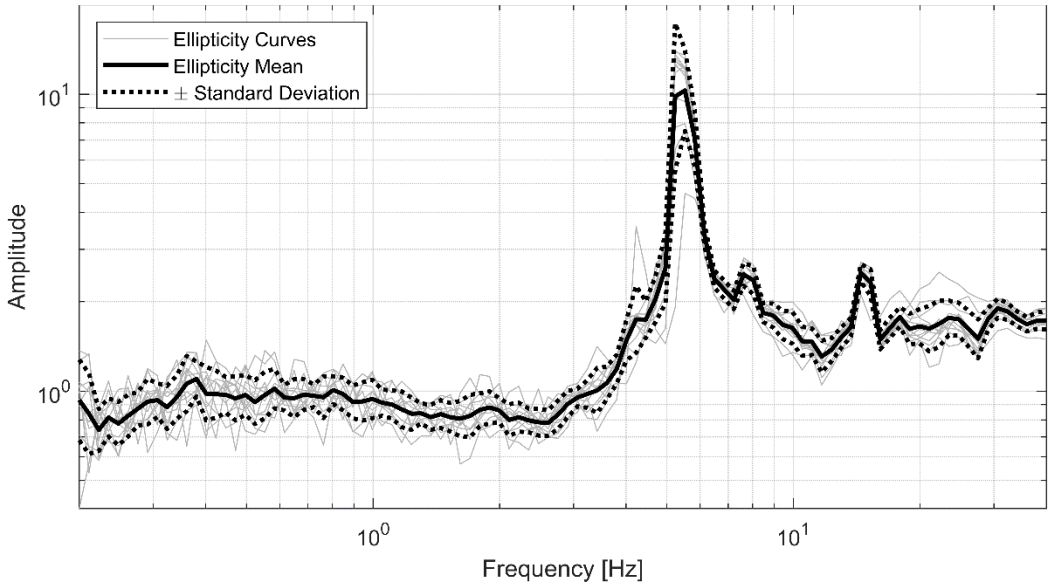

Figure D-7: R-wave ellipticity curve of seismic station B01

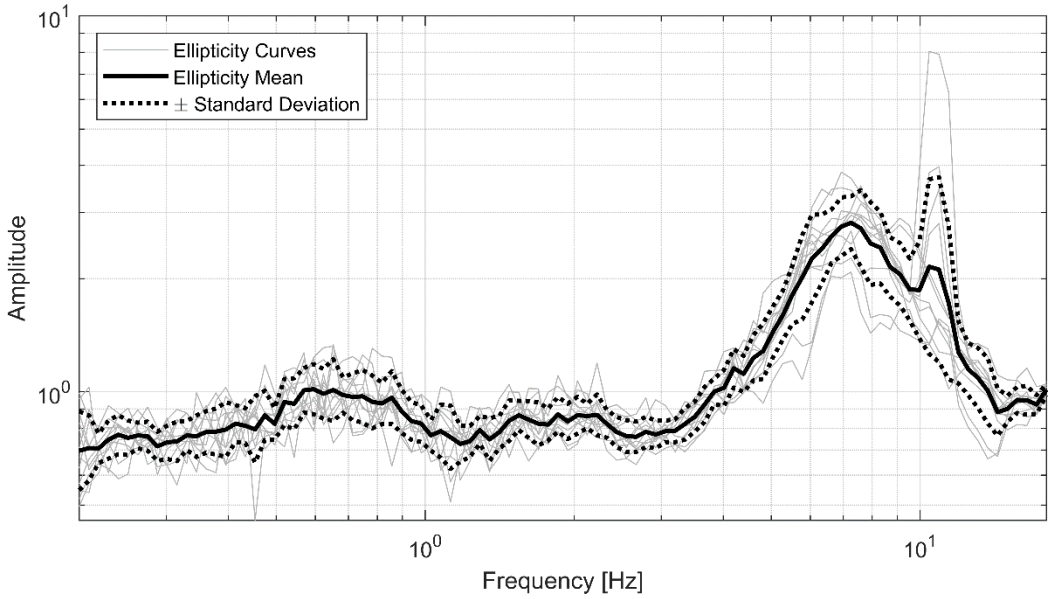

Figure D-8: R-wave ellipticity curve of seismic station X50B

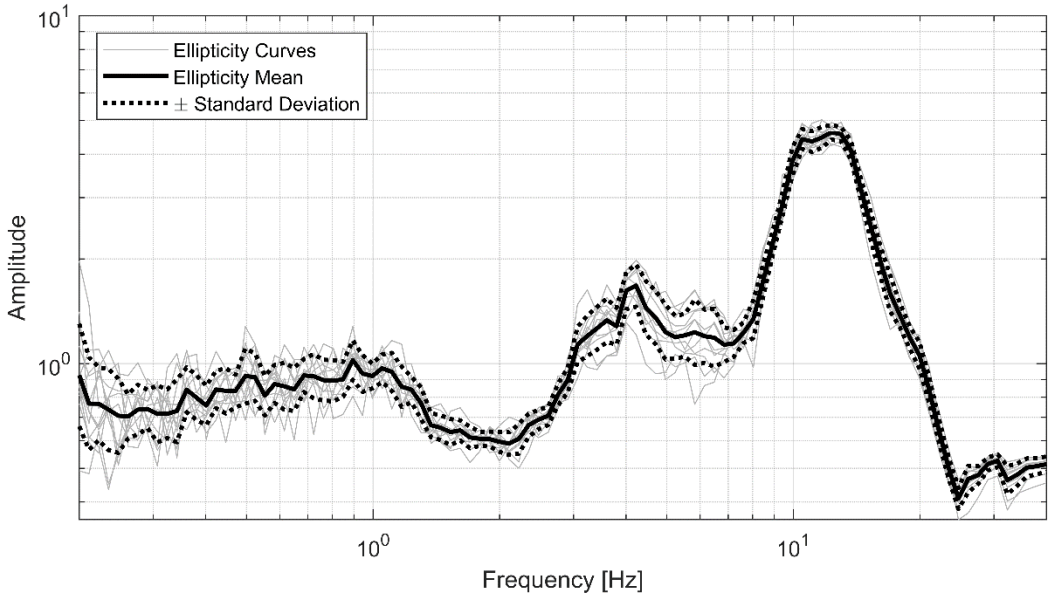

Figure D-9: R-wave ellipticity curve of seismic station X48A

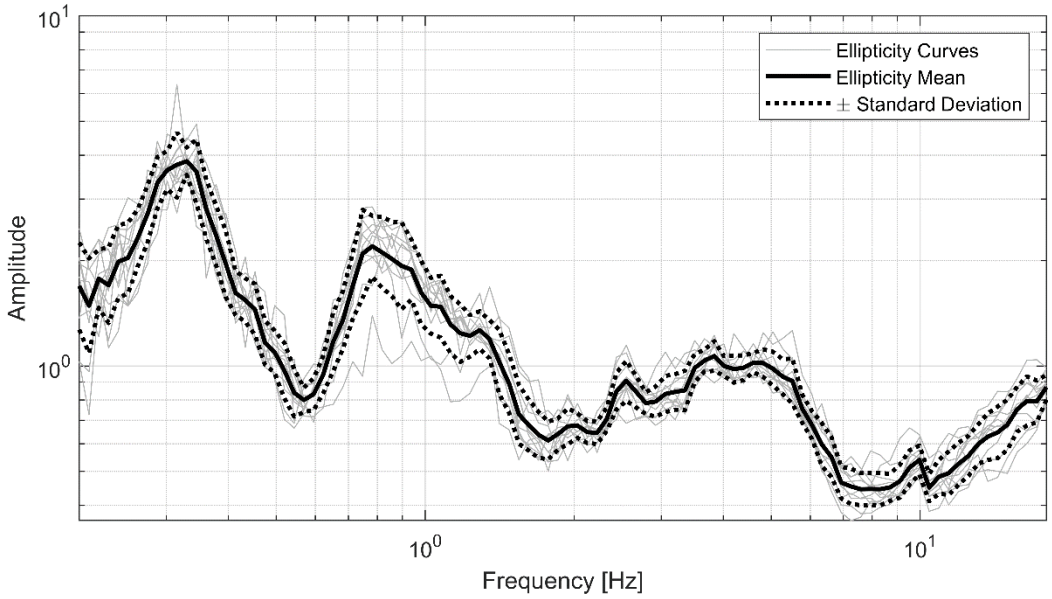

Figure D-10: R-wave ellipticity curve of seismic station 251A

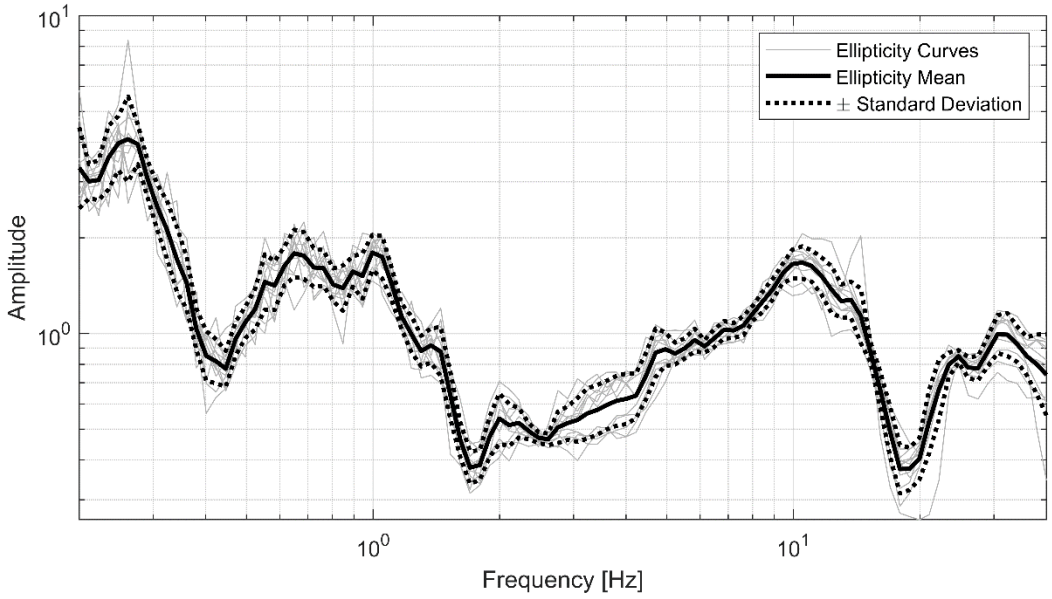

Figure D-11: R-wave ellipticity curve of seismic station 250A

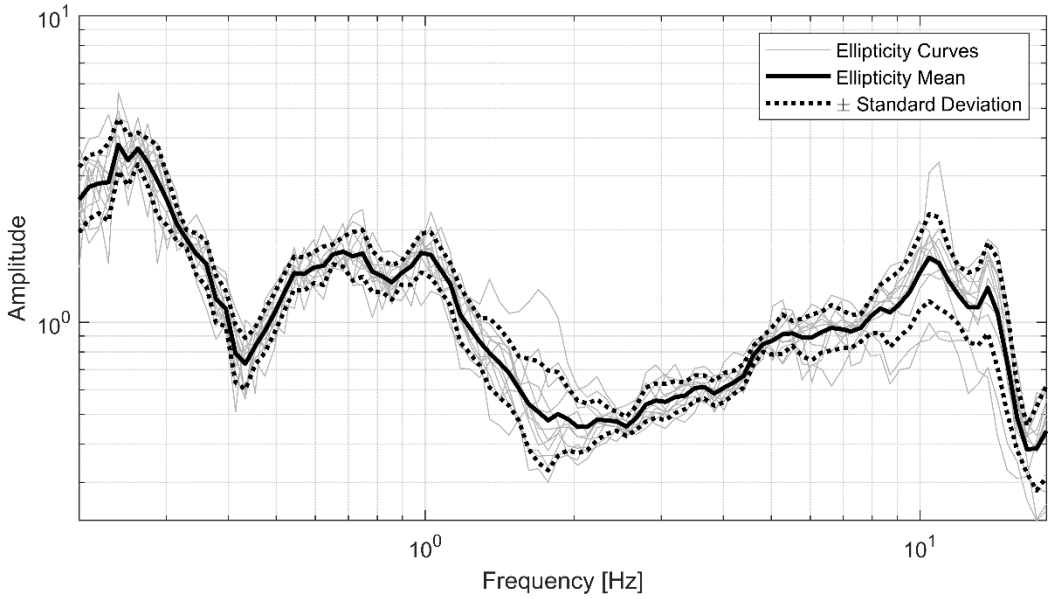

Figure D-12: R-wave ellipticity curve of seismic station 250A-V

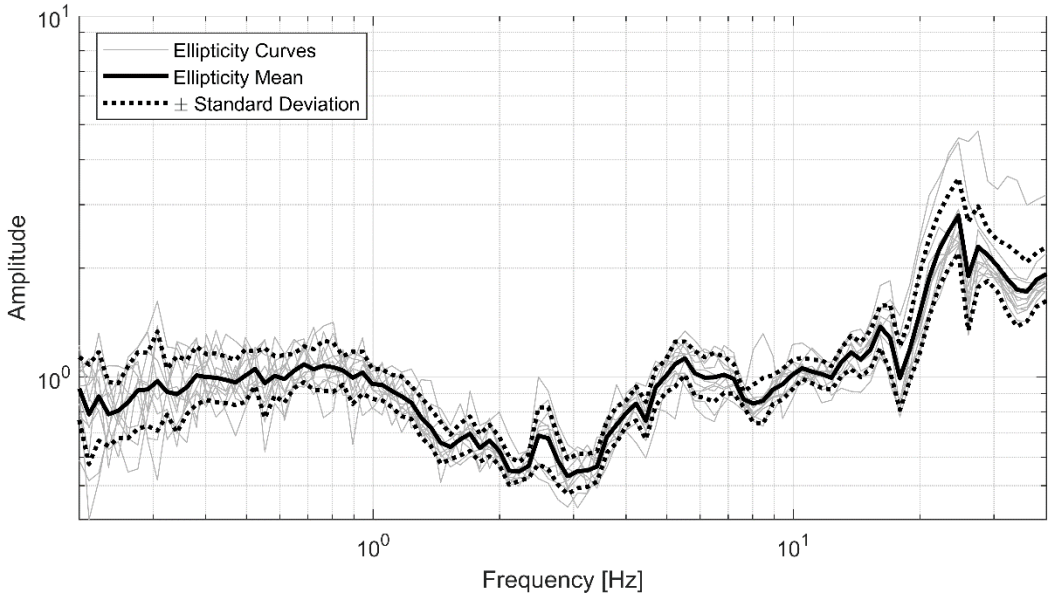

Figure D-13: R-wave ellipticity curve of seismic station B01X

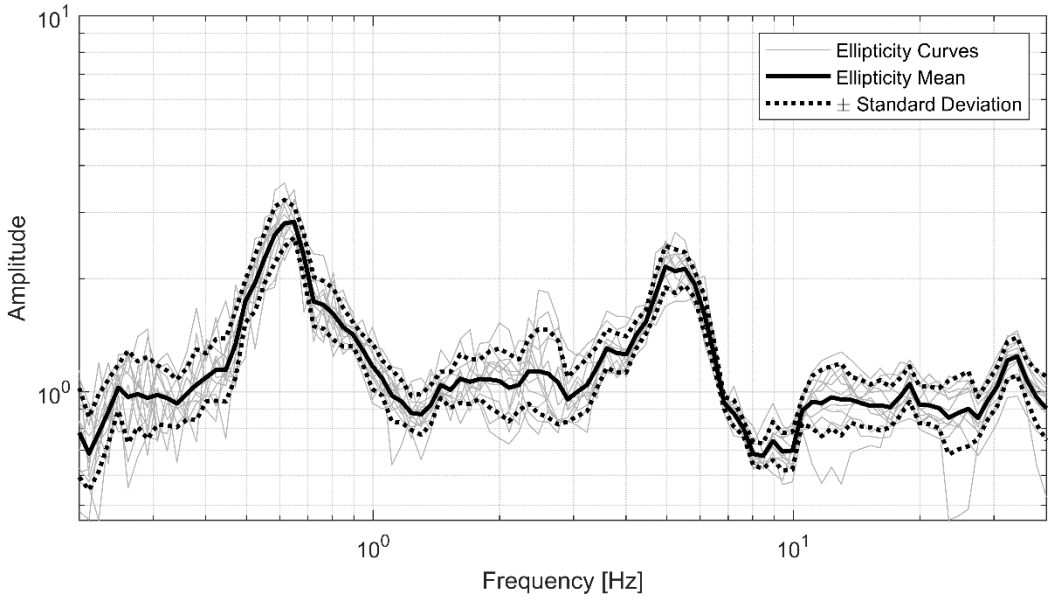

Figure D-14: R-wave ellipticity curve of seismic station Z47B

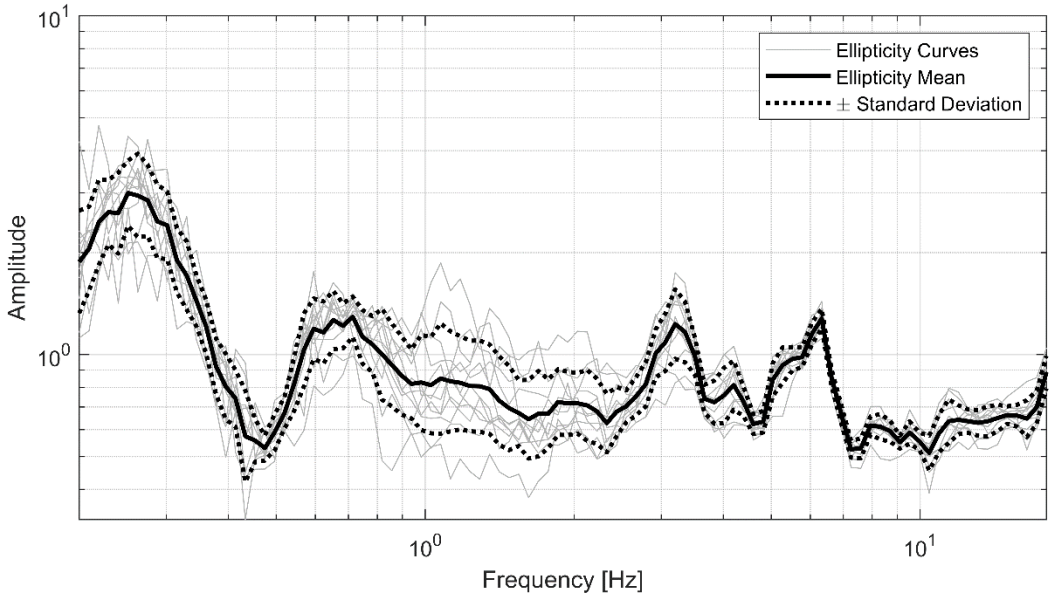

Figure D-15: R-wave ellipticity curve of seismic station 147A

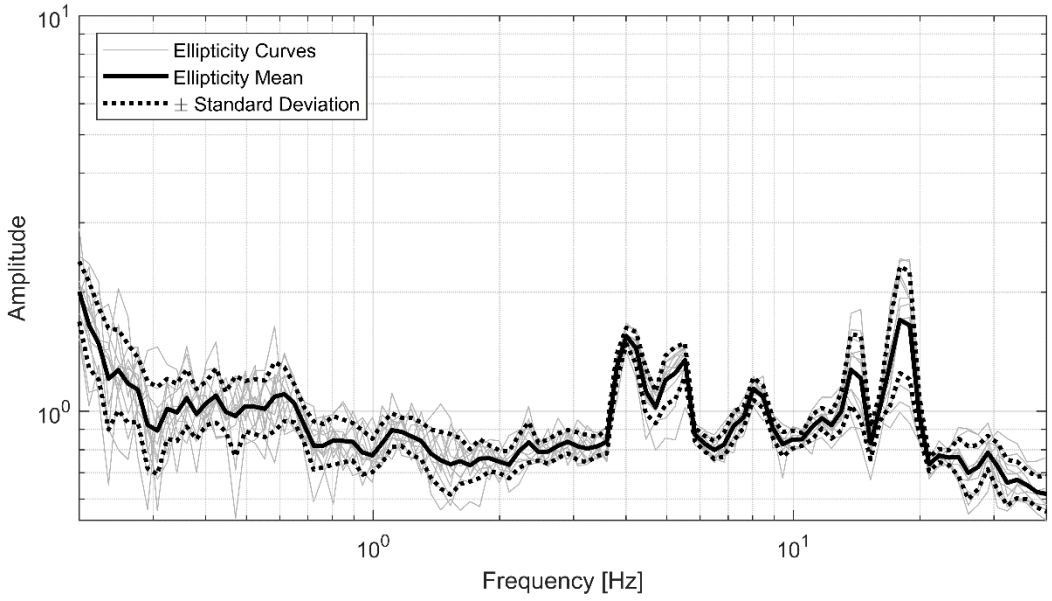

Figure D-16: R-wave ellipticity curve of seismic station F1AL

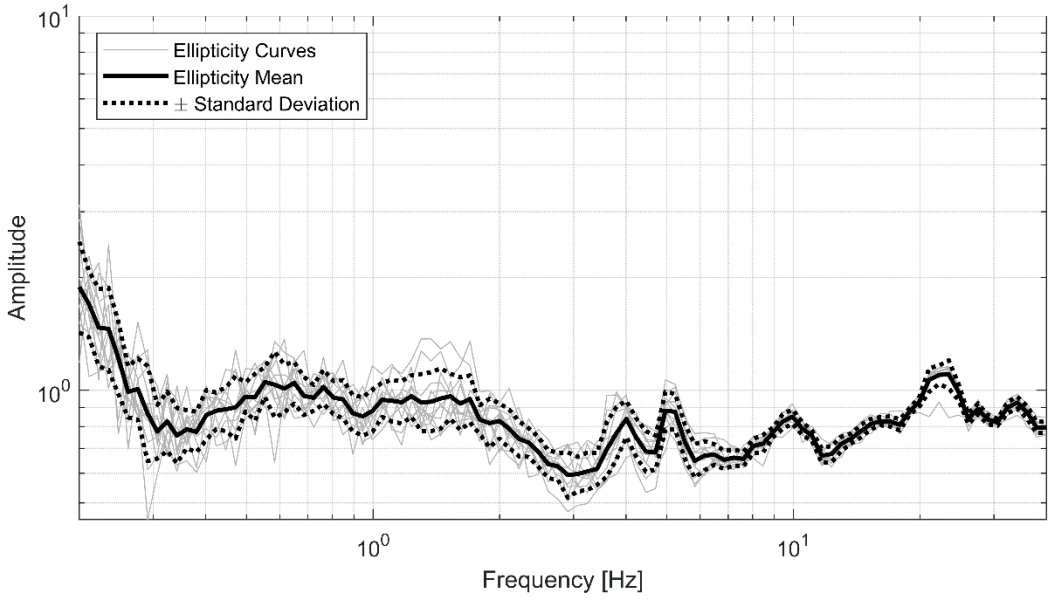

Figure D-16: R-wave ellipticity curve of seismic station S2AL

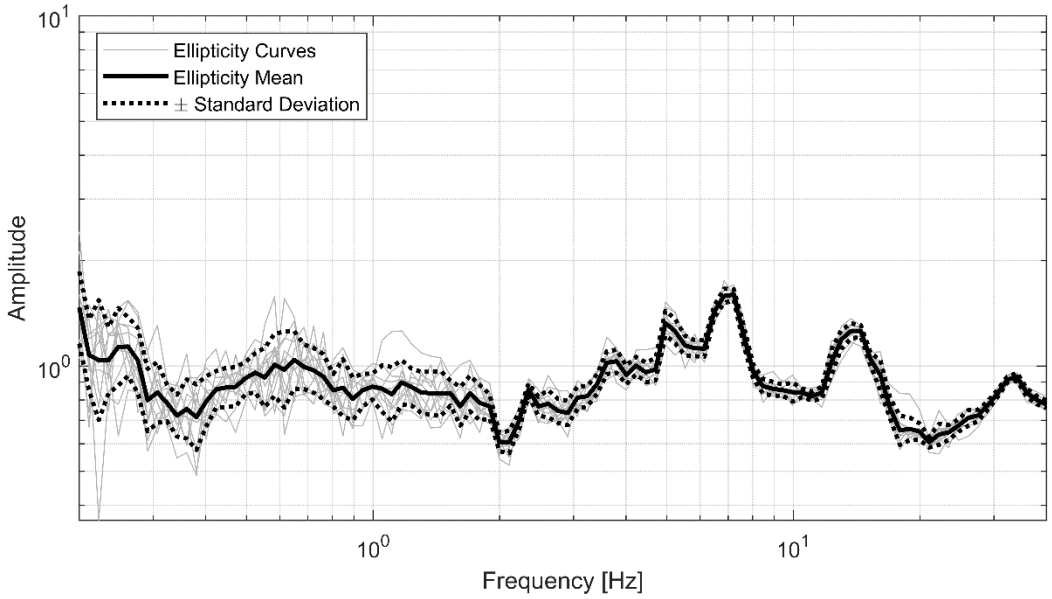

Figure D-17: R-wave ellipticity curve of seismic station S1AL